Effective Utilisation of Pressure Transients in Pipeline Systems

by

Ayaka Kashima

This report is identical to a thesis of the same name submitted in partial fulfilment for the degree of Doctor of Philosophy in Civil Engineering

Research Report 2015 - 11

Department of Civil Engineering
University of Canterbury
Christchurch, New Zealand
2015

Abstract

Fluid transients are potentially devastating phenomena in pipelines. However, some of their attributes can bring benefits to various areas of research. This thesis explores three different effective ways to use transients. The considered applications include pipeline condition assessment, unsteady flow measurements and investigation on the dynamic behaviour of hydraulic systems. The analyses involve numerical simulations by a Method of Characteristics and transfer matrix models and experimental investigations using the laboratory pipeline system at the University of Canterbury.

An impulse response function (IRF) as a transient-based condition assessment technique is studied experimentally in this thesis, and potential challenges with its use in real systems are identified and methods for improvement are presented. The proposed frequency-domain based technique achieves some enlargement and sharpening of the IRF pulses, but the extent of enhancement is constrained by a low-pass filter for noise removal. Another proposed method yields a cleaner and sharper IRF and the IRF pulses become more detectable because of multi-scale cross correlations and a wavelet-based denoising technique.

A flow metering technique known as the Kinetic Pressure Difference method is verified in order to assess its applicability in various flow conditions. The observed errors in the numerical and experimental studies are comparable to the accuracy of the existing commercial flow meters in steady flow measurements, demonstrating the potential of this method. It is identified that the system wave speed is the critical parameter for accurate flow measurements. An additional study is conducted to confirm the ability of the method to capture the change in a steady flow.

Transients are also used in this thesis for the investigation on the dynamic characteristic of leaks. Two approaches are taken for the experimental investigation. One method assesses the frequency dependent effects from the dilation of the leak reflection in the time domain. For all leak sizes considered, no significant dilation is observed, implying the absence of frequency dependency. The other approach observes the change in the frequency components of the transient signals after interacting with leaks. A comparison between the results with and without the leak exhibited some difference. Between the two approaches, the one based on the frequency-domain observations makes use of a greater amount of information from the transients and is expected to represent the unsteady leak characteristics more precisely.

Acknowledgements

First of all, I would like to express my most sincere gratitude to my primary supervisor, Dr. Pedro Lee, who has given me continual support from my undergraduate years through to the end of my PhD. His passion for research firstly motivated me to take up the PhD and secondly has been my stimulation during my research. His constructive criticism, based on his extensive knowledge in the area of this research, was vital in the completion of this thesis. I also appreciate his patience with my writing which has improved my English skills. I will treasure the experience and knowledge he has given me over the years.

I wish to also thank my co-supervisors, Dr. Mark Davidson, Dr. Roger Nokes and Dr. Mohamed Ghidaoui for their feedback and encouragement. Their comments and suggestions, often coming from a different angle to Dr. Lee's, have strengthened this thesis and I am thankful for their involvement.

My thanks also go to the laboratory technicians Mr. Ian Sheppard, Mr. Alan Stoke, Mr. Kevin Wines and Mr. Michael Weavers for their technical support and also for sharing the challenges of using the brand-new pipeline system with me.

In addition, I would like to thank both my former and current fellow PhD students, Mr. Jeff Tuck, Mr. Adi Ramakanth and Dr. Colin Whittaker for their company and valuable discussion.

Finally my friends and family deserve special mention. Their support and encouragement were essential in keeping my sanity in times of crisis during my PhD. I am grateful for this research as it has given me the opportunity to reaffirm the invaluable relationships I have with these people.

Table of Contents

List of Figures

List of Tables

List of Notations

A	=	pipe cross-sectional area
A_L	=	cross-sectional area of leak
A_O	=	cross-sectional area of orifice
a	=	wave speed
b	=	shift parameter (cross correlation)
C	=	unsteady friction coefficient
C^*	=	shear decay coefficient
C_d	=	discharge coefficient
C_dA_L	=	lumped leak discharge coefficient
c	=	arbitrary constant
	=	target signal (cross-correlation)
D	=	pipe diameter
E	=	root mean square error
	=	$E_{Profile}$
E_{Volume}	=	error in volumetric measurement
E_{Max}	=	error in maximum flow pulse amplitude
erf	=	complex error function
F	=	fundamental frequency of system
	=	frequency response function
F_{ij}	=	FRF describing the relationship between the *j*th input and the *i*th output
$[F]$	=	frequency response matrix
f	=	Darcy-Weisbach friction factor
	=	frequency
f_c	=	cut-off frequency
f_{cd}	=	cut-off frequency of dilation filter
f_{cn}	=	cut-off frequency of noise filter
f_s	=	frequency of perturbation
G	=	transient generator
$[G_{uu}]$	=	input cross-spectral matrix
$[G_{yu}]$	=	cross-spectral matrix between input and output
g	=	gravitational acceleration

H = instantaneous head

H_L = head at leak

H_0 = steady state head

H_{L0} = steady state head at leak

h = head perturbation about steady conditions (frequency domain)

h^* = head perturbation about steady conditions (time domain)

$h^{*\prime}$ = dimensionless head perturbation (time domain) (= h^*/H_0 or $h^*/\max(h^*)$)

h_L = head perturbation about steady conditions at a leak (frequency domain)

h_L^* = head perturbations about steady conditions at a leak (time domain)

h_L' = dimensionless leak head perturbation (frequency domain)

I = impulse response function

J = total friction loss per unit length

J_S = friction loss per unit length due to steady friction

J_U = friction loss per unit length due to unsteady friction

j = $\sqrt{-1}$

L = total length of the pipeline

L_T = distance between two transducers

L_T' = dimensionless distance between two transducers (= L_T/L)

l = length of a pipe section

l_a = distance between two pressure transducers

l_b = distance from the most downstream pressure transducer to point of flow prediction

l_g = distance from flow prediction point to transient source

Q = instantaneous flow

Q_L = instantaneous flow at leak

Q_0 = steady state flow through pipe

Q_{L0} = steady state flow at leak

q = flow perturbation about steady conditions (frequency domain)

q^* = flow perturbations about steady conditions (time domain)

$q^{*\prime}$ = dimensionless flow perturbation (time domain) (= q^*/Q_0 or $q^*/\max(q^*)$)

q_L = leak flow perturbation about steady conditions (frequency domain)

q_L^* = leak flow perturbation about steady conditions (time domain)

q_L' = dimensionless leak flow perturbation (frequency domain)

q_s	=	size of introduced flow oscillation
R	=	resistance term (= $R_S + R_U$)
Re	=	Reynolds number = (VD/ν)
Rs	=	steady resistance factor
R_U	=	unsteady resistance factor
r_{yc}	=	coefficient of cross correlation between target signal, c and output, y
s	=	scale of wavelet
	=	scale of truncated sinc signal
T	=	period of system
T	=	pressure transducer
T_R	=	recurrence period
T_S	=	period of pipe section (= $2L_T/a$)
T_S'	=	dimensionless period of pipe section (= T_S/T)
t	=	time
t'	=	dimensionless time (= t/T)
t^*	=	time used in convolution integral
U	=	input to the system (frequency domain)
u	=	input to the system (time domain)
V	=	flow velocity
W	=	weighting function (unsteady friction)
	=	window function (noise removal)
x	=	distance along the pipe
Y	=	output from the system (frequency domain)
y	=	output from the system (time domain)
Z_a	=	terminal impedance
Z_b	=	terminal impedance
Z_C	=	characteristic impedance for pipe
z_L	=	elevation at the leak
ΔH	=	change in head (Joukowsky equation)
	=	system head loss
	=	head loss across orifice
ΔQ	=	change in flow
$\Delta Q'$	=	dimensionless change in flow (= $\Delta Q/Q_0$)

Δt	=	time increment in MOC simulations
	=	time width of signal
$\Delta t'$	=	dimensionless time width of signal (= $\Delta t/T$)
$\delta t'$	=	dimensionless time lag (= $\delta t/T$)
μ	=	propagation constant
Π	=	dimensionless parameter derived from the nonlinear term in the momentum equation
τ	=	orifice opening coefficient (= $C_d A_L / (C_d A_L)_{REF}$)
	=	dummy variable (convolution integral)
	=	dimensionless time (unsteady friction weighting function)
τ_0	=	orifice opening coefficient at steady state (= $(C_d A_L)_0/(C_d A_L)_{REF}$)
ν	=	kinematic viscosity
ω	=	angular frequency

Chapter 1 Introduction

Pipelines are the most widely used means for the transportation of water due to their safe and economical properties and are essential assets for maintaining our high quality of life (Cosham *et al*. 2007, Teixeira *et al*. 2008, Kishawy and Gabbar 2010, El-Abbasy *et al*. 2014, Nayak 2014). In order to meet the increasing water demand, new pipelines are laid continually. According to the American Water Works Association, 19,000 kilometres of new water distribution pipelines are installed each year worldwide (Smith *et al*. 2000). In addition to water, pipelines are also used to transport oil and gas across continents. Oil and gas pipelines supply energy needs and are critical to the economies in most countries. By 2007, there were approximately 3,500,000 km of pipelines for oil and gas around the world (Hopkins 2007).

One threat to pipeline systems is fluid transients. They are pressure fluctuations generated when the flow condition changes from steady state. Flow changes occur due to various reasons, for example, from the opening or closing of valves and gates and the starting and stopping of pumps (Chaudhry 1987, Wylie and Streeter 1993, Collins *et al*. 2012). The large positive and negative pressure of a transient can result in pipe bursts and collapses respectively and the force exerted by the transient can loosen pipe joints (Chaudhry 1987, Collins *et al*. 2012 Wang *et al*. 2014). Whilst fluid transients have the potential to cause catastrophic failures and loss of life when their magnitude exceeds the strength capacity of the system, they can also be a useful tool for pipeline systems in a number of ways if they are carefully controlled.

1.1 Objectives

The aim of this thesis is to investigate the effective uses of fluid transients in pipeline systems. The three applications discussed in this research are:

1. Condition assessment of pipeline systems
2. High speed unsteady flow measurement
3. Quantification of dynamic characteristics of hydraulic elements

1.1.1 Use of transients in condition assessment of pipeline systems

Many pipeline systems are approaching the end of their designed service life and aging pipelines suffer from blockage and leakage which reduce the operational efficiency and create wastage of valuable resources (Colombo *et al*. 2009, Hughes 2012, Nayak 2014). Blockages impede the fluid flow and cause an increase in pumping costs and degradation of the quality of the fluid (Duan *et al*. 2013, Meniconi *et al*. 2013). Leaks in water distribution systems places further stress on existing water scarcity problems and necessitate extra pumping and treatment costs (Colombo and Karney 2002, 2009). In the case of gas and oil pipelines, leakage also causes threats to public health and the environment (Vítkovský *et al*. 2003a, Chatzigeorgiou *et al*. 2015).

Pipeline leaks occur for several reasons including corrosion, welding defects, corrosion and poor workmanship (Liou and Tian 1995, Nayak 2014, Ozevin and Yalcinkaya 2014) and the occurrence of leaks increases with the age of the pipes. Since many pipelines around the world are due for replacement, a significant portion of water and energy is lost through leakage per year. Some of the reported percentages of water loss around the world are: 22.8% in England and Wales, 34.9% in Scotland, 13% in Canada, 9% in Germany, 39% in Indonesia and 43% in Malaysia (Japan Water Research Center 2013, Colombo *et al*. 2009). Despite the high leakage rate around the world, Tokyo managed to reduce the leakage rate from 20% to 2% in 2012 (Takadou 2011, Shibata 2014). This low leakage rate was achieved by a well-planned pipeline management scheme and early detection and repair of leaks (Shibata 2014). Tokyo Waterworks Bureau reported that lowering the leakage rate reduced the amount of distributed water by 240 million cubic metres per year and the operational cost by ¥JPN4.8 billion per year. This accomplishment in Tokyo highlights the importance of condition assessment of pipeline systems.

Leak detection in Tokyo relies on acoustic means which is the most widely used leak detection technique (Eiswirth and Burn 2001, Thornton *et al*. 2008, Cataldo *et al*. 2014, Shibata 2014). Despite its popularity, it demands a high level of user experience and has a low operational range (~ 250 m) (Tafuri 2000, Beck *et al*. 2005, Colombo *et al*. 2009). Considering the extensive pipeline network of Tokyo and the cost and time required for personnel training, the acoustic approach is an expensive and time-consuming technique.

With an aging population and the development of water-saving technology, it will become a challenging task to secure sufficient funds to sustain the water pipeline management program in Japan in the future. Ministry of Health, Labour and Welfare of Japan estimates the cost for pipe renewal to grow to approximately ¥JPN1000 billion in 2025 which exceeds the estimated available funds (Shibata 2014). Thus, a fault detection technique with a low labour cost and a high operational range is essential and methods based on fluid transients are a good candidate (Chaudhry 1987, Colombo *et al*. 2009, Lee *et al*. 2014).

Fluid transients have been used in several fault detection methods such as the time-domain reflectometry techniques (Jönsson and Larson 1992, Silva *et al.* 1996, Brunone 1999, Covas and Ramos 1999, Ferrante and Brunone 2001, Jönsson 2001, Vítkovský *et al.* 2003a, Kim 2005, Lee *et al*. 2007a, b, Meniconi *et al*. 2011a, b, 2012, Gong *et al*. 2012) and the inverse transient analysis (Liggett and Chen 1994, Vítkovský *et al*. 2007). One of the time-domain reflectometry techniques makes use of an impulse response function (IRF) which defines the characteristics of a system that is depicted by a box in Figure 1.1. An input signal, $u(t)$, enters the system and it is modified according to the IRF. The modified signal is detected as an output of the system, $y(t)$.

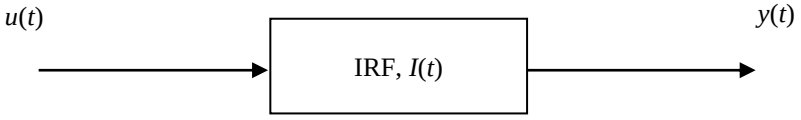

Figure 1.1 – Schematic of a system with input and output signals

An advantage of the IRF is that it refines the measured pressure response and gives a more defined reference point for a subsequent localization process, such as the determination of the occurrence time of a signal. Figure 1.2 shows a comparison of a pressure trace measured in a numerical pipeline system and the IRF of the system. The time, *t'*, and the amplitude of the pressure fluctuation, *h*'*, in Figure 1.2 are normalised by the period of the pipeline system and the steady head at the measurement point respectively. The occurrence times of the signals match between the two traces but the IRF has impulses instead of pulse signals of a finite width.

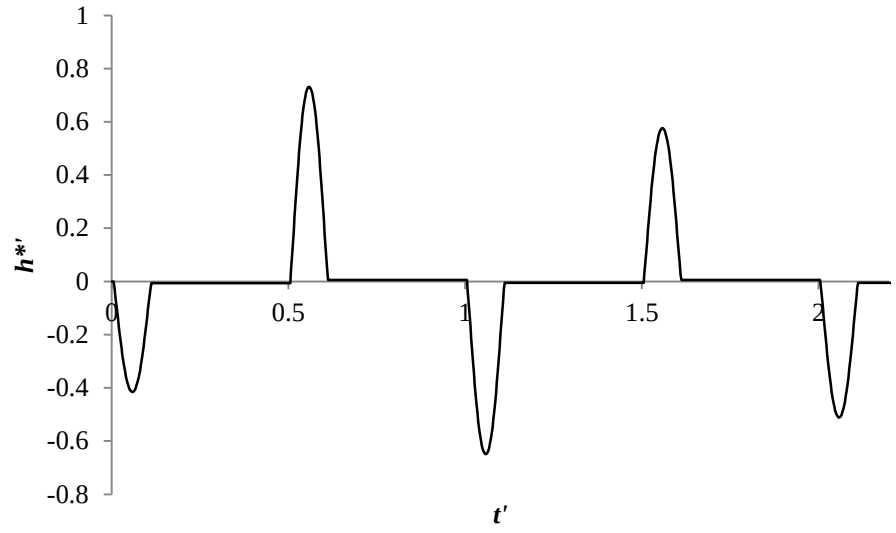

(a) Pressure trace measured in the numerical pipeline system

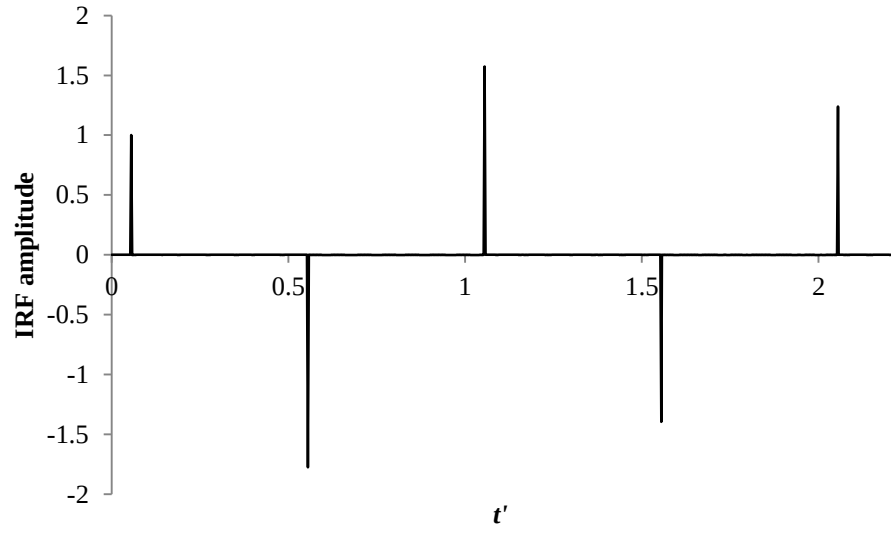

(b) IRF determined from the pressure trace in (a)

Figure 1.2 – Comparison between measured pressure trace and determined IRF

In addition to the field of hydraulics, the IRF is also used in other applications such as damage inspection of large structures (Sabra *et al*. 2007, Todorovska and Trifunac 2008, Prieto *et al*. 2010), in the study of unsteady aerodynamic behaviour (Guendel and Cesnik 2001, Silva *et al*. 2005), and to examine the influence of economic shocks and to forecast the reaction of variables to the shocks (Raufi and Bahar 2012, Hatemi-J 2014).

While the use of the IRF provides advantages over measured signals, its extraction from data acquired in real systems suffers from background noise, limited signal bandwidth and signal

dilation in the time domain. The resultant IRF differs considerably from its theoretical form as shown in Figure 1.2 (b). This thesis presents methods to improve the conventional IRF.

The IRF can be extracted from one system parameter and in the field of hydraulics, pressure is the most easily-obtainable variable. It is not exclusive to the extraction of the IRF, but past research in this area has been largely based on pressure measurements alone. The ability to obtain both flow and pressure information in unsteady flows will provide a more complete picture of real transient flow behaviour and can have a significant impact on the research efforts in this area. An unsteady flow measurement technique that makes use of transients is investigated in this thesis.

1.1.2 Use of transients in unsteady flow measurement

The accurate measurement of unsteady flow rate in pressurised pipelines is very important in a large number of industrial, engineering research and laboratory processes. In the food and beverage sector the quality of the product depends largely on the correct measurement of each ingredient and is carefully monitored using real time flow measurements (Mangell 2008). The flow information is required also in the control of pipeline systems with piston pumps or fast switching valves, for the monitoring of pharmaceutical processes with fast-batch filling systems, or for the efficient operation of internal combustion engines to maintain the optimum fuel to air ratio which minimises the emission of harmful exhaust gases (Unsal *et al*. 2006, Brereton *et al*. 2008, Manhartsgruber 2008). Furthermore, the ability to measure rapid flow changes is important for the research efforts into unsteady friction, pipe-wall viscoelasticity, fluid-structure interaction, as well as the application of fluid transient signals for pipe defect detection (Rachid and Mattos 1998, Pezzinga 2000, 2009, Wang *et al*. 2002, 2005, Lee *et al*. 2005a, b, YongLiang and Vairavamoorthy 2005, Soares *et al*. 2008, Ferrante *et al*. 2011). While pressure transducers with sampling rates capable of capturing a transient pressure wave are common, a device capable of measuring flow at the same speed is not commercially available.

This thesis gives an overview of some commercial flow meters with emphasis on some key attributes for an ideal unsteady flow meter and presents a detailed verification of a flow measurement technique known as the Kinematic Differential Pressure (KDP) method. This

method determines flow rates at a point in a pipeline system from pressure measurements and the known relationship between the pressure and flow in unsteady flow. It inherits the advantages of pressure sensors in that it has a fast response time and non-intrusive nature. The KDP method has shown its potential as a high speed flow measurement technique in past studies (Yokota *et al*. 1992, Washio *et al*. 1996, Manhartsgruber 2008) and it is further tested in this thesis in a range of system conditions in order to assess its practicability in real world flow conditions.

Transient pressure and flow data give an insight into the behaviour of hydraulic elements (valves, pumps, leaks) in unsteady flow which may differ from that in steady flow. Such information will extend the current knowledge of these elements and is vital for the establishment of their mathematical models and consequently, cost-effective designs and effective management tools (Martin and Burrows 1976, Yamaguchi 1976, Hayase *et al*. 1995, Prenner 2000). This thesis uses transient pressure and flow information to investigate the dynamic characteristics of leaks.

1.1.3 Use of transient in study of dynamic characteristics of hydraulic element

Due to the negative impacts of pipe defects on the network, a large body of research has been carried out on the development of fault detection methods over the years (Liggett and Chen 1994, Silva *et al*. 1996, Covas and Ramos 1999, 2010, Ferrante and Brunone 2003, Vítkovský *et al.* 2006, Wang *et al*. 2005, Lee *et al*. 2008, Peng *et al*. 2012, Gong *et al*. 2012, Meniconi *et al*. 2013, Srirangarajan *et al*. 2013, Duan *et al*. 2013). However, in comparison, studies concerning their unsteady characteristics are few, particularly under unsteady transient flow conditions. More complete knowledge of pipe defects can improve the existing transient-based fault detection techniques such as the inverse transient method whose effectiveness hinges on an accurate transient model of the system of interest (Covas *et al*. 2001).

This thesis examines the behaviour of leaks in unsteady flow using time- and frequency-domain based methods. More specifically, the work aims to determine whether the leaks exhibit frequency-dependent effects in unsteady flow. A phenomenon is said to be frequency dependent if its influence on one or more frequency components of a signal is different from

that on other frequency components. Such differences appear as attenuation, dilation and smoothing of the signal in the time domain. Frequency-dependent phenomena commonly seen in pipeline systems include unsteady friction, viscoelasticity and fluid-structure interaction (Ramos *et al*. 2004, Bergant *et al*. 2001, Soares *et al*. 2008, Duan *et al*. 2010).

The method in the time domain assesses the frequency-dependency of the leak from the dilation of reflections from the leak. The method correlates a reference signal of varying widths with the detected transient signals and measures the signal dilation in terms of the width of the reference signal. The frequency-domain based method involves the extraction of frequency response matrix (FRM) of the leak. Similar to the IRF, the FRM depends solely on the component and is independent of the connected system. In acoustics, acoustic properties such as acoustical impedances and transmission factors are essential for the evaluation and understanding of an object and these properties can be extracted from the FRM (To and Doige 1979, Kojima and Edge 1994). Lung and Doige (1983) investigated exhaust mufflers using this approach and found excellent agreement between the theoretical and experimental results. In the area of hydraulics, objects such as rigid pipe sections, flexible hoses (Johnston *et al*. 1994), pumps (Stirnemann *et al*. 1987) and hydraulic silencers (Kojima and Edge 1994) have been studied from the determined FRM. The accuracy of the results in these studies showed the validity of the approach. The frequency-domain analysis makes it possible to observe the extent of the unsteady leak effects on individual frequency components which has not been done before.

1.2 Thesis outline

The literature review is given in Chapter 2 in which the principle behind the fault detection technique with the IRF is explained and the past IRF-based fault detection work is reviewed. This chapter also introduces some existing flow metering techniques and the previous research on the dynamic characteristics of orifice-based elements. Chapter 3 presents the fundamental equations of unsteady pipe flow which are converted to suitable forms for numerical modelling in the time and frequency domains. Chapter 4 gives information on the numerical and experimental pipeline systems used in this thesis. Chapters 5, 6 and 7 contain the work related to the objectives of this thesis and the contents of these chapters are

identified in more detail in the next chapter. Finally, the findings in Chapter 5 to 7 are summarised in Chapter 8.

1.3 Publication list

The publications produced during this research are listed below.

Journal papers

1. Duan, H., Lee, P.J., Kashima, A., Lu, J., Ghidaoui, M., and Tung, Y. (2013). Extended Blockage Detection in Pipes Using the system Frequency Response: Analytical Analysis and Experimental Verification. Journal of Hydraulic Engineering, 139(7), 763-771.

2. Kashima, A., Lee, P.J., Nokes, R. (2012). Numerical errors in discharge measurements using the KDP method. Journal of Hydraulic Research, 50(1) 98-104.

3. Kashima, A., Lee, P.J., Ghidaoui, M.S., Davidson, M. (2013). Experimental verification of the kinetic differential pressure method for flow measurements. Journal of Hydraulic Research, 51(6) 634-644.

In the journal article 1, the thesis author played a role of an experimentalist and conducted laboratory experiments. The remaining articles are related to Chapter 6 of this thesis and they were written based on the laboratory data and analyses conducted by the thesis author with guidance from the co-authors.

Conference papers

1. Kashima, A., Lee, P.J., Nokes, R. (2010). Accuracy of instantaneous flow rate estimation using pressure measurements. 17th Australasian Fluid Mechanics Conference 2010, 182-185.

2. Brunone, B., Meniconi, S., Lee, P.J., Kashima, A., Ferrante, M. (2011). Impulse response function and wavelet analysis of transient pressure signals for leak detection in pipes. Urban Water Management: Challenges and Opportunities - 11th International Conference on Computing and Control for the Water Industry, CCWI 2011.

3. Kashima, A., Lee, P.J., Ghidaoui, M.S., Davidson, M. (2012). Modelling errors in flow measurements using the KDP method. BHR Group - 11th International Conferences on Pressure Surges, 667 – 677.

4. Kashima, A., Lee, P.J., Ghidaoui, M.S. (2012). A selective literature review of methods for measuring the flow rate in pipe transient flows. BHR Group - 11th International Conferences on Pressure Surges, 733 – 742.

5. Tuck, J., Lee, P.J., Kashima, A., Davidson, M., Ghidaoui, M.S. (2012). Transient analysis of extended blockages in pipeline systems. BHR Group - 11th International Conferences on Pressure Surges, 101 – 112.

The conference papers 1, 3 and 4 of the list above are related to Chapter 6 of this thesis. The roles of the thesis author and the co-authors were the same as for the journal articles 2 and 3. For the conference paper 2, the thesis author analysed the laboratory data to determine the impulse response function of the system under test. The thesis author assisted the first author in conducting experiments for the conference paper 5.

Chapter 2 Literature Review

This chapter provides a review of past work related to the aims of the thesis: pipeline condition assessment, unsteady flow measurement and the unsteady behaviour of leaks.

2.1 Literature review on pipeline condition assessment technologies and impulse response function

The demand for water and energy around the globe has driven continual installation and expansion of pipeline infrastructure. Compared to the effort and money spent on the development of new pipeline systems, however, the management of existing pipelines has been given relatively little attention. The recent increase in the number of pipeline accidents due to the deterioration of the pipelines and their impact on the economy and surrounding environment have urged the development of condition assessment methodologies. Examples include methods of visual inspection (Black 1992, Thornton *et al*. 2008), electromagnetic waves (Graf 1990, Jol and Smith 1995, Hazelden *et al*. 2003, Bimpas *et al*. 2011, Ayala–Cabrera *et al*. 2013) and acoustic waves (Fuchs and Riehle 1991, Tafuri 2000, Martins and Seleghim 2010, Khulief *et al*. 2012, Yang *et al*. 2013, Nayak 2014). Many other assessment techniques are commercially available and their comprehensive summary can be found in Liu *et al*. (2012).

The application of the above-mentioned methods to long transmission mains is hampered by their limited operational range and some require high level of experience and training for operation and data interpretation (Eiswirth and Burn 2001, Beck *et al*. 2005, Colombo *et al*. 2009). As an alternative, the integrity of pipelines can be examined using transients. Transient-based methods for pipeline condition assessment have been developed in the last two decades and these methods can be categorised into three groups: the inverse transient method, the frequency response method and the transient reflection method (Duan *et al*. 2010, Liu *et al*. 2012). The inverse transient method carries out inverse calibration of a numerical model and faults are detected and located by minimizing the difference between the measured and computed transient trace (Liggett and Chen 1994, Nash and Karney 1999, Vítkovský *et al*. 2002, 2003b, Covas and Ramos 2010). The frequency response method

seeks changes to the frequency response function of the system imposed by anomalies (Covas and Ramos 1999, Ferrante and Brunone 2003, Vítkovský *et al*. 2003a, Kim 2005, Lee *et al*. 2005a, b, 2006a, b, 2008b, Duan *et al*. 2011, 2012a, b, 2013, 2014). The transient reflection method employs the principle of time-domain reflectometry.

Time-domain reflectometry (TDR) makes use of the reflecting characteristic of transients to detect faults in a pipeline. In the application of TDR, a transient pressure signal is generated and transmitted along a pipeline. If there is a singularity in the pipe, part of the signal is reflected as illustrated in Figure 2.1. Figure 2.1 (a) indicates a path taken by a transient wave generated in the middle of a pipeline system. A leak is positioned some distance away from the generator. A pressure transducer is placed in between the generator and the leak and the measured pressure trace is shown in Figure 2.1 (b). The time, t', and the amplitude of the pressure fluctuation, $h^{*'}$, in the figure are normalised by the period of the pipeline system and the steady head at the measurement point respectively.

The transient wave propagates through the system and is detected by the transducer ("A" in Figure 2.1 b). When it arrives at the leak, it partially reflects and the reflected signal travels back toward the transducer ("B" in Figure 2.1 b). The reflected signal appears in the pressure trace and exposes the leak in the system.

The location of the leak is determined relative to the pressure measurement point. The time lag between the arrival of the generated and reflected signals ($\delta t'$ in Figure 2.1 b) along with the wave speed of the system gives the distance to the leak from the transducer. Due to the simplicity in application and analysis, TDR has been used in numerous publications (Jönsson and Larson 1992, Silva *et al.* 1996, Brunone 1999, Covas and Ramos 1999, Ferrante and Brunone 2003, Jönsson 2001, Vítkovský *et al.* 2003a, Kim 2005, Lee *et al*. 2007a, b, Meniconi *et al*, 2011a, b, 2012, Gong *et al*. 2012).

Success with TDR hinges on the accurate determination of arrival times of signals which are detected by visual inspection. The signals must have clear reference points for accurate inspection. Such a requirement poses difficulties in the application of TDR in real systems. Real pipeline systems have sources of disturbance that are unrelated to a fault and these disturbances may mask the fault-reflected signals. In addition, pressure waves are modified

from dispersive effects and reflected signals can become smooth, making it difficult to accurately determine the arrival times and hence the location of the faults (Vítkovský *et al*. 2003a, 2007). In order to improve the accuracy in estimated fault locations, an impulse response function (IRF) can be employed.

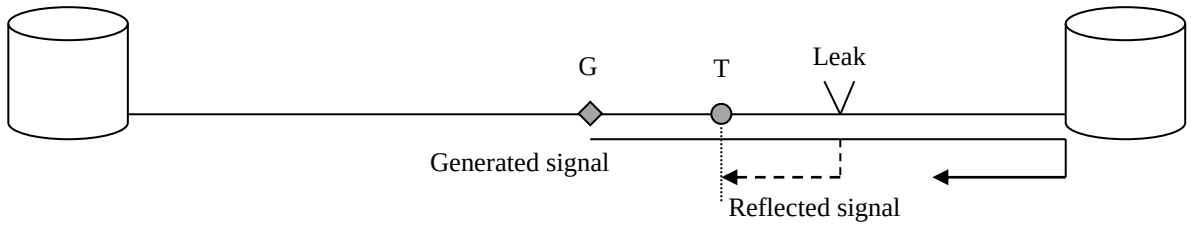

(a) Wave path taken by the transient pressure signal. The transient generator and pressure transducer are given symbols "G" and "T" respectively

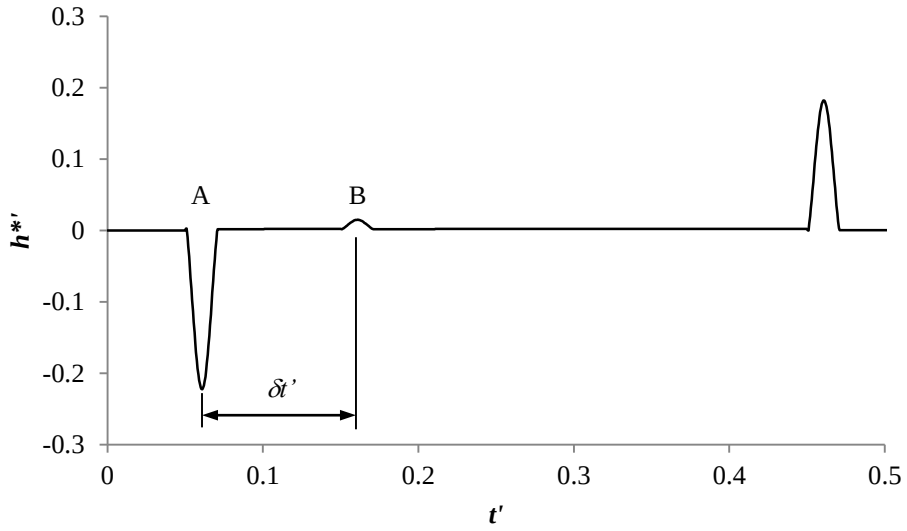

(b) Measured pressure trace

Figure 2.1 – Illustration of TDR technique

An IRF is a good supplementary tool for other time-domain reflectometry methods owing to its ability to convert the output signals into sharp impulses as briefly illustrated in the previous chapter. This conversion enables more accurate determination of the arrival times. The IRF has been applied to detect both discrete and distributed faults in pipelines (Liou 1998, Vítkovský *et al*. 2003a, Lee *et al*. 2007a, Gong *et al*. 2012). The use of IRF in fault detection was first proposed by Liou (1998) in which the IRF was used to determine the steady-state hydraulic grade line along a pipeline. A leak was detected from changes in the hydraulic grade line that results from different flow rates—and hence friction losses—either

side of the leak. Vítkovský *et al*. (2003a) extracted IRFs from fault-free pipelines and pipelines with leaks and/or blockages. In the numerical illustrations, the reflected signals off the faults appeared as impulses and their locations were correctly determined. The approach used in this work was experimentally validated by Lee *et al*. (2007a) who also showed the effect of noise and signal bandwidth on the extracted IRF. The signal bandwidth defines the range of useful frequencies in the signal and the inclusion of frequency components beyond the signal bandwidth in the extraction process results in significant distortion of the resultant IRF. As a mitigation measure, a window function was employed to remove the higher frequencies and an improvement was observed. The leak location estimated from the IRF had an error of 0.65% which was better than the result from the raw pressure trace. Gong *et al*. (2012) utilised the IRF to determine the location and length of a pipe section with different wall thickness. The raw pressure data showed two reflected signals indicating the boundaries of the pipe section and these signals were sharpened in the IRF. The errors in the determined location and length were 0.7% and 17.6% of the theoretical values respectively.

The previous publications have shown that the current IRF extraction procedure is able to refine the raw pressure signals, but it cannot convert them into impulses as numerically demonstrated. There are a few factors responsible for this difference which will be discussed in Chapter 5. The chapter also provides a more detailed review of the current IRF extraction procedure and proposes methods for improvement.

2.2 Literature review on existing flow meters

Given the importance of accurate flow measurements, past research efforts have produced a number of different flow metering techniques. This section presents a review of the main types of commercial flow meters, with particular attention on their characteristics such as their intrusiveness, physical size, and response time. Limitations of the existing commercial flow meters in measuring rapidly varying unsteady flows are highlighted and the need for a new type of flow measuring method that utilises dynamic pressure measurements is discussed.

The commercial flow meters considered here are the differential pressure, Coriolis, electromagnetic, ultrasonic and the Laser Doppler velocimetry meters.

2.2.1 Differential pressure flow meters

By far the most widely used flow metering technique is the differential pressure meter and it relates the flow rate to the differential pressure across a pressure-loss-inducing element (Doebelin 1990, Mangell 2008). Differential flow meters have one of the lowest initial setup costs when compared to other devices, but despite this advantage the need for a pressure-loss element in the pipeline creates irrecoverable energy losses as well as significant disruptions to the flow behaviour (Doebelin 1990). The size of these meters also increases with the pipe size and can become inconvenient for large systems. The major constraint when using differential pressure meters in unsteady flow is that the underlying Bernoulli's equation is derived under the assumption of steady flow and is unable to cope when flows are changing rapidly. The response times of orifice meters were tested under low frequency (2 Hz) pulsating flow in Wiklund and Peluso (2002) and the results were presented in Henry *et al*. (2003). A response time of over 100 milliseconds was measured for this type of meter and this long response time makes them incapable of measuring higher frequency flow changes, such as the fuel injection process in internal combustion engines or transient flows in a pipeline system both of which have flow changes in the order of milliseconds (Clark *et al*. 2008, Catania and Ferrari 2009).

2.2.2 Coriolis flow meters

Apart from the slow response, one of the limitations of orifice flow meters is the need for a pressure-loss element that disrupts the flow as well as increasing the operational costs of the system. Flow meters that do not have this requirement are clearly desirable. One such flow meter is a Coriolis flow meter in which the flow travels through a vibrating bent tube. As the tube oscillates in one direction, the fluid at the tube entrance experiences an opposing Coriolis force to the fluid at the exit. These opposing Coriolis forces result in an additional twisting on top of the vibration. Position sensors are installed on either side of the tube to measure the amount of twist—which is also known as the phase shift—and this quantity is proportional to the mass flow (Clark *et al*. 2008).

Recent developments have seen the response time of Coriolis flow meters improve substantially (Clark and Cheesewright 2006, Clark *et al*. 2008, Henry *et al*. 2003), and after

correcting for measurement error these meters are seen to respond within 35 milliseconds of an excitation. Some commercial Coriolis flow meters now have the response time of 20 ms. Despite their high response rate, Coriolis flow meters require the entire flow to travel through a specially designed flexible tube and are limited to a pipe diameter of two inches or less (Mangell 2008). A technique that has a similar response rate to the Coriolis flow meter and yet does not have the limitation regarding system size is the electromagnetic flow meter.

2.2.3 Electromagnetic flow meters

Electromagnetic flow meters were used to give reference time traces for the development of the Coriolis flow meter in Clark and Cheesewright (2006) because of their fast response time (Catania and Ferrari 2009, Clark and Cheesewright 2006, Doebelin 1990). The operational principle of magnetic flow meters is based on Faraday's Law of induction, which states that the voltage induced as a conductive fluid passes at right angles through a magnetic field is proportional to the velocity of that fluid. Magnetic flow meters make use of magnetic coils to generate a magnetic field. As a conductive fluid flows through the magnetic field, a voltage is induced which is measured by meter electrodes.

Commercial electromagnetic flow meters can achieve a response time of 20 - 30 milliseconds and do not create any obstructions to the flow. However, as with the above-mentioned flow meters, they need to be inserted at the point of flow measurement within the pipeline system and the size of the meter increases with the pipe size. Furthermore, since Faraday's law of induction only applies to conductive fluids, working fluids for magnetic flow meters are limited by their conductivities. Some commercial magnetic flow meters can deal with fluids with conductivities as low as 0.5μS/cm, however, gasoline has a conductivity of 10^{-8}μS/cm and cannot be measured by magnetic flow meters (Catania and Ferrari 2009, Doebelin 1990). The pipeline material must also be non-conductive and metallic pipes require installation of a non-conductive rubber liner for these meters to operate accurately.

2.2.4 Flow measurement technique using Laser Doppler Velocimetry

Similar to the electromagnetic and Coriolis flow meters, laser Doppler Velocimetry (LDV) is another technique that imposes substantial restrictions on the pipe and fluid properties in

exchange for measurement response time. LDVs measure local flow velocity using the Doppler principle and determine the velocity profile in the pipe. A flow rate can then be determined by integrating the measured velocity profiles over the pipe cross-section. In this technique, a coherent laser beam is emitted from the source and it is split into two beams. The paths of these beams are made to cross at the measurement location inside a transparent pipe section. When the two beams cross, an interference pattern of superpositioned light waves occurs (Figure 2.2). This pattern is disturbed by reflecting particles in the fluid passing that point and the changes in the light intensity can be related to the fluid velocity. LDV provides local velocity information at a point which is either repeated over the cross section of the flow to provide the velocity profile or an assumption is made regarding the shape of the velocity profile (Brereton *et al*. 2008, Brunone and Berni 2010, Durst *et al*. 1996, Unsal *et al*. 2006).

The LDV method has excellent dynamic response with a possible response time of the order of microseconds (Doebelin 1990). However, the need for fluid to be seeded with reflecting particles as well as a transparent pipe section for beam transmission makes this a method unsuitable for field conditions. In addition, the cost of setting up a LDV system is amongst the highest of all flow measurement methods and can be prohibitive in most applications.

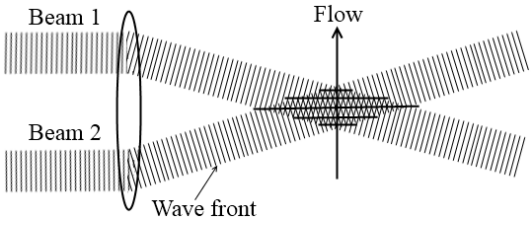

Figure 2.2 – Formation of interference pattern due to superposition of two beams

2.2.5 Clamp-on ultrasonic flow meters

There remains a need for rapid response flow meters that are capable of measuring rapidly varying unsteady flow without requiring significant changes to an existing pipe system. Flow meters that can measure flow through external devices such as clamp-on ultrasonic flow meters appear ideal for this purpose. Pressure disturbances in the fluid propagate at a velocity that is the sum of the fluid flow velocity and the pressure wave speed (Doebelin 1990), with the disturbance travelling faster in the direction of the flow. Transit time meters have sending

and receiving transducers which measure the difference between the times required by an ultrasonic wave to travel from the sender to the receiver (T_1 in Figure 2.3) and then from the receiver back to the sender (T_2 in Figure 2.3). This time difference is proportional to flow rate (Catania and Ferrari 2009, Skwarek *et al*. 2001).

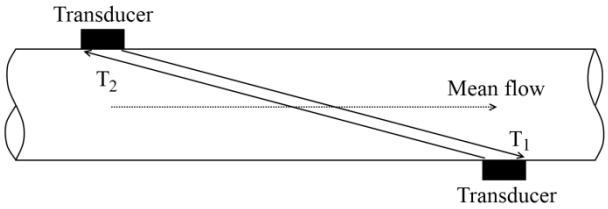

Figure 2.3 – Clamp-on transit time flow meter

Commercial clamp-on flow meters can be applied to a range of pipe materials and are most accurate when the ratio of the pipe diameter to wall thickness is greater than 10. While their non-intrusive properties are advantageous, measurement equipment as a whole requires some clearance at a measurement point which must also be readily-accessible to a user. In addition, clamp on ultrasonic flow meters generally have a response time of hundreds of milliseconds, which is well above the relevant transient flow time scales.

An ideal flow meter should be inexpensive, small in size with a fast response time and cause minimum disruption to the existing flow. However, none of the commercial flow meters can satisfy all of these requirements. Currently, no commercial flow meter is capable of capturing rapidly varying unsteady flow without placing significant restrictions on the pipe material, opacity and fluid content. Alternatively, a number of attractive techniques exist in the research literature that makes use of the behaviour of unsteady flows within the pipeline to determine the flow rate.

Unsteady flows are caused by changes to the pipeline system such as the operation of pumps, turbines, valves or the sudden injection of fluid. Every event creates pressure and flow disturbances, known as fluid transients that propagate through the system at high speeds.

The pressure changes from fluid transients can be measured using strain-gauge or piezoelectric pressure sensors (Catania and Ferrari 2009, Lee *et al*. 2006) which have a very high response rate and are available at a very low cost. These sensors are physically small

and can be flush mounted into the pipe wall causing minimum disturbance to the flow. Most importantly, commercial pressure sensors can have a response time of the order of microseconds making them ideal for capturing high-speed pressure variations from fluid transients.

While the pressure changes from the transient can be captured at over 100 kHz using these commercially available pressure transducers, no method exists for the capture of the flow rate at these sampling frequencies. Methods capable of translating the easily obtained high-speed pressure measurements into flow measurements are clearly advantageous and these methods are the focus of the subsequent sections. The flow rates produced from these methods are at the same sampling frequency as the original pressure signals and are well beyond the capability of all currently available commercial flow sensors.

In the following sections, three methods for determining flow rate from high-speed pressure measurements are discussed. The first method uses the Joukowsky equation which relates a change in flow to a change in pressure at a point in the system. The second and third methods are those used in Catania and Ferrari (2009) and Washio *et al*. (1996) which use two pressure measurements to calculate flow rate. These two methods are derived from the same set of equations but they are manipulated differently to give slightly different outcomes. The last two methods are compared to each other and the advantages of the method in Washio *et al*. (1996) are discussed.

2.2.6 Flow measurement with Joukowsky equation

The relationship between a change in flow and a change in pressure can be described by the Joukowsky equation (Wylie and Streeter 1993):

$$\Delta H = \pm \frac{a}{gA} \Delta Q \tag{2.1}$$

where ΔH and ΔQ are the change in pressure head and flow at a point in the system respectively. Equation 2.1 shows that any change in flow is related to a corresponding change in head at the same point in the system. The sign in the equation takes into account the

direction of the measured wave propagation. The positive sign is used when a wave propagates in the direction of the base flow and the negative sign is used for waves travelling in the opposite direction to the base flow (Chaudhry 1987, Wylie and Streeter 1993).

Figure 2.4 (a) illustrates a numerical pipeline system in which the validity of Equation 2.1 in capturing a step change in flow generated by a downstream-boundary inline valve is tested. The change in flow, $\Delta Q'$, is normalized by the initial steady flow. Friction effects are initially neglected for simplicity. The change in flow rate at a point three-quarters of the way along the pipeline is calculated using Equation 2.1. The pressure measured at the same point and the result is shown in Figure 2.4 (b). The minus sign in Equation 2.1 was used in the calculation because the measurement point observes a transient wave that initially travels in the direction opposite to the base flow. In the figure, the true response from the Method of Characteristics (MOC) model and predicted flow changes are shown with the broken and solid lines respectively. The details of the MOC model are found in Chapter 3.

Figure 2.4 (b) shows that Equation 2.1 correctly predicts the flow up to time $t' = 0.4375$. At this point in time, the first reflected wave from the upstream boundary arrives at the measurement point on its way to the closed valve. Since this wave is now propagating with the direction of the initial flow, the use of the minus sign in Equation 2.1 is no longer valid and the plus sign in Equation 2.1 should be used. In this example, system parameters such as the pipe length, generator location and boundary conditions are known which make it possible to predict the wave propagation direction at any point in time. However, in real systems, the signal is a combination of many transient events and in such a situation it is not possible to detect the wave direction from a single pressure transducer.

When a head loss due to steady friction is considered in the system in Figure 2.4 (a), the error in the predicted flow response is not limited to the sign used in Equation 2.1. Figure 2.5 shows the true and predicted flow responses as the broken and solid lines in the system with friction. The figure gives a close-up of the change in flow due to the first positive wave to highlight the error in the predicted flow response. The figure shows that Equation 2.1 overestimates the change in flow in addition to the sign error due to the change in the wave propagation direction.

The example has shown that the knowledge of wave propagation direction is essential for accurate flow calculation using Equation 2.1. The difference in arrival times of the signal at each transducer will determine the direction of the wave propagation and the correct sign correction can be applied to Equation 2.1. Despite this possible correction, the example has shown that the Joukowsky equation for flow calculation will be inaccurate in systems with significant friction loss and will be unable to cope with typical unsteady flow situations with multiple superpositioned wave fronts.

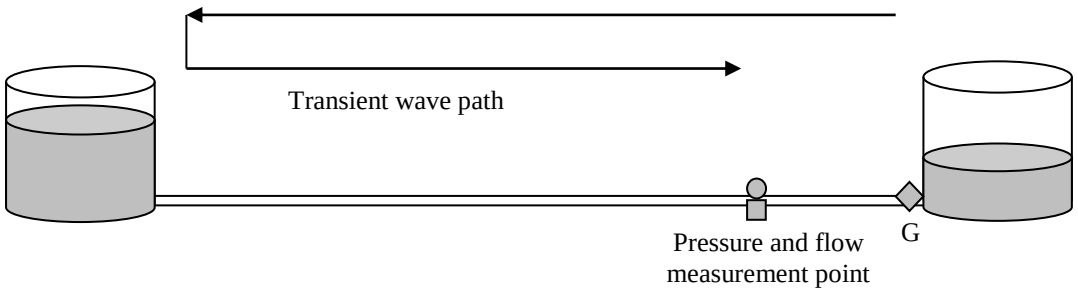

(a) Test setup

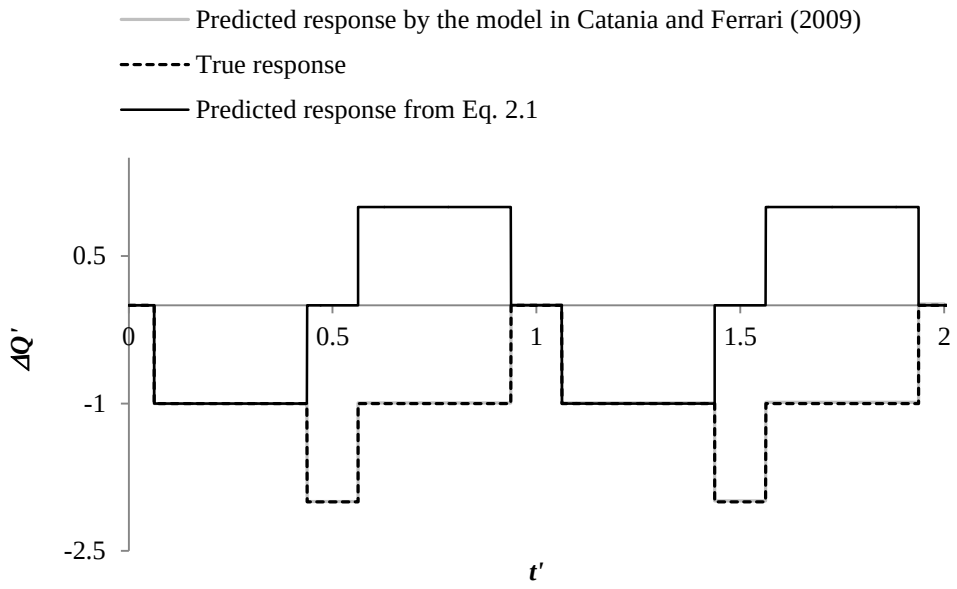

(b) Flow response at the three-quarter point from the upstream boundary (broken line) and that predicted using Equation 2.1 with the minus sign (solid line). The grey line shows the predicted flow response from the model proposed in Catania and Ferrari (2009)

Figure 2.4 – Flow estimation using the Joukowsky equation (Equation 2.1) in a frictionless system

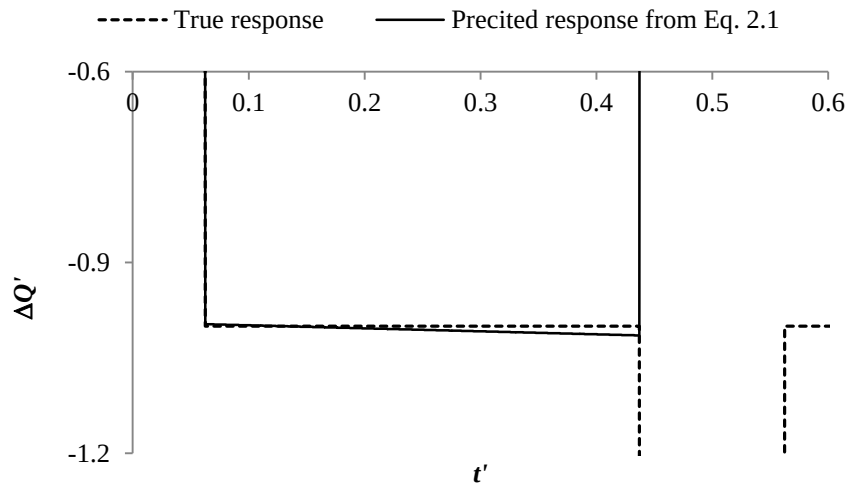

Figure 2.5 – Flow estimation using the Joukowsky equation (Equation 2.1) with the inclusion of frictional effects

2.2.7 Method developed in Catania and Ferrari (2009)

In Catania and Ferrari (2009), an equation for the relationship between the flow and pressure head under unsteady flow which incorporates friction effects was proposed and is an improvement on the Joukowsky equation. The technique uses the sum of the pressure differences on either side of a control volume and a friction force to determine the total net force on the fluid. After taking fluid compressibility into account, this net force is equated to the acceleration of the fluid within the control volume. The measurement of the pressure difference across the control volume in real time allows the calculation of the flow change from an initial value. The unsteady momentum and mass equations are combined to give a first-order nonlinear differential equation for the spatially-averaged flow rate within the control volume and its solution is generated with a first-order Runge-Kutta numerical scheme. The resulting equation computes the flow rate by summing up the differential pressure history measured at two points in the system as given in Equation 2.2.

$$\overline{G_k} = \overline{G_0} + \Delta t \sum_{j=0}^{k-1} \frac{p_{up,j} - p_{down,j}}{l} A \tag{2.2}$$

where $\overline{G_k}$ = space-averaged mass flow rate at time t_k and $\overline{G_0}$ = space-averaged mass flow rate at time t_0. The technique removes the limitation of the Joukowsky equation where the wave propagation direction must be determined prior to the calculation of the flow rate.

Figure 2.4 (b) shows the accurate prediction using this method for the scenario shown in Figure 2.4 (a) with the grey line.

It is important to note that the calculation of the spatially averaged flow rate from two pressure measurements assumes small spatial variations in head and flow. While this assumption is valid for small spacing of the pressure transducers, significant errors can result when this spacing is increased. The proposed model was further tested using the numerical pipeline shown in Figure 2.6. The system was bounded by constant head reservoirs on both ends and the flow at the end of the system was perturbed by a transient generator (labelled as G in the figure) at a magnitude that was 1% of the base flow of the system. The flow rate was predicted at the middle of the system (q_2 in Figure 2.6) using the pressure measurements on either side of the flow prediction point (h_1 and h_3). The dimensionless distance between the pressure measurement points was varied from $L_T' = 0.002$ to 0.1. Note that L_T' of 0 was omitted from the analysis as it suggests the transducers are located at the same point. The distance is normalised by the pipe length.

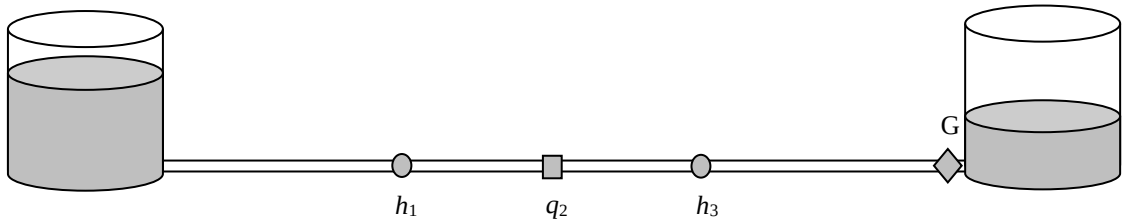

Figure 2.6 – Setup for testing methods in Catania and Ferrari (2009) and Washio *et al.* (1996)

The difference between the theoretical and predicted flow responses is given by the error, E, which is a root mean sum of the error across all the frequency components of the signal and is plotted against the dimensionless transducer spacing, L_T' in Figure 2.7 with the solid line. The results show that the error grows with the transducer spacing and the error exceeds 20% at the dimensionless spacing of 0.1.

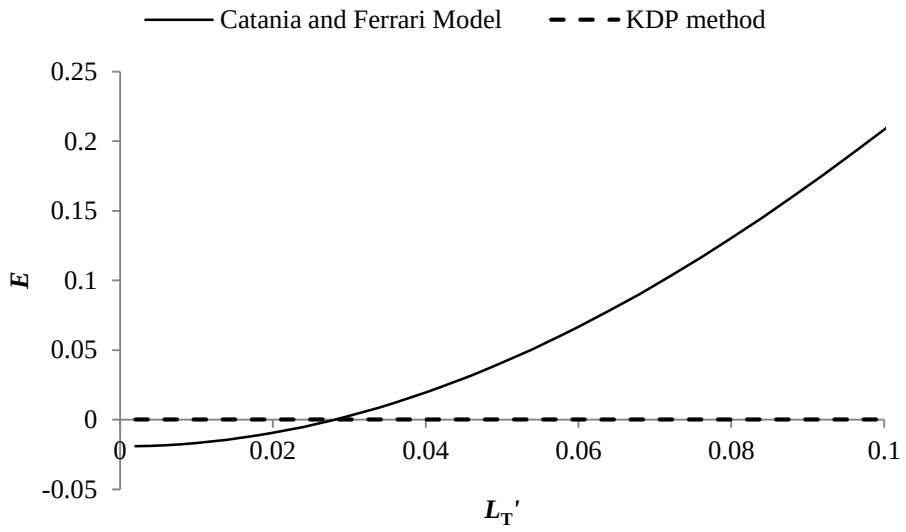

Figure 2.7 – Error in the flow rate prediction calculated by the model in Catania and Ferrari (2009) and by a modified version of the KDP method described in Washio *et al*. (1996)

2.2.8 Method used in Washio *et al*. (1996)

A method for estimating unsteady flow rate using the dynamic relationship between pressure and flow rate at two points in the system was proposed in Yokota *et al*. (1992) and it theoretically places no limitation on measurement spacing. The theory behind the proposed technique is based on the work done in D'Souza and Oldenburger (1964) where an expression for the dynamic relationship between pressure and flow rate in the Laplace domain was derived and a similar relation was also developed in Chaudhry (1987) in the frequency domain.

This method was extended in Washio *et al*. (1996)—and called the *Kinetic Differential Pressure* (KDP) method—to give an equation for the unsteady flow rate at point 3 using the pressure measurements at points 1 and 2 (Figure 2.6) as given in Equation 2.3.

$$q_3 = -\frac{\cosh(\mu L_{T2})}{Z_c \sinh(\mu L_{T1})}\Delta h + \frac{\cosh(\mu L_{T2}) - \cosh(\mu(L_{T1}+L_{T2}))}{Z_c \sinh(\mu L_{T1})}h_2 \qquad (2.3)$$

where L_{T1} = distance between the pressure measurement points 1 and 2, L_{T2} = distance between the pressure measurement point 2 to the flow prediction point (point 3), μ = propagation constant and Z_c = characteristic impedance for the pipe section. The propagation

constant and characteristic impedance will be introduced in Section 3.2. This formulation has an advantage over the one used in Yokota *et al*. (1992) in that the unsteady flow rate can be determined without installing a pressure transducer at the point of interest. Such a characteristic is useful when there is not enough space at the point of interest or where the point of interest is in a sensitive location where any flow disturbances, even minimum ones from the pressure sensors are not permitted.

The formulation given in Washio *et al*. (1996) provides flexibility in pressure and flow measurement points, where any combinations of two pressure measurements can be used to predict flow rate at any of the three points (points 1, 2 or 3) in Figure 2.6. Furthermore, unlike the method developed in Catania and Ferrari (2009), the model in Washio *et al*. (1996) gives flow rates at the point of interest directly instead of a spatial average across the control volume. The same numerical runs for testing the method in Catania and Ferrari (2009) were repeated to investigate the accuracy of the KDP method as a function of the transducer spacing. For these runs, the equation for the flow rate at point 2 was derived as a function of the pressure inputs at points 1 and 3 (Figure 2.6) so that the configuration of the measurement points matches the one for the model in Catania and Ferrari (2009). The result is plotted in Figure 2.7 with the broken line. The KDP prediction error is shown to be relatively insensitive to all tested transducer spacing with the average error of 2.3×10^{-3}%—a significant improvement on the model in Catania and Ferrari (2009).

This flow metering technique was experimentally verified in Manhartsgruber (2008), Chen *et al*. (2006) and Washio *et al*. (1996). In these works, the accuracy of the method was examined only in laminar flow. A discrete signal was generated in Manhartsgruber (2008) and a sinusoidally oscillating flow was tested in Chen *et al*. (2006) and Washio *et al*. (1996). For the purpose of supporting the use of this technique in real systems, the method used in Washio *et al*. (1996) will be further tested numerically and experimentally in Chapter 6, by considering its application with three types of signals. The scale of the laboratory pipeline system is an order of magnitude larger than that of the testing systems used in the above-mentioned papers. Thus, it is possible to test the method under multiple flow regimes. Specifically, tests under turbulent flow will be valuable in promoting the method. Furthermore, this thesis explores the possibility of using the method in estimating a change in steady flow.

2.3 Literature review on the dynamic behaviour of leak

A leak is classified as an orifice-based element. Orifices are commonly used for measuring steady flow rates through a pipe and they can provide flow measurements with high accuracy despite their simple structure (Earles and Zarek 1965, Funk *et al*. 1972, Kawamata *et al*. 1977, Tamura and Iwamoto 2005). The characteristic of the orifice and other orifice-based elements in steady flow is described by the following orifice equation:

$$Q_0 = C_d A_o \sqrt{2g|\Delta H|} \tag{2.4}$$

where Q_0= mean flow rate, C_d = discharge coefficient, A_o = cross sectional area of the orifice, g = acceleration due to gravity and ΔH = head loss across the orifice. The discharge coefficient, C_d, in Equation 2.4, is a lumped constant which represents resistance to flow and is assumed to be constant for steady flow. As a result of its popularity for flow measurements, extensive research has been done on the behavioural characteristics of the orifice under steady flow and its thorough understanding in steady state flow has been obtained (McCloy, 1966).

Despite the extensive knowledge on the steady state behaviour of orifices, information regarding the unsteady dynamic, or time-varying, behaviour of orifice-based elements is limited. It is generally assumed that the steady orifice characteristics are also applicable to unsteady flow conditions, but some studies have shown differences in the orifice behaviour in steady and unsteady flows (Daily *et al*. 1956, Earles and Zarek 1963, Trengrouse *et al*. 1966, Funk *et al*. 1972, Washio *et al*. 1996).

The differences between the steady and unsteady characteristics of the orifice have been observed through the deviations in the discharge coefficient in Equation 2.4. Kawamata *et al*. (1977) experimentally determined the discharge coefficient in decelerating flows. The comparison with the steady state coefficient revealed that the discharge coefficient in unsteady flow was larger and grew with deceleration rate and severity of the orifice constriction. Earles and Zarek (1965) and Trengrouse *et al*. (1966) determined the discharge coefficient from the incident and reflected pressure signals measured upstream of the orifice. The results in Trengrouse *et al*. (1966) indicated that the difference between the steady and

unsteady discharge coefficients varied depending on the orifice-to-pipe area ratio and a maximum error of 7% was observed when the ratio was small.

Gajan *et al*. (1992) investigated the relationship between the discharge coefficient and the velocity profile measured immediately upstream of an orifice and found that the discharge coefficient for the orifices with the large orifice-to-pipe ratio (low constriction severity) was sensitive to the velocity profile. In pulsating flow, the velocity profile changes cyclically and the discharge coefficient also undergoes cyclic variation. Tamura and Iwamoto (2005) presented the velocity profiles measured downstream of an orifice in steady and unsteady pulsating flow. The results showed that the time averages of the velocity profiles measured in unsteady flow were barely affected by the flow pulsation, but the instantaneous velocity profiles exhibited some fluctuations near the centreline of the pipe and the amount of fluctuation decreased with an increase of the pulsation frequency. While no discussion regarding the subsequent effect on the discharge coefficient was given by the authors, it can be deduced from the findings in Gajan *et al*. (1992) that the discharge coefficient in unsteady flow is expected to differ from the steady coefficient more significantly when the pulsation frequency is low.

Numerous researchers looked into the dynamic behaviour of an orifice using the reflected and transmitted waves produced when a transient signal interacts with the orifice (Contractor 1965, Earles and Zarek 1965, Funk *et al*. 1972, Prenner 2000). Contractor (1965) compared the measured pressure data with the predictions from the theoretical model based on classical wave theory with steady state behaviour. The comparison indicated a significant difference due to the omission of unsteady resistance effects. Earles and Zarek (1965) also used reflected waves from a sharp-edged orifice fitted at the end of a pipeline to study the dynamic behaviour of the orifice. The ratios of orifice-to-pipe diameter ranged from 0 to 1 with 6 intermediate values. The comparison between the theoretical results from the steady-orifice equation and the experimental results showed that the deviation increased as the orifice constriction severity decreased. Prenner (2000) used a pipeline system where the orifice was fitted to a T-junction. The experiments were run with eight different base flow conditions and orifices with four different diameters. The amplitudes of the transmitted and reflected waves were presented as a proportion of the amplitude of the incident wave and the ratios were referred to as a transmission factor. The experimentally obtained transmission factors

consistently deviated from the computed ones based on the steady-state relationship. It was stated that factors affecting the amount of the deviation were the direction of the base flow, the pressure wave direction and the orifice size. It was concluded that orifices with a constriction ratio greater than 1:32 can be described by the steady orifice relationship with moderate accuracy.

The steady orifice equation is also used to simulate the behaviour of leaks. Kim (2008) demonstrated the effect of leaks of different magnitudes and location on a pressure response both numerically and experimentally. The leaks were created by loosening the fittings of the laboratory pipeline. Transient events were initiated by a rapid closure of a solenoid-driven valve which had the average closure time of 4 milliseconds. The steady orifice equation was used to numerically describe the leak effects in unsteady flow. The comparison between the simulated and measured pressure responses showed a good agreement in terms of their magnitude and phase. Due to the noise in the measured pressure responses, only a match in the general shape of the responses was observed.

Al-Khomairi (2005) tested the suitability of the steady orifice equation for describing the relationship between the flow out of a leak and the pressure head at the leak in unsteady flow. A transient flow condition was established by continuous opening and closure of the valve upstream of the leak which created the flow perturbation having the time scale of seconds. The leak flow was measured by a flow meter and the measured flow trace was compared to the leak flow computed from the steady orifice equation. Five leaks of different shapes were considered in the study and some of them exhibited a change in the opening area during the transient state due to the variation of the pressure at the leak. The simulated result matched well with the experimental result when the leak area was not deformed, but the steady orifice equation could not describe the leak flow accurately once the leak area varied with pressure. It was stated that the deviation arose from the use of the discharge coefficient which had been obtained in steady flow and it did not take the change in the leak area into account. The presented results suggested that the steady orifice equation can describe the relationship between the flow and head at the leak with sufficient accuracy for small to moderate leak sizes as these leaks generally have better resistivity to area change.

The studies done by Cassa *et al*. (2010) and Ferrante (2012) are related to the work by Al-Khomairi (2005). Ferrante (2012) used a leak in pipes of different material to determine the relationship between the pressure head and flow at the leak. The time scale of the introduced flow unsteadiness was so large that the system was passing through a sequence of quasi-steady states. The experimental data demonstrated that the predictions from the steady orifice equation were valid provided the leak area remains the same in unsteady flow, but once the leak area varied with the pressure head at the leak, the steady orifice equation could no longer interpret the physical phenomenon, which agreed with the findings in Al-Khomairi (2005). The head-flow relationship for the leak with changing area gave the same trend as the change in the effective area of the leak with pressure, confirming that the difference from the steady relationship was a result of the leak area variation. In the case of a high density polyethylene pipe, the head-flow relationship exhibited a hysteresis behaviour where two distinct values of the leak flow were associated to one value of the leak head. Such behaviour cannot be modelled by the steady orifice equation because of its bijective nature. Similar to the cases with the metal pipes, this behaviour was a result of the hysteresis variation of the leak opening area.

The hysteresis behaviour was also observed in the studies with orifices. Burger *et al*. (1956) and Washio *et al*. (1996) examined the unsteady characteristics of an orifice by observing the head-flow relationship across it. In steady flow, the head-flow relationship showed a quadratic relationship according to the steady orifice equation. A transient flow was created by a sinusoidal flow generator with the highest pulsation frequency of 289.4 Hz. The resultant graph exhibited a hysteresis phenomenon. Note that, in these studies, a possibility of a change in the orifice opening area during the transient state was not mentioned by the authors and hence the relation of the observed hysteresis behaviour to the area variation was unknown.

The hysteresis behaviour represents a dependency on time history which is described by a time convolution. Considering that the convolution is used to model unsteady friction which is known to introduce frequency-dependent effects into the response, the observed hysteresis in these studies implies that the orifices and leaks have the same kind of influence on the signals as unsteady friction.

The purpose of this study is to confirm the frequency dependent nature of the leak from the changes imposed on transient signals by the leak. This study considers the leak behaviour in rapidly-changing flows with time scales in the order of milliseconds, which is considerably smaller than that employed by Al-Khomairi (2005) and Ferrante (2012). A small time scale means that it is possible to observe changes to higher frequency components of a signal where the attribute of the signal is embedded. Such information is considered critical when one wishes to distinguish one hydraulic component from another. While the transient time scale is comparable to the one used in Kim (2008), this study will provide additional insight into the unsteady leak behaviour by examining its effect on both pressure and flow responses. For the leak size and the wall thickness of the pipeline, it is reasonable to assume that the opening area of the leak remains unchanged in these transient flows based on the work by Al-Khomairi (2005) and Ferrante (2012). The present work will give an insight into the unsteady leak behavior from a different angle to what has been done to date.

In Chapter 7, analyses will be conducted in the time and frequency domains. The time-domain approach is based on the multi-correlation analysis (MCA) which will be introduced in Chapter 5 and aims to quantify the degree of signal dilation in terms of the time scale of the analysing signal. The frequency-domain based method produces a system response—similar to the impulse response—of the leak from measured pressures. This approach has successfully been applied to study the dynamic behaviour of hydraulic silencers (Kojima and Edge 1994, Earnhart *et al*. 2010), a cavitating Venturi (Marie-Magdeleine *et al*. 2012), automotive compressors and mufflers (Hua and Herrin 2013, Rousselet *et al*. 2013), and porous materials (Utsuno *et al*. 1989, Song and Bolton 2000, Bonfiglio *et al*. 2005, Kunio *et al*. 2009). The application of this approach to leaks is one of new contributions of this thesis and a successful outcome will support the use of the approach to a wider area of research.

Chapter 3 Governing Equations

The behaviour of unsteady pipe flows is governed by the one-dimensional unsteady momentum and continuity equations (Chaudhry 1987, Wylie and Streeter 1993):

$$\frac{1}{gA}\frac{\partial Q}{\partial t}+\frac{\partial H}{\partial x}+\frac{fQ|Q|}{2gDA^2}=0 \tag{3.1}$$

$$\frac{a^2}{gA}\frac{\partial Q}{\partial x}+\frac{\partial H}{\partial t}=0 \tag{3.2}$$

where Q = instantaneous flow, t = time, x = distance along the pipeline, a = system wave speed, g = acceleration due to gravity, f = Darcy-Weisbach friction factor, D = pipe diameter, A = cross-sectional area of the pipe and H = instantaneous piezometric head at the centreline of the pipe above the specified datum. These equations assume elastic pipe behaviour, weakly compressible fluids and flow velocities that are significantly smaller than the pressure wave speed such that the advective terms may be ignored.

Transient simulations can be done in the time or the frequency domain. The numerical scheme in the time domain is known as the Method of Characteristics (MOC) and the scheme in the frequency domain is referred to as the transfer matrix (TM) model. The governing equations (Equations 3.1 and 3.2) need to be modified for use in these models, as will be described in this chapter.

3.1 Method of Characteristics

The Method of Characteristics (MOC) transforms Equations 3.1 and 3.2 into total differential equations (Wylie and Streeter 1993) which can then be integrated to give the head and flow at a point in a pipe.

Multiplying the continuity equation in Equation 3.2 by a variable, λ and adding it to the momentum equation (Equation 3.1) leads to:

$$\lambda \frac{\partial H}{\partial t} + \lambda \frac{a^2}{gA} \frac{\partial Q}{\partial x} + \frac{1}{gA} \frac{\partial Q}{\partial t} + \frac{\partial H}{\partial x} + \frac{fQ|Q|}{2gDA^2} = 0 \tag{3.3}$$

Grouping the head and flow gives:

$$\frac{1}{gA}\left(\frac{\partial Q}{\partial t} + \lambda a^2 \frac{\partial Q}{\partial x} \right) + \lambda \left(\frac{\partial H}{\partial t} + \frac{1}{\lambda} \frac{\partial H}{\partial x} \right) + \frac{fQ|Q|}{2gDA^2} = 0 \tag{3.4}$$

Conversion from the partial derivatives to the total derivatives is made using the chain rule:

$$\frac{dQ}{dt} = \frac{\partial Q}{\partial t} + \frac{dx}{dt} \frac{\partial Q}{\partial x} \tag{3.5}$$

$$\frac{dH}{dt} = \frac{\partial H}{\partial t} + \frac{dx}{dt} \frac{\partial H}{\partial x} \tag{3.6}$$

Examination of Equation 3.4 with Equations 3.5 and 3.6 reveals:

$$\frac{dx}{dt} = \lambda a^2 = \frac{1}{\lambda} \tag{3.7}$$

The value of λ is therefore:

$$\lambda = \pm \frac{1}{a} \tag{3.8}$$

By substituting these values of λ into Equation 3.7, the relationship between x and t is obtained:

$$\frac{dx}{dt} = \pm a \tag{3.9}$$

When $\frac{dx}{dt} = a$, Equation 3.4 is

$$\frac{1}{gA}\frac{dQ}{dt}+\frac{1}{a}\frac{dH}{dt}+\frac{fQ|Q|}{2gDA^2}=0 \tag{3.10}$$

and when $\frac{dx}{dt}=-a$:

$$\frac{1}{gA}\frac{dQ}{dt}-\frac{1}{a}\frac{dH}{dt}+\frac{fQ|Q|}{2gDA^2}=0 \tag{3.11}$$

Equation 3.10 and 3.11 are known as the positive and negative characteristic equations (denoted as C^+ and C^-). These equations have the restriction that they are valid only if Equation 3.9 is satisfied.

The characteristic equations are usually represented in the *x*-*t* plane. In this plane, Equation 3.9 results in two straight lines with slopes of ±1/*a* as shown in Figure 3.1. These lines are called characteristic lines and they represent the path travelled by a transient signal.

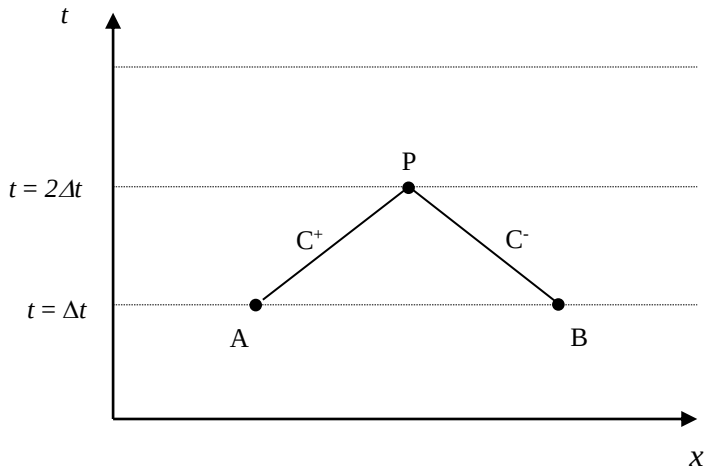

Figure 3.1 – Characteristic lines in the *x*-*t* plane

Equations 3.10 and 3.11 can be integrated along their respective characteristic lines in order to give expressions for the head and discharge at point P in Figure 3.1 with the knowledge of the head and discharge conditions at time *t* = *t*.

$$\frac{1}{gA}\int_A^P dQ+\frac{1}{a}\int_A^P dH+\frac{f}{2gDA^2}\int_A^P Q|Q|dt=0 \tag{3.12}$$

$$\frac{1}{gA}\int_B^P dQ + \frac{1}{a}\int_B^P dH + \frac{f}{2gDA^2}\int_B^P Q|Q|dt = 0 \tag{3.13}$$

The equations are integrated using a finite difference approximation for the friction term (the last term in Equations 3.12 and 3.13), which limits the time and space increment to be small (Jaeger 1977). Using the known flow conditions Q_A and Q_B for friction terms in Equations 3.12 and 3.13, the characteristic equations become:

$$\frac{1}{gA}(Q_P - Q_A) + \frac{1}{a}(H_P - H_A) + \frac{fQ_A|Q_A|\Delta t}{2gDA^2} = 0 \tag{3.14}$$

$$\frac{1}{gA}(Q_P - Q_B) - \frac{1}{a}(H_P - H_B) + \frac{fQ_B|Q_B|\Delta t}{2gDA^2} = 0 \tag{3.15}$$

Equations 3.14 and 3.15 form a set of simultaneous equations with two unknowns, Q_P and H_P and they can be solved only when the conditions at a previous time step ($t = t$) are known. Normally, transient simulations start from steady state conditions ($t = 0$) which are used as the conditions at point A and B in Equations 3.14 and 3.15.

Transient modelling using the characteristic equations produces a grid shown in Figure 3.2. At each time step, the head and flow at the intersection of the characteristic lines are determined. For a finer grid, the distance and time increments can be adjusted according to Equation 3.9.

Note that either a head or flow condition (or a relationship between them) must be supplied at system boundaries at each time step and the other unknown condition is determined from either the positive or negative characteristic equation. More details on the MOC are found in Chaudhry (1987) and Wylie and Streeter (1993). The verification of the MOC model is provided in Section 3.4.

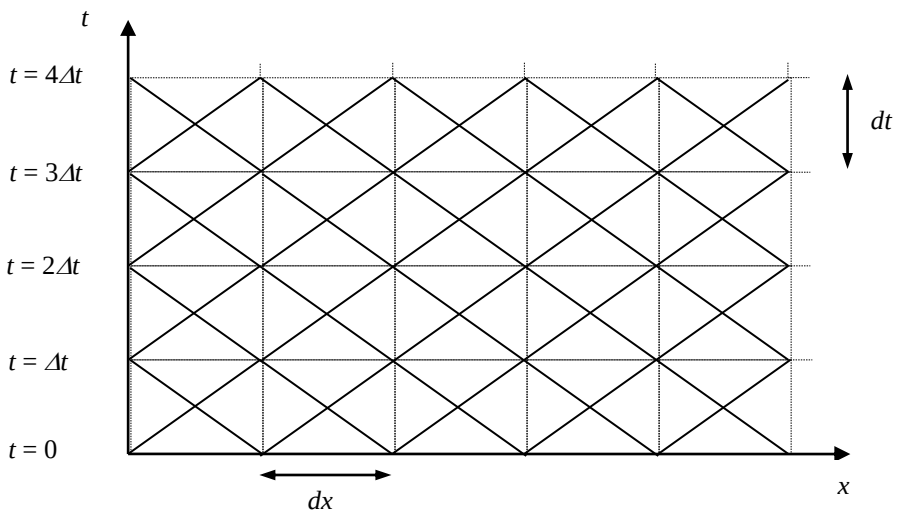

Figure 3.2 – Characteristic grid

3.1.1 Inclusion of leak in the Method of Characteristics

The discharge out of a leak is modelled by the orifice equation:

$$Q_L = C_d A_L \sqrt{2g\left(H_L - z_L\right)} \tag{3.16}$$

where C_dA_L = lumped leak coefficient, H_L = head at the leak and z_L = elevation head at the leak.

The head and flow either side of the leak is determined from the characteristic equations (Equations 3.14 and 3.15) and the equations for head and mass conservation across the leak:

$$H_{PU} = H_{PD} = H_L \tag{3.17}$$

$$Q_{PD} = Q_{PU} - Q_L \tag{3.18}$$

where the subscripts U and D denote the upstream and the downstream side of the leak. A side discharge valve for generation of transients can also be modelled by the orifice equation by varying the lumped leak coefficient.

An alternative numerical model for transient simulation, known as the transfer matrix (TM) model, will be introduced in the following section. This model simulates the transient

behavior in the frequency domain and offers greater computational efficiency compared to the MOC especially when a phenomenon such as unsteady friction is incorporated in the simulations (Suo and Wylie 1989). In addition, the TM model enables the simulation at any point in the numerical pipeline system without the restriction on the time and space discretization. Such flexibility will be convenient when estimating flow rates as will be discussed in Chapter 6.

3.2 Transfer matrix model

The equations for the TM model are derived from the same governing equations as the MOC model. The derivation requires decomposition of the instantaneous flow and head in Equations 3.1 and 3.2 into two parts:

$$Q = Q_0 + q^* \tag{3.19}$$

$$H = H_0 + h^* \tag{3.20}$$

where Q_0 = time-averaged mean flow, q^* = flow perturbation about the mean state, H_0 = time-averaged mean pressure head and h^* = head perturbation about the mean state.

Substitution of Equations 3.19 and 3.20 into Equations 3.1 and 3.2, and knowing that the mean head and discharge are time invariant and the mean discharge is constant along the pipeline give the equation for the perturbed flow component as:

$$\frac{1}{gA}\frac{\partial q^*}{\partial t} + \frac{\partial H_0}{\partial x} + \frac{\partial h^*}{\partial x} + \frac{f\left(Q_0 + q^*\right)^2}{2gDA^2} = 0 \tag{3.21}$$

$$\frac{a^2}{gA}\frac{\partial q^*}{\partial x} + \frac{\partial h^*}{\partial t} = 0 \tag{3.22}$$

If $q^* << Q_0$, then:

$$(Q_0 + q^*)^2 = Q_0^2 + 2Q_0q^* \tag{3.23}$$

The partial derivative of the base head with respect to distance along the pipe, x is equivalent to the rate of steady friction loss. Thus it can be replaced with:

$$\frac{\partial H_0}{\partial x} = -\frac{fQ_0{}^2}{2gDA^2} \tag{3.24}$$

Incorporating Equations 3.23 and 3.24 give:

$$\frac{1}{gA}\frac{\partial q^*}{\partial t} + \frac{\partial h^*}{\partial x} + \frac{fQ_0 q^*}{gDA^2} = 0 \tag{3.25}$$

By the separation-of-variable method, h^* can be eliminated from Equations 3.22 and 3.25:

$$\frac{1}{gA}\frac{\partial^2 q^*}{\partial t^2} - \frac{a^2}{gA}\frac{\partial^2 q^*}{\partial x^2} + \frac{fQ_0}{gDA^2}\frac{\partial q^*}{\partial t} = 0 \tag{3.26}$$

Assuming that each frequency component of the flow perturbation can be described by:

$$q^* = \mathbf{Re}(q(x)e^{j\omega t}) \tag{3.27}$$

where q is a complex variable as a function of x and "**Re**" is the real part of the complex variable. Substitution of Equation 3.27 into Equation 3.26 and further manipulation yields:

$$\frac{d^2 q}{dx^2} = \mu^2 q \tag{3.28}$$

in which μ is known as the propagation constant and given by:

$$\mu = \sqrt{-\frac{\omega^2}{a^2} + \frac{j\omega g A R_S}{a^2}} \tag{3.29}$$

with $j = \sqrt{-1}$. The steady state resistance term R_S is:

$$R_S = \frac{fQ_0}{gDA^2} \tag{3.30}$$

for turbulent flows, and:

$$R_S = \frac{32\nu}{gD^2A} \tag{3.31}$$

for laminar flows. The term ν is the kinematic viscosity of the fluid.

The general solution of Equation 3.28 is:

$$q = c_1\sinh(\mu x) + c_2\cosh(\mu x) \tag{3.32}$$

where c_1 and c_2 are arbitrary constants.

If the head fluctuation is assumed similar to the flow fluctuation, it has the form:

$$h^* = \mathbf{Re}(h(x)e^{j\omega t}) \tag{3.33}$$

Using Equations 3.22 and 3.33, the equation for h can be written as:

$$h = -\frac{a^2\mu}{gA\omega j}\left(c_1\cosh(\mu x) + c_2\sinh(\mu x)\right) \tag{3.34}$$

The two arbitrary constants are determined from the known conditions at a point in the pipeline where $x = 0$ ($h = h_1$, $q = q_1$ at $x = 0$). Substituting these conditions into Equations 3.32 and 3.34 gives the he constants c_1 and c_2 as:

$$c_1 = -\frac{gA\omega j}{a^2\mu}h_1 \tag{3.35}$$

$$c_2 = q_1 \tag{3.36}$$

Using these constants, the head ($h = h_2$) and flow ($q = q_2$) at $x = l$ are obtained by:

$$q_2 = -\frac{h_1}{Z_c}\sinh(\mu l) + q_1 \cosh(\mu l) \tag{3.37}$$

$$h_2 = h_1 \cosh(\mu l) - q_1 Z_c \sinh(\mu l) \tag{3.38}$$

in which $Z_c = \frac{\mu a^2}{j\omega g A}$ and is known as the characteristic impedance for the pipe section. Equations 3.37 and 3.38 can be expressed in the matrix notation as:

$$\begin{pmatrix} q_2 \\ h_2 \end{pmatrix} = \begin{bmatrix} \cosh(\mu l) & -\frac{1}{Z_c}\sinh(\mu l) \\ -Z_c \sinh(\mu l) & \cosh(\mu l) \end{bmatrix} \begin{pmatrix} q_1 \\ h_1 \end{pmatrix} \tag{3.39}$$

The TM model was initially developed for oscillatory signals, but it can be used for any shaped signals as the TM model decomposes a complex transient signal into a sum of sinusoids and simulates how each of these sinusoids is transferred from one point to another (Lee *et al*. 2013). Because a sinusoid oscillates about zero, the TM model can only simulate the behaviour of the perturbed portion of the head and flow which are superimposed on the steady conditions.

3.2.1 Inclusion of leak in the transfer matrix model

For the frequency-domain representation of the leak, the orifice equation in Equation 3.16 is converted into a matrix form through a similar procedure described in the preceding section. Dividing the orifice equation by the steady flow out of the leak (Q_{L0}) yields:

$$\frac{Q_L}{Q_{L0}} = \frac{C_d A_L}{(C_d A_L)_0} \frac{\sqrt{(H_L - z_L)}}{\sqrt{(H_{L0} - z_L)}} \tag{3.40}$$

in which the subscript '0' denotes the steady state values. Similar to Equations 3.19 and 3.20, decomposing the instantaneous flow and head into the steady and time-varying perturbation components give:

$$Q_L = Q_{L0} + q_L^* \tag{3.41}$$

$$H_L = H_{L0} + h_L^* \tag{3.42}$$

If a constant leak opening area is assumed, $C_dA_L/C_dA_{L0} = 1$, Equation 3.40 can be rewritten as:

$$1 + \frac{q_L^*}{Q_{L0}} = \sqrt{1 + \frac{h_L^*}{H_{L0} - z_L}} \tag{3.43}$$

Each frequency component of the flow and head perturbations is described in a similar manner to Equations 3.27 and 3.33:

$$q_L^* = q_L(x)e^{j\omega t} \tag{3.44}$$

$$h_L^* = h_L(x)e^{j\omega t} \tag{3.45}$$

in which q_L and h_L are complex variables and are function of x only. Substituting Equations 3.44 and 3.45 into Equation 3.43 gives:

$$1 + \frac{q_L e^{jwt}}{Q_{L0}} = \sqrt{1 + \frac{h_L e^{jwt}}{H_{L0} - z_L}} \tag{3.46}$$

Equation 3.46 can be simplified down to:

$$q_L = \frac{Q_{L0}}{2(H_{L0} - z_L)} h_L \tag{3.47}$$

The equivalent forms of Equations 3.16 and 3.17 in the frequency domain are:

$$h_L = h_U = h_D \tag{3.48}$$

and:

$$q_L = q_U - q_D \tag{3.49}$$

Replacing q_L and h_L in Equation 3.47 with q_U, q_D and h_U, Equation 3.49 becomes:

$$q_D = q_U - \frac{Q_{L0}}{2(H_{L0} - z_L)} h_U \tag{3.50}$$

Finally, in the matrix form:

$$\begin{bmatrix} q_D \\ h_D \end{bmatrix} = \begin{bmatrix} 1 & -\frac{Q_{L0}}{2(H_{L0} - z_L)} \\ 0 & 1 \end{bmatrix} \begin{bmatrix} q_U \\ h_U \end{bmatrix} \tag{3.51}$$

The derived TM model is linear because the unsteady momentum and orifice equations are linearized. Differences between the linear TM model and the nonlinear MOC are assumed negligible if the magnitude of the perturbation is small (Balcomb *et al*. 1961, Suo and Wylie 1989, Covas *et al*. 2005, Lee *et al*. 2005a, 2007a, Lee and Vítkovský 2008, Sattar and Chaudhry 2008). This assumption is verified in the next section.

3.2.2 Verification of the transfer matrix model

Transient behaviour in a numerical pipeline system is simulated by the MOC model and the TM model. The pipeline is 2000 m long and the system contains a side discharge valve at the middle of the system and each end of the system is bounded by constant head tanks as shown in Figure 3.3. Section 4.1 contains the detailed parameters of the numerical pipeline system. Transients were introduced through the rapid opening and closure of the side discharge valve (denoted as G in Figure 3.3) situated in the middle of the system. The signal had a magnitude of 1 m and the width of 10 Δt, where Δt is the time increment in the MOC simulation. The base flow through the system had a flow Reynolds number of 7.34×10^5 and a steady friction factor, f = 0.0145. The two models predicted pressure perturbation at 600 m from the upstream boundary.

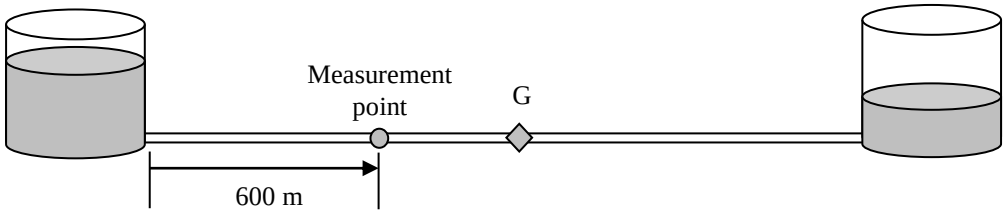

Figure 3.3 – Test setup

Simulations by the TM model in this pipeline system require an overall transfer matrix which is a combination of Equation 3.39 and a transfer matrix for the valve. The side discharge valve has a transfer matrix similar to Equation 3.51, but with a varying valve opening area and it is given as:

$$\begin{bmatrix} q_D \\ h_D \end{bmatrix} = \begin{bmatrix} 1 & -\dfrac{Q_{L0}}{2(H_{L0} - z_L)} \\ 0 & 1 \end{bmatrix} \begin{bmatrix} q_U \\ h_U \end{bmatrix} + \begin{bmatrix} -\dfrac{Q_{L0}\Delta\tau}{\tau_0} \\ 0 \end{bmatrix} \tag{3.52}$$

in which $\tau_0 = (C_d A_L)_0/(C_d A_L)_{REF}$ and $\tau = \tau_0 + \Delta t^* = (C_d A_L)/(C_d A_L)_{REF}$. The term, $(C_d A_L)_{REF}$ is a reference leak opening. Equation 3.52 is obtained following the similar derivation given in Chaudhry (1987) and Lee (2005). The overall transfer matrix relates the head and flow conditions at the system boundaries and it is produced by multiplying the individual transfer matrices from the downstream boundary (Chaudhry 1987).

The time plots from the two models are presented in Figure 3.4 (a) where a good match between the two traces is seen. In the figure, the time, *t'*, and the amplitude of the head fluctuation, *h*'*are normalised by the period of the pipeline system and the steady head at the measurement point respectively. These time traces are plotted against each other in Figure 3.4 (b) to observe the relationship between the magnitudes of the predicted pressure traces from the two models. The gradient of the linear trend line through the plot and the R^2 value of 1 confirm the accuracy of the TM model and indicate that the pipeline system behaves linearly with the signal magnitude of 1 m. The next example considers the signal magnitude of 30 m and the responses from the two models are compared in Figure 3.4 (c). A linear trend line through the data points gives the gradient of 1.0012 implying that the TM model slightly overestimates the transient behaviour. This is because the pipeline system behaves nonlinearly with this size of the transient and hence the linear TM model can no longer give an accurate prediction of the transient behaviour.

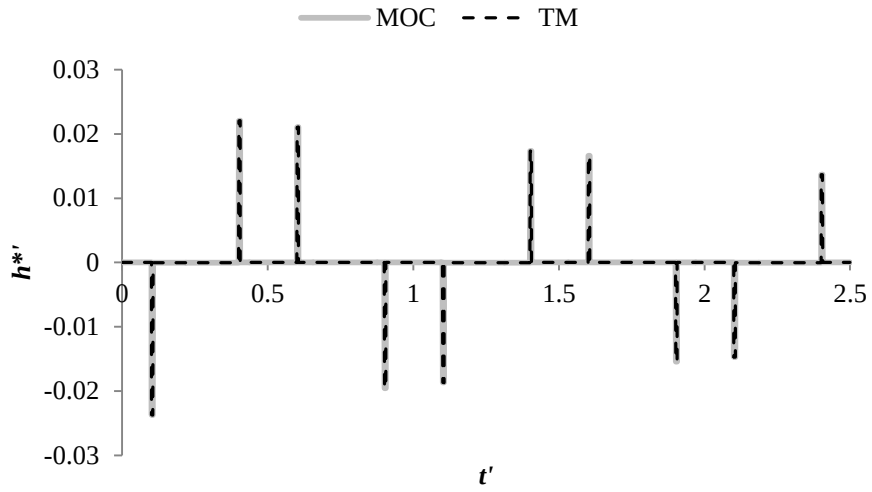

(a) Simulated transient traces against time

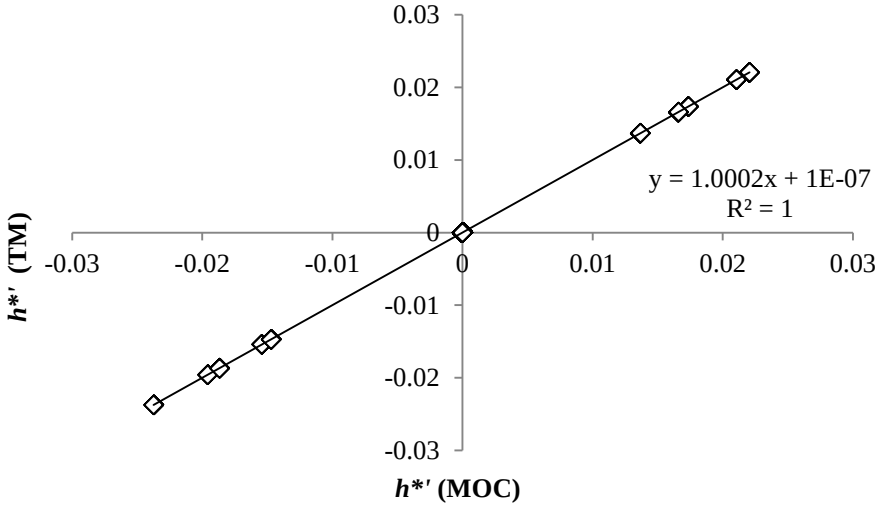

(b) Direct comparison of the two traces when the signal magnitude is 1 m

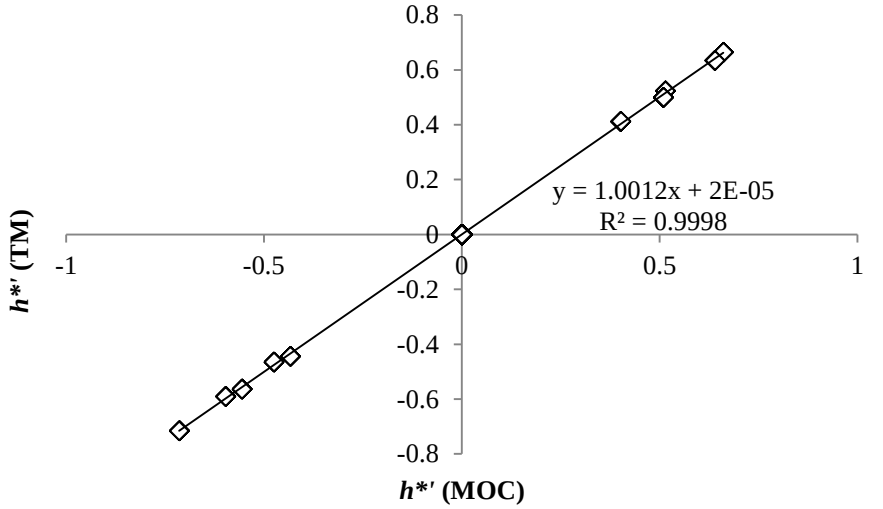

(c) Direct comparison of the two traces when the signal magnitude is 30 m

Figure 3.4 – Comparison between the transient traces generated by the MOC and the TM model

As some analyses conducted in this thesis rely on linear system analysis, it is important to keep the transient size small so that the pipeline system behaves in a linear manner. Linearity is an important property for system analysis as it allows the decomposition of the signal into its frequency components, analysis of the response from each component and eventually determining the total response by summing all the responses. This principle forms the foundation of several methods of system analysis such as impulse response extraction as described in Chapter 5. The maximum magnitude of the transient generated in the laboratory is 10 m and the validity of the linear assumption with this signal magnitude is tested on the numerical pipeline system having the same system parameters as the laboratory pipeline as described in Chapter 4. The comparison of the simulation results from the two models is given in Figure 3.5 which shows the result from the MOC model matches to that from the TM model, thus confirming that a transient having a magnitude of 10 m is sufficiently small for the laboratory pipeline system at the University of Canterbury. Note that an allowable magnitude of a transient for system linearity depends on the size of a pipeline system.

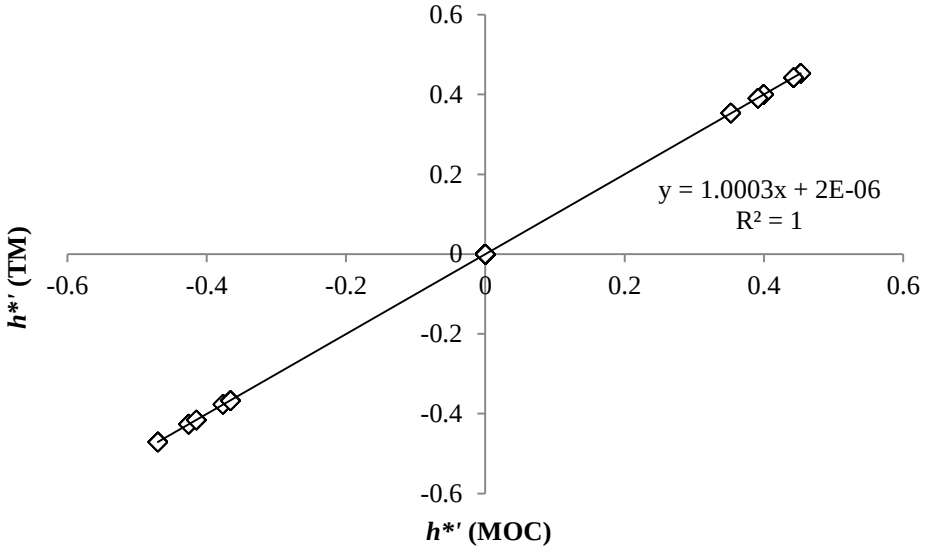

Figure 3.5 – Comparison between the transient traces generated by the MOC and the TM model (for laboratory pipeline system). Pressure trace measured 12.5 m from the upstream boundary. The size of the signal is 10 m.

The resistance terms appearing in the MOC and the transfer matrix equations only take into account the steady state friction. It has been observed in numerous studies that the steady friction alone cannot produce sufficient damping of the signal (Daily *et al*. 1956, Holmboe and Rouleau 1967, Vardy *et al*. 1993, Bergant and Simpson 1994, Bergant *et al*. 2001, Vítkovský *et al*. 2006). The extra damping is caused by additional shear stresses incurred

from the fluid acceleration and deceleration in transient flows and this phenomenon is known as unsteady friction.

3.3 Unsteady friction

With the consideration of unsteady friction effects, the total amount of energy loss is given by:

$$J = J_S + J_U \tag{3.53}$$

in which J = total friction loss, J_S = friction loss per unit length due to steady friction and J_U = friction loss per unit length due to unsteady friction. The steady friction term, J_S is given by:

$$J_S = \frac{fV|V|}{2gD} \tag{3.54}$$

where V = average velocity of the fluid. Two common one-dimensional unsteady friction models are the instantaneous acceleration-based model and the convolution-based model.

The instantaneous acceleration-based model was first developed by Daily *et al*. (1956) who suggested that the instantaneous acceleration may be affecting the shear stress along the pipe wall. The proposed form of the unsteady friction term J_S is:

$$J_U = \frac{C}{g}\frac{\partial V}{\partial t} \tag{3.55}$$

where C = unsteady friction coefficient which is either determined experimentally or numerically using another model and $\partial V/\partial t$ = temporal acceleration. Numerous researchers investigated and modified this model for improvement (Carstens and Roller 1959, Brunone *et al*. 1991, Vardy and Brown 1995, Bergant *et al*. 1999, Pezzinga 2000, Vítkovský *et al*. 2000). However, it was found in Vítkovský *et al*. (2006) that even the improved model of Vítkovský *et al*. (2000) failed to give accurate predictions of some types of transient events.

The convolution-based model was first implemented by Zielke (1968) with the following unsteady friction term:

$$J_U = \frac{16\nu}{gD^2}\int_0^t \frac{\partial V}{\partial t}(t^*)W(t-t^*)dt^* = 0 \tag{3.56}$$

where the integral term is known as the convolution integral (Ambardar 1999, Ljung 1999), W = weighting function and t^* = time used in the convolution integral. This model relates the wall shear stress for transient laminar flow to the instantaneous mean velocity and the weighted past velocity changes in the pipe cross-section. The weighting function given by Zielke (1968) is only for laminar flow, but other researchers found the weighting function for turbulent flows (Vardy *et al*. 1993; Vardy and Brown 1995, 2003, 2004). In Vítkovský *et al*. (2006), the convolution-based model was tested using the weighting functions of Zielke (1968) for laminar flow and Vardy and Brown (1995) for turbulent flow. Comparison with the experimental tests showed that, while the model was unable to give the correct longer-term behaviour of the transient signal, its first few cycles of the oscillation were well predicted. The convolution-based model was also utilised by other researchers in the past for transient simulations (Covas *et al*. 2004, Vítkovský *et al*. 2007, Adamkowski and Lewandowski 2012, Duan *et al*. 2012, Lee *et al*. 2013, Meniconi *et al*. 2013). The convolution-based model has an advantage when carrying out the frequency-domain simulations because the convolution in the time domain is equivalent to a multiplication in the frequency domain. For these reasons, the unsteady friction is computed by the convolution-based model in this thesis. For laminar flow, the weighting function, W is computed using the weighting function model presented in Zielke (1968). The unsteady friction model proposed in Vardy and Brown (1995) is employed for smooth pipe turbulent flow. The calibrated friction factors of the laboratory pipeline indicates that the laboratory system produces laminar and smooth pipe turbulent flows. The calibration results are presented in Section 4.5.

3.3.1 Time-domain representation of unsteady friction

When incorporating Equation 3.57 in the MOC model, it takes the following form:

$$\frac{1}{gA}\frac{\partial Q}{\partial t}+\frac{\partial H}{\partial x}+\frac{fQ|Q|}{2gDA^2}+\frac{16\nu}{gD^2}\sum_{j=1}^{k-1}\left(V_{i,j+1}-V_{i,j-1}\right)W(\tau)=0 \tag{3.57}$$

where the subscripts *i* and *k* are the space step and the time step in the MOC simulations and τ = dimensionless time which is given by:

$$\tau=\frac{4\nu}{D^2}(k-j)\Delta t \tag{3.58}$$

In Zielke (1968), two forms of the weighting function for laminar flows were given. For $\tau \leq$ 0.02,

$$W(\tau)=\sum_{j=1}^{6} m_j \tau^{0.5j-1} \tag{3.59}$$

and for τ > 0.02

$$W(\tau)=\sum_{j=1}^{5} e^{-n_j\tau} \tag{3.60}$$

where m_j = {0.282095, -1.25, 1.057855, 0.9375, 0.396696, -0.351563} and n_j = {26.3744, 70.8493, 135.0198, 218.9216, 322.5544}.

The weighting function for smooth pipe turbulent flows is (Vardy and Brown 1995):

$$W(\tau)=\frac{1}{2\sqrt{\pi\tau}}e^{\left(-\frac{1}{C^*}\tau\right)} \tag{3.61}$$

where *C** is the shear decay coefficient, which depends of the Reynolds number of the steady flow in the following way:

$$C^*=\frac{7.41}{\mathrm{Re}^{\kappa}} \tag{3.62}$$

and

$$\kappa = \log_{10}\left(\frac{14.3}{\mathrm{Re}^{0.05}}\right) \tag{3.63}$$

In Equations 3.62 and 3.63, Re is the Reynolds number (= VD/ν).

3.3.2 Frequency-domain representation of unsteady friction

Substitution of Equations 3.19 and 3.20 into Equation 3.56 and incorporation of Equation 3.23 to simplify the resulting equation gives:

$$\frac{1}{gA}\frac{\partial q^*}{\partial t} + \frac{\partial h^*}{\partial x} + \frac{f|Q_0|}{gDA^2}q^* + \frac{16\nu}{gD^2A}\int_{-\infty}^{t}\frac{\partial q^*}{\partial t}(t^*)W(t-t^*)dt^* = 0 \tag{3.64}$$

Implementing the assumptions of Equations 3.27 and 3.33 and dividing through by $e^{j\omega t}$ leads to:

$$\frac{j\omega}{gA}q + \frac{\partial h}{\partial x} + \frac{f|Q_0|}{gDA^2}q + \frac{16\nu}{gD^2A}\frac{j\omega}{e^{j\omega t}}q\int_{-\infty}^{t}e^{j\omega t^*}W(t-t^*)dt^* = 0 \tag{3.65}$$

Similar to Equation 3.58, the weighting function can be expressed in terms of the dimensionless time, τ through:

$$\tau = \frac{4\nu}{D^2}(t-t^*) \tag{3.66}$$

Substituting Equation 3.66 into Equation 3.65 and some rearranging gives the momentum equation as a function of frequency, ω:

$$\frac{j\omega}{gA}q + \frac{\partial h}{\partial x} + \frac{f|Q_0|}{gDA^2}q + \frac{4j\omega}{gA}q\int_{0}^{\infty}e^{\left(-\frac{j\omega D^2}{4\nu}\tau\right)}W(\tau)d\tau = 0 \tag{3.67}$$

In the transfer matrix equations, the resistance term appears in the propagation constant, μ. When unsteady friction is included, the steady state resistance term, R_S is replaced by the overall resistance term, R which is a sum of the resistance from steady and unsteady friction.

$$R = R_S + R_U \tag{3.68}$$

where:

$$R_S = \frac{f|Q_0|}{gDA^2} \tag{3.69}$$

$$R_U = \frac{4j\omega}{gA}\int_0^{\infty} e^{\left(-\frac{j\omega D^2}{4\nu}\tau\right)} W(\tau) d\tau \tag{3.70}$$

Vítkovský *et al*. (2003b) presented the frequency-domain representation of the Zielke (1968) weighting function as:

$$R_U = \sum_{j=1}^{6} R_{U1,j} + \sum_{j=1}^{5} R_{U2,j} \tag{3.71}$$

in which

$$R_{U1,1} = \frac{4j\omega}{gA} m_1 K \tag{3.72a}$$

$$R_{U1,2} = \frac{4j\omega}{gA}\frac{m_2}{b}\left(1 - e^{-0.02b}\right) \tag{3.72b}$$

$$R_{U1,3} = \frac{4j\omega}{gA}\frac{m_3}{b}\left(0.5K - \sqrt{0.02}e^{-0.02b}\right) \tag{3.72c}$$

$$R_{U1,4} = \frac{4j\omega}{gA}\frac{m_4}{b^2}\left[1 - e^{-0.02b}\left(0.02b + 1\right)\right] \tag{3.72d}$$

$$R_{U1,5} = \frac{4j\omega}{gA}\frac{m_5}{b^2}\left[0.75K - \sqrt{0.02}e^{-0.02b}\left(0.02b + 1.5\right)\right] \tag{3.72e}$$

$$R_{U1,6} = \frac{4j\omega}{gA}\frac{m_6}{b^3}\left[2 - e^{-0.02b}\left(0.0004b^2 + 0.04b + 2\right)\right] \tag{3.72f}$$

$$R_{U2,j} = \frac{4j\omega}{gA}\left(\frac{e^{-0.02\left(b+n_j\right)}}{b+n_j}\right) \tag{3.72g}$$

where $K = \sqrt{\pi / b}erf\left(\sqrt{0.02b}\right)$ and $b = j\omega D^2/(4\nu)$.

The frequency-domain version of Vardy and Brown (1995) model is also given in Vítkovský *et al*. (2003b) as:

$$R_U = \frac{2j\omega}{gA}\left(\frac{1}{C*} + \frac{j\omega D^2}{4\nu}\right)^{-\frac{1}{2}} \tag{3.73}$$

The unsteady friction effect is included using these models in the numerical simulations presented in this thesis unless otherwise stated.

3.4 Verification of the Method of Characteristics model

For numerical analyses, the MOC model produces a transient trace that is considered to represent the transient behavior in real systems and hence the validity of the analyses hinges on its accuracy. The accuracy of the MOC model used in this thesis was firstly verified using a numerical transient trace given in Kim (2008). A transient was generated by the closure of the solenoid valve at the downstream end of a tank-pipe-valve system. The initial flow velocity was 0.0599 m/s with the flow Reynolds number of 1300. The pipeline was 37.46 m long with an internal diameter of 22.1 mm. Further details of the pipe system are found in Kim (2008). Since the flow was laminar, the unsteady friction model by Zielke (1968) was incorporated in the simulation as well as the steady friction. The MOC model discretised the pipe into 100 subsections with a computation time step of 2.79×10^{-4}s. The comparison between the transient trace in Kim (2008) and the response predicted from the MOC model for the present work is shown in Figure 3.6. An excellent match between the two traces is found and the accuracy of the MOC model has been verified.

The predicted result from the MOC model was also compared to the measured pressure response in the laboratory pipeline in Figure 3.7. The side discharge valve next to the closed downstream boundary was closed in 0.022 seconds to generate the transient signal. The initial flow through the valve gave a flow Reynolds number of 2800. The unsteady friction model by Vardy and Brown (1995) was used to predict the unsteady friction effects. The MOC model well predicts the attenuation and the shape of the measured transient trace. The shown level of match is similar to published results (Lee 2005, Vítkovský *et al*. 2006).

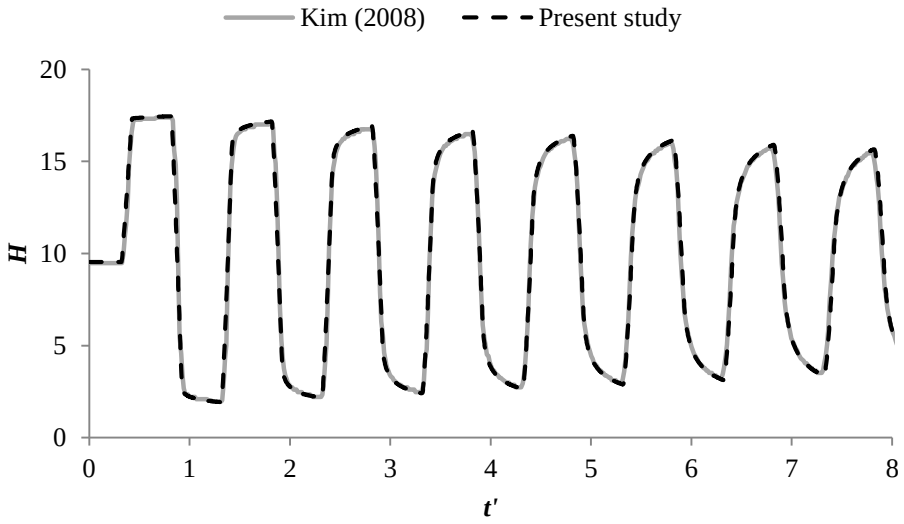

Figure 3.6 – Comparison between the numerical transient trace generated in Kim (2008, Figure 5.17) and that from the MOC model used in this thesis

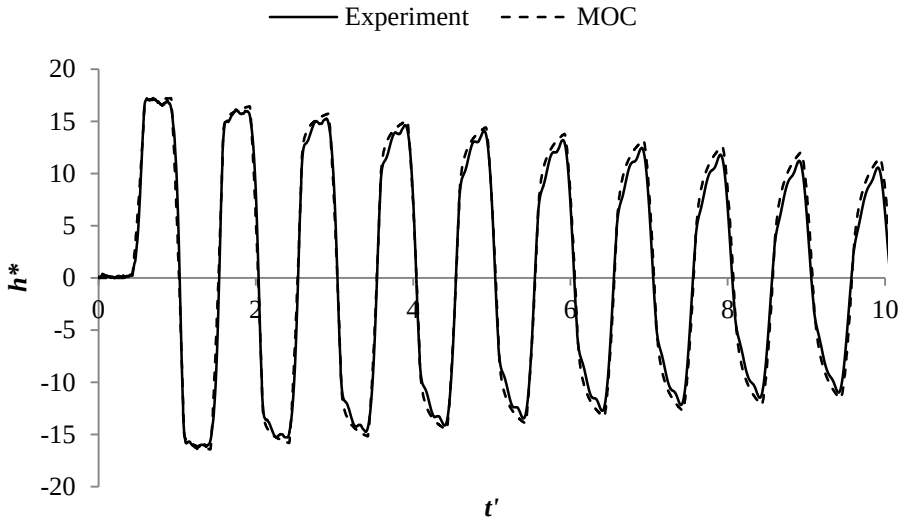

Figure 3.7 – Comparison between the numerical trace generated by the MOC model and the measured trace from the laboratory pipeline system

Two numerical models—the MOC model and the TM model—were described in this chapter along with the models for leak and unsteady friction. They are used to predict the transient behaviour in the laboratory pipeline system whose details are covered in the next chapter.

Chapter 4 Pipeline Apparatus for Numerical and Experimental Analyses

The analyses presented in this thesis are carried out both numerically and experimentally. The numerical analysis provides flexibility in the system configuration, Reynolds number and the method for generating the transient signal. The numerical model has the advantage of being able to produce results that cannot be obtained experimentally. Numerical simulations were also used to design experimental tests. The pipeline system in the hydraulics laboratory at the University of Canterbury is used for the experimental investigations.

4.1 Numerical pipeline system

The numerical system consists of a 2000-m long pipeline that is bounded by constant head reservoirs, which give a head difference across the pipeline between 5 to 30 m. The pipe diameter is 0.3 m and its relative roughness is made small so that the pipe can be assumed smooth. The pipe is laid horizontally and the wave speed of the system is 1000 m/s. Measurement points and transient generators can be placed anywhere in the system. The positions of the pressure and flow measurement points and the generators are indicated by a circle, square and a diamond respectively, as shown in Figure 4.1. Transient responses of the system are produced by a finely discretised Method of Characteristics (MOC) model which divides the pipe into 1000 reaches. The system can include pipe defects such as leaks if required. The characteristics of the leak can vary and will be specified for each analysis along with its location.

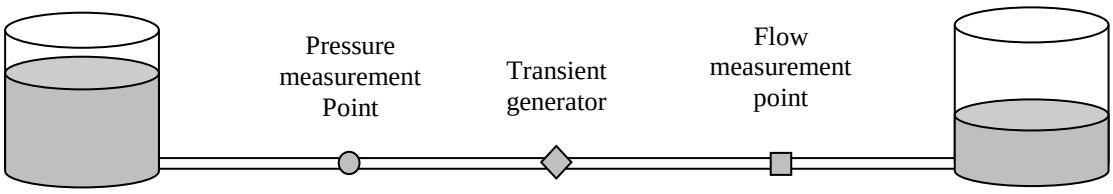

Figure 4.1 – Schematic of numerical pipeline system

4.2 Laboratory pipeline system

The laboratory system was newly built in 2009 and the thesis author was responsible for commissioning of the system and associated instrumentation. A schematic of the laboratory pipeline system is shown in Figure 4.2. It consists of a stainless steel pipe of 42.247 m length, 22.25 mm internal diameter and 1.6 mm wall thickness. The bursting pressure head of the pipe is 8580 m. Pipe segments of approximately 2 m and 6 m, and multiple test sections of 0.2 m are assembled with zero-tolerance flange connections to form one straight pipeline. There are inline valves at either end of the pipe and the pipe length becomes 41.647 m when the downstream valve is closed. The pipe is set at a constant angle of 3.5˚, resulting in the height difference of 2.509 m between the two ends of the pipe. The pipeline is fixed by wall-mounted supports located every 0.5 m to minimise fluid structure interaction.

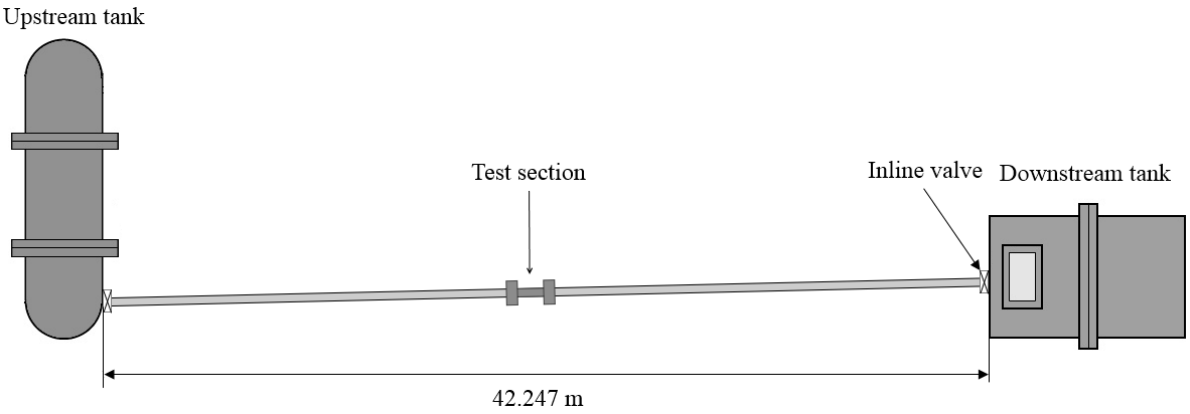

Figure 4.2 – Schematic of laboratory pipeline system

The pipe is bounded by pressurized tanks that are part filled with water. At the upstream system boundary, there is a cylindrical tank that is 3.49 m in height with a diameter of 0.491 m (Figure 4.3a). To construct this tank, three circular cylinders were flange-connected to form the middle section of the body, and semi-spherical sections were welded to the cylinders to form the top and bottom of the tank. The wall thickness of the cylinders and the ends are 4 mm and 3mm respectively. The downstream tank is in the form of a cylinder with a diameter of 0.981 m and a length of 2.33 m (Figure 4.3c). It has a viewing window on its side (42 cm by 20 cm) and the water level inside the tank can be observed through a clear acrylic plate of 2.5 cm in thickness. Both tanks are proven to withstand a pressure head of 100 m.

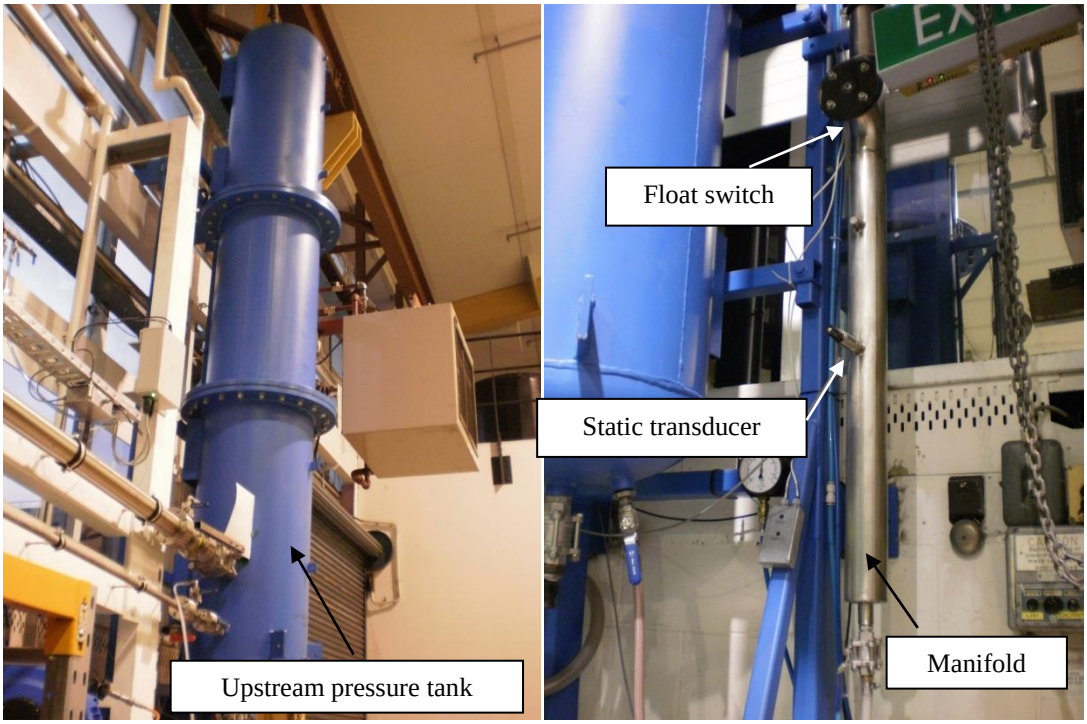

(a) Upstream tank **(b) Manifold attached to the upstream tank**

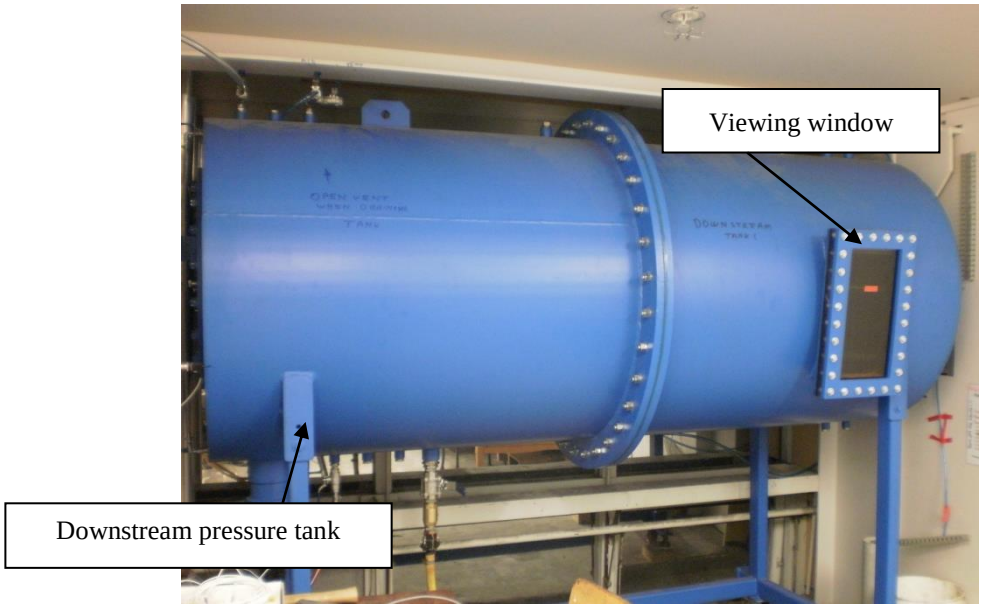

(c) Downstream tank

Figure 4.3 – Components of the laboratory pipeline system

The tanks were filled with city mains water and before entering the tank, the water was filtered with a mesh with 5 µm holes to remove impurities. The tanks are accompanied by a manifold for the measurement of pressure and water level inside the tank (Figure 4.3b). The water level is measured by a float switch (Cynergy3 SSF211) that is installed inside the

manifold. The switch is initially tilted by 15˚ and the tilt angle decreases as it is pushed up by the rising water level. The switch sends out a signal when it becomes horizontal.

The tank is pressurised by pumping air into the tank from an air compressor. The pressure is regulated at the air intake and by two pressure controlling solenoid valves situated at the top of the tank. These controlling valves maintain the set pressure within the tanks while transient tests are undertaken. One valve is to control the air entering the tank and the other acts as an air vent. The pressure inside the tank is monitored by a static transducer attached to a manifold next to the tank. The position of the static transducer is levelled so that it is situated at the same height as the centre of the pipe-tank boundary. A pressure relief valve is installed on top of the tank and it is set to activate it if the inside pressure head exceeds 35 m.

On the pipeline, test sections for the installation of pressure transducers, side discharge valves and a solenoid valve can be inserted (Figure 4.4). Each section is made of stainless steel and has a length of approximately 0.2 m. The internal diameter of the pipe section is the same as the main pipeline to minimise flow disturbance. The system can have six test sections at a time and their location can be altered by changing the order of pipe segments.

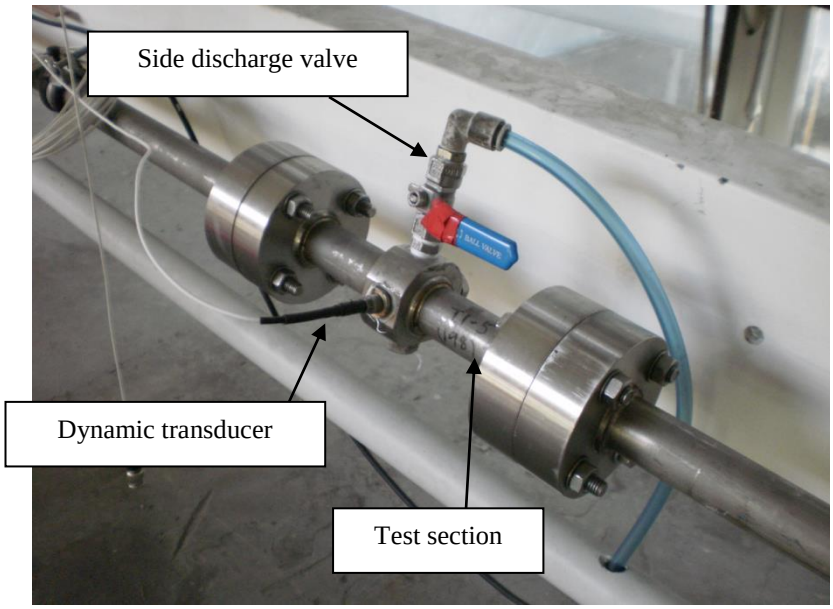

Figure 4.4 – Test sections with a dynamic transducer and a side discharge valve

The system wave speed was measured experimentally using two or more pressure transducers. The transducers were placed at a known distance apart and a transient signal was generated. The two transducers detected the signal with a certain time lag corresponding to the time it took for the signal to arrive at each transducer. This time lag and the distance between the transducers were used to determine the system wave speed. The average wave speed of the system is 1350 m/s which is similar to the wave speed for the steel pipe system in Szymkiewicz and Mitosek (2014). The wave speed is sensitive to the air content of the water and so it was measured at the start of each experiment.

The steady flow was measured by observing the decrease in water level in the upstream tank. With a certain system head loss, the time taken for the water level to go from one height to the other was measured. A floating switch was placed at these heights, indicating the timing of the start and the end of the measurement. For example, with the system head loss of 30 m, the steady flow was 0.0015 m^3/s. From this steady flow, a flow velocity, Reynolds number and a friction factor were calculated to be 3.74 m/s, 83100 and 0.023 respectively.

4.3 Data acquisition system

Static transducers (Gems sensors 2200/2600 series) used in the system have a nominal pressure range of 6 bars, with the accuracy of 0.25% of the full measurement range. Prior to experiments, the static transducers were calibrated using a dead weight tester to determine their voltage offset which they experience. The voltage offset is the difference in readings made by the transducers and the known pressure applied by weights. The static transducers are useful when measuring static or slowly changing pressures but they are not suited to measure dynamic or rapidly changing transient pressures.

Dynamic transducers were used to measure rapidly changing pressures. The dynamic transducers (ICP Dynamic Pressure Sensor, Model 102A07) have an absolute pressure head range of 0 to 34.5 m with the uncertainty being rated at ± 1%. A rise time of the transducer is 2×10^{-5} seconds. In some experiments, the relative accuracy between transducers was critical and the relative accuracy in the magnitude and phase was determined experimentally prior to such experiments. A group of transducers were attached around a flange of a test section so that they are at the same location relative to the system boundary. A transient signal was

generated 12.23 m away from the transducers. The measured signals are presented in Figure 4.5, which were sampled at 100,000 Hz for greater accuracy. The time, *t'*, and the amplitude of the pressure fluctuation, *h*'*, in the figure are normalised by the period of the pipeline system and the steady head at the measurement point respectively.

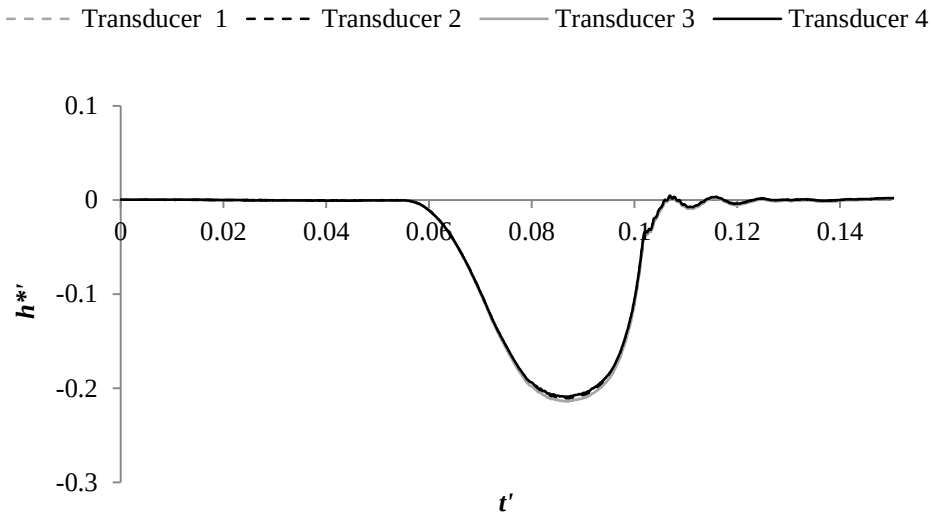

Figure 4.5 – Transient signals measured by 4 pressure transducers

With respect to Transducer 1, the maximum head and the signal width difference, as an indication of phase difference, observed were 1.96% and 0.98% respectively. The amplification factors of Transducers 2, 3 and 4 were modified so that the measured magnitude from these transducers matches that of Transducer #1, reducing the amplitude difference to the order of 0.01%. The error in the signal width could not be avoided with the available transducers and the measurement instruments.

Pressure data was recorded using LabVIEW software (National Instrument, version 8.2). The analogue data acquired from the transducers was converted to digital signals by an A/D converter. The maximum single channel sampling rate was one million samples per second. It is possible to take a pressure measurement from seven dynamic transducer and six static transducers simultaneously. The pressures were sampled at a frequency of 10,000 Hz unless otherwise stated.

4.4 Transient generator

Fluid transients were generated by a side discharge valve or an electronically controlled solenoid valve. The side discharge valve produced a step change in pressure by quickly opening or closing the valve. It is the easiest method of transient generation and has been used in numerous studies (Bergant *et al*. 1999, Vítkovský 2001, Stephens *et al*. 2005). By placing the valve close to the open system boundary, it was possible to obtain a pulse signal. The fast closure of the side discharge valve created a high pressure wave that propagated away from the valve in both directions. When the wave front moving downstream impinges upon the system boundary it was reflected as a pressure restoring wave that moved upstream, following the high pressure wave. Superposition of these two waves gave a pressure pulse. While the pulse created by the side discharge valve had a longer duration than that from the solenoid valve, it had a larger magnitude and was suitable in cases of larger system base flow. The side discharge valves used in this research were stainless steel ball valves with a diameter of 8 mm and a maximum pressure head rating of 713.6 m.

The use of the solenoid valve (BACCARA GEM-SOL GEM-B-23) had some advantages over the side discharge valve. At times the closure of the side discharge valve generated transients that it exceeded the maximum detectable range of the transducers. Also the underlying assumption for the transfer matrices of the pipe is that it is a linear system. In order not to violate this assumption it is important to keep the signal size small (Chaudhry 1987, Smith 1999). The solenoid valve could repeatedly reproduce transients that were small enough (~ 10 m) for the assumption of linearity to be valid.

The solenoid valve is a “normally-closed” valve with an orifice diameter of 1.6 mm. The valve has a maximum operating differential pressure head of 120 m. The opening time of the valve can be selected on a controller connected to the valve. The valve can move from fully closed to fully opened in as fast as 5ms under a head of 30 m. The solenoid valve and the controller are shown in Figure 4.6 and a typical signal obtained from the solenoid valve is presented in Figure 4.5.

Other types of input signals have been considered in the literature such as sinusoids (Zielke *et al*. 1968, Chaudhry 1987, Mohapatra and Chaudhry 2011) and pseudo random binary signals

(Balcomb *et al*. 1961, Liou 1998, Lee 2005), both of which are classified as a continuous signal. The use of these signals requires a settling time in which the system comes to the steady 'oscillatory' state before taking measurements. In the case of a sinusoidal input, the apparatus can include a rotary motor and its smooth movement must be ensured for a generation of a pure sinusoid (Brekke 1984). Due to these potential complications, only a discrete signal is considered in this work.

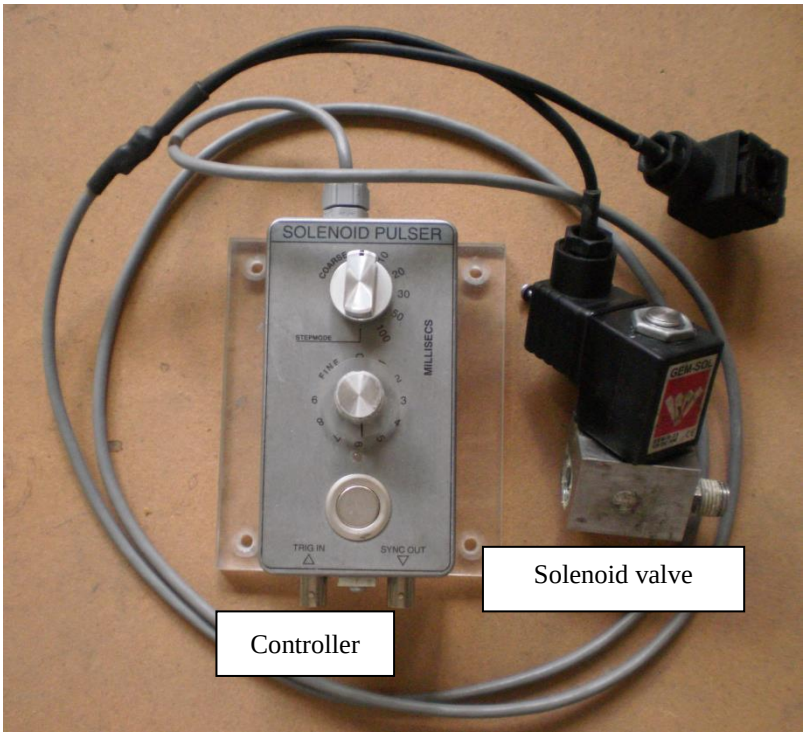

Figure 4.6 – Solenoid valve used for transient generation and the controller

4.5 Friction factors of laboratory pipeline system

Friction factors of the laboratory pipeline system were experimentally determined from the measured pressure difference between the upstream and downstream boundary of the system and the measured flow rate. The flow rate was controlled by the head difference between the boundary tanks. The head difference ranged from 0.5 to 3 bar and all experiments for this thesis were conducted within this range of head. The determined friction factors are tabulated in Table 4.1 as well as the friction factors for a smooth pipe read off the Moody diagram (Moody and Princeton 1944).

Re	Measured friction factor, f	Smooth pipe friction factor
22700	0.0251	0.0248
40800	0.0221	0.0217
54000	0.0207	0.0204
64900	0.0201	0.0196
74600	0.0196	0.0191
83200	0.0190	0.0186

Table 4.1 – Friction factors of the laboratory pipeline system

The result indicates that the measured friction factors are similar to the smooth pipe friction factors. Therefore, it is concluded that the laboratory pipeline produces laminar and smooth pipe turbulent flows for the head difference between 0.5 and 3 bar.

Chapter 5 Improvements on Conventional Impulse Response Function

Desirable properties of a pipeline condition assessment technique include: high accuracy and time efficiency, environment-friendly, non-destructive, simple implementation, easy data interpretation, portability and low manpower demand. Amongst the existing techniques, transient-based methods have these characteristics and can be applied to a range of pipeline faults. This chapter focuses on one of the transient-based assessment methods which employs an impulse response function. The impulse response function is a description of the behaviour of a system as briefly introduced in Chapter 1. The extraction procedure of the impulse response function involves an injection of input signals to the system and the measurement of the response (output signal). The conventional extraction procedure is demonstrated using numerical and experimental data, highlighting the issues associated with it. Two methods for improvements are proposed in this chapter.

5.1 Introduction to impulse response function

A system can be considered as a component or a network of components that produces an output signal in response to an input signal and it is symbolically depicted in Figure 5.1. In the figure, *u* and *y* are the input and output signals as a function of time *t*.

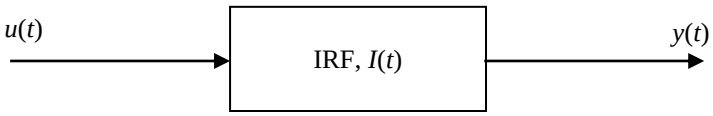

Figure 5.1 – Schematic of a system with input and output signals

The input signal enters the system and it is modified by the system. A summary of the modifications imposed by the system onto the input is known as the *impulse response function* (IRF) and is given a symbol *I* in Figure 5.1. The IRF provides the time-domain response of the system to a unit impulse. The output signal is produced from the convolution between the input signal and the IRF. A schematic of the convolution process is given in Figure 5.2. In the figure, the input signal consists of a series of impulses where each impulse

is expected to produce an output from the system according to the impulse response. Each of these responses is a scaled and shifted version of the system impulse response. As the system is considered to be linear, the overall response from the input signal is constructed by combining the three impulse responses.

The convolution is mathematically written as (Lynn 1982, Ambardar 1999, Ljung 1999):

$$y(t) = u(t) * I(t) = \int_{-\infty}^{\infty} u(\tau) I(t-\tau) d\tau \tag{5.1}$$

where τ = dummy variable. The integral in Equation 5.1 is known as the *convolution integral*. Extraction of the IRF from the measured input and output of the system in the time domain through deconvolution is not desirable as it is mathematically intensive (Smith 1999, Ambardar 1999). As an alternative, the IRF can be obtained using the fact that it possesses a frequency-domain counterpart called the frequency response function (FRF). The IRF and the FRF are a Fourier transform pair, meaning that the conversion from one to the other is done by performing a fast Fourier transform (FFT).

Convolution in the time domain corresponds to multiplication in the frequency domain (Lynn 1982, Smith 1999) and thus the equivalent of Equation 5.1 in the frequency domain is given by:

$$Y(f) = F(f).U(f) \tag{5.2}$$

where Y and U are the Fourier transformed output and input respectively, F = FRF and f = frequency. Deconvolution is an inverse operation of convolution and thus in the frequency domain deconvolution is carried out as a simple division. The quotient is the FRF and the corresponding IRF is determined by taking the inverse Fourier transform (Smith 1999).

$$I(t) = \Im^{-1}\left(\frac{Y(f)}{U(f)}\right) \tag{5.3}$$

where $\Im^{-1}$ denotes the inverse Fourier transform.

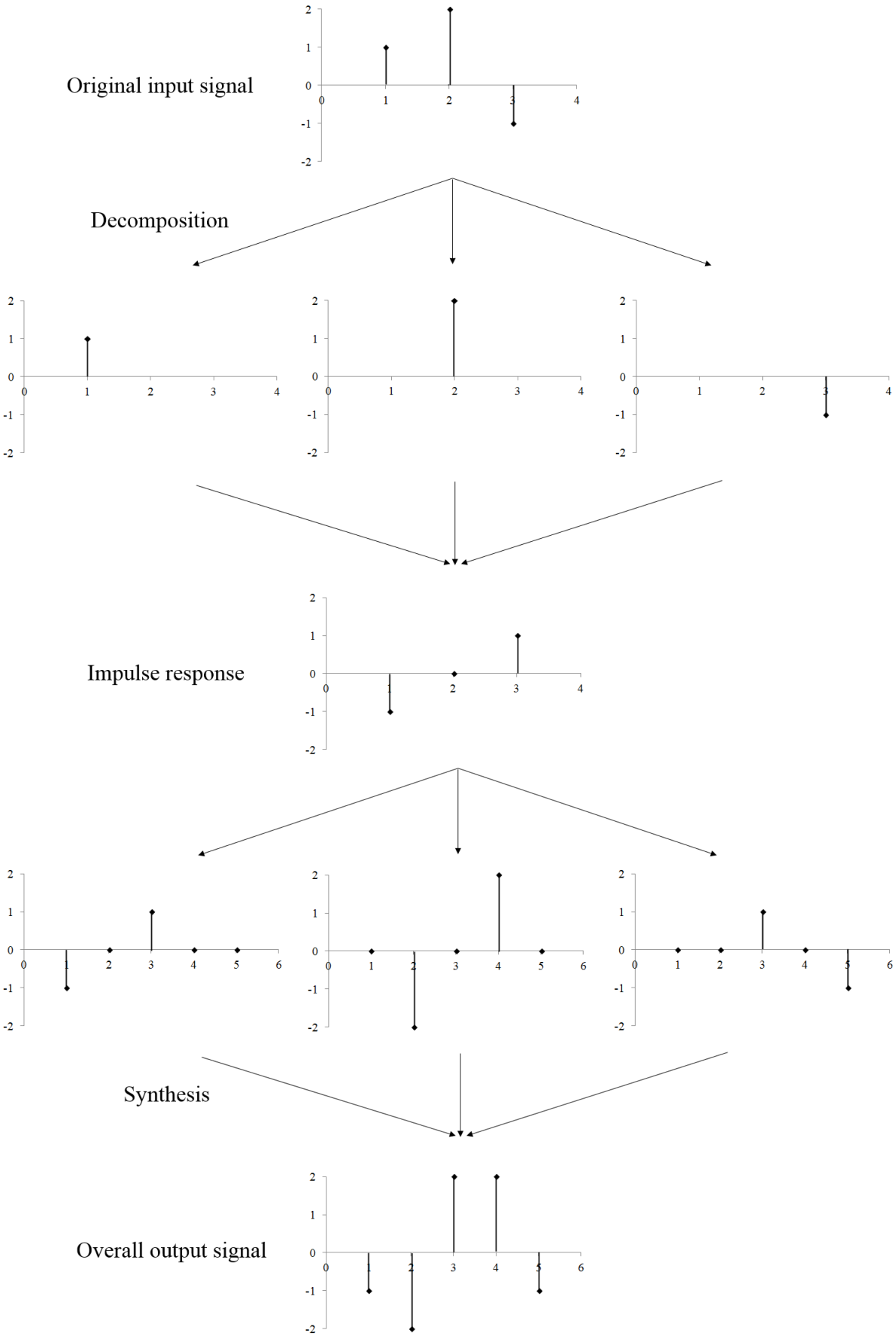

Figure 5.2 – Schematic of the convolution process

This system response extraction method assumed that the system is linear and the use of the IRF for analyses of pipelines is valid provided the size of the input signal is small (Balcomb *et al*. 1961, Chaudhry 1987, Suo and Wylie 1989, Lee *et al*. 2007a). In Chapter 3, the validity of the linear assumption was demonstrated with a transient signal of 10 m in magnitude.

5.2 Application of impulse response function extraction procedure on pipeline systems

In a pipeline system, the "system" in Figure 5.1 can consist of the pipes, connections, valves and other elements within the pipe system that will influence the response. The output signal, *y* for a pipeline system is the measured pressure response. Figure 5.3 presents a pressure trace measured at the transient generating valve which is placed at the middle of a numerical pipeline system. The time, *t'*, and the amplitude of the pressure fluctuation, *h*'*, in the figure are normalised by the period of the pipeline system and the steady head at the measurement point respectively. The transient, a pulse shaped signal, is injected to the system. Unsteady friction is neglected in this example to clearly illustrate the operation of the IRF extraction process.

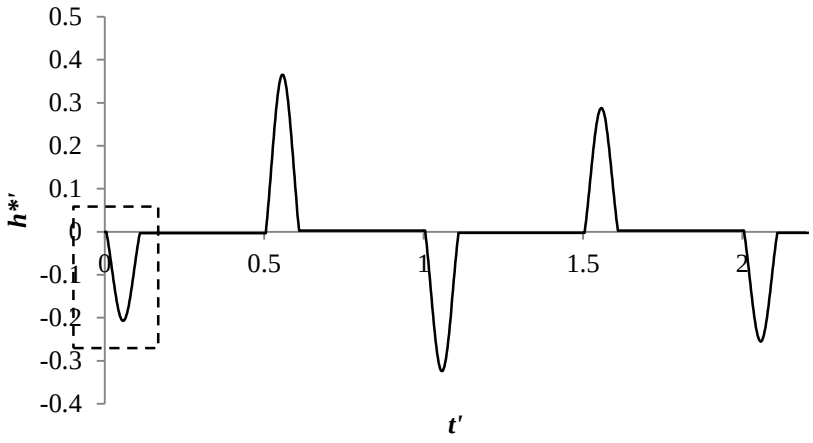

Figure 5.3 – Pressure trace with the pulse signal

The input signal, *u* used for extracting IRF can be extracted from the measured pressure. In Figure 5.3, the first pressure pulse (boxed in the figure) is associated with the valve movement that produces the transient and thus it can be considered as the input signal. Examples of other possible input parameters are the valve opening ratio (Mpesha *et al*. 2001,

2002, Mohapatra and Chaudhry 2011), the voltage input if the valve is solenoid driven (Beck *et al*. 2002), or the induced flow perturbation by the valve (Lee *et al*. 2007a, Duan *et al*. 2012a, b). All of these input parameters have been observed to give the IRF, however, the use of pressure input simplifies analyses. As illustrated with Figure 5.3, a single pressure sensor is adequate for measuring both the input and the output signals. Furthermore, accurate knowledge of the system parameter such as the system wave speed is not necessary and the resultant IRF is dimensionless.

These input and output signals are initially Fourier-transformed and the IRF is determined according to Equation 5.3 and is shown in Figure 5.4. Each pulse in the output is replaced by a single impulse in the IRF. The sharpness of each reflection is increased, providing a greater clarity in the reflection time and a corresponding increase in the spatial resolution of the subsequent fault detection (Lee *et al*. 2007a). Valves are typically used for transient generation; however, they cannot make a sharp maneuver due to mechanical inertia and often produce smooth signals with no distinct reference points. The use of such signals in localizing faults can be erroneous and additional difficulty arises in the presence of background noise which is superimposed on the measured signal. Therefore the refinement of the reflections into the form of sharp pulses through the IRF extraction process has significant practical advantages in fault detection.

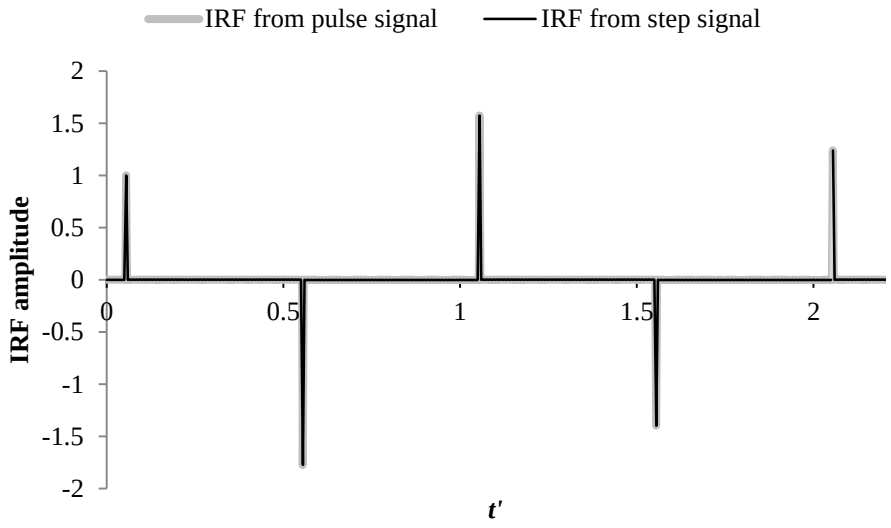

Figure 5.4 – IRFs extracted from the pulse and step signals in Figures 5.3 and 5.5

The IRF is a complete specification of the system behaviour and it remains the same regardless of the shape of the input signal provided the bandwidth is the same. To illustrate this property, a step signal is created by a closure of a side discharge valve with the valve manoeuvre time of 0.2 s. The measured trace at the valve is given in Figure 5.5 (a) along with the change in the pressure at the valve. The step signal produces the output signal which looks significantly different from the pulse case (Figure 5.3) while the characteristics of the underlying system are the same.

The extraction of the IRF from this trace introduces additional complexities. For the Fourier transform to exist, the integral of the signal must be finite (Lynn 1982). The step function violates this requirement and hence its frequency spectrum cannot be obtained by the conventional Fourier transform. However, the valve manoeuvre which produces the transient ends at the time of 0.24 s (or the dimensionless time of 0.06 in the figure) and the rest of the trace cannot be considered as the input as it does not excite the system further. Hence the input signal shown in Figure 5.5 (a) needs to be corrected so that it only contains the part which is related to the valve movement. Since the system is assumed linear and time-invariant, changes to the input also apply to the corresponding output. The correction procedure is covered in more detail in Lee *et al*. (2004). The corrected output signal is presented in Figure 5.5 (b) as well as the original step output. The first pressure rise boxed in the figure is used as the input for the extraction process.

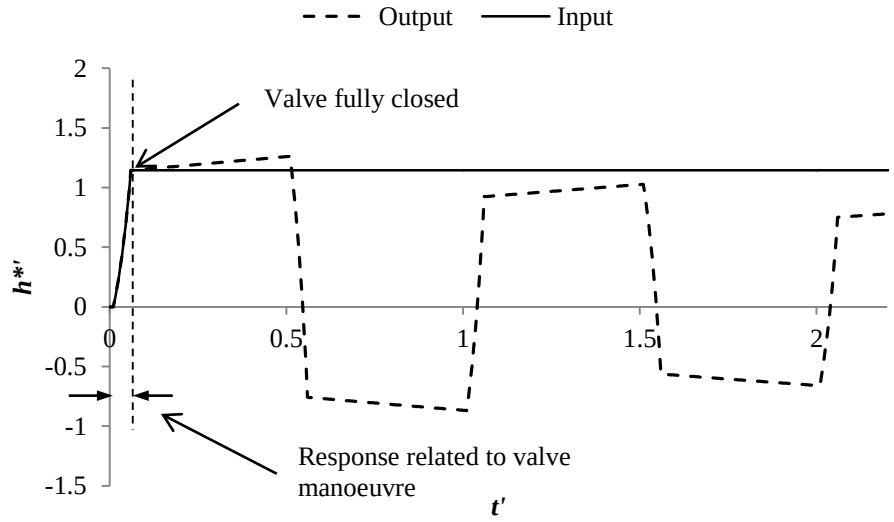

(a) Step input and measured output

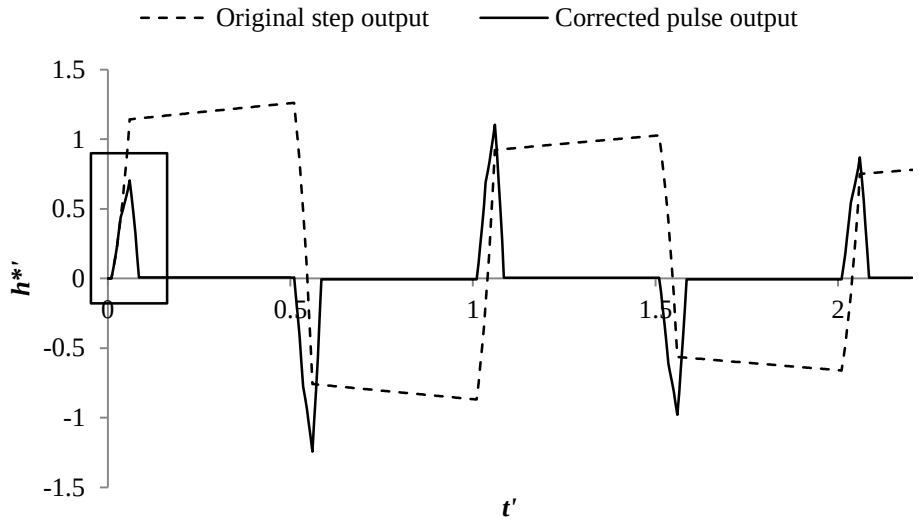

(b) Step-to-pulse conversion of the signal

Figure 5.5 – IRF extraction with step signal

In Figure 5.4, the resultant IRF perfectly overlaps with the IRF from the pulse signal. This example has demonstrated that the form of the IRF is independent of the shape of the input signal. This is an advantage of using the IRF for condition monitoring compared to the use of measured time-domain signals as it makes it possible to compare tests from one day to another regardless of the type of the transient signal used in each test. If two sets of data from the same pipeline system look as different as Figures 5.3 and 5.5 (a), they cannot be compared directly and give useful information about the condition of the system. The use of the time-domain signal for system monitoring also requires a separate time trace obtained from a fault-free system which is circumvented when using the IRF extraction procedure.

Consider another case where the signal undergoes shape changes due to unsteady friction. Unsteady friction imposes signal dispersion as well as an additional loss of magnitude. Therefore the resultant IRF of the system where unsteady friction is included is different from the steady-friction case and both are shown in Figure 5.6 (a). The IRF of the unsteady-friction system is shown by the black line and the IRF of the steady-friction system is given by the grey line. The form of the transient signal is a pulse which is identical to the one shown in Figure 5.3. While the first IRF pulse from the unsteady-friction system is an impulse, each subsequent reflection is formed from a group of impulses of different magnitudes. In Figure 5.6 (b), the IRFs in the range between t' = 2 to 2.2 in Figure 5.6 (a) are re-plotted to highlight

the complexity imposed by the shape change. The unsteady friction dilates the transient signal as it travels the system and the shape of the signal becomes dissimilar to the input signal (Brunone 1999, Lee *et al*. 2007a). A pair of pulses of different shapes cannot be related by a single impulse and the dilated portion of the signal needs to be described by additional impulses as indicated by a box in Figure 5.6 (b). These additional impulses reduce the clarity of the subsequent impulse response, especially in the presence of system noise and closely spaced reflection sources.

Representation of a pulse with multiple impulses means that the total energy of the pulse is divided into these impulses. The magnitude of the primary impulse is therefore smaller than the IRF from the steady-friction system as seen in Figure 5.6. Since the secondary impulses describe the dilated portion of the signal, they start taking a greater portion of the total magnitude as the dilation of the signal becomes more substantial with time, increasing the decay rate of the IRF with time.

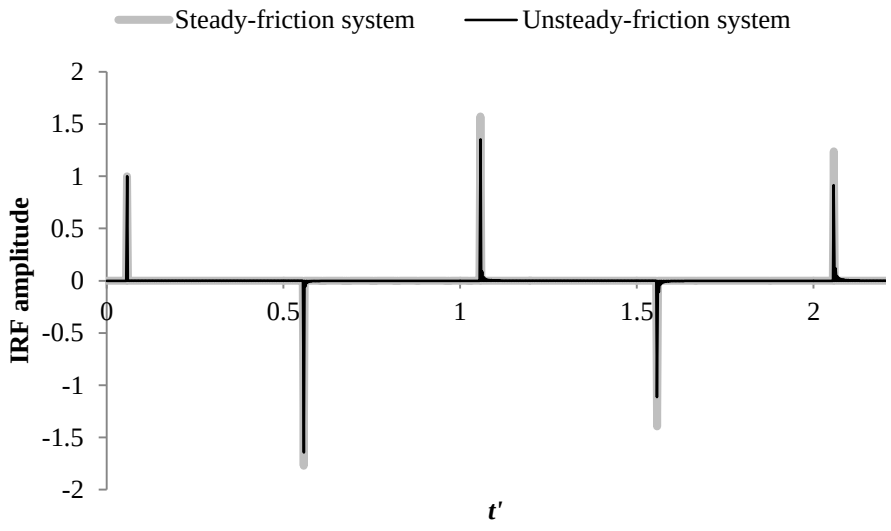

(a) IRF of the numerical pipeline system with and without unsteady friction

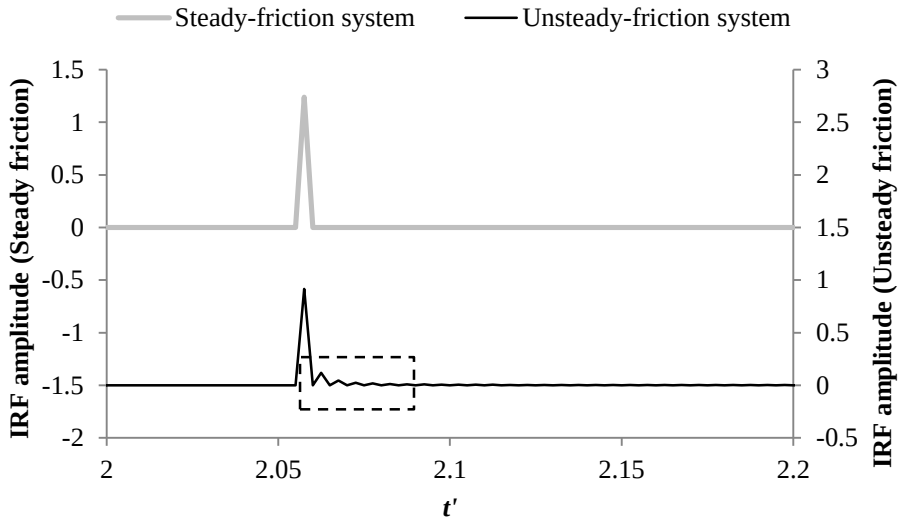

(b) Enlarged view of (a)

Figure 5.6 – IRF of the numerical pipeline system with and without unsteady friction

5.3 Experimental extraction of impulse response function

An experimentally extracted IRF contains additional complexities relative to the numerical example due to the presence of background noise and the limited bandwidth of the injected signal (Li *et al*. 1994, Lee *et al*. 2007a). To demonstrate these complexities an output signal was measured next to the closed downstream boundary of a system and a solenoid-driven valve was installed as a transient generator at the same point. Following the same procedure used for the numerical examples, the first pulse in the measured signal was used as the input. The input signals in the time- and the frequency domains are presented in Figures 5.7 (a) and (b). The duration of the input signal is 5 ms (equivalent to the dimensionless time width of 0.041) and the spectral amplitude of the input spectrum decreases to 5% of its maximum amplitude by approximately 517 Hz which is equivalent to the dimensionless frequency, *f'*, of 63. The frequency is normalized by the fundamental frequency of the pipeline system. The extracted IRF is presented in Figure 5.7 (c).

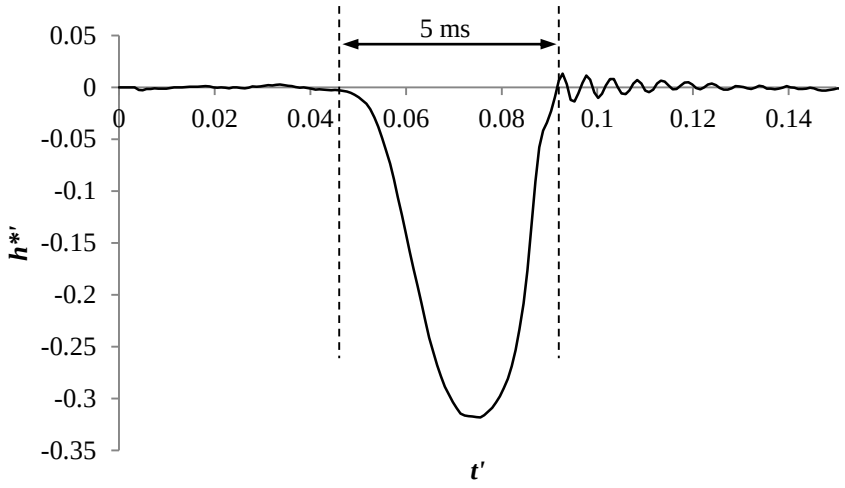

(a) Input signal in the time domain

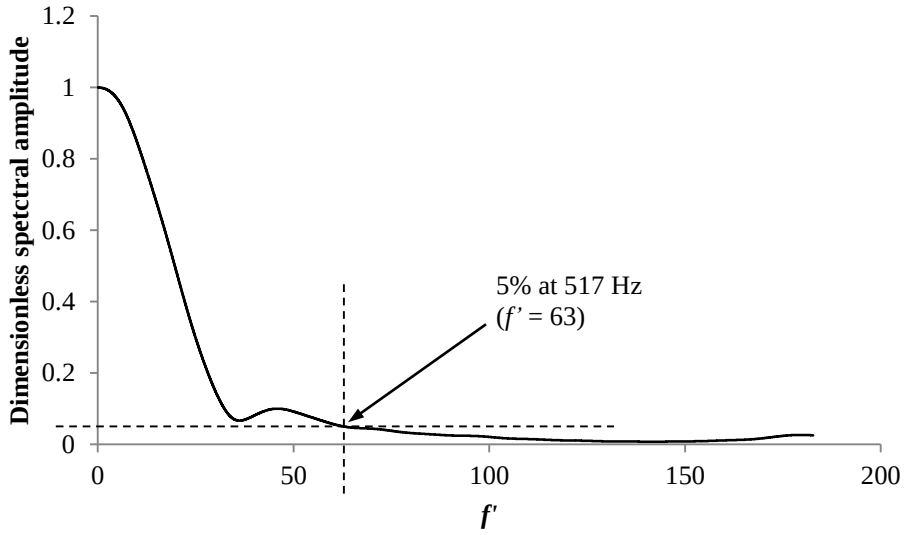

(b) Frequency spectrum of the input signal, normalised by its maximum magnitude

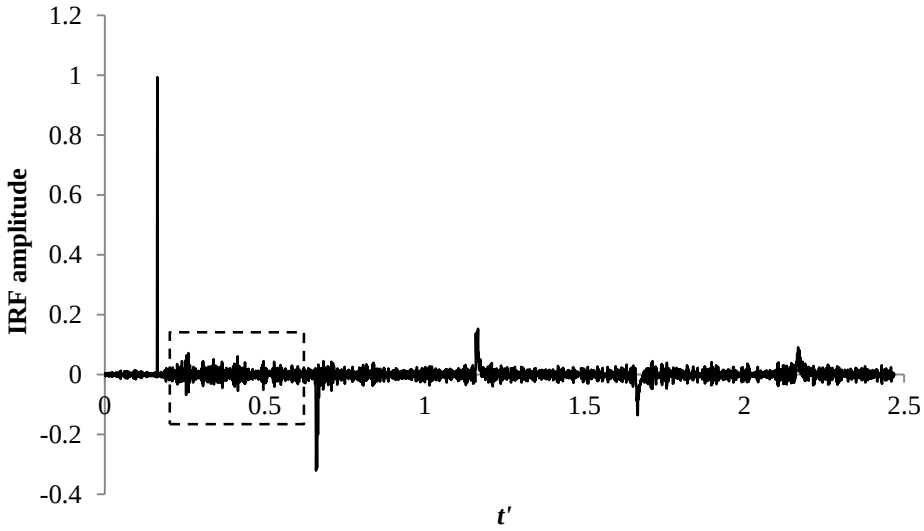

(c) IRF of the laboratory pipeline

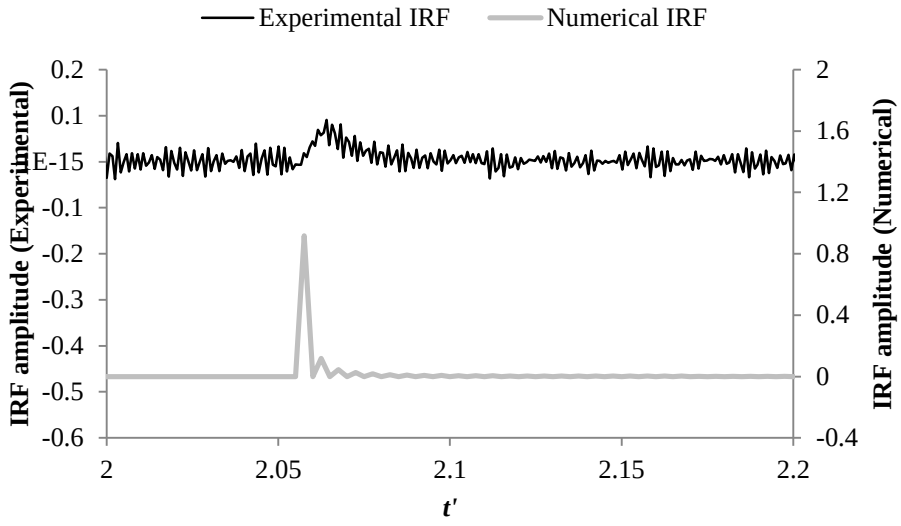

(d) Comparison between the numerical and the experimental IRF

Figure 5.7 – Experimental extraction of IRF of the laboratory pipeline system

Similar to the previous numerical results, only the first IRF pulse is in the form of an impulse. Unlike the numerical result in Figure 5.6, however, each of the subsequent IRF pulse is not in the form of a series of impulses as shown in Figure 5.7 (d) in which the fifth IRF pulse from the numerical IRF with unsteady friction and the experimental IRF are compared. Instead, the limited frequency content in the input signal meant that the impulses were merged to form a pulse of some width.

The IRF extracted from real systems also contains noise as boxed in Figure 5.7 (c). This noise arises from the frequency components outside the bandwidth of the input signal and is caused by background vibrations and flow turbulence. Similar noise was observed in previous impulse response extraction in Liou (1998) and Lee *et al*. (2007a) and in some system the noise can completely overwhelm the response impulses. Since the pipeline is assumed to be linear, the output from the system should have the same frequency range as the input (Lynn 1982). The frequency components outside this range do not hold useful information about the system and so they need to be filtered out prior to the inverse Fourier transform. Applying this filtering process, the equation for the IRF (Equation 5.3) is rewritten as:

$$I(t) = \Im^{-1}\left(W(f) \times \frac{Y(f)}{U(f)} \right) \tag{5.4}$$

where $W(f)$ is a filter window. Various shapes of the filter window are available. In Lee *et al*. (2007a), the Hamming and the Blackman windows were tested due to their ability to smoothly reduce the magnitude of high frequency components, thus avoiding Gibb's phenomenon—oscillations in time arising from abrupt changes in the frequency spectrum (Smith 1999). In this study, the Blackman window was utilised due to its better denoising ability than the Hamming window (Lee *et al*. 2007a). The Blackman window with a cut-off frequency, f_c of 517 Hz ($f_c' = f_c / F = 63$ where F is the fundamental frequency of the system) is presented in Figure 5.8 (a) and the denoised IRF using this filter is shown in Figure 5.8 (b).

The Blackman filter has successfully removed the high frequency noise and sections of the IRF between the system reflections are now relatively quiescent. However, this filtering process has imposed an undesirable distortion to the IRF. Compared to the unfiltered IRF in Figure 5.7 (c), the pulses in Figure 5.8 (b) are dilated so that all pulses are no longer an impulse including the first pulse. In removing the high frequency noise, the Blackman filter has removed the high frequency components of the IRF pulses and since the sharpness of a pulse is governed by the amount of the high-frequency components within the pulse, the pulses are now more dilated. This reduces the value of one advantage of using the IRF for pipeline diagnostics. This problem is most evident in situations where the noise has a frequency spectrum that overlaps with the system response.

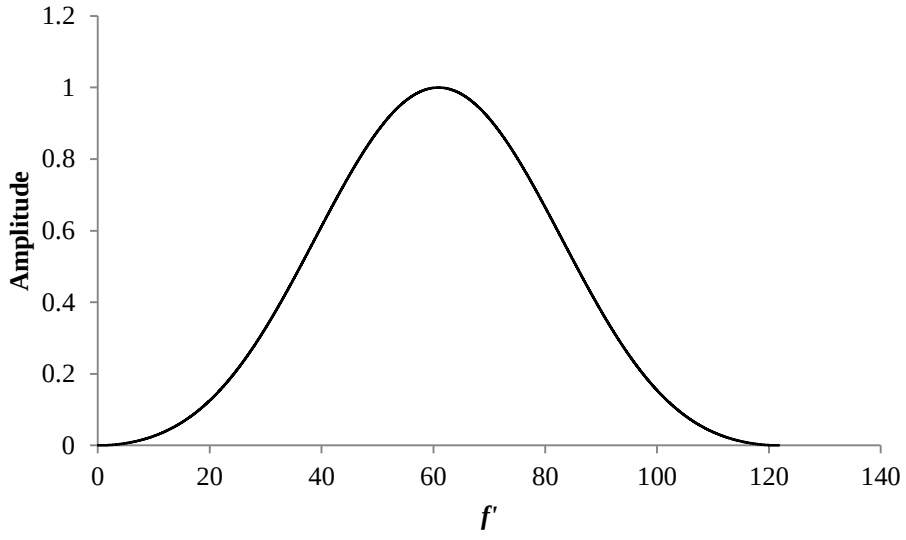

(a) Blackman filter having the cut-off frequency of 517 Hz ($f_c' = 63$)

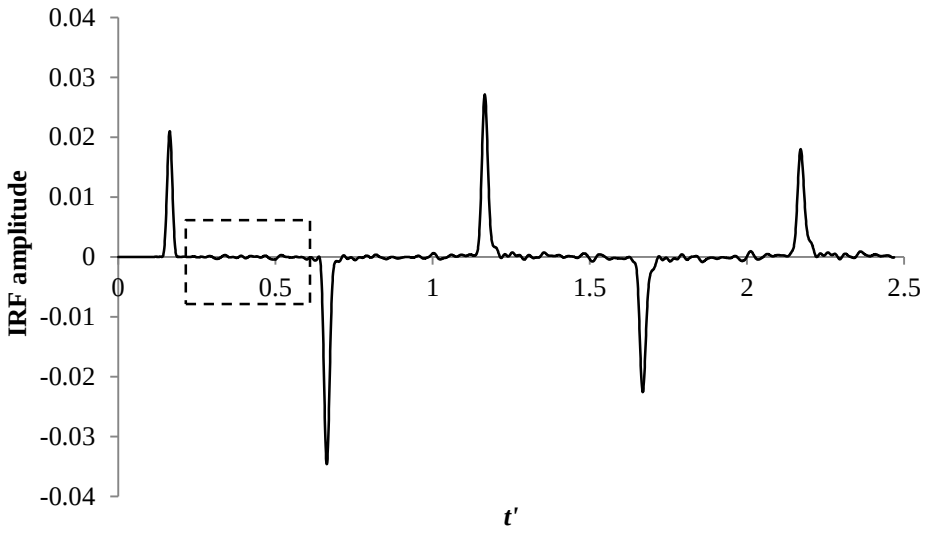

(b) IRF after the application of the filter

Figure 5.8 – Denoised IRF

The effect of the Blackman window on the IRF magnitude is demonstrated in Figure 5.9, where three windows of different cut-off frequencies were used to extract the IRF: 259 Hz (f_c' = 32), 517 Hz (f_c' = 63) and 2068 Hz (f_c' = 252). The figure shows the first IRF pulse from each case. It is evident that the absolute magnitude of the IRF pulses decreases as the cut-off frequency reduces, removing more frequency components. Such a result is expected as the removal of frequency components in the FRF reduces the total energy of the signal in the time domain.

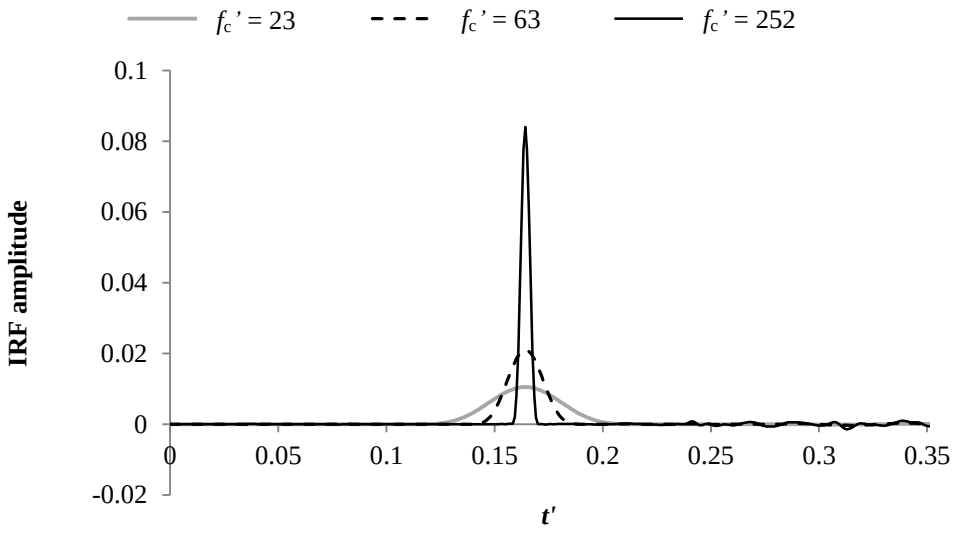

Figure 5.9 – IRFs obtained using three different Blackman windows

5.4 Proposed improvements to the impulse response function

The standard procedure for extracting IRF from real pipeline systems involves a denoising process and the use of a filtering window for denoising—referred to as the Blackman method in this thesis—has been explained previously. Figure 5.10 shows the extraction procedure schematically. The procedure demonstrated in the previous section is boxed in the figure. As demonstrated, a transient signal becomes dilated in real pipeline systems and this signal dilation reduces the clarity of the IRF reflections. The Blackman method causes further dilation of the IRF reflections and the effect of the filter is more severe on signals with low frequency bandwidth as will be illustrated in Section 5.6.

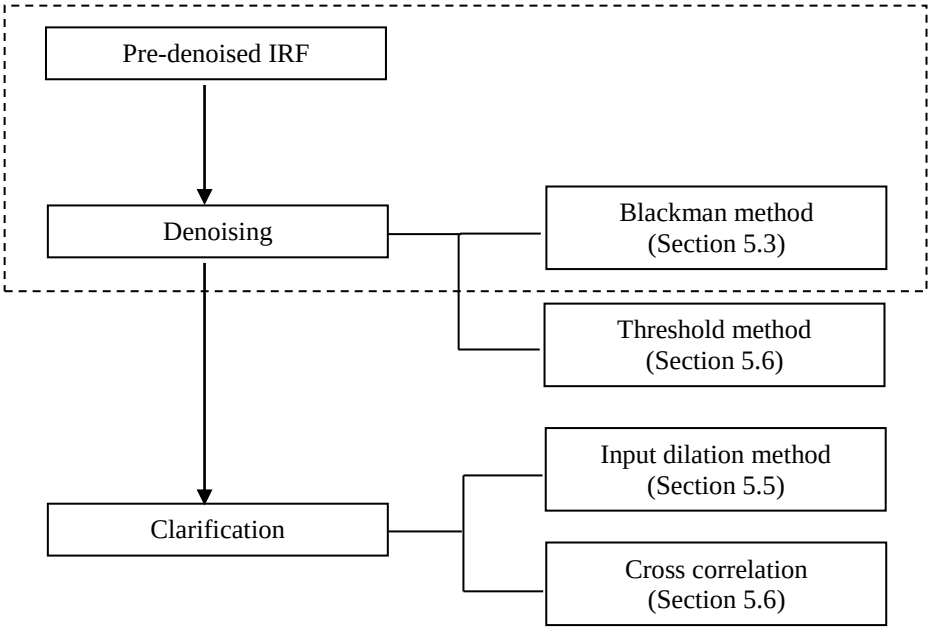

Figure 5.10 – IRF extraction procedure with proposed methods for improvement

Reflecting the observations from the previous section, three approaches for improvement are proposed in this thesis: the input-dilation method, the threshold method and a cross correlation. The threshold method is an alternative denoising method to the Blackman method and the other two techniques attempt to enhance the clarity of the IRF pulses by addressing the issue of signal dilation. The input-dilation method is presented first which is employed along with the Blackman method for denoising. The threshold method is coupled with multiple correlation processes and the combined technique is termed the multi-correlation analysis (MCA) in this thesis and it will be discussed in Section 5.6.

In order to better highlight the improvements brought about by these methods, they will be implemented on data measured in the laboratory pipeline with a single leak and two leaks. In the single-leak system, the leak is located 27.06 m from the upstream boundary and the second leak is added 14.84 m from the upstream boundary for the two-leak system. Transient signals in the following analyses are in the form of a pulse produced by a solenoid-driven valve situated at the downstream boundary of the system.

5.5 Input dilation method

The first method proposed for clarifying IRF pulses explores the possibility of using a dilated input signal for the extraction of the IRF. In Section 5.3, it was observed that the shape difference between the input and the output pulses led to the dilation and the reduction in the magnitude of the IRF pulses. By using a dilated input signal which is more consistent with the output pulses, the extracted IRF is expected to show some improvement over its original form.

The input signal is dilated by applying the Blackman window to its frequency spectrum as it ensures the smooth dilation of the signal. For the reason discussed later in Section 5.6.2, the input dilation method is used in conjunction with the Blackman method. For clarity, the Blackman window used in the IRF extraction procedure is termed noise filter and the one to dilate the input signal is named dilation filter in this work. Since each reflected pulse in the measured response is dilated to a different degree, the input signal must also be dilated to different scales and the IRF is calculated with each dilated input. Examples of the dilated input signals are shown in Figure 5.11 (a) (labelled as "Dilated input 1" and "Dilated input 2"). The cut-off frequencies of the dilation filter, f_{cd}, for these signals are 1034 Hz and 517 Hz (f_{cd}' = 126 and 63) respectively. The original input signal is included in the figure for comparison. The frequency spectrum of Dilated input 2 is given in Figure 5.11 (b) which has a smaller magnitude and a narrower bandwidth than the spectrum of the original input. Dilated input 2 has frequency components with zero spectral amplitude beyond the cut-off frequency of the dilation filter. These characteristics make the corresponding time-domain signal smaller and more dilated than the original signal. While the degree of signal dilation in

the time domain seems minor, the imposed change to the frequency spectrum is significant that it will alter the resultant IRF.

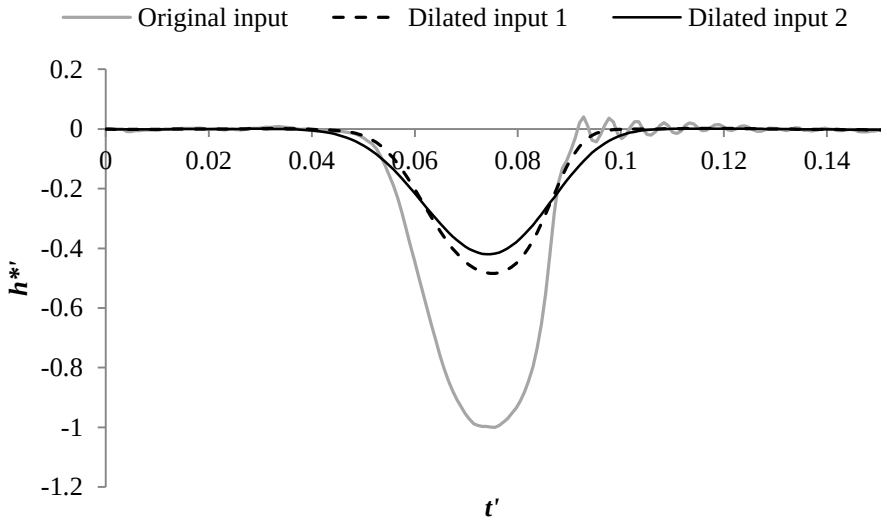

(a) Original input and dilated inputs, normalised by the maximum magnitude of the original input signal

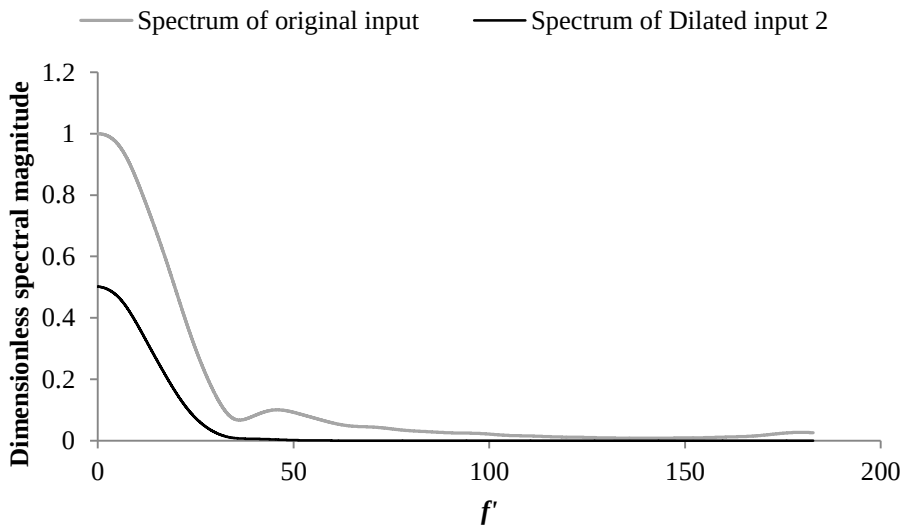

(b) Frequency spectra of the original signal and Dilated input2. The spectral magnitude is normalised by the maximum spectral magnitude of the original input signal

Figure 5.11 – Time- and frequency-domain representation of the original and dilated input signal

Note that this method requires the cut-off frequency of the dilation filter, f_{cd}, to be larger than that of the noise filter, f_{cn}, and this requirement is illustrated in Figure 5.12 where the spectra of the output and two inputs, Input A and Input B are compared. These inputs are produced by dilating the original input signal by the dilation filters of different cut-off frequencies.

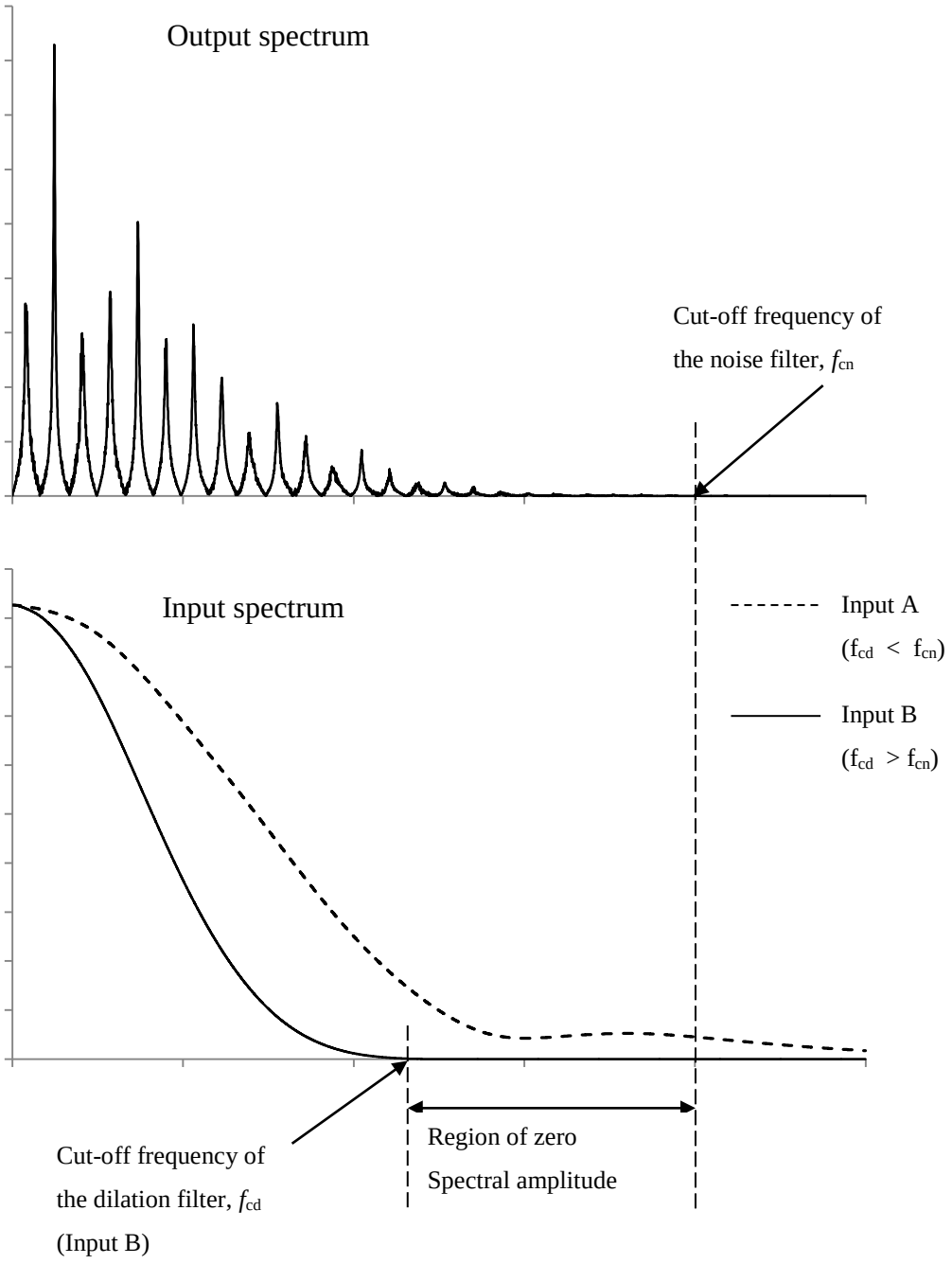

Figure 5.12 – Frequency spectra of the output and two inputs, Input A and Input B, dilated by the Blackman filters of different cut-off frequencies

For Input A, the cut-off frequency of the dilation filter is greater than that of the noise filter and hence the resultant spectrum is nonzero for the frequency range up to the cut-off frequency of the noise filter. In contrast, the spectrum of Input B contains a region with zero spectral amplitude in between the two cut-off frequencies due to the cut-off frequency of the dilation filter being smaller than that of the noise filter. Since the FRF is given as the division of the output spectrum by the input spectrum, the calculation with Input B is invalid and the

IRF cannot be determined. The lower limit for the cut-off frequency of the dilation filter ensures there will be no division by zero in the calculation of the FRF.

Since the noise filter has the cut-off frequency of 517 Hz (f_{cn}' = 63), the test range of the cut-off frequency of the dilation filter, f_{cd} was set from 517 Hz to 1034 Hz (f_{cd}' = 63 to 126) at a step of 50 Hz. IRFs were determined from each dilated input and the results are given in Figure 5.13 (a). Compared to the IRF with the original input signal, the use of the dilated input signal increased the magnitude and the sharpness of the pulse. The IRFs obtained using Dilated input 1 and Dilated input 2 are extracted from the results in Figure 5.13 (a) and re-plotted in Figure 5.13 (b) along with the original IRF. Between the two inputs, Dilated input 2 produced a greater enhancement in both the magnitude and the sharpness. The first IRF pulse has the magnitude which was 4.77 times larger than the original pulse and its width was 40% of the original. For the leak reflection circled in the figure, the factor of increase in the magnitude was 6.57 and the width was reduced by 76%.

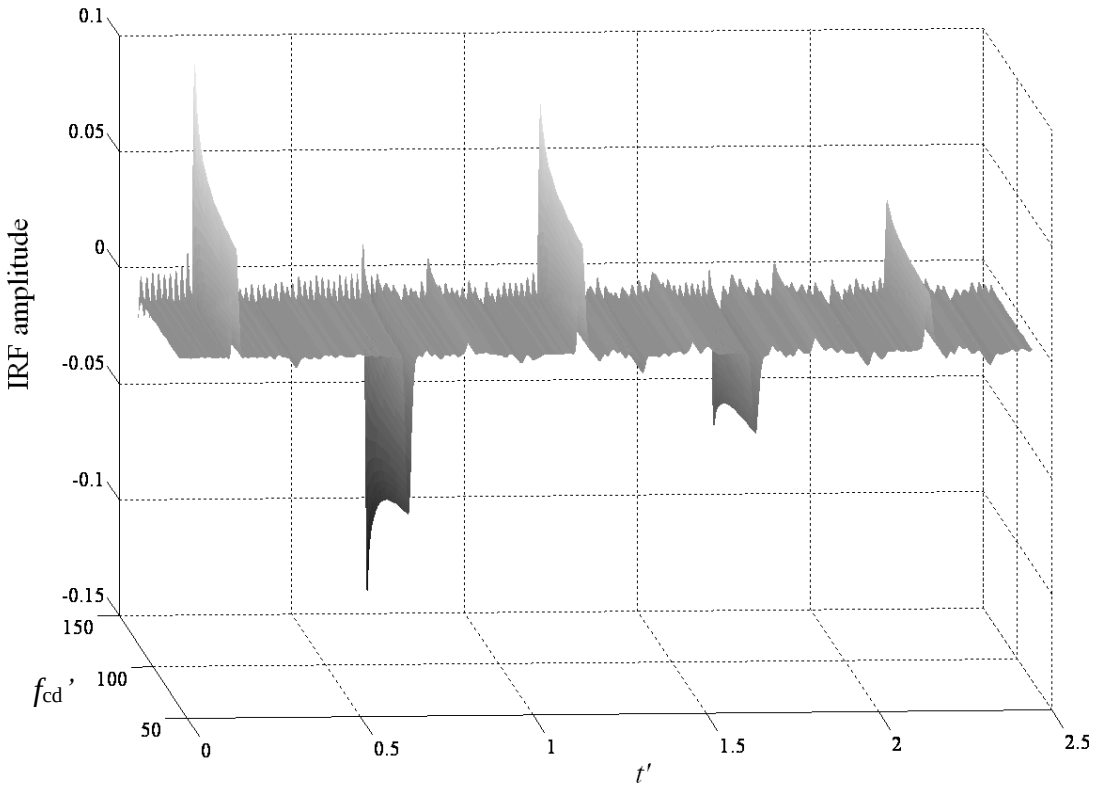

(a) Results from the input-dilation method

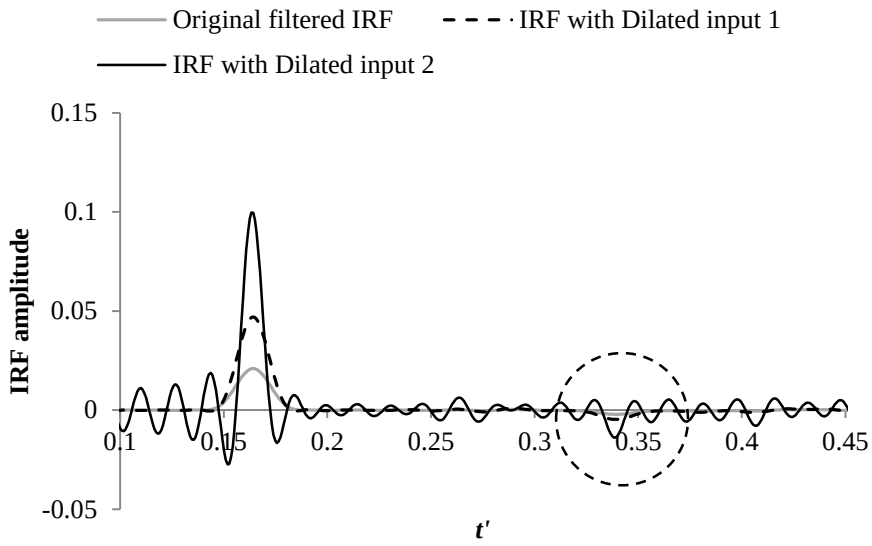

(b) IRFs extracted from Dilated input 1 and Dilated input 2

Figure 5.13 – Results from the input-dilation method

The mechanism behind the magnitude and sharpness enhancement by the input-dilation method is explained with the aid of the FRF. It was observed in Figure 5.11 (b) that the spectral amplitude of the dilated input is lower than that of the original input and thus the FRF obtained from the dilated input will have a larger magnitude as shown in Figure 5.14. Since the magnitudes of the FRF and the corresponding IRF are proportional to each other, the larger FRF will result in the larger IRF.

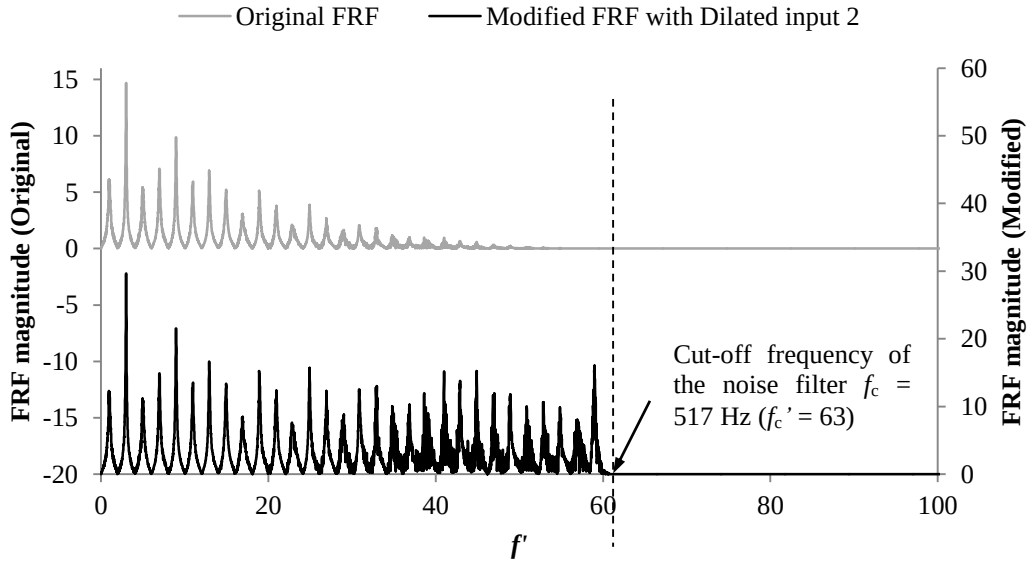

Figure 5.14 – Comparison between the original FRF and the FRF with Dilated input 2. Both FRFs have been filtered by the noise filter of the width f_{cn} = 517 Hz (f_{cd}' = 63)

Notice that the dilated input increased the magnitude of the FRF for the entire bandwidth, but proportionally, the higher frequency components were enlarged to a greater extent than the lower frequency components. This increase in the weight of high frequency components within the FRF translates to the sharpening of the IRF pulses. However, the final cut-off frequency for the FRF is set by the noise filter and hence it is not possible to sharpen the IRF pulse to an impulse.

Figure 5.14 explains why the maximum enhancement in magnitude and sharpness is achieved when the cut-off frequencies of the noise filter and dilation filter are equal. With this frequency, the overall magnitude of the input spectrum is the smallest possible and a division by this spectrum leads to a larger FRF and IRF. This smallest input spectrum also amplifies the high frequency components of the FRF to maximum which produces the maximum sharpness.

The input dilation method enhances the magnitude and sharpness of the IRF pulses by increasing the magnitude of the FRF, but it brings about different problems. As seen in Figure 5.13 (b), the dilated input has increased the noise in the IRF and introduced an additional ‘ringing’ noise around the edge of the IRF pulses. This ringing noise is due to the Gibbs phenomenon which is conventionally avoided by the smooth reduction of the high frequency components created by the noise filter. However, the high frequency components are now amplified by the dilated input, producing an abrupt change at the boundary between the non-zero region and the zero region of the spectrum (Figure 5.14). Hence the extracted IRF contains ringing noise from the Gibbs phenomenon. The increased noise magnitude will make it more difficult to isolate small signals such as reflections off pipe defects in the IRF.

The input-dilation method deals with signals in the frequency domain. Changes made to a frequency spectrum often manifest themselves as ringing noise in the time domain unless they are applied in a smooth manner. The above analysis has also shown the limit of the Blackman method. In the subsequent section, the multi-correlation analysis (MCA) is introduced which employs the threshold method for denoising as an alternative to the Blackman method.

5.6 Multi-correlation analysis

The MCA proposed in this work is a two-step approach consisting of denoising using wavelets and signal enhancement via multiple cross correlations. As seen in Section 5.3, denoising is an essential part of the IRF extraction process. The Blackman method dilates the IRF reflections by removing high frequency content of the corresponding FRF. An ideal denoising method effectively removes high frequency noise while keeping high frequency components of the IRF pulses.

Denoising is one of the major applications of wavelets. A wavelet has its finite energy concentrated around a point and thus, by comparing it with the signal, it can differentiate important signals from noise. The IRF pulse has its energy concentrated in a small number of wavelet dimensions and hence its correlation with an appropriate wavelet will be relatively high compared to noise that has its energy spread over a large number of coefficients.

Further enhancement is achieved by addressing the issue of signal dilation. The input-dilation method made the input signal resemble the output pulses through dilation in the frequency domain, which led to the amplification of the noise in the IRF. In the time domain, a procedure that deals with similarity between two signals is a cross correlation. It is commonly used in applications such as detection of targets in radar or sonar signals (Phillips and Parr 1995, Smith 1999) and delay estimation (Ambardar 1999). It was also used to detect leaks and other pipeline features (Beck *et al*. 2005). Incorporation of correlation is known as a matched filter in the field of signal processing. The correlation emphasises signals that are contaminated by noise and maximises the signal-to-noise ratio which in turn improves the processed results (Lynn 1982, Ambardar 1999).

5.6.1 Threshold method for denoising

The wavelet-based denoising technique proposed by Donoho and Johnstone (1994) is employed in this work which will be referred to as the threshold method hereafter. In this technique, a noisy signal is first decomposed into scaled and shifted wavelets via wavelet transform. The results are known as the wavelet coefficients and for denoising, the wavelet coefficients which are lower than a certain threshold are eliminated and a good

approximation of the noise-free signal is obtained via an inverse transform of the thresholded wavelet coefficients. Despite its simplicity, this method has shown a superior performance on a broad range of noise-corrupted signals (Coifman and Dohono 1995, Liu *et al*. 2009, Chen *et al*. 2010).

The threshold and the way of thresholding can be selected to provide the best result in each application. A universal threshold was proposed by Donoho and Johnstone (1994) and many other thresholds are available in the literature (Fodor and Kamath 2003, Guo *et al*. 2008, Chen *et al*. 2010). In Chen *et al*. (2010), the threshold was set based on the maximum magnitude of the wavelet coefficient in noise intervals at each scale. This approach is taken in this work as it was shown to give an IRF with less noise and over-smoothing than the Blackman method as presented in the next section.

In terms of the thresholding method, there are two options, namely, hard thresholding and soft thresholding. The former is simpler of the two and it sets the wavelet coefficients whose values are lower than the threshold to zero. Soft thresholding carries out the same operation as hard thresholding but it shrinks the nonzero coefficients towards zero, giving a gradual change between the zero and nonzero coefficients. As an illustration, an IRF from a fault-free pipe was denoised by these methods and the outcome is compared in Figure 5.15. Some noise blips are visible in the output from hard thresholding (boxed in Figure 5.12 a). The boxed section of the IRFs is magnified and presented in Figure 5.15 (b). It is observed in the figure that the results from both the hard- and soft thresholding have the noise blips at the same locations in time, however, their magnitudes are much smaller with soft thresholding. Hard thresholding keeps or removes noise coefficients and those that pass the thresholding process appear as noise blips in the output with their magnitudes almost unchanged from the pre-denoised state. In contrast, soft thresholding shrinks the noise coefficients, thereby reducing the magnitude of the noise in the output (Joy *et al*. 2013). As soft thresholding was found to produce cleaner results, it is employed in this work.

The threshold-based denoising method was originally implemented with a discrete wavelet transform (DWT). In the CWT, the wavelet is stretched continuously by all possible integer factors. By contrast, the DWT shrinks the signal by powers of 2 and the wavelet remains unchanged during the entire operation. The shrinkage is done by discarding every other value

of the transformed signal before going through another round of decomposition. This process is known as downsampling and it potentially leads to aliasing problems which hinder the perfect reconstruction of the signal (Bradley 2003, Fugal 2009). The downsampling also makes the DWT shift variant, meaning that the DWT of a translated version of a signal is not the translated version of the DWT of the signal. The shift-variant nature of the DWT results in artifacts appearing in the reconstructed signal (Pan *et al*. 1999, Dragotti and Vetterli 2000, Bradley 2003, Liu *et al.* 2009). The DWT is therefore not particularly suitable for denoising.

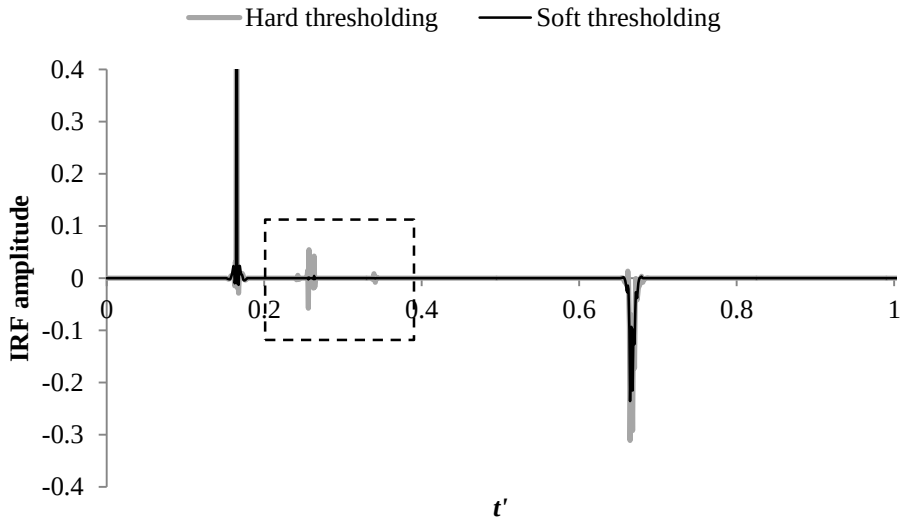

(a) Denoised by hard thresholding and soft thresholding

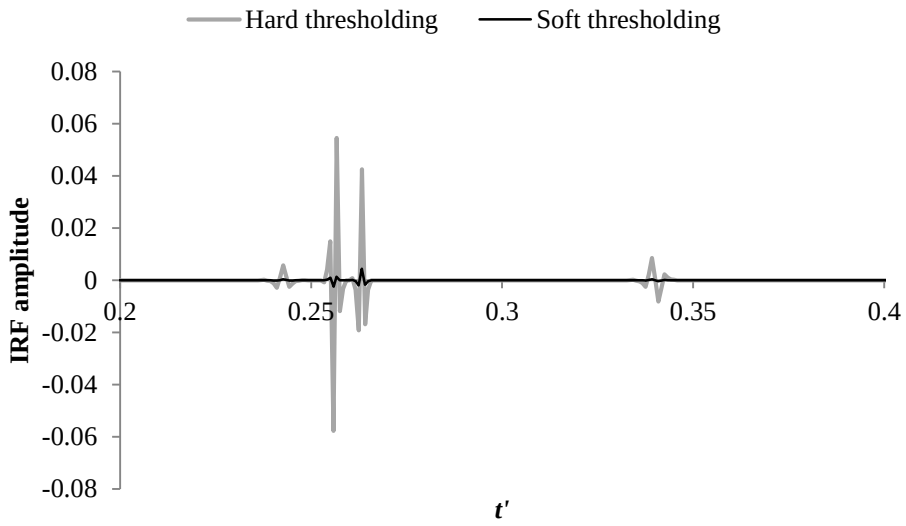

(b) Enlarged view of (a)

Figure 5.15 – Comparison between the hard thresholding and the soft thresholding

Numerous researchers including Chen *et al*. (2010) used a stationary or undecimated wavelet transform (UDWT) as a substitute for the DWT. The UDWT is a shift-invariant version of the DWT and its computation omits the downsampling of the signal and dilates the wavelet dyadically instead (Gyaourova *et al*. 2002, Bradley 2003, Guo *et al*. 2008, Fugal 2009, Liu *et al*. 2009).

The approach for the selection of threshold proposed in Chen *et al*. (2010) would work well with the IRF of the intact system in Figure 5.7 (c) as the reflections are already visible in the unfiltered state and thus the noise interval can be determined accordingly. However, as stated in their paper, their approach is not appropriate when the noise is so heavy that the reflections are completely immersed in it. The IRF from a leaky system is an example of such a case. In this work, the filtered IRF by the Blackman filter is used to obtain an approximate idea of pulse locations in order to identify the noise interval to be used in the subsequent denoising process. This process will be illustrated in Section 5.6.5.

5.6.2 Comparison between threshold method and Blackman method

Both the threshold method and the Blackman method remove the high frequency components from the original FRF. The IRF extracted from the intact (fault-free) laboratory pipeline were denoised by the two methods for comparison and are shown in Figure 5.16. Note the difference in the scale of the y-axis of Figures 5.16 (a) and (b). The Coiflets 1 wavelet (coif1) was used to decompose the IRF to the wavelet coefficients. The level of decomposition was 1 meaning only the original unstretched wavelet—known as the mother wavelet—was used for decomposition. The cut-off frequency of the Blackman filter was chosen so that the similar level of cleanliness to the thresholded result was achieved. The figure clearly indicates the difference in the performance of the two denoising methods in terms of the sharpness and the magnitude of the IRF reflections.

As has been discussed, the Blackman method dilates IRF reflections whereas the threshold method keeps the first reflection as an impulse. The magnitude of the thresholded IRF is slightly lower than the original IRF. The Blackman method reduced the IRF amplitude by two orders of magnitude. Reasons for these differences can be extrapolated from their corresponding FRFs which are given in Figure 5.17.

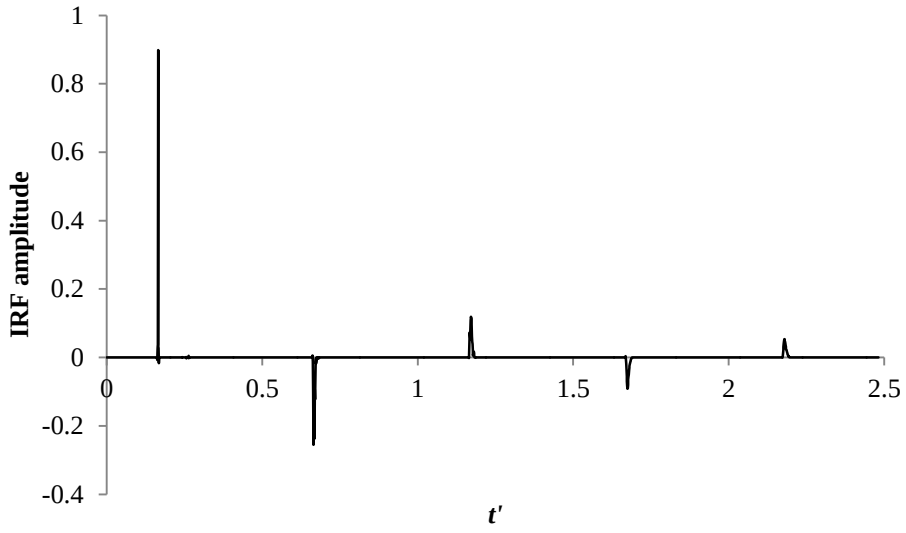

(a) Threshold method

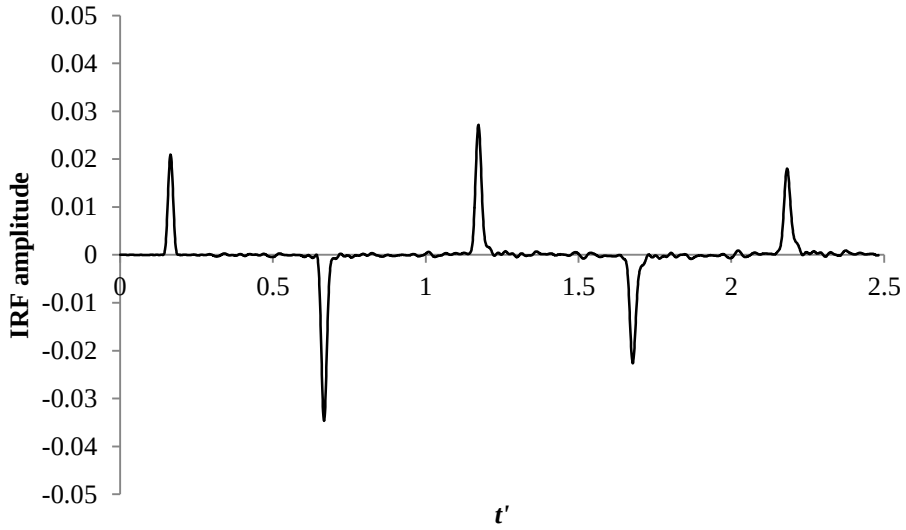

(b) Blackman method

Figure 5.16 – Comparison of two denoising methods in terms of IRF

The Blackman method multiplies a bell-shaped filter (see Figure 5.8 a) to the spectrum and the frequency components outside the filter are removed. Due to the shape of the window, the rate of reduction of the higher frequency components is greater than that of the lower frequency components. As the amount of the higher frequency components within the signal affects its sharpness, it is expected that the filtered IRF loses the sharpness of the signal as observed in Figure 5.16 (b).

The Blackman-filtered IRF (Figure 5.16 b) reveals that some low-frequency noise is left in the IRF. Initially the noise in the IRF has a frequency spectrum with full frequency coverage. The application of the filter removes the high-frequency noise, but part of the low-frequency noise remains in the signal due to the uneven removal of the frequency components mentioned above.

The threshold method, on the other hand, removes a certain magnitude from all frequency components. Since more high-frequency components are left in the signal, the sharpness of the pulse is maintained. In addition, by not limiting the bandwidth of the FRF, the thresholded IRF reflections essentially retains the shape of the pre-denoised reflections. The denoising by thresholding is more complete than the Blackman method as it removes both low and high frequency noise. Comparison between the two denoising methods continues in the following section with a signal with a low frequency bandwidth. This aims to verify the use of the threshold method on a smooth signal which is frequently encountered in the field or laboratories.

Note that, because the threshold method does not alter the bandwidth, it cannot be used along with the input dilation method. By dilating the input signal using the Blackman filter, part of the FRF becomes invalid due to division by zero. This part of the FRF needs to be removed prior to the inverse Fourier transform; however, it cannot be done by the threshold method.

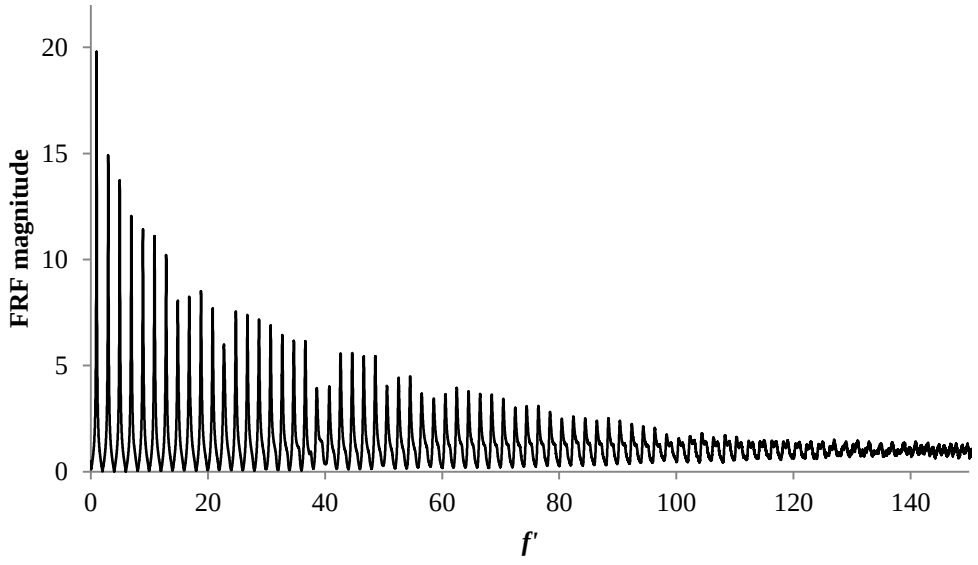

(a) Without denoising

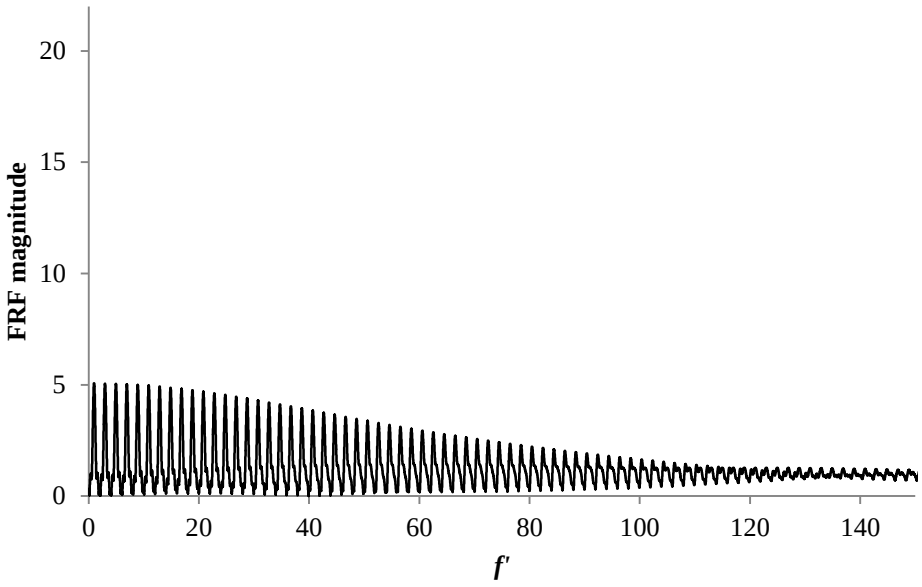

(b) Threshold method

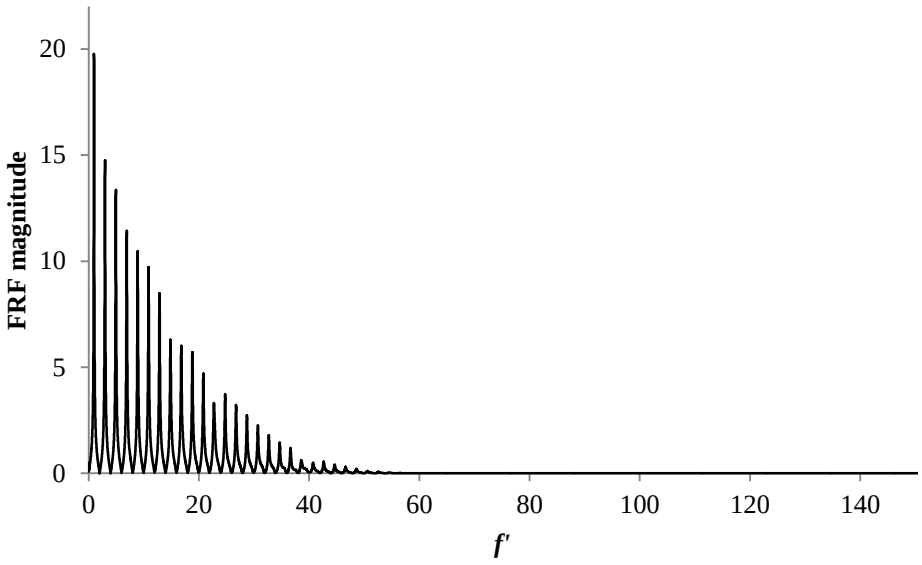

(c) Blackman method

Figure 5.17 – Comparison of two denoising methods in terms of FRF

5.6.3 Effect of frequency content of signal

The experimental analysis so far used a pulse signal with a width of 5 ms. A transient in field studies is often generated by a closure of a side discharge valve (Stephens *et al*. 2005) and a signal duration (valve manoeuvre time) can be longer than 5 ms. The signal duration is inversely related to the amount of frequency content of the signal. Effects of the low

frequency content of the signal were investigated using three signals with different closure times: 20 ms for Signal 1, 35 ms for Signal 2 and 50 ms for Signal 3 as shown in Figure 5.18 (a). These signals are presented with a time lag to clearly show the manoeuvre time of each signal.

The denoised IRFs are presented in Figure 5.18 (b). Comparing the denoised IRFs with Signal 1 and Signal 3, it is clear that the Signal 3 shows fewer pulses than Signal 1 and the relative magnitude of these pulses are smaller than that of IRF1. This is simply because Signal 3 has less capacity to carry information about the system due to its low frequency bandwidth and so the pulses in the later periods could not be extracted properly. This phenomenon is associated with the extraction procedure of the IRF and not with the denoising. The threshold method gave similar results with all the signals, implying that the method is independent of signal bandwidth. For comparison, the IRF from Signal 3 was denoised by the Blackman method and the denoised IRF is shown in Figure 5.18 (c). The cut-off frequency of the Blackman filter was 51.7 Hz which removes the high frequency noise to a similar level as the thresholded IRFs in Figure 5.18 (b). The IRF pulses are dilated significantly and the whole trace appears almost like a continuous wave. With a signal of low frequency content, the cut-off frequency of the Blackman window becomes small which then leads to the significant distortion of the IRF. This comparison has demonstrated that the threshold method is a superior denoising tool to the Blackman method for signals of various frequency contents.

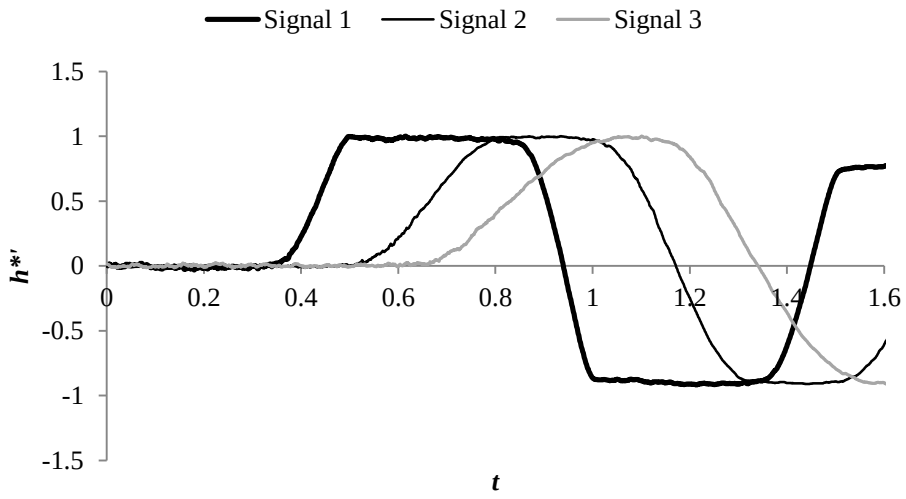

(a) Closure profile of the three signals, normalised by the maximum magnitude of each signal

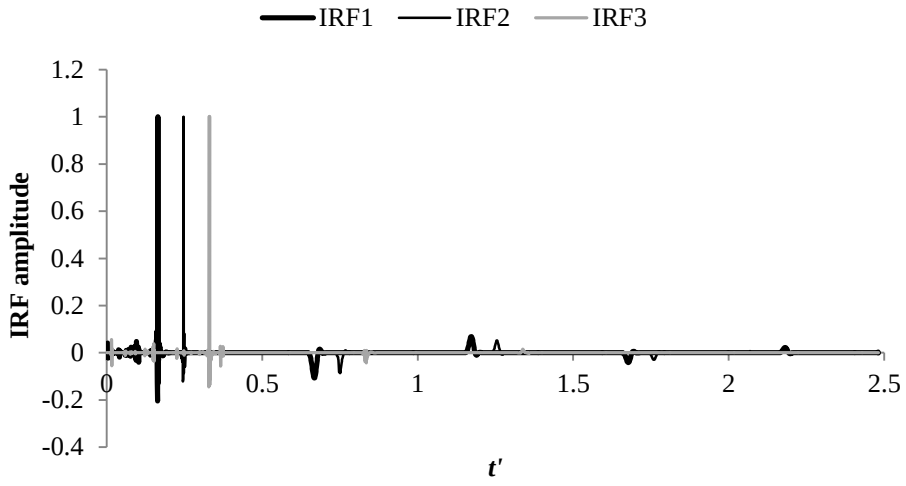

(b) Denoised IRF

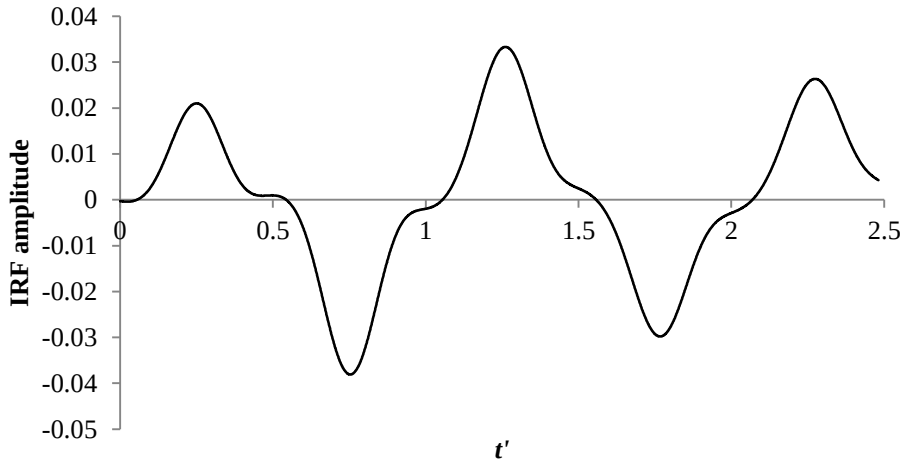

(c) Denoised IRF using the Blackman window

Figure 5.18 – Effect of the low frequency content of the signal on the denoising methods

The threshold method removes noise from an IRF while keeping the distortion to the IRF minimal. A shortcoming of that is the secondary IRF pulses remain small and they need to be highlighted for the ease of a subsequent fault detection process. The next section presents the use of cross correlation on the denoised IRF for additional improvement.

5.6.4 Cross correlation with sinc signal

Cross correlation has a similar mathematical expression to the convolution integral (Lynn 1982, Phillips and Parr 1995, Ambardar 1999):

$$r_{yc} = \sum_{-\infty}^{\infty} y(t)c(t-b) \tag{5.5}$$

where r_{yc} is the coefficient of cross-correlation between the target signal, c and the measured output, y and b is the shift parameter. In this work, the measured output is an extracted IRF. The value of r_{yc} is a measure of how much the IRF pulses resemble the target signal at the location, b. Similar to the input-dilation method, the target signal will be dilated to different degrees to cater for the IRF pulses of different scales. Equation 5.5 is then modified as follows:

$$r_{yc} = \sum_{-\infty}^{\infty} y(t)c\left(\frac{t-b}{s}\right) \tag{5.6}$$

where s is the scale of the target signal and it only has an integer value. An ideal target signal shares the same features as the IRF pulses. As discussed in the earlier section, if the injected signal has a limited frequency content, or once the IRF pulses lose their high frequency components, the IRF pulses will be a pulse of finite width. Therefore, the target signal needs to be in a form of a pulse. From these reasons, a sinc function was selected as the target signal. The sinc function is frequently encountered in the field of signal processing. Every time-domain signal has a corresponding frequency-domain waveform and these are called a Fourier-transform pair and the sinc function is a Fourier-transform pair of a rectangular pulse (Phillips and Parr 1995, Ambardar 1999, Smith 1999). The mathematical expression of the sinc function is given by:

$$\text{sinc}\,(t) = \frac{\sin(\omega t)}{\omega t} \tag{5.7}$$

The sinc signal is a sine wave with an oscillation frequency, ω, that decays in amplitude as $1/t$ as shown in Figure 5.19 (a) where the sinc functions of three different oscillation frequencies are presented. All sinc signals are calculated for the time ranging from - 0.4 s to + 0.4 s in the increment Δt of 0.01 s. As the oscillation frequency decreases, the width of the central main lobe of the sinc function increases. Such a characteristic is useful in imitating the dilated IRF

pulses and the existence of the explicit mathematical equation means that the stretching of the target signal can easily be done.

As only the positive part of the main lobe of the function is required as the target signal, it is truncated when it becomes negative for the first time (counted from the time $t = 0$). The truncation process is depicted in Figure 5.19 (b). The truncated signal is symmetrical and has a well-defined peak which will be important in locating the reflections. The initial oscillation frequency of the sinc signal is set to 350 rad/s so to produce an impulse with the time increment Δt of 0.01 seconds. The sinc signal can be dilated by changing the time increment as $\Delta t/s$ where s is the integer scale goes from 1 to a desired scale.

This multi-correlation process examines the similarity between the IRF and the target signal of different scales. This process is similar to the operation of a continuous wavelet transform (CWT) which is a well-known technique of scale analysis. The difference between the two methods is the target signal. In a CWT, the target signal is a waveform of a finite length called wavelet which oscillates about its base. Wavelets from the Coiflets family (coif1) and the Daubechies family (db8) are shown in Figure 5.20 as an example. Both wavelet types are commonly used in wavelet-based analyses. The Coiflets wavelet (coif1) is near-symmetrical and has a pulse-like shape with small oscillating part at its sides as indicated in the figure while the Daubechies wavelet (db8) exhibits the oscillatory nature of the wavelet more strongly. These wavelets are correlated with the signal multiple times while being stretched at each run. Similar to the cross-correlation, results from the CWT reveal how well the wavelets of various scales resemble a certain section of the signal. The oscillatory side bands of the wavelets lead to ringing issues around the IRF reflections as observed with the Gibb's phenomenon. The use of the CWT is therefore less suitable for the purpose of the present analysis.

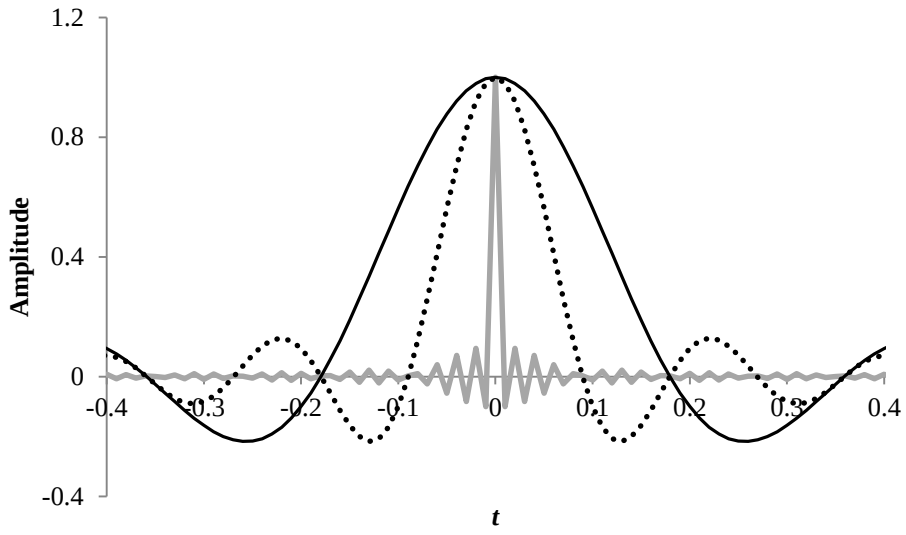

(a) Sinc functions of three different frequencies

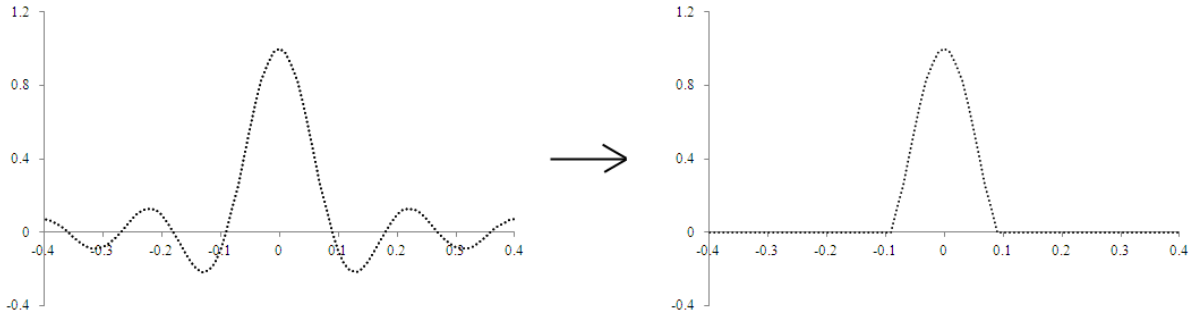

(b) Truncation process of the sinc function

Figure 5.19 – Sinc signals used in the multi-correlation process

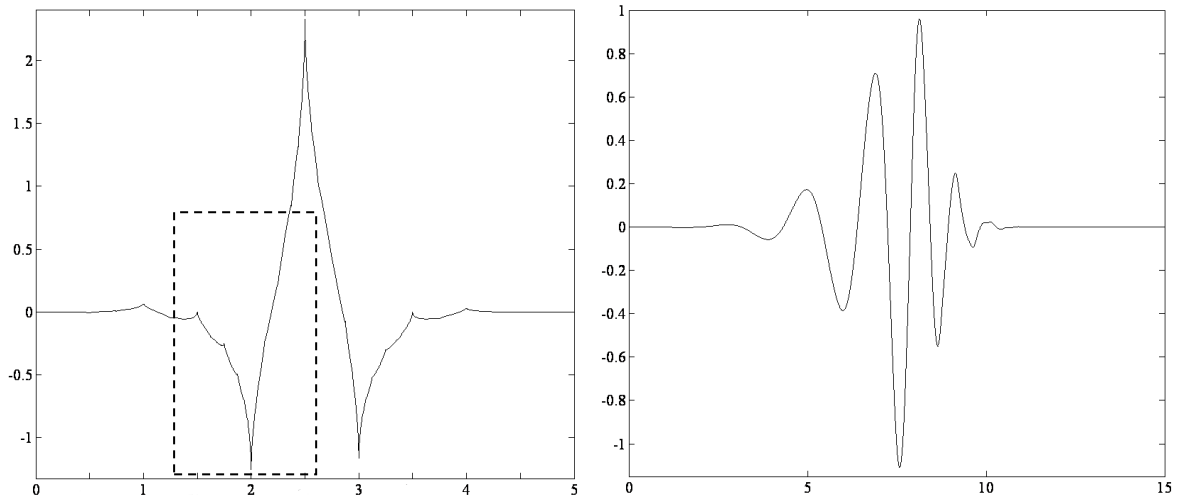

Figure 5.20 – Wavelets of the types; Left: coif1, and Right: db8

5.6.5 Coupling of cross correlation and threshold method

The MCA proposed in this thesis carried out in the following order:

1. Denoise the extracted IRF by the threshold method
2. Calculate the correlation between the denoised IRF and the truncated sinc signal in a form of an impulse
3. Stretch the sinc signal and repeat the correlation with the denoised IRF until the width of the correlated signal matches the time scale of the measured signal

The IRF from the leak system was analysed by the MCA. Prior to the denoising, the filtered IRF was obtained to identify the noise intervals. The cut-off frequency of the filter was 517 Hz. Figure 5.21 presents the original and filtered IRF which manifests the leak reflections in between the boundary reflections. The first leak reflection is identified in the figure. From this filtered result, the sections from t' = 0.21 to 0.31, and from t' = 0.37 to 0.62 were selected as the noise intervals (boxed in the figure). The final threshold was determined as the average of the thresholds obtained from these sections. The Coiflets 1 wavelet (coif1) was used as the mother wavelet and the level of decomposition was 3 which gave the best denoised results. It is important to use the right decomposition level to avoid a loss of useful frequencies or incomplete denoising (Tang *et al*. 2009). The sinc signal for the cross-correlation was stretched to a scale, *s* of 20. The sharpest and the most stretched sinc signals are presented in Figure 5.22 where the sharpest signal is an impulse.

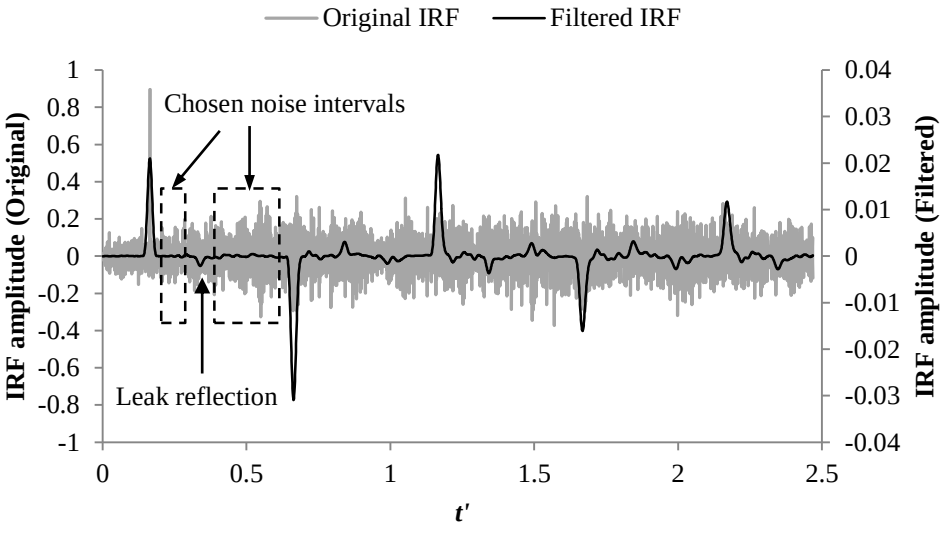

Figure 5.21 – Determination of the noise intervals

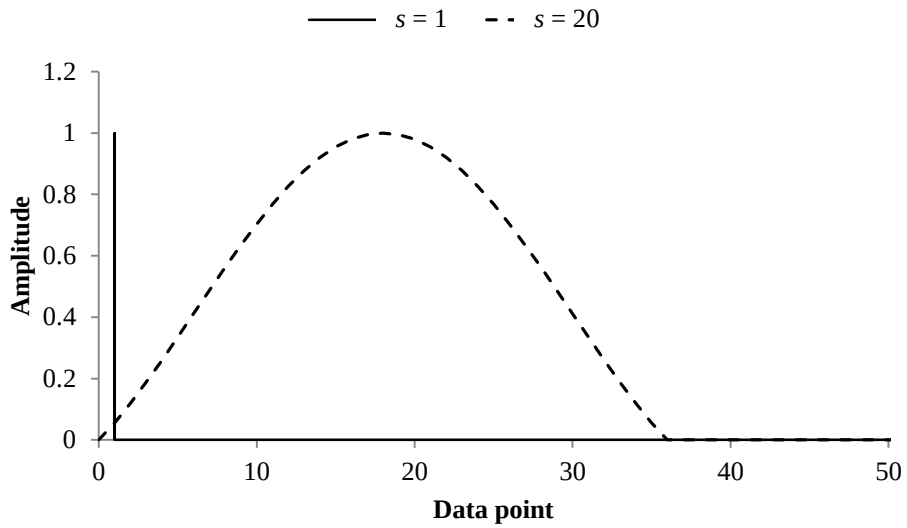

Figure 5.22 – Sinc signal of scales 1 and 20

The result from the MCA is presented in Figure 5.23. Compared to the original IRF, the response in between the reflections contains almost no noise and the secondary reflections were magnified by the correlation process. The leak reflections are also visible as circled in the figure.

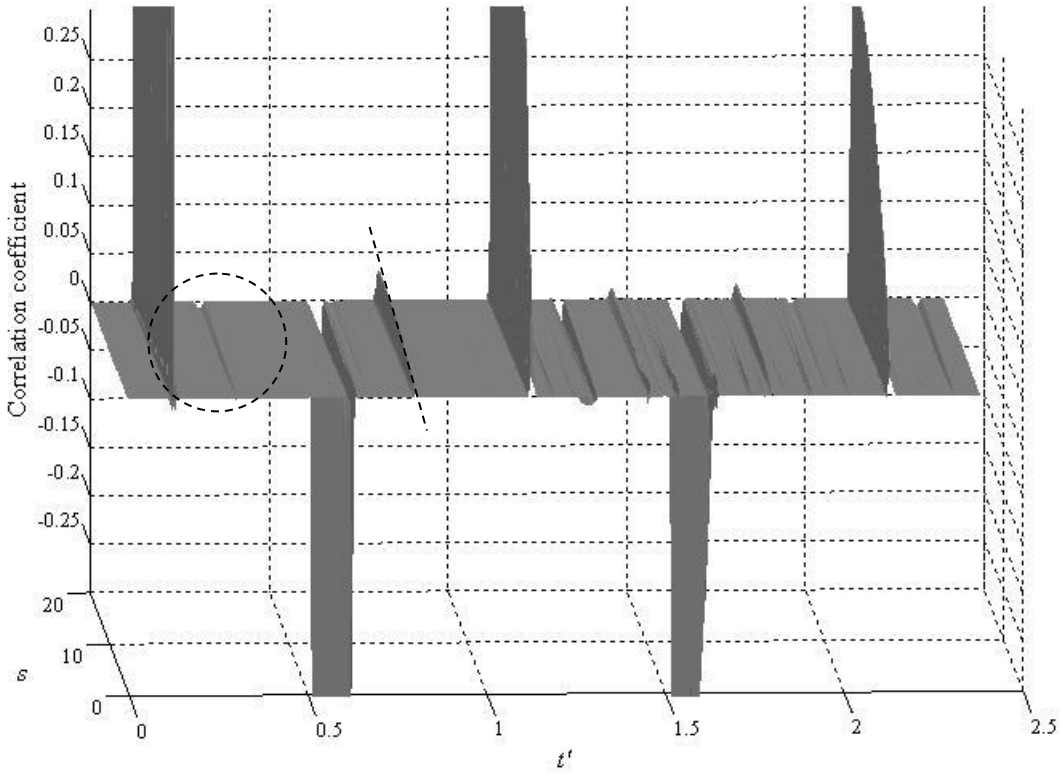

Figure 5.23 – MCA result with a single leak

Unlike the noise components which normally have short timescales, the IRF pulses continuously give high correlation with the dilated sinc signals and this creates ridge or trough lines across the scales. The ridge line created by the second leak reflection is indicated in the figure by the broken line. This line will provide an additional confirmation of the presence of the signature signals, which cannot be provided by conventional IRF.

The magnitudes of the first reflection in the filtered IRF and the MCA results were compared. Given the absolute magnitude of the two traces differs, they were normalised by the magnitude of first pulse in each trace. The scale of the MCA was increased to 28 so that the widths of the first pulse in the two traces are the same. The first leak reflection in the MCA trace had a relative magnitude of 0.66%, whereas the filtered IRF gave the relative magnitude of 10%. On this basis the conventional filtered IRF appears to be better than the MCA results, however, the leaks are more clearly identified through the presence of ridges or troughs in the MCA correlation coefficients. The effective denoising by the threshold method also increases the clarity of the IRF reflections. Furthermore, the MCA results include traces of various scales so that the location can be identified using the reflections in their sharpest state. Thus, the MCA is an attractive alternative to the conventional method.

5.6.6 System with multiple leaks

The MCA was also applied to the IRF extracted from the laboratory pipeline with two leaks. Similar to the IRF of the single-leak case, neither the boundary reflections nor the leak reflections were identifiable from the original IRF in Figure 5.24 (a). After applying the Blackman filter (f_c = 517 Hz), the noise sections were determined by avoiding the leak reflections (identified in the figure). The noise intervals boxed in the figure have the time range of t' = 0.21 to 0.31, and t' = 0.37 to 0.46. The MCA result is given in Figure 5.24 (b) in which the leak reflections in the first period are circled. Other parameters related to the denoising process were the same as the ones used in the single-leak example.

Compared to the MCA results from the single-leak system (Figure 5.23), the leak reflections in the later periods are less visible, although the magnitude of the first leak reflection in the original output was almost identical in both the single- and two-leak systems. This is because

the amount of signal dilation was more significant in the two-leak system so that the leak reflections become more dissimilar to the input signal, reducing their magnitudes in the IRF. The magnitude is further lowered by the denoising process to the level that the MCA cannot pick up. Such an outcome in not specific to the MCA and the same phenomenon was observed with the use of the Blackman window (Figure 5.24 a). Normally the presence of leaks is detected from the information given in the first period of the IRF and thus the clarity of the leak reflections in the later period is not a major concern for the scope of this work.

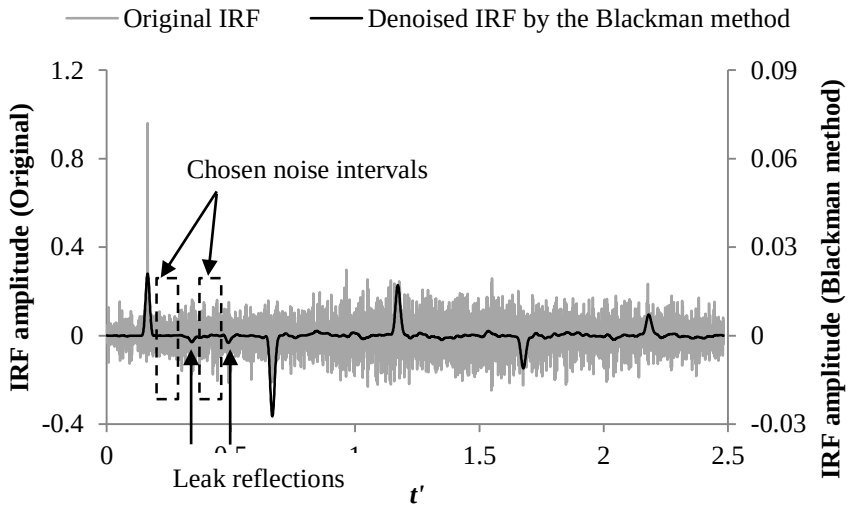

(a) Original and filtered IRF

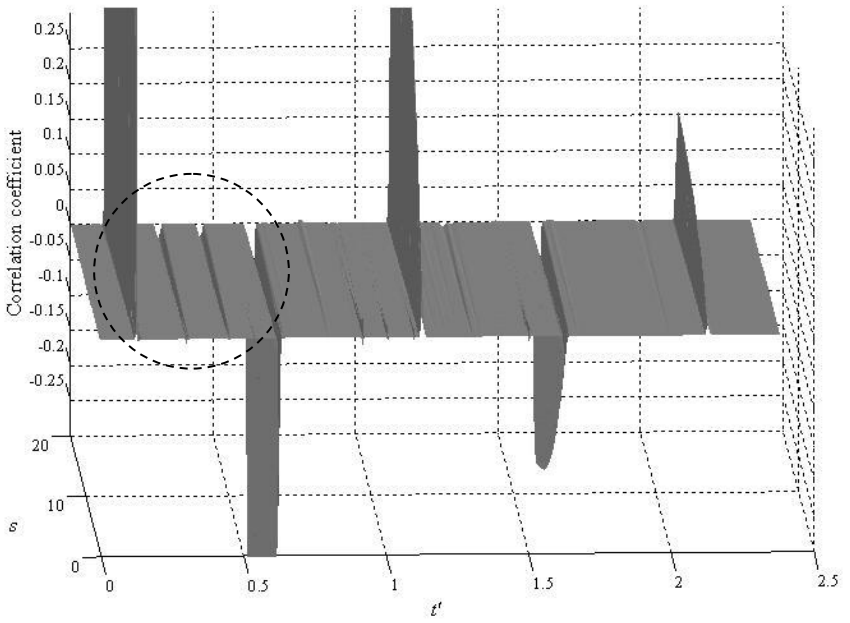

(b) MCA results

Figure 5.24 – Results with the two-leak system

5.7 Comparison of the proposed methods

Two methods are proposed for improving the conventional IRF that is affected by the phenomenon of signal dilation. The input-dilation method tackled the problem in the frequency domain, whereas the MCA dealt with it in the time domain. Outcomes from these methods were different and Table 5.1 summarises the improvements brought about by each methods as well as the advantages and disadvantages of each compared to the conventional IRF.

Methods	Improvements / advantages	Disadvantages
Input-dilation method	• Sharpens the pulses • Enlarges the pulses • Lower memory space requirement compared to the MCA	• The sharpest possible pulse width is limited by the noise filter • Causes and amplifies the ringing noise around the pulses
MCA	• Can have a range of different scales • Gives additional confirmation of the presence of pulses by producing a line of maximum across the scales • Incorporates the threshold denoising method which gives cleaner results than the Blackman method	• High memory space requirement • The magnitude of the leak signal is small

Table 5.1 – Improvements brought about by the three proposed approaches

In terms of the memory requirement, the input-dilation method requires the least in the two methods because the computation is relatively simple (multiplication and division) and the modified IRF has the same length as the original IRF. For the MCA, the "shift-multiply-sum" operation is carried out and so the computational complexity and the memory space requirement increase. In addition, computation of cross correlation increases the signal length to $2N$-1 where N is the length of the IRF. If an extracted IRF contains a large number of data points and a lack of memory space becomes an issue, a small section of the IRF can be treated by the MCA method at a time without the loss of accuracy.

While it is not shown, the performance of these methods was tested and verified with a total of 30 datasets obtained from the laboratory pipeline system with and without leaks and the results were similar to what has been presented in this section.

5.8 Summary

In pipeline systems, a transient signal becomes dilated as it travels through the system. In other words, the scale of the output pulses will be different from that of the input signal. This difference in the scale leads to the dilation of the IRF pulses and the reduction in their magnitude. In addition, the IRF dilation is enhanced by the use of a low-pass filter for denoising which makes it harder to locate the reflections. In this chapter, two methods were proposed to improve the conventional IRF. Both methods tackled the issue of time scale difference and aimed to enhance the clarity of the IRF pulses. Experimental data from the laboratory was used to test these methods. Note that as the characteristics of any linear time-invariant system can be described by its IRF, the range of applicability of the proposed methods is not limited to pipeline systems.

The input-dilation method uses input signals which are dilated to a different degree in the extraction of the IRF. This dilation is aimed to improve the similarity between the input and the output pulses. The results show that the use of the dilated input signals improve the sharpness and the magnitude of the IRF, but it also amplified the noise in the IRF and caused the Gibbs phenomenon to occur around the edges.

The MCA was proposed as the second method and it has two components: denoising and enhancement. For denoising, a technique based on wavelets was used which produced cleaner results than the use of a low-pass filter. Furthermore, this technique does not limit the signal bandwidth and hence can keep the original shape of the IRF reflections. The denoised IRF was then correlated with a target signal—called the sinc signal—which was a truncated central lobe of the continuous sinc function. The correlation process was repeated with sinc signals with different scales. The performance of the MCA was tested in the systems with single and multiple leaks. The resultant IRF successfully revealed the leak reflections which were originally buried amongst noise. While their relative magnitudes were smaller than that

of the conventional IRF, the detection of these pulses was supported by the presence of ridge and trough lines produced by the successive correlation process.

The proposed methods were able to give some degree of improvement to the conventional IRF. However, the MCA is a more attractive alternative to the conventional procedure as the coupled denoising technique gives superior results to the use of a low-pass filter. The MCA ensures the sharpest signal width, which is beneficial when locating the IRF pulses.

Chapter 6 Unsteady Flow Measurement using Kinetic Pressure Difference Method

Flows in pipeline systems are classified into two types; steady flow and unsteady flow. While steady flow measurements using commercial flow meters are very accurate and have measurement errors of typically 0.2% to 5% (Pereira 2009), the review of existing flow meters in Chapter 2 revealed the absence of a flow metering technique which fully captures rapidly changing flows. A promising technique known as the Kinetic Pressure Difference method uses measured transient pressure for flow measurement which enables the determination of flow rates at a sampling rate of over 200,000 Hz. Due to the nature of the underlying equations, this method is designed to measure perturbing flow rates about a steady mean flow. The mathematical background of the method is given first, followed by its numerical and experimental verifications. Additional consideration is given to the application of the method for instantaneous flow measurements at the end of the chapter.

6.1 Equations for prediction of flow response

The KDP method utilises the transfer matrix model presented in Chapter 3. The transfer matrix equations for the pipe segments '*a*' and '*b*' in Figure 6.1 are:

$$\begin{pmatrix} q_2 \\ h_2 \end{pmatrix} = \begin{bmatrix} F_{a11} & F_{a12} \\ F_{a21} & F_{a22} \end{bmatrix} \begin{pmatrix} q_1 \\ h_1 \end{pmatrix} \tag{6.1}$$

$$\begin{pmatrix} q_3 \\ h_3 \end{pmatrix} = \begin{bmatrix} F_{b11} & F_{b12} \\ F_{b21} & F_{b22} \end{bmatrix} \begin{pmatrix} q_2 \\ h_2 \end{pmatrix} \tag{6.2}$$

where h, q = complex-valued fluctuating head and flow responses at a particular frequency and the subscript denotes the location of these responses in Figure 6.1. The entries of the matrix are given as $F_{s11} = F_{s22} = \cosh(\mu l_s)$, $F_{s12} = -\sinh(\mu l_s)/Z_c$ and $F_{s21} = -Z_c \sinh(\mu l_s)$, where l is the length of the pipe section, $\mu = \sqrt{\left(-\omega^2/a^2 + jgA\omega R/a^2\right)}$, $j = \sqrt{-1}$, $Z_c = \mu a^2/j\omega gA$ as given in Chaudhry (1987) and the subscript s is an indicator function which takes on values

of *a* or *b*. The overall resistance term *R* appears in the propagation operator, μ, can take into account both steady and unsteady friction effects.

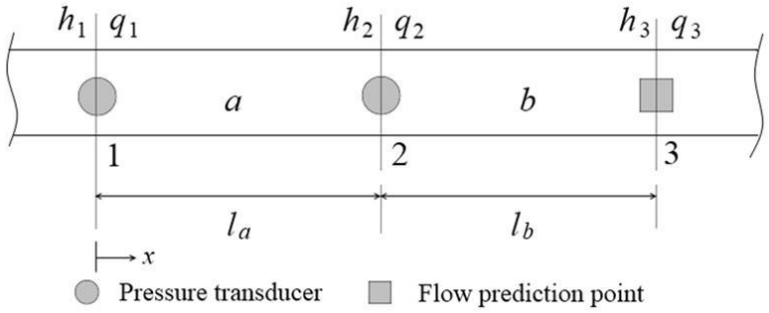

Figure 6.1 – Pipe section with two subsections 'a' and 'b'

When determining a flow response at point 2, the equation is derived from the transfer matrix in Equation 6.1:

$$q_2 = F_{a12}h_1 + F_{a11}\left(\frac{h_2 - F_{a22}h_1}{F_{a21}}\right) \tag{6.3}$$

A flow response at point 3 can be obtained by combing Equations 6.1 and 6.2 and produces an explicit expression as a function of two measured pressure fluctuations in the pipeline (points 1 and 2):

$$q_3 = F_{b12}h_2 + F_{b11}\left(F_{a12}h_1 + F_{a11}\left(\frac{h_2 - F_{a22}h_1}{F_{a21}}\right)\right) \tag{6.4}$$

The use of two transfer matrices in the KDP method provides flexibility in the flow prediction point as it allows the point to be located away from the points of pressure measurement. Equation 6.4 shows that the time-varying flow component at a point can be calculated from two pressure measurements, h_1 and h_2, spaced l_a apart in the pipeline. Note that, while the term KDP method was used only for the formulation given in Equation 6.4 in Washio *et al*. (1996), the use of Equation 6.3 for flow prediction is also referred to as the KDP method in this thesis as the underlying equation for these equations is the same.

Given that the KDP method requires the pressure measurement at two points, its operation may appear similar to existing orifice or Venturi meters. The working principle of the orifice meter is based on Bernoulli's equation and this is only applicable to steady or slowly changing flows (Zhao *et al*. 1987, Streeter *et al.* 1998, Nakamura *et al*. 2005, Brereton *et al*. 2008). The KDP equations instead are based on the 1D unsteady momentum and mass equations to model the transient behaviour and therefore can deal with rapidly-changing flows.

There are a number of requirements for implementation of the KDP method. Firstly users must know the system parameters such as the system wave speed, distances between pressure transducers and the pipe diameter. It is also important to know whether the sections include any hydraulic devices in which case their transfer matrices must be incorporated in Equation 6.3 and/or 6.4. In addition, since the KDP method is based on the transfer matrix equations, its accuracy hinges on the significance of the missing nonlinear term in the unsteady momentum equation. The influence of the neglected nonlinear term is studied in the next section.

6.2 Validity of linear assumption

With the manipulation of the unsteady momentum and continuity equations, the subsequent equation for the time-varying flow component can be derived:

$$\frac{1}{gA}\frac{\partial^2 q^*}{\partial t^2} - \frac{a^2}{gA}\frac{\partial^2 q^*}{\partial x^2} + \frac{fQ_0}{gDA^2}\frac{\partial q^*}{\partial t} + \frac{f}{2gDA^2}\frac{\partial q^{*2}}{\partial t} = 0 \qquad (6.5)$$

Introducing the following non-dimensional parameters:

$$q^{*\prime} = \frac{q^*}{q_s},\ t' = f_s t,\ x' = \frac{f_s}{a}x$$

in which q_s = the size of the introduced flow perturbation and f_s = the frequency of the measured perturbation. Nondimensionalising Equation 6.4 using these parameters gives:

$$\frac{\partial^2 q^{*'}}{\partial t'^2} - \frac{\partial^2 q^{*'}}{\partial x'^2} + \frac{4 f Q_0}{D^3 \pi f_s} \frac{\partial q^{*'}}{\partial t'} + \frac{2 f q_s}{D^3 \pi f_s} \frac{\partial q^{*'^2}}{\partial t'} = 0 \tag{6.6}$$

As described in Chapter 3, the transfer matrix equations are derived by neglecting the last nonlinear term in Equation 6.6. From this nonlinear term, the following three dimensionless parameters are defined:

$$\Pi_1 = \frac{f Q_0}{D^3 f_s}, \quad \Pi_2 = \frac{q_s}{Q_0}, \quad \Pi_3 = \frac{f_s}{F}$$

where F = the fundamental frequency of the system. The dimensionless parameter, Π_1 depends on the characteristics of the system under consideration while the dimensionless constants, Π_2 and Π_3 depend on the relative size and frequency of the perturbation signal. The parameters Π_1 and Π_3 are combined to give an idea of the system resistance. Neglect of the nonlinear term—which is a product of the three dimensionless parameters—places bounds for the size of the flow perturbation. As the size of the flow perturbation increases, the system is driven further away from the linear bounds and significant errors should result. A limit on the measured signal size relative to the base condition must therefore exist for the accurate operation of the KDP method and it is numerically investigated by varying the derived dimensionless parameters.

The setup of the numerical pipeline system is shown in Figure 6.2. The transient source (labelled as *G* in the figure) and the flow prediction point are at the middle of the system and the transducers are positioned at the end and middle of the upstream half of the system. The type of signal introduced to the system is a continuous sinusoid in order to induce a resonance phenomenon which puts the system under extreme conditions. Also since any complex signal in time perturbed about a stationary mean can be represented as a summation of continuous sinusoids, the system behaviour in response to sinusoidal signals can be considered as the building blocks for the system response of more complex signals (Lynn 1982). Hence the use of a sinusoidal signal provides a generic quantification of the numerical error in the technique that is representative of any complex perturbation in the system.

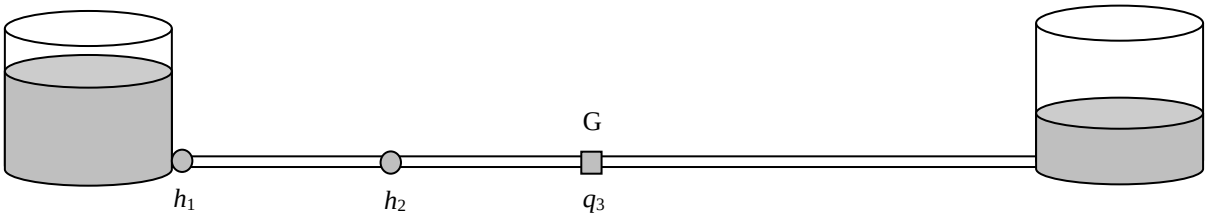

Figure 6.2 – Schematic of the test setup

The error in the magnitude of the predicted flow perturbation about the mean state, E is defined as the non-dimensional Root-Mean-Square (RMS) difference in frequency spectra predicted from the MOC and KDP models. The choice of error definition is subjective and it depends on intended applications. Herein, the ability of the KDP method for predicting the entire signal profile is of interest and hence the use of the RMS across the entire frequency spectrum is considered appropriate. The error in phase between the two models was found to be small compared with the magnitude error and therefore is ignored. To highlight the nature of the error arising from the linearization of the governing equation, other complex phenomena such as unsteady friction and viscoelasticity, which can be modelled linearly in both MOC and transfer matrices, are ignored in the numerical study.

The effects of the system and signal characteristics are presented in Figure 6.3. The system size parameter, Π_1, is altered by the steady flow rate, Q_0 ranging between 0.01 to 1 m^3/s while other parameters inside Π_1 are kept constant. This flow range is expected to cover a wide range of applications of the KDP method in the field. The relative signal size Π_2 is varied from 1 to 50% of the mean flow rate at which point part of the system experiences flow reversal and it is expected to be the most extreme case. In Figure 6.3 (a), the system is excited at the non-harmonic frequency of the system for $\Pi_3 = 1.5$.

Figure 6.3 (a) shows the KDP numerical error if the system oscillates about a non-resonant frequency. The results indicate that the numerical error increases with the perturbation size (Π_2). This trend is due to the linear approximation made in the derivation of the transfer matrix equations. The size of the neglected nonlinear term grows as the system is perturbed with larger amplitude signals.

The numerical errors at different perturbation frequencies are shown in Figure 6.3 (b), in which the perturbation signal was varied up to 6^{th} harmonic of the system. The plot contains the numerical KDP errors for 3 different perturbation sizes, namely 10%, 30% and 50% of the steady flow through the system. The maximum error results for the largest perturbation size of 50% supporting the finding in Figure 6.3 (a). Distinct error spikes were also seen at resonant frequencies at which point the largest error was over 80%. A consequence of system resonance is the amplified magnitude of the flow and pressure fluctuations which may cause severe damage to a system (Chaudhry 1987, Wylie and Streeter 1993). The high-amplitude fluctuations also led to the violation of the linear approximation used in the derivation of the transfer matrix equations.

The maximum numerical error of 1% in Figure 6.3 (a) indicates that the linearization of the governing equation does not have a significant effect provided that the system is not driven near or at resonance. From the observations, the KDP method appears numerically accurate for a wide range of pipe systems characteristics.

In the development of the transfer matrix equations, known conditions at two points in the system are introduced to solve the arbitrary constants. This process brings in length parameters to the problem and these parameters are used to define the positions of two pressure transducers and a position of interest for the measurement of the time-varying flow rate in the KDP method. An additional study into the impact of the system configuration on the KDP accuracy will determine if an optimum system configuration exists for this technique and will be useful for the subsequent experimental study.

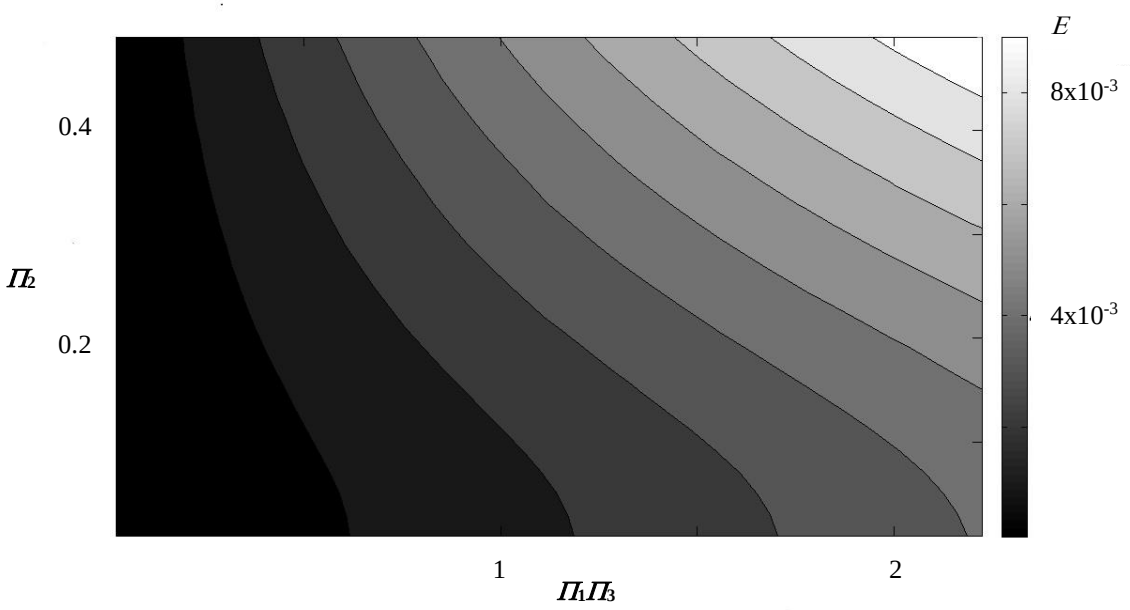

(a) Effect of system and signal properties as system is excited at frequency between first and second harmonics $\Pi_2(\Pi_1\Pi_3)$

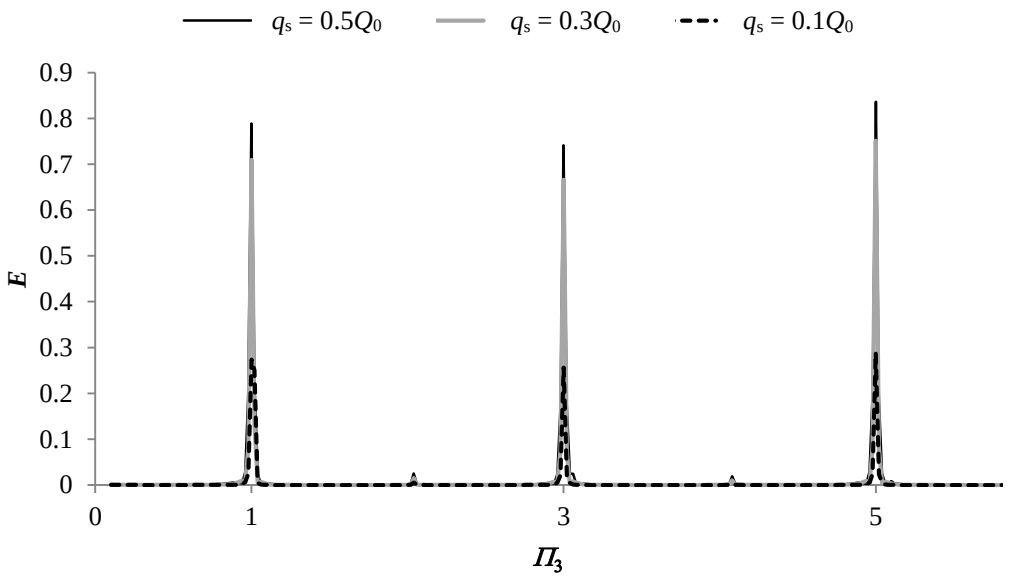

(b) Error trend with frequency of excitation signal $E(\Pi_3)$

Figure 6.3 – Linearization error in KDP flow predictions

6.3 Optimum configuration for the Kinetic Differential Pressure method

The three length parameters to be examined are l_a', l_b' and l_g' (Figure 6.4) where l_a' is the distance between the two pressure transducers, l_b' is measured from the most downstream pressure transducer to the point of flow prediction and l_g' is the distance from the flow prediction point to the signal source. While l_g' does not appear in the KDP equations, this length parameter represents the position of the KDP components within the system and the investigation on the effect of l_g' can further assess the practicality of the method. All distances are normalised by L, the total pipe length.

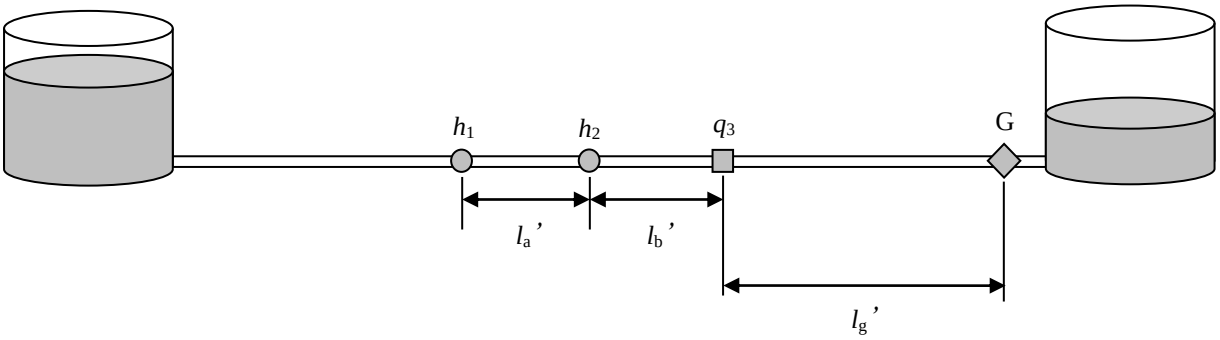

Figure 6.4 – Three lengths parameters in the KDP equation

The extremes of each length parameters were used to examine its influence on the accuracy of the method. The maximum and minimum values of each parameter were 0.798 and 1×10^{-3} respectively. A pulse signal with the magnitude of 1% of the steady flow was injected to the system at a point 1800 m from the upstream boundary. In all scenarios, the RMS error between the flow responses given by the MOC and the KDP method was found to be in the order of 0.01%, indicating that there is no restriction in the positioning of transducers and the flow prediction point.

This section has demonstrated that the KDP method is numerically accurate provided that the linear assumption is not violated. The verification of the method continues in the next section in which the method will be implemented in the laboratory pipeline system. The application of the KDP method in real systems introduces additional sources of errors, some of which are the presence of noise in the measurements and the inaccurate estimates of the system parameters. Effects of these sources of error on the accuracy of method will also be studied.

6.4 Experimental verification of the Kinetic Differential Pressure method

The experimental verification of the KDP method was conducted using the laboratory pipeline whose schematic is shown in Figure 6.5. The pressure in the tanks was adjusted to create laminar and turbulent flow conditions. The inline valve at the downstream end of the system was closed to establish a static steady state condition.

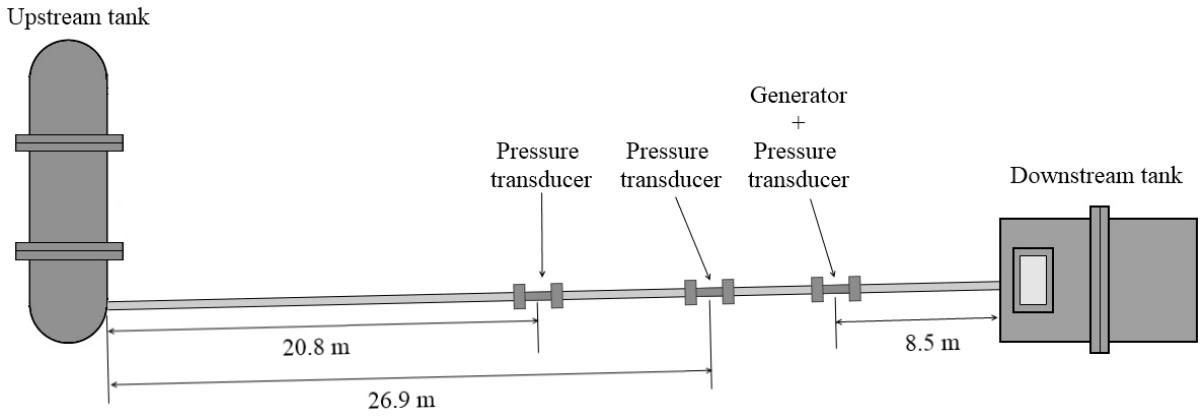

Figure 6.5 – Schematic of the test setup for the experimental verification

Controlled flow perturbations for the validation of the KDP method are introduced using two hydraulic devices; an electronically controlled solenoid valve and a manually operated side discharge valve which are located 8.5 m from the downstream reservoir. Example pressure traces created by the solenoid valve and the side discharge valve are presented in Figures 6.6 (a) and (b) respectively. The time, *t'*, and the amplitude of the pressure fluctuation, *h*'*, in the figure are normalised by the period of the pipeline system and the steady head at the measurement point respectively. The introduced flow perturbations are in the form of sharp pulses which contain a wide spectrum of frequencies for the rigorous testing of KDP method. This type of perturbation is encountered in many real life situations, including industrial batch filling processes as well as internal combustion engines. The pulse from the solenoid valve is created by rapidly opening the valve followed immediately by a sharp closure, with a pulse duration in time of 8 ms. The solenoid valve is used under static and laminar flow conditions. In turbulent flow, a flow pulse is created from the manual operation of a side discharge valve which is placed close to a reservoir boundary, in this case the downstream boundary. The side discharge valve is initially open and then rapidly shut, creating a high pressure wave that propagates away from the valve in both directions. When the wave front

moving downstream impinges upon the reservoir boundary it is reflected as a pressure restoring wave which moves upstream, following the high pressure wave. The sum total of these two waves is a pressure pulse. The duration of the pulse created in this way is 24 ms.

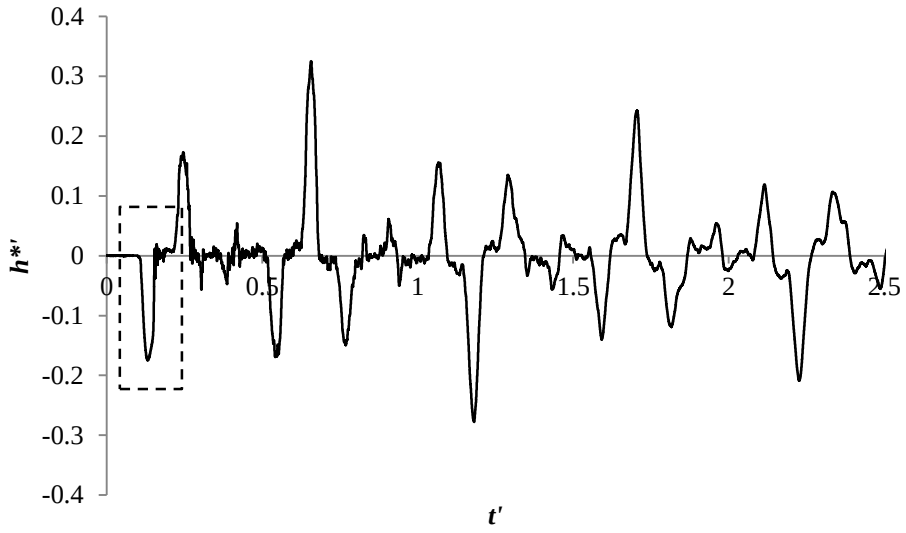

(a) Transient produced by the solenoid valve

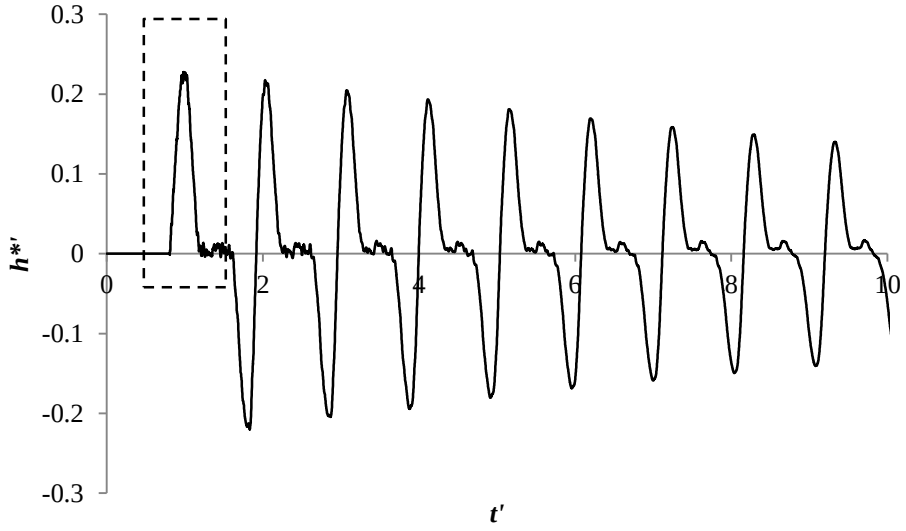

(b) Transient produced by the side discharge valve

Figure 6.6 – Measured transient traces

In the following experimental verification, only the first pulse of the entire transient trace is used (as boxed in the Figure 6.6). However, the method also works in the presence of boundary reflections provided all the pressure transducers for the method detect the same reflections. This second requirement is owing to the assumption that, when going from the

time to the frequency domain, the transferred signal in time repeats itself indefinitely. Hence, if a part of signal was missing from one of the measured traces, the missing part would not be properly acknowledged by the method.

Pressure traces for the KDP method are measured using piezoelectric transducers located 20.8 m and 26.9 m from the upstream reservoir. The pressure sensors are accurate to 1% of the measured pressure. The distance between the transducers and the time difference between the two measured pressure signals were used to determine the system wave speed. The experimental verification of the KDP method was conducted with and without a steady base flow. The flow Reynolds number ranged from 325 to 53400.

The accuracy of the KDP method is given as the absolute difference between a measured flow response and a predicted flow response by the KDP equations. The true flow response is obtained from the pressure response measured at the generator through the Joukowsky equation. The system wave speed is very sensitive to the air content of fluid and it can be difficult to obtain its true value. The error in the wave speed leads to the error in the height of the flow pulse. In order to minimise the error, the pulse height was adjusted according to the measured discharge volume from the generator. In the case of the solenoid valve, a transparent tube was connected to the valve outlet. A rise in the water height inside the vertical tube and the tube diameter provide the volume of fluid released by the valve operation. The rise was measured by a vernier scale and the maximum standard deviation of the measurements was 2.0%. For the tests under turbulent flow condition, the wave speed was estimated from the measured discharge out of the side discharge valve and the pressure measured at the valve. The discharge was estimated from the measured mass of water during a certain period of time and the standard deviation of the discharge measurement was 2.3%.

The accuracy of the KDP is quantified by three norms. The difference in the area under the flow pulse signal over time provides the error in the volumetric measurement of the discharge, E_{Volume}. The error in capturing the maximum flow pulse amplitude is given the symbol, E_{Max}. Finally, the difference in the spectral content of the predicted response describes the error in the shape of the flow pulse profile, E_{Profile} and it is given as a root mean sum of the error across all the frequency components of the signal. All three errors are given relative to the true response.

Previous studies on the KDP method included only unsteady friction for laminar flow (Washio *et al*. 1996) and the technique was only studied under laminar flow condition. This study provides the experimental investigation of the KDP method under static, laminar and turbulent flow conditions with the flow Reynolds numbers ranging up to the smooth pipe turbulent zone.

6.4.1 Static steady state condition

Under the static steady state condition, four different pulse sizes were used. The maximum flow magnitudes of those pulses were 1.38×10^{-5} m^3/s (Case 1), 1.51×10^{-5} m^3/s (Case 2), 1.83×10^{-5} m^3/s (Case 3), and 2.39×10^{-5} m^3/s (Case 4). The choice of the pulse size was governed by the limitations of the solenoid valve. The predicted responses for each pulse size are shown in Figure 6.7 and errors are summarised in Table 6.1. The flow on the y-axis is normalised by the respective maximum flow amplitude. The results show that the average error across all pulse sizes is in the order of 0.1%. The KDP method captured the maximum flow rate well but the error in the pulse profile was relatively large for all pulse sizes. The largest error in these tests was 2.0% for the biggest pulse size and the errors were found to generally increase with the pulse magnitude.

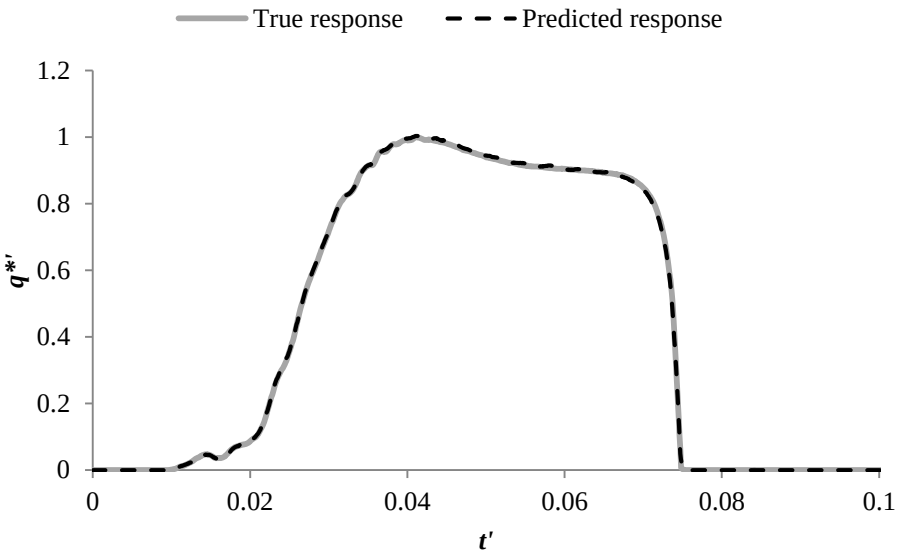

(a) Case 1

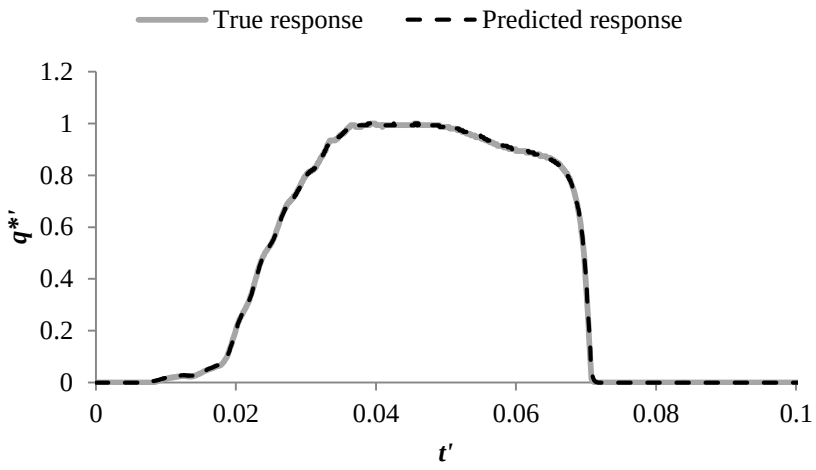

(b) Case 2

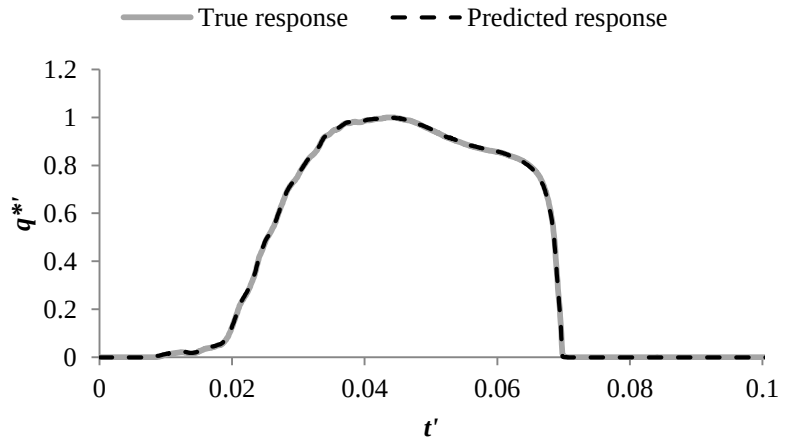

(c) Case 3

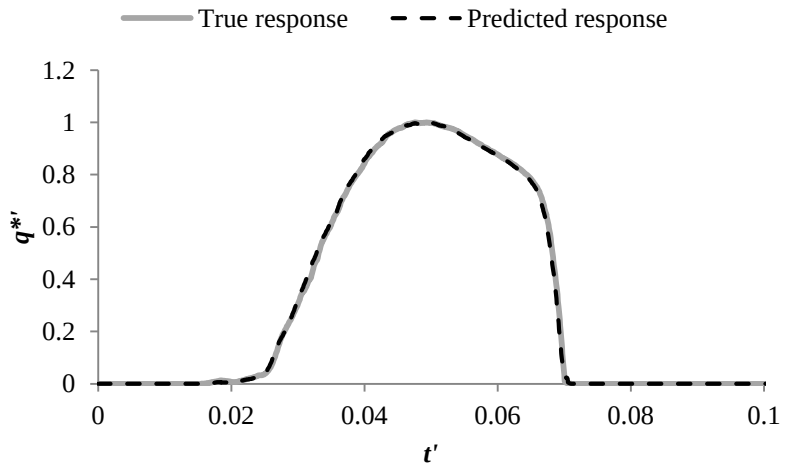

(d) Case 4

Figure 6.7 – Comparison between the predicted and true responses in static steady state condition

Case number	E_{Volume}	E_{Max}	$E_{Profile}$
Case 1	0.38%	0.34%	0.81%
Case 2	0.81%	0.14%	0.82%
Case 3	0.36%	0.26%	0.73%
Case 4	0.41%	0.17%	2.00%

Table 6.1 – Summary of percentage errors in the flow predictions of different flow pulse magnitudes

Tests were also conducted under laminar and turbulent flow conditions as discussed in the next sections.

6.4.2 Laminar flow condition

A flow pulse was created in laminar flow with five different Reynolds numbers. The Reynolds number was varied from 325 to 1640. The maximum magnitude of the flow perturbation in each test case was 1.38×10^{-5} m^3/s (Case 5), 1.36×10^{-5} m^3/s (Case 6), 1.31×10^{-5} m^3/s (Case 7), 1.27×10^{-5} m^3/s (Case 8) and 1.24×10^{-5} m^3/s (Case 9) respectively. The flow prediction from the KDP method is compared with the true flow pulse in Figure 6.8 and the errors in the KDP flow prediction are shown in Table 6.2.

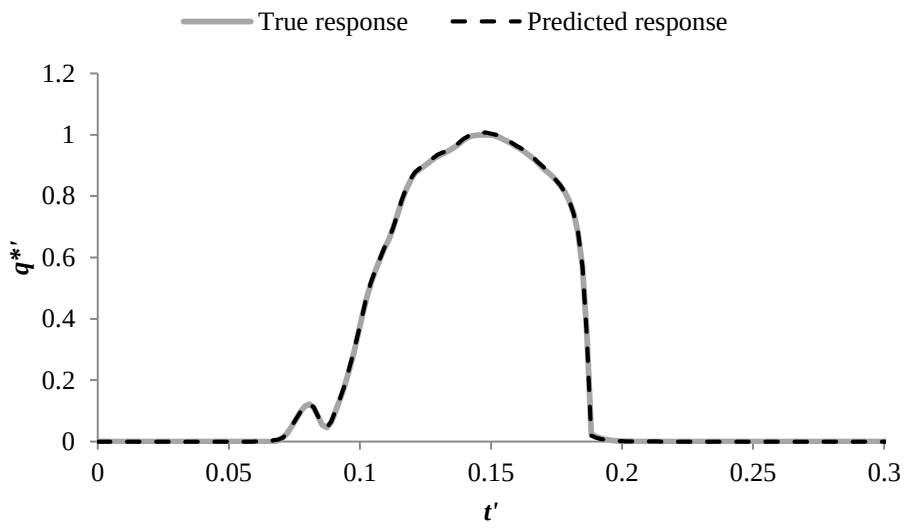

(a) Case 5

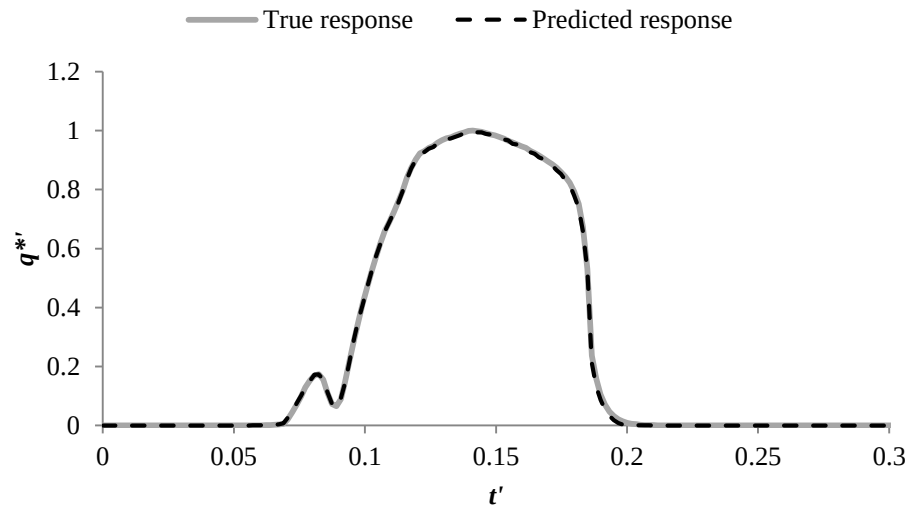

(b) Case 6

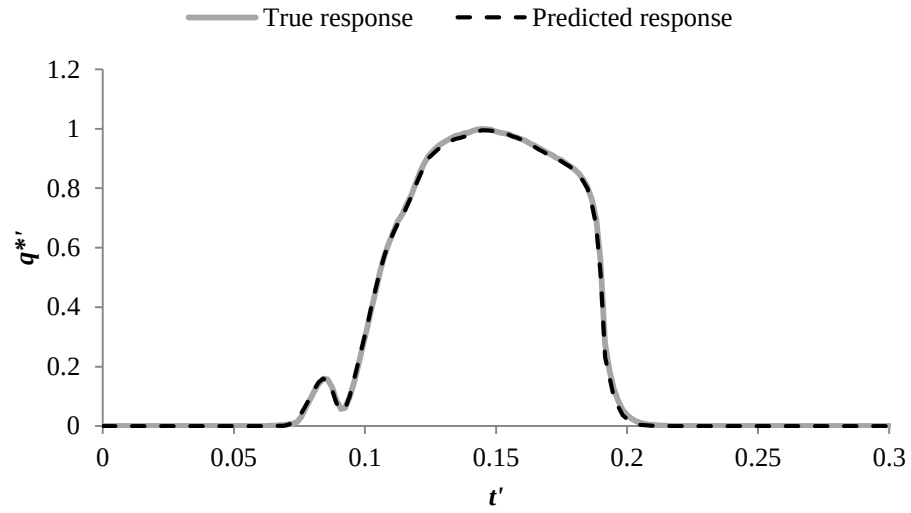

(c) Case 7

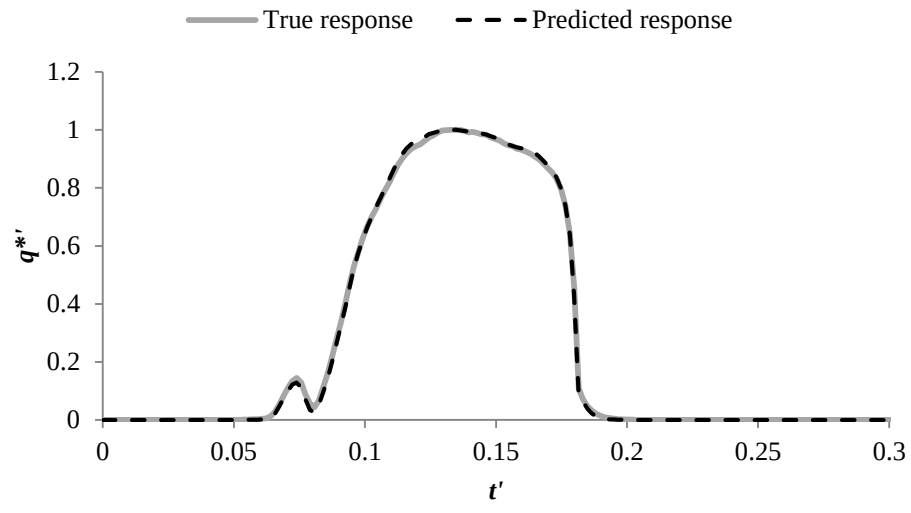

(d) Case 8

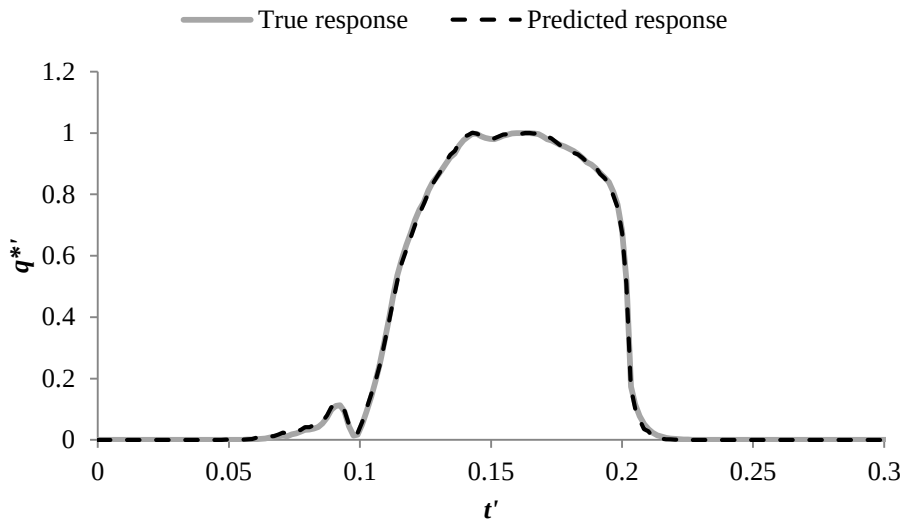

(e) Case 9

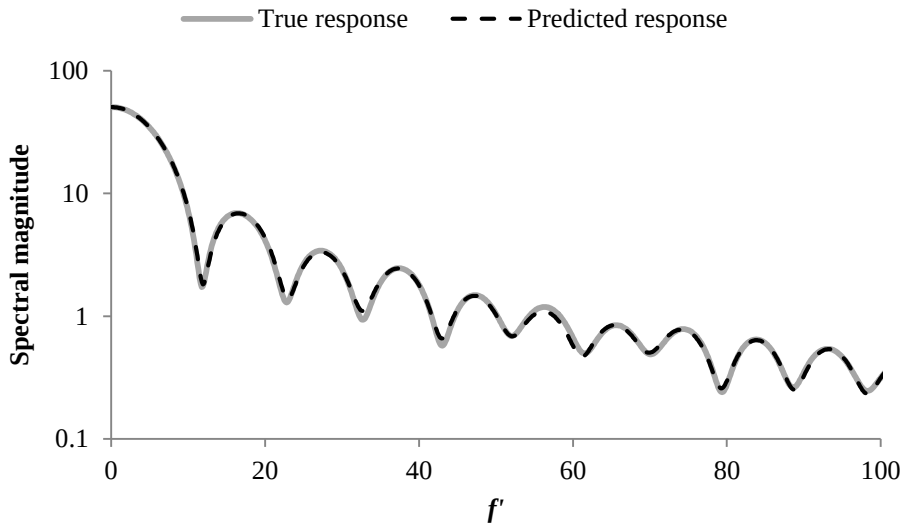

(f) Frequency spectra of responses in (e)

Figure 6.8 – Comparison between the predicted and true responses in laminar flow condition

Case number	E_{Volume}	E_{Max}	$E_{Profile}$
Case 5 (Re = 327.9)	0.78%	0.21%	1.61%
Case 6 (Re = 593.4)	0.69%	0.31%	1.14%
Case 7 (Re = 845.2)	0.57%	0.69%	1.48%
Case 8 (Re = 1164.5)	1.04%	0.32%	1.67%
Case 9 (Re = 1641.2)	1.31%	1.07%	2.11%

Table 6.2 – Summary of average errors in the flow predictions in various laminar flows

As shown in Figure 6.8, the predictions from the KDP method matched well with the true flow responses. The frequency spectra of the flow pulses in Figure 6.8 (e) are given in Figure 6.8 (f) where a good match between the true and predicted frequency spectra was found, which agreed with the well-matching time responses in Figure 6.8 (e). The errors given in Table 6.2 indicate that the prediction accuracy degraded with the Reynolds number. The average error in the KDP prediction was in the order of 0.1% which confirms the applicability of the method in the laminar flow condition.

6.4.3 Turbulent flow condition

The flow Reynolds number was increased to create five turbulent flow conditions. The Reynolds number ranged from 28900 to 53400. A comparison of the true and predicted flow pulses in Figure 6.9 show that the predictions by the KDP method are generally accurate except for discrepancies in the fine details of the pulse shape. For a better inspection of the shape difference, the frequency spectra of the flow pulses in Figure 6.9 (e) are presented in Figure 6.9 (f). In the figure, the true and predicted spectra match well up to a dimensionless frequency of approximately 4, implying that the KDP method captured the general form of the flow pulse that is described by lower frequency components. However, the predicted spectrum differs from the true spectrum significantly at higher frequencies and this difference corresponds to the discrepancy in the fine details of the signal shape observed in the time domain.

As indicated in Table 6.3, overall, the errors were larger than the static and laminar flow cases and the greatest error was found in the prediction of the shape of the signal profile, with a maximum error of 6.41%. The prediction accuracy degraded for the tests in the turbulent flow condition due to the presence of background noise associated with the base flow. The transfer matrix model predicts the transient behaviour at a point by transferring the measured transient information from another point, using the knowledge of the system between the two points. The base-flow-induced noise is, however, not characterised by the given transfer matrix model and hence the superimposed noise on the true and predicted transients will be different from each other. Since the noise is more significant in turbulent flows than in laminar flows, the discrepancies in the noise prediction is expected to increase, which has been demonstrated by the current set of results. Nevertheless, given that the average error was

in the order of 1% in the turbulent flow condition, the presented results have shown that the KDP method can measure rapid changes in flow with acceptable accuracy for the considered range of Reynolds number.

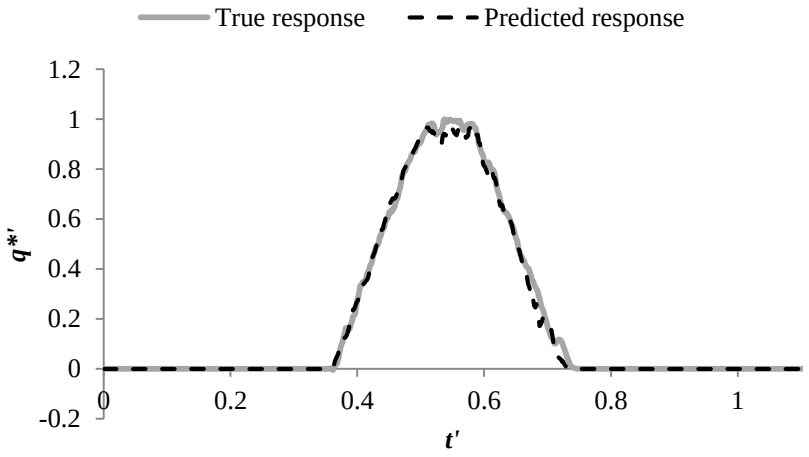

(a) Case 10

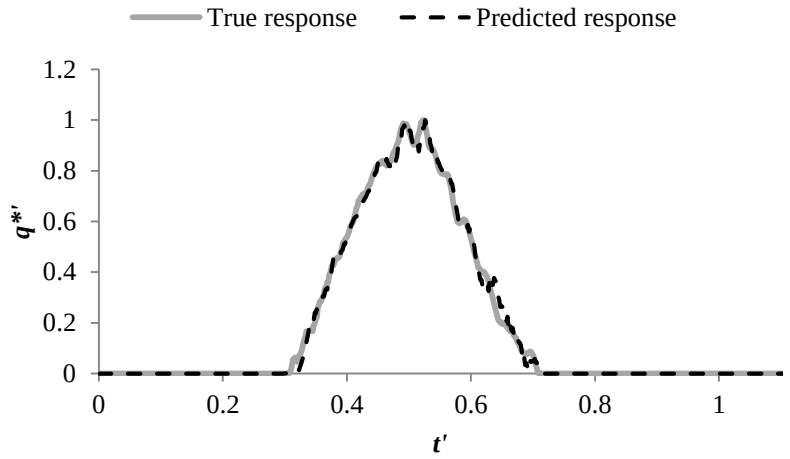

(b) Case 11

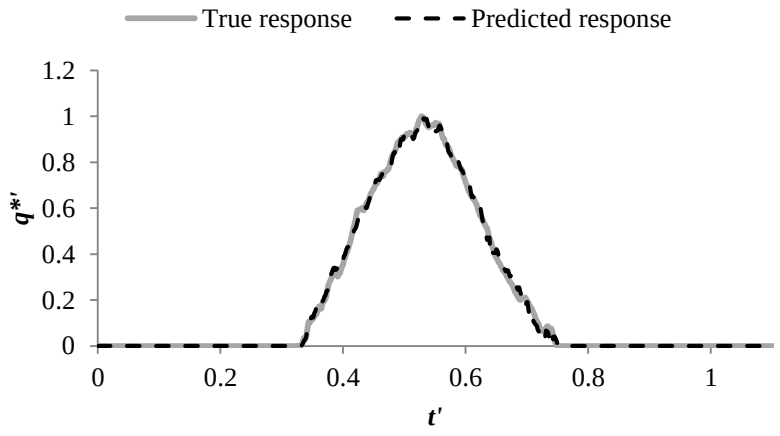

(c) Case 12

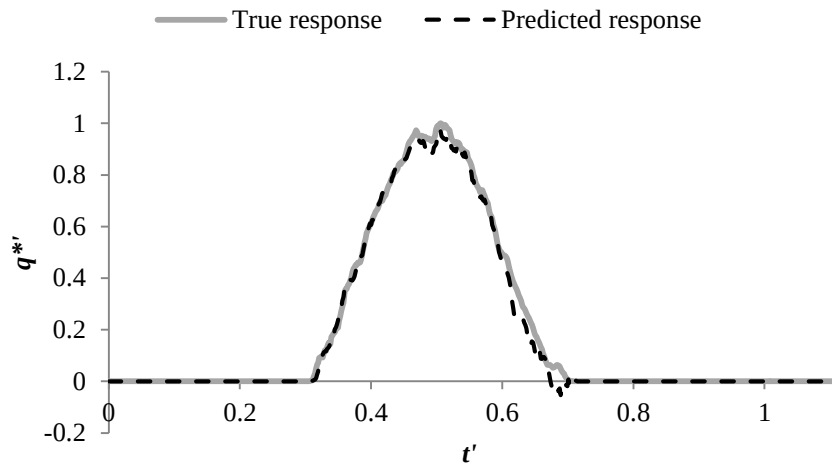

(d) Case 13

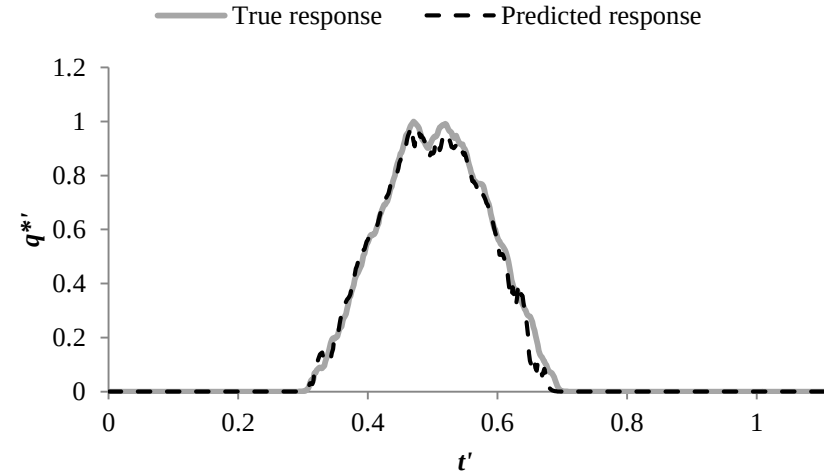

(e) Case 14

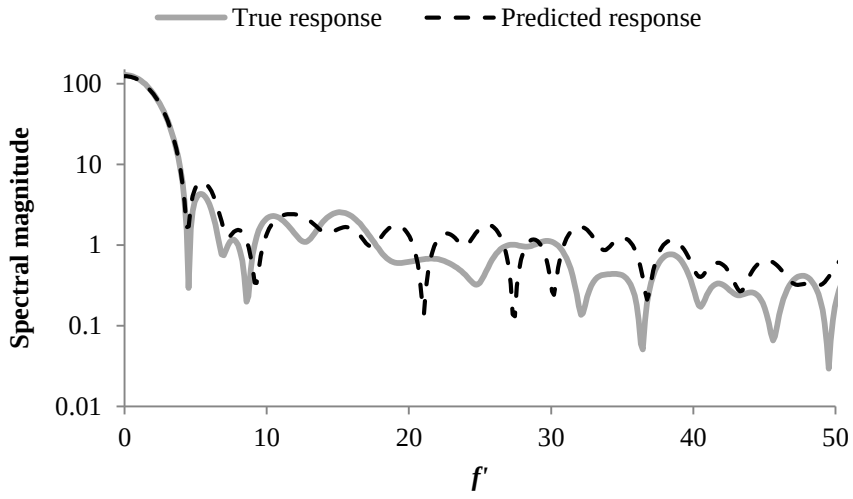

(f) Frequency spectra of responses in (e)

Figure 6.9 – Comparison between the predicted and true responses in turbulent flow condition

Case number	E_{Volume}	E_{Max}	$E_{Profile}$
Case 10 (Re = 28933.8)	1.87%	2.04%	4.27%
Case 11 (Re = 36309.8)	1.32%	0.11%	5.31%
Case 12 (Re = 42624.7)	0.84%	0.91%	3.92%
Case 13 (Re = 48248.6)	3.83%	1.77%	6.41%
Case 14 (Re = 53374.9)	1.87%	1.93%	5.48%

Table 6.3 – Summary of average errors in the flow predictions in various turbulent flows

6.5 Effect of input parameter error on the accuracy of the Kinetic Differential Pressure method

The operation of the KDP method requires the estimation of a number of system and flow parameters and these are used as the inputs to the model. In real pipelines, the input parameters will often contain errors and their effect on the accuracy of the method forms an important consideration in this study.

Investigations were carried out using the numerical pipeline system whose schematic is shown in Figure 6.10. The downstream boundary is open to create a base flow through the system which has the Reynolds number of 7.3×10^5. A flow perturbation source is located at the middle of the system producing a flow pulse of a magnitude of 1% of the steady base flow. The pressure response is measured at points located 700 m and 900 m from the upstream reservoir.

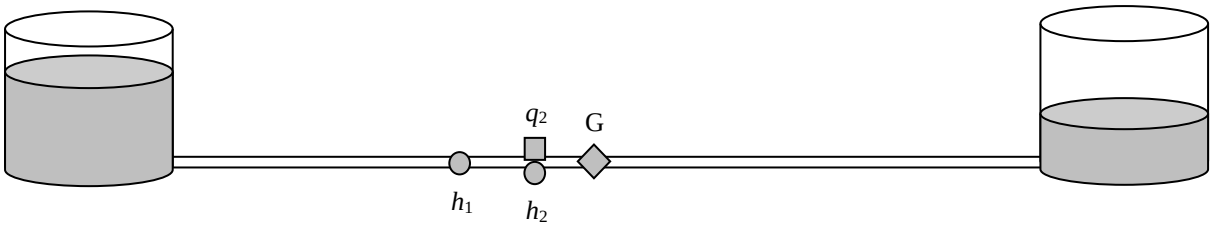

Figure 6.10 – Schematic of the test setup for the sensitivity study

The sensitivity of the KDP method to the accuracy of the input parameters was tested analytically using Equation 6.7 which gives the flow response at the point 900 m from the upstream boundary:

$$q_2 = \frac{h_1}{Z_c}\operatorname{csc}h(\mu l_a) - \frac{h_2}{Z_c}\coth(\mu l_a) \tag{6.7}$$

System parameters involved in this calculation are the pipe diameter (D), the pipe friction factor (f), the base flow (Q_0), the system wave speed (a) and the transducer spacing (l_a). For the study of sensitivity, Equation 6.7 was differentiated with respect to these system parameters and the resultant equations are given in Equation 6.8 to 6.12. The derivatives were determined for all frequencies and the magnitude of the largest frequency component was used as an indicator of the significance of the parameter. For a valid assessment, the obtained value was normalised by the value of the respective input parameters. The results are summarised in Table 6.4.

The results show that the influence of the transducer spacing and the system wave speed was in the order of 2 to 3 times larger than other input parameters and the robustness of the KDP equations against estimation errors in the pipe friction factor and the base flow through the system is evident. Although it is not shown here, the sensitivity of Equation 6.7 was also tested numerically and it reached the same conclusion as the above analytical study.

$$\frac{\partial q_2}{\partial D} = -\frac{h_1}{Z_c}\left[\frac{1}{Z_c}\frac{\partial Z_c}{\partial D}\operatorname{csc}h(\mu l_a) + l_a\frac{\partial \mu}{\partial D}\operatorname{csc}h(\mu l_a)\coth(\mu l_a)\right] + \frac{h_2}{Z_c}\left[\frac{1}{Z_c}\frac{\partial Z_c}{\partial D}\coth(\mu l_a) + l_a\frac{\partial \mu}{\partial D}\operatorname{csc}h^2(\mu l_a)\right] \tag{6.8}$$

$$\frac{\partial q_2}{\partial f} = -\frac{h_1}{Z_c}\left[\frac{1}{Z_c}\frac{\partial Z_c}{\partial f}\operatorname{csc}h(\mu l_a) + l_a\frac{\partial \mu}{\partial f}\operatorname{csc}h(\mu l_a)\coth(\mu l_a)\right] + \frac{h_2}{Z_c}\left[\frac{1}{Z_c}\frac{\partial Z_c}{\partial f}\coth(\mu l_a) + l_a\frac{\partial \mu}{\partial f}\operatorname{csc}h^2(\mu l_a)\right] \tag{6.9}$$

$$\frac{\partial q_2}{\partial Q_0} = -\frac{h_1}{Z_c}\left[\frac{1}{Z_c}\frac{\partial Z_c}{\partial Q_0}\operatorname{csc}h(\mu l_a) + l_a\frac{\partial \mu}{\partial Q_0}\operatorname{csc}h(\mu l_a)\coth(\mu l_a)\right] + \frac{h_2}{Z_c}\left[\frac{1}{Z_c}\frac{\partial Z_c}{\partial Q_0}\coth(\mu l_a) + l_a\frac{\partial \mu}{\partial Q_0}\operatorname{csc}h^2(\mu l_a)\right] \tag{6.10}$$

$$\frac{\partial q_2}{\partial l_a} = \frac{\mu}{Z_c}\left[-h_1\coth(\mu l_a)\operatorname{csc}h(\mu l_a) + h_2\operatorname{csc}h^2(\mu l_a)\right] \tag{6.11}$$

$$\frac{\partial q_2}{\partial a} = -\frac{h_1}{Z_c}\left[\frac{1}{Z_c}\frac{\partial Z_c}{\partial a}\operatorname{csc}h(\mu l_a) + l_a\frac{\partial \mu}{\partial a}\operatorname{csc}h(\mu l_a)\coth(\mu l_a)\right] + \frac{h_2}{Z_c}\left[\frac{1}{Z_c}\frac{\partial Z_c}{\partial a}\coth(\mu l_a) + l_a\frac{\partial \mu}{\partial a}\operatorname{csc}h^2(\mu l_a)\right] \tag{6.12}$$

Parameter	Maximum value
Pipe diameter, D	9.27×10^{-7}
Friction factor, f	2.93×10^{-8}
Base flow, Q_0	2.93×10^{-8}
Transducer spacing, l_a	8.18×10^{-5}

System wave speed, a	8.17×10^{-5}

Table 6.4 – Results of the sensitivity study

Predicted responses in the cases of the incorrect pipe diameter and transducer spacing are presented in Figure 6.11 (a) and (b) respectively. The flow on the y-axis is non-dimensionalised by the initial steady state flow. The predicted response with correct input parameters is represented by the grey line and the broken line indicates the prediction with the incorrect input parameter. In each graph, the tip of the flow pulse is enlarged and presented in a separate window for easier comparison.

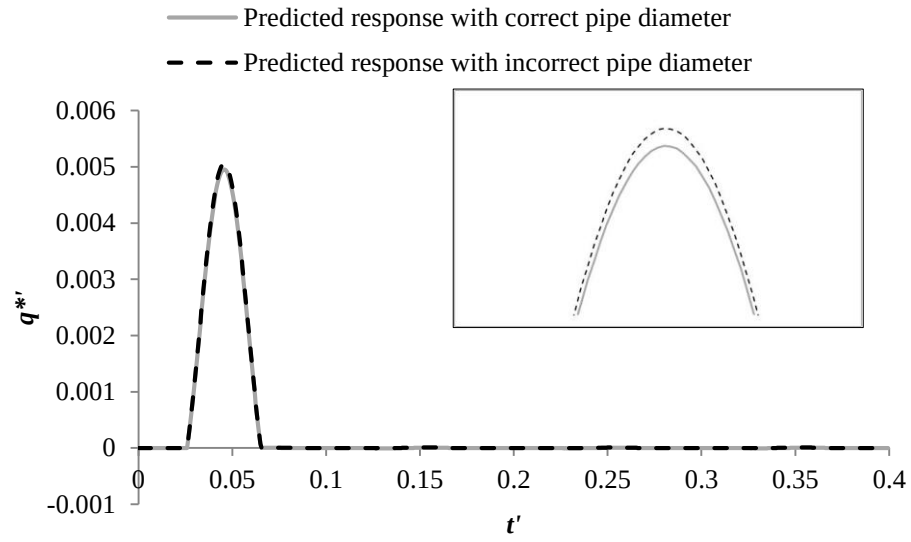

(a) Predicted flow response with incorrect pipe diameter

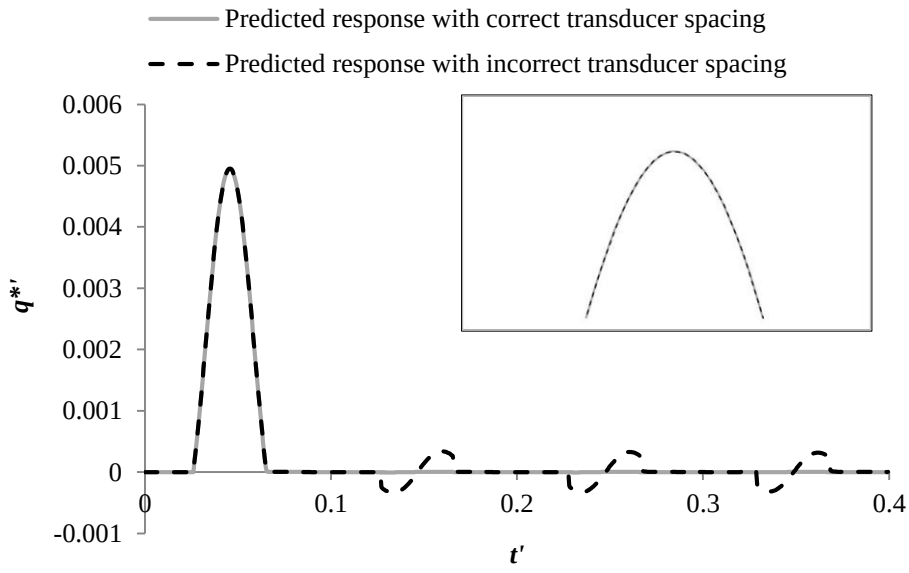

(b) Predicted flow response with incorrect transducer spacing

Figure 6.11 – Predicted flow responses with incorrect system parameters

Figure 6.11 clearly shows that errors in the pipe diameter and the transducer spacing have a different impact on the predicted trace. The error in the pipe diameter led to a change in the characteristics of the pulse. It was found that the incorrect friction factor and the base flow also affect the pulse in a similar way. On the other hand, the error in the transducer spacing caused minimal change to the pulse characteristics, but instead, it gave rise to numerical contamination which repeats regularly for the rest of the response. The same phenomenon was observed in the case with the incorrect wave speed and further study found that the noise profile was identical for the same ratio of the transducer spacing to the wave speed.

The periodic nature of the noise points to the hyperbolic sine and cosine functions of the transfer matrix as the source of the contamination. The transfer matrix method simulates the transient behaviour by first decomposing the signal to a set of frequency components and then transfers them a given distance along the pipe and at a given wave speed in the form of hyperbolic sine and cosine waves. The system wave speed and the length of the pipe are therefore central to the transfer matrix model and are used to characterise the fundamental behaviour of the pipe segment of interest. The mismatch between the true and estimated system characteristics is a result of the discrepancy between the observed and actual periods of the pipe segment bounded by the transducers, and it manifests itself as numerical contamination in the predicted flow response.

The relationship between the error in the period T_S (= $2L_T/a$, where L_T is the transducer spacing) and the noise profile was investigated through two test scenarios. In the first scenario, noise profiles from two different travel times were compared. The two dimensionless travel times T_S' (= T_S/T) were 0.1 and 0.15. In both cases, the travel time was estimated 1% greater than the correct value. The second scenario examined the effect of the varying error in the travel time on the noise profile. In this test, the correct dimensionless period was 0.1 and it was assumed incorrect by 0.5% (solid grey line), 1% (broken black line), 1.5% (broken grey line), 3% (dotted black line), 5% (solid black line) and 10% (dotted grey line) greater than the correct value.

Results from the first scenario are presented in Figure 6.12 (a). The broken and solid lines indicate the case with the dimensionless period of $T_{S1}' = 0.1$ and $T_{S2}' = 0.15$ respectively. It is observed that, with the dimensionless period of 0.1, the noise repeats with a dominant recurrence period, T_{R1} of 0.101 which coincides with the estimated dimensionless period. When the dimensionless period was 0.15, the recurrence period, T_{R2} was 0.1515 which again agrees with the estimated dimensionless period of the pipe segment. The influence of the error in the period on the noise profile is illustrated in Figure 6.12 (b) which shows that the noise magnitude increases proportionally to the error in the period. The results from the two sets of studies support the idea that the noise is related to disagreement in the estimated and actual periods of the pipe segment.

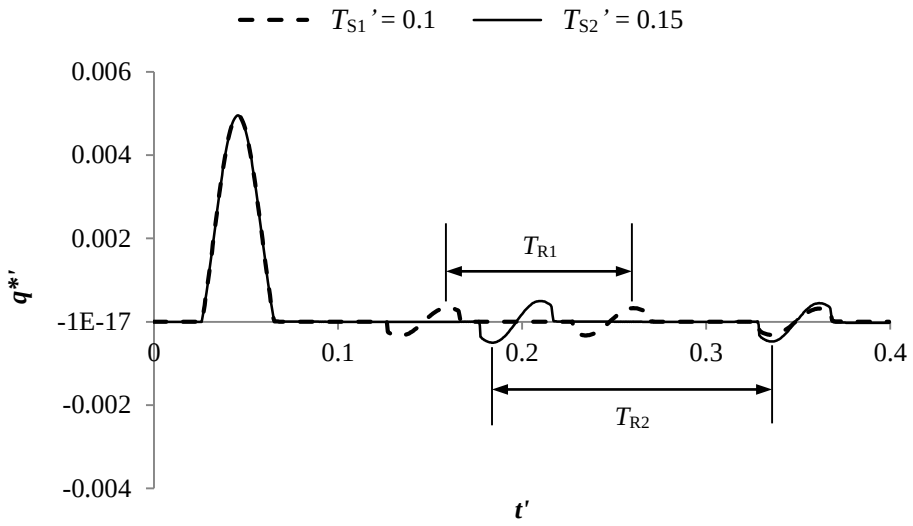

(a) Recurrence period of noise. The broken line represents the noise with the dimensionless period T_{S1}' of 0.1 and the solid line represents the noise with the dimensionless period T_{S2}' of 0.15

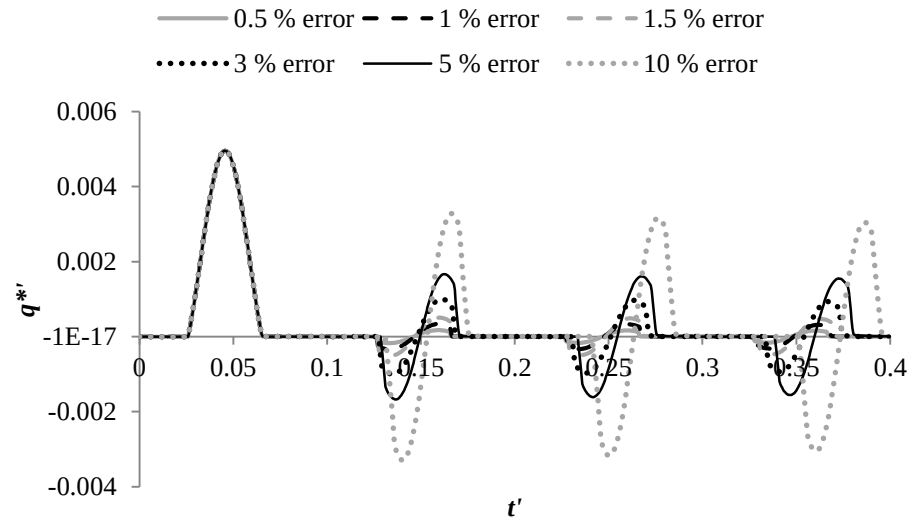

(b) Noise profiles when period is estimated 0.5%, 1%, 1.5%, 3%, 5%, and 10% greater than the correct value

Figure 6.12 – Repeating noise in the predicted flow response

The error in the input parameters degrades the quality of flow predictions. The sensitivity analysis showed that the quality of the predicted response hinges on the accuracy of the estimated characteristic time of the pipe segment bounded by the pressure transducers. The impact of the noise becomes more problematic when dealing with continuous signals where the contamination will be superposed on the predict flow trace. Depending on the degree of error in the period, the correct transient trace might not be clearly visible. In this section, the verification of the KDP method was carried out using discrete pulse signals, commonly seen in the batch processing applications or fuel injection lines. For these signals, the parts of the flow predictions that are related to the real response can be clearly identified as they do not overlap with the part of the signal affected by the numerical contamination. The noise can therefore be removed from the response and does not affect the accuracy of the results. However, it is important to note that this distortion of the predicted flow response would need to be addressed before the technique can be applied in more complex and longer duration flow measurement situations.

6.6 Case study: Application of the KDP method with a continuous step wave

The previous sections verified the KDP method as a method for predicting discrete flow perturbations. With this type of flow perturbation, a system eventually comes back to the initial steady state conditions. Such behaviour of the system is an important factor for accurate flow predictions using the method because, in the derivation of the transfer matrix equations, it is assumed that the perturbation can be represented by one or more sinusoids which oscillate about an unchanging mean state. Generation of a step perturbation goes against this assumption as it drives the system conditions to go from one state to another during a transient state. While the violation of this assumption is expected to introduce an additional error in flow predictions, the significance of which is yet to be demonstrated and it is the aim of this case study to address this issue.

The test configuration is shown in Figure 6.13 (a). The two pressure measurement points (points 1 and 2 in the figure) and the flow estimation point (point 3 in the figure) have the

dimensionless distances of 0.3, 0.5 and 0.7 measured from the upstream boundary. These distances are normalised by the length of the pipe, *L*. A side discharge valve, which acts as a transient generator, *G*, is placed at the same point as the flow prediction point as indicated in the figure. The valve is initially closed and a negative pressure disturbance is produced by its instantaneous opening. The magnitude of the disturbance is 2.87% of the steady mean flow. Figure 6.13 (b) shows the instantaneous pressure, *H*, measured at point 1. The instantaneous pressure is a sum of the steady and unsteady (perturbating) pressure responses. The pressure is normalised by the steady head at the measurement point. As indicated in the figure, the pressure at the end of the trace is different from the starting pressure due to the change in the base flow created by the valve opening.

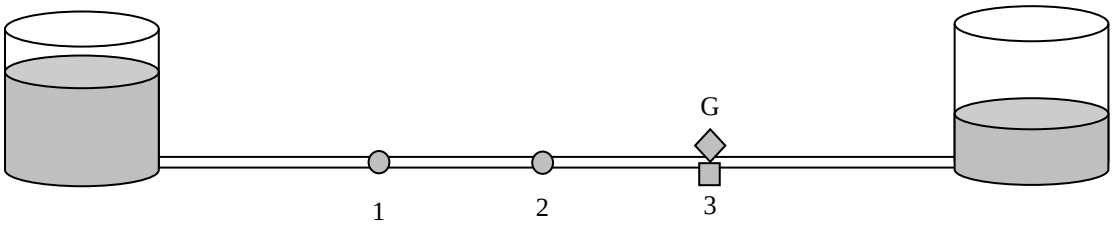

(a) Test configuration

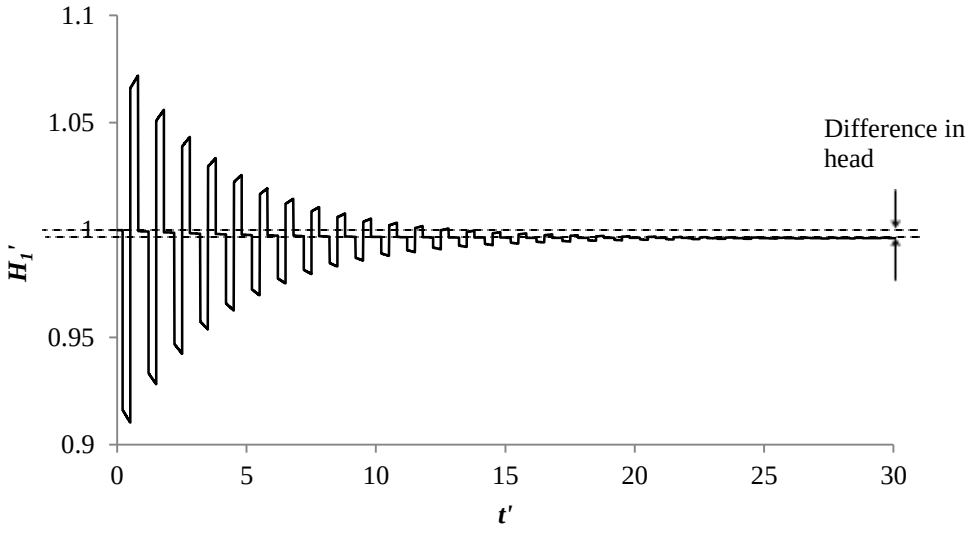

(b) Instantaneous pressure measured at point 1

Figure 6.13 – Test setup and the measured pressure traces

The predicted flow response from the pressures measured at points 1 and 2 is compared with the true flow response in Figure 6.14 (a). The KDP method captured the form of the flow perturbation very well and the two flow responses appeared to be similar. However, it was

found that the flows were perturbating about slightly different mean flows as shown in Figure 6.14 (b), which is an enlarged view of the section of the flow response, boxed in Figure 6.14 (a). For the section shown in the figure, the two mean flows differ by 0.43%. This difference is attributed to the changing mean states of the measured pressure responses.

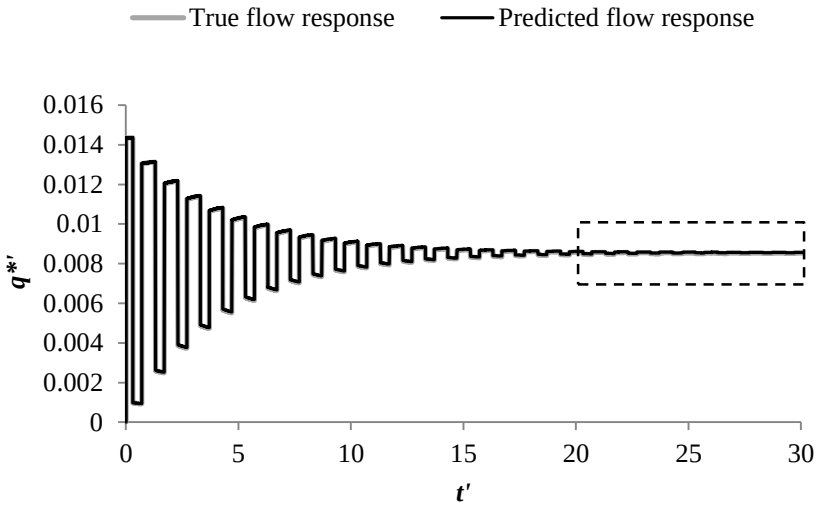

(a) Comparison between the true and predicted flow responses

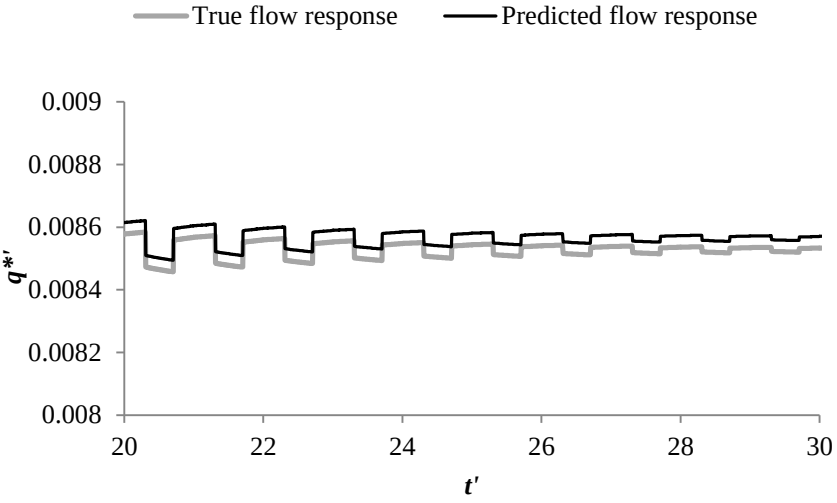

(b) Enlarged view of the boxed section in (a)

Figure 6.14 – Predicted flow response

For confirmation, the pressure traces are modified so that the pressure at the start and end of the traces are the same by taking away the time-shifted versions of themselves from the originals. The resultant pressure traces consist of a series of discrete pressure pulses instead of a continuous step wave as illustrated in Figure 6.15 (a). In the figure, the base pressure of

the original pressure trace was removed for ease of comparison with the modified trace. The predicted flow response from the modified pressure traces is presented in Figure 6.15 (b) for the time range between t' = 25 to 30, along with the true flow trace which has been modified in the same manner as for the pressure traces. Unlike Figure 6.14 (b), the two flow responses match very well both in terms of the shape of the flow perturbation and the mean flow on which the perturbation takes place.

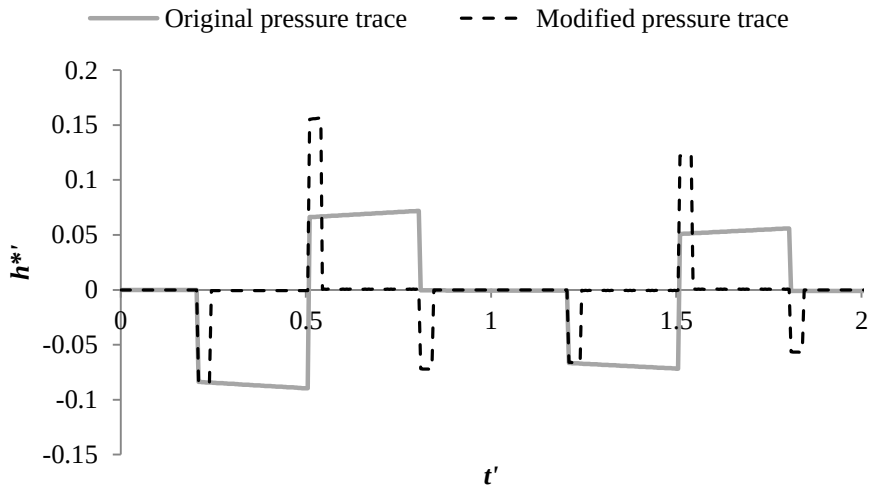

(a) Modified pressure response

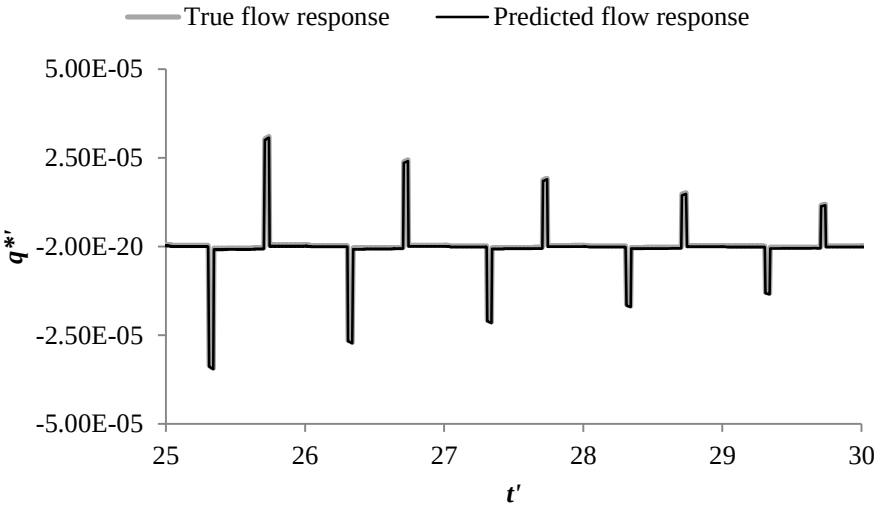

(b) Predicted flow response from the modified pressure traces

Figure 6.15 – Predicted flow response from the modified pressure traces

The error in the predicted flow response is expected to grow with the size of the step signal which corresponds to the difference between the mean flows before and after the transient

state. A larger signal prompts a more significant transition from the original steady state to the next and violates the assumption of the unchanging mean state to a greater degree. The simulation was repeated with larger transients, having the magnitudes of 8.62%, 17.2% and 25.9% of the mean flow. Note that, with these transient sizes, the error from the KDP method due to linearization is insignificant. The errors in the predicted mean flows are tabulated in Table 6.5 under the heading, "System 1". The results show an increase in the error with the transient size, thus confirming the anticipated relationship between the magnitude of the transient and the accuracy of the method.

	Relative transient size (q / Q_0)	Error	
		System 1	System 2
Signal 1	2.87%	0.43%	0.43%
Signal 2	8.62%	1.26%	1.26%
Signal 3	17.2%	2.43%	2.44%
Signal 4	25.9%	3.53%	3.54%

Table 6.5 – Summary of simulation results

To further clarify the dependence of the error on the relative transient size, the above simulations were repeated in a different numerical pipeline system (denoted as System 2) whose system parameters are given in Table 6.6 along with that of the original system (System 1) for comparison. Other system parameters which are not included in the table are the same as that of the original system. Both pipelines were split into the same number of reaches in the MOC simulations. The size of the transient signals relative to the mean flow was kept the same as in the previous simulation.

Parameters	System 1	System 2
Pipe length, L	2000 m	300 m
Wave speed, a	1000 m/s	300 m/s
Pipe diameter, D	0.3 m	0.03 m
System head loss, ΔH	30 m	3 m

Table 6.6 – Comparison of system parameters for System 1 and System 2

The test results are given in Table 6.5, under the heading “System 2”, which are identical or very close to the results found in System 1. It is evident, therefore, that the accuracy of the predicted flow responses does not depend on the size of the underlying system, but only on the size of the transient relative to the mean flow.

The observed errors are still sufficiently small to say that the KDP method can be used with step signals with moderate accuracy for the considered range of transient sizes. The implication of this outcome is that it is possible to determine an instantaneous flow without the aid of other flow meters. The instantaneous flow rate is a combination of the steady flow rate measured prior to the generation of the transient and the flow perturbation predicted by the KDP method. The steady flow rate can be determined from a difference in pressure measured at two points (point 1 and point 2 in Figure 6.1) and the Darcy-Weisbach equation via an iterative procedure.

6.7 Summary

The Kinetic Differential Pressure (KDP) method for measuring the unsteady flow has advantages in terms of the high sampling rate, minimal disturbance and low space requirement over other techniques. The use of pressure transducers means that the existing transducers in the system may be used for flow measurements, which reduces initial costs. The unique advantage of the method is its flexibility in the flow measurement point.

The KDP method is based on the linear transfer matrix equations which are derived by neglecting the nonlinear term in the unsteady momentum equation. The numerical accuracy of the method depends on the significance of this neglected term. Three dimensionless parameters which describe the system and signal characteristics were derived from the neglected nonlinear term. They took a range of values in order to produce situations with different system and signal conditions and the results showed when the method would fail. The numerical error was significant if the system was excited at its resonant frequency but it was only of the order of 1% for non-resonance frequencies for all tests. The error size indicates that the linear approximation of the governing equation has a small effect regardless of the system and the signal characteristics, if the system is not driven at its resonant frequency.

Experimental verification of the method was carried out using the laboratory pipeline system. The accuracy of predicted flow responses was quantified in terms of three parameters: the accuracy in predicting the discharge volume, the maximum flow and the shape of the flow pulse. The study showed that the average error was in the order of 0.1% for the static steady state and the laminar flow conditions, and 1% for the turbulent flow condition. These results indicate that the KDP method was able to predict the flow response with acceptable accuracy. The greatest error occurred in the shape of the flow profile with a maximum error of 6.41%.

The sensitivity of the KDP method was also studied. It was found that the errors in the pipe diameter, friction factor or the base flow lead to a change in the flow pulse characteristics while the errors in the transducer spacing or the system wave speed contaminates the predicted response with periodically repeating noise. This numerical noise is a reflection of disagreement between the theoretical and actual periods of the pipe segment bounded by the transducers. The noise amplitude and its recurrence frequency are a function of the degree of error in the period. The effect of noise is not severe when dealing with a discrete pulse signal and the current study shows the validity of the method for this signal type. For continuous signals and long-period flow measurements, the input parameters, especially the period of a pipe section must be carefully measured to avoid significant numerical contamination.

Finally, the KDP method was applied in a case where the mean state of the system changes with time. The underlying equations of the KDP method were derived on the basis that the system perturbation occurs about the unchanging mean state. The significance of the violation of this assumption was examined numerically by generating a step wave. It was found that while the KDP method gave the correct shape of the flow perturbation, it could not perfectly capture the shift of the mean flow with time. The error in the mean flow was found to be a function of the transient size relative to the mean flow and the error of 3.53% was resulted when the size of the transient was 25.9% of the mean flow. This degree of error suggests that the application of the KDP method with step signals can give satisfactory results.

Chapter 7 Investigation on Unsteady Dynamic Behavior of Leaks

Flows encountered in real pipelines are seldom steady and yet knowledge regarding the unsteady behaviour of hydraulic components or pipe defects such as blockages and leaks is limited. Insufficiency of such knowledge hinders the accurate modelling of the interaction between transients and hydraulic elements or pipeline faults. The target element of this chapter is a leak. The literature review in Chapter 2 presented the past studies on orifice-based elements which suggested the possibility of them exhibiting frequency dependent effects in unsteady transient flows. This study aims to confirm the frequency dependent behaviour of leaks from the changes imposed on transient signals by a leak. The method of analysis introduced in Chapter 5 and the flow measurement technique verified in Chapter 6 are utilised in the investigations which are carried out in the time and frequency domains.

7.1 Time-domain based method for study into frequency dependent effects of leaks

The time-domain based method determines the significance of the frequency dependent effects from the dilation of pressure signals. A pressure trace measured in the laboratory pipeline shown in Figure 7.1 (a) demonstrates how the pressure pulse is progressively dilated by unsteady friction. In the figure, the time, *t'*, and the amplitude of the pressure fluctuation, *h*'*are normalised by the period of the pipeline system and the steady head at the measurement point respectively. The first and last pulses of the trace (boxed in the figure) are compared in Figure 7.1 (b) where these pulses are referred to as Pulse #1 and Pulse #17 respectively. It is observed that Pulse #17 was dilated and its width became twice as large as that of Pulse #1.

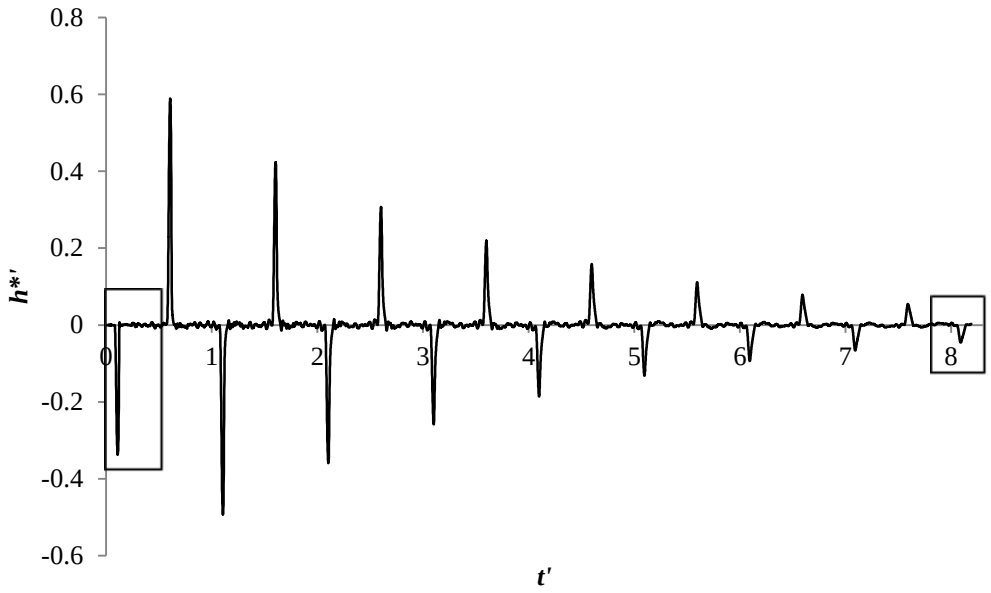

(a) Pressure trace obtained in the laboratory pipeline system

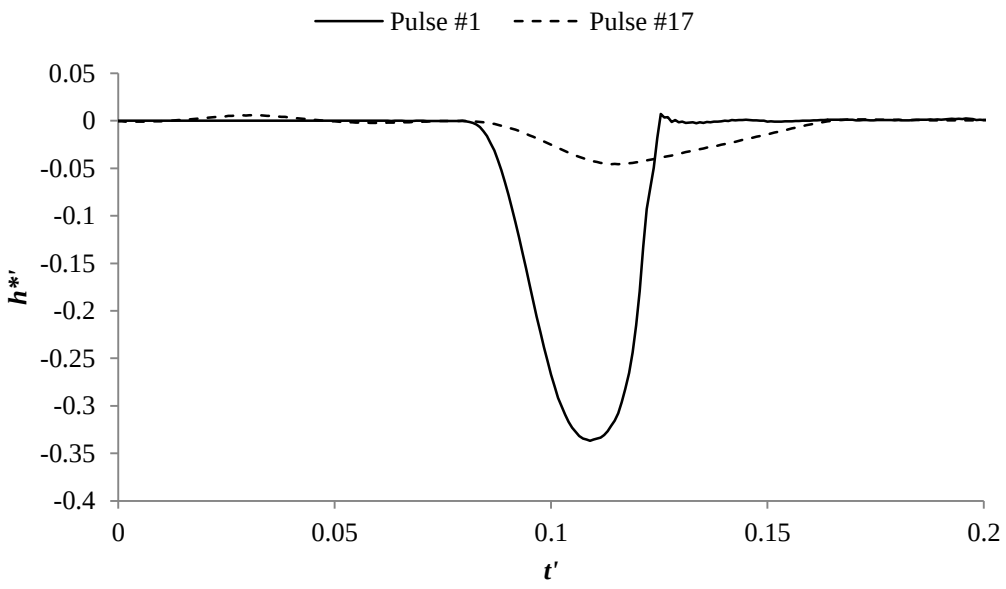

(b) Comparison between the first (Pulse #1) and last (Pulse #17) pulses in (a)

Figure 7.1 – Measured pressure response

The degree of signal dilation can be observed and quantified through comparisons with a reference signal. Such an analysis is possible via a wavelet transform which decomposes the signal by comparing it with a wavelet signal of a varying scale and position. A wavelet is an oscillating waveform of a finite length and the term ‘scale’ refers to the length of the wavelet in time (if dealing with time-domain signals) and, as the scale increases, the wavelet becomes stretched. The “Mexican Hat” wavelet signal of various scales is shown in Figure 7.2 (Fugal

2009). The Mexican Hat wavelet of scale 1 (s = 1, drawn by the grey line in Figure 7.2) is constructed from 17 data points (= 16 Δt, where Δt is the sampling period) in MATLAB. As the scale increases to 2, the wavelet is stretched to 33 data points (32 Δt). The Mexican Hat wavelet of scale 5 is depicted by 81 data points (80 Δt).

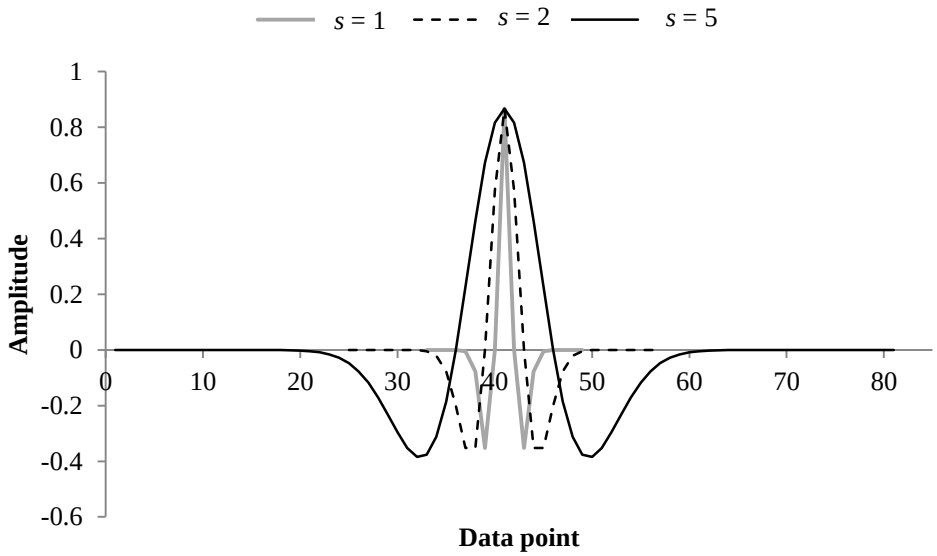

Figure 7.2 – The Mexican Hat wavelet of different scales

The wavelet signal of a certain scale is multiplied by the signal under test and the product is summed. This summed value is the wavelet coefficient which is analogous to a cross-correlation coefficient and shows the level of resemblance of a particular section of the signal to the wavelet of the particular scale. This characteristic can be used to measure the dilation of a pulse signal. When the shapes of the signal and the wavelet match, the wavelet coefficient will be its maximum. As an illustration, a numerical transient trace in Figure 7.3 (a) was transformed through a continuous wavelet transform (CWT) using a wavelet from the Coiflets family (coif1) and the result is plotted in Figure 7.3 (b). Friction effects were ignored to focus on the ability of the CWT. The scale of the wavelet ranged from 1 to 80. In Figure 7.3 (b), an increase in the wavelet coefficient with scale was observed. Figure 7.3 (c) shows the enlarged view of the top of the second pulse (boxed in Figure 7.3 b).

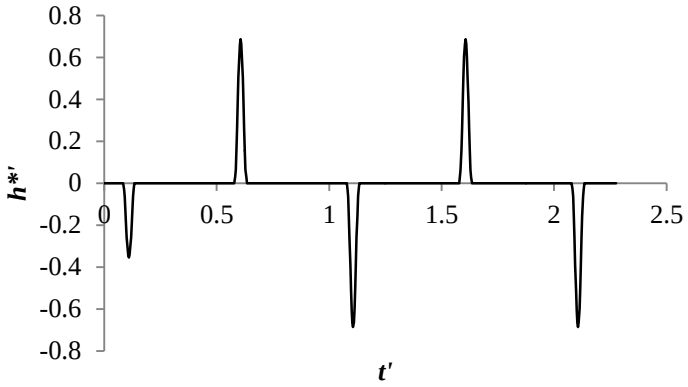

(a) Numerical pressure trace

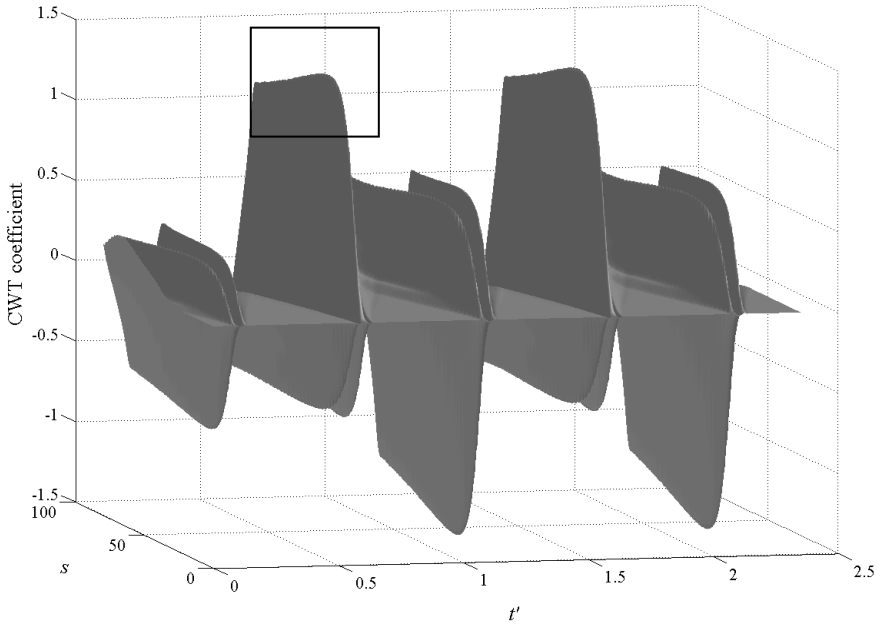

(b) 3D plot of the wavelet result

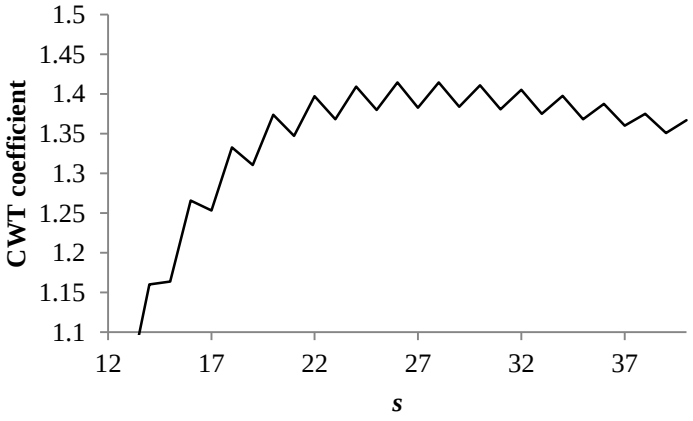

(c) Trend of the wavelet coefficient

Figure 7.3 – Illustration of the continuous wavelet transform on a numerical pressure trace

The wavelet coefficient gave an increasing trend up to the scale of 26, implying an improvement in the similarity—indicated by the wavelet coefficients—between the pulse signal and the wavelet of a particular scale. However, fluctuations in the coefficient were observed with scale due to the oscillating-nature of the wavelet signal and other pulses in Figure 7.3 (a) also gave similar results. This fluctuation creates uncertainty about the scale of best match to the signal under investigation.

As an alternative to an oscillating wavelet, the use of a truncated sinc signal was proposed in Section 5.6.4 and the method was called the multi-scale correlation analysis (MCA). This method is modified in the next section to suit the purpose of the current study.

7.2 Methodology – Multi-scale correlation analysis with normalisation term

The MCA decomposes a signal in the same manner as the CWT, but with a truncated sinc signal instead of a wavelet. The truncated sinc signal is produced by extracting the main lobe of a continuous sinc signal. The truncation process is shown in Figure 5.19 in Section 5.6.4. The sinc signal can be stretched by shrinking the time increment of the function. This is how wavelets, which possess an explicit mathematical equation, are stretched in the wavelet transform (Fugal 2009). Through the stretching, the maximum amplitude of the sinc signal remains constant. However, the effective width of the signal increases with the scale, which consequently increases the resultant correlation coefficients as observed in Figure 7.4. This figure shows the correlation coefficients, r_{yc} between the pressure trace in Figure 7.3 (a) and a set of truncated sinc signals. Unlike the CWT result in Figure 7.3 (b), the correlation coefficients in Figure 7.4 increase continuously, as indicated for the second pulse. Although this characteristic was useful in emphasizing the IRF pulses in Section 5.6.5, it is not possible to tell which sinc signal is best correlated with a particular pulse signal. To enhance the applicability of the MCA, a normalising parameter is introduced.

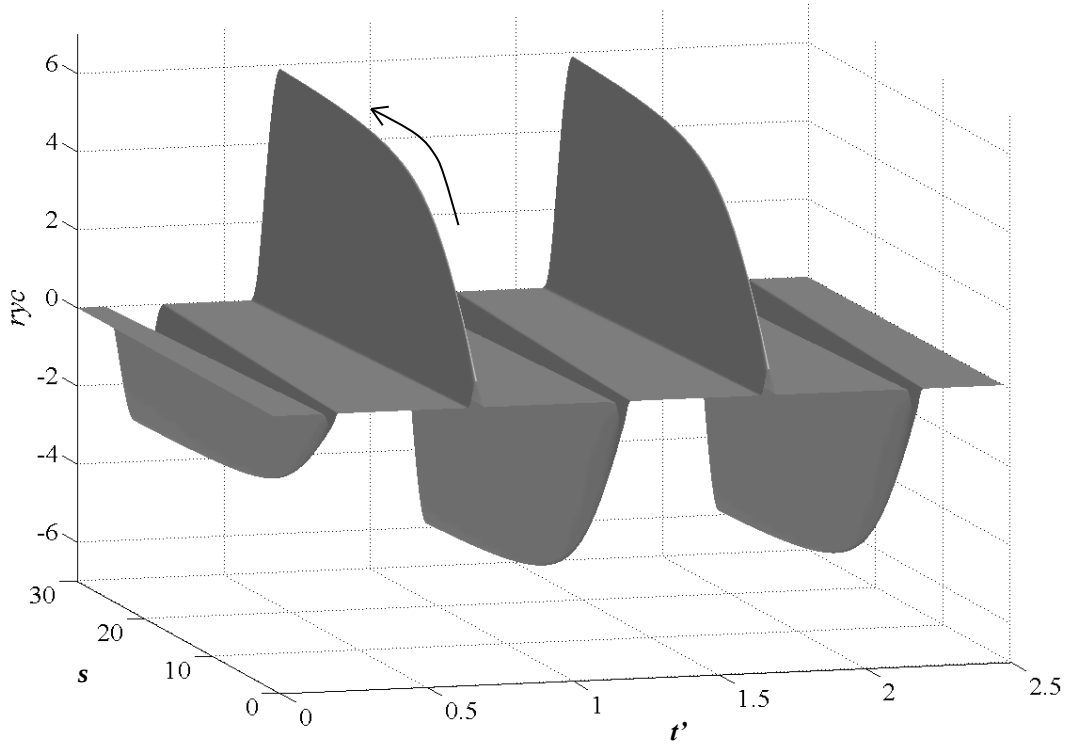

Figure 7.4 – MCA result on the pressure trace in Figure 7.3 (a)

Normalisation keeps the energy of the scaled sinc signal equal to the energy of the sinc signal of scale 1 and this allows a direct comparison of the correlation coefficients at each scale (Young 1993, Torrence and Compo 1998, Fugal 2009). The normalised correlation coefficient indicates the level of shape similarity between the signal of interest and the analysing sinc signal of a particular scale. The greatest correlation occurs with the sinc signal of the closest shape. In the CWT, the energy of the stretched wavelet increases proportionally to its scale and a similar trend is observed for the truncated sinc signal. Because of this resemblance, the same normalizing parameter as the CWT is employed in this work. The equation used in the MCA analysis is thus given by:

$$r_{yc}(s,b) = \frac{1}{\sqrt{|s|}} \int_{-\infty}^{\infty} y(t) c\left(\frac{t-b}{s}\right) dt \tag{7.1}$$

In the following analyses, the sinc signal of scale 1 has its oscillation frequency of 350 rad/s with the time increment of 0.01 seconds. The normalised sinc signals of scales 1, 2 and 3 are

shown in Figure 7.5. For each scale, the time width of a sinc signal, Δt, increases by 0.2 ms ($\Delta t' = 0.0016$, where $\Delta t' = \Delta t/T$). The normalising parameter reduces the signal amplitude as the width increases.

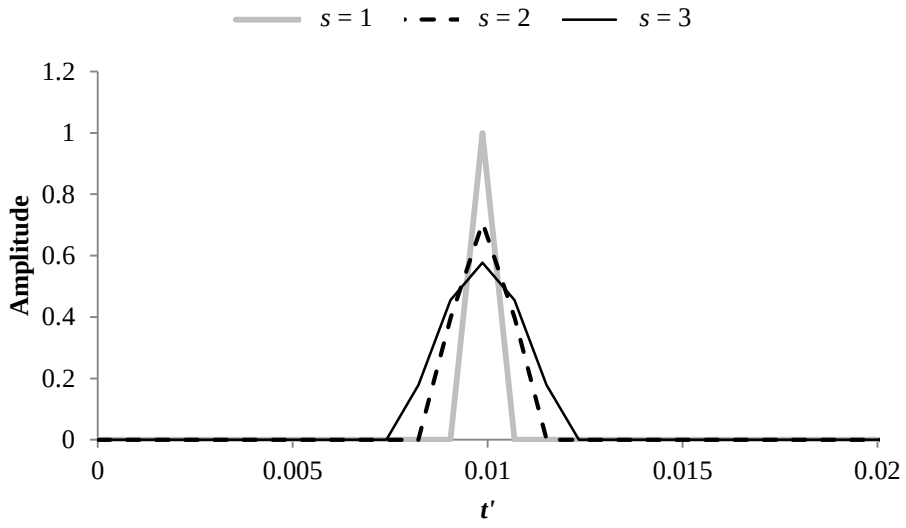

Figure 7.5 – Normalised sinc signals of scales, s = 1, 2 and 3

The pressure trace in Figure 7.3 (a) was re-analysed using Equation 7.1 and the result is presented in Figure 7.6 (a). The inclusion of the normalising term successfully produced the result that is similar to that from the wavelet transform (Figure 7.3 b). The trend of the correlation coefficient at the tip of the second pulse is shown in Figure 7.6 (b). The similarities between Figures 7.6 (a) and (b), and the wavelet results in Figures 7.3 (b) and (c) confirm the validity of the MCA for the study of signal dilation. The results from the MCA are better than those from the CWT because the fluctuation in the coefficient was removed and there is a single maximum point (marked with a circle in the figure) without ambiguity.

It is observed in Figure 7.6 (a) that the correlation coefficient, r_{yc} increased rapidly up to some point and started to decrease gradually after reaching the maximum value. The reason for this tendency can be explained by Figure 7.6 (c), where the sinc signals of three different scales are compared with the first pulse of the pressure trace in Figure 7.3 (a). The scales of the sinc signal are 1, 8 and 20 and the sinc signal of scale 8 gave the maximum correlation value according to Figure 7.6 (a). As expected, this sinc signal is a closest match to the pressure pulse (in terms of width). The sinc signals of scale 1 and 20 are examples of the poorly matched sinc signals. The signal of scale 20 gave a larger coefficient than that of scale 1, since it covers the entire width of the pulse signal and so the product of the two signals

remains moderately large after reaching its maximum value. The rapid increase in the coefficient with smaller scales was caused by the expansion of the nonzero area of the sinc signal and the consequent increase in the product.

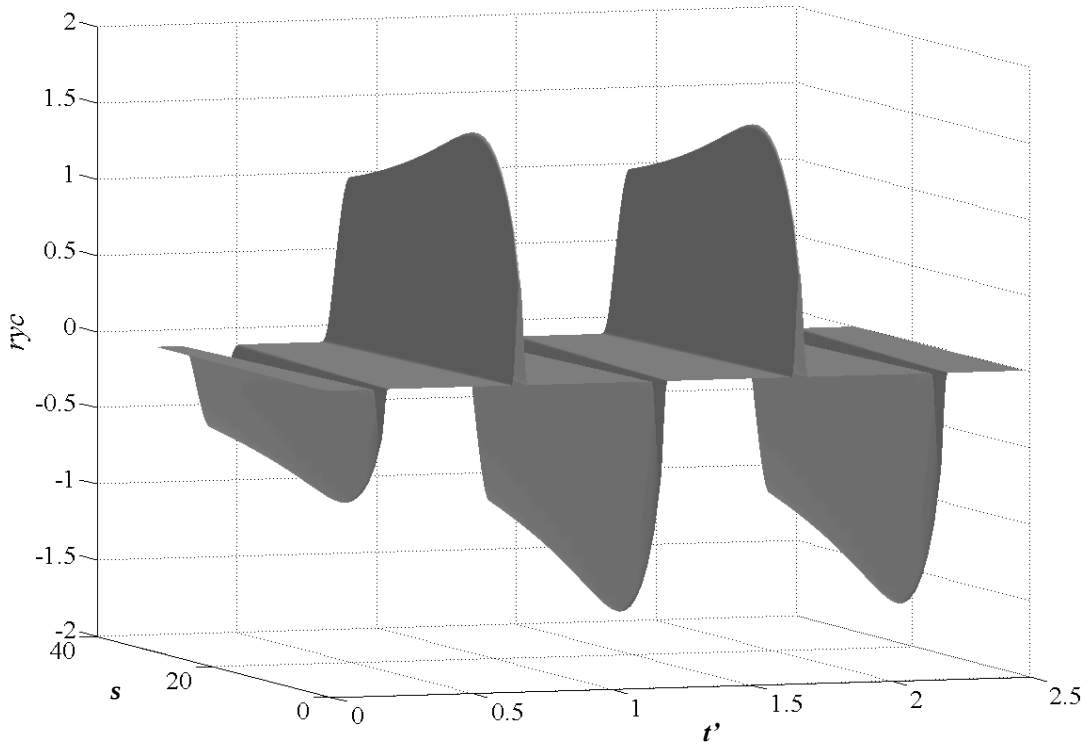

(a) 3D plot of the MCA result

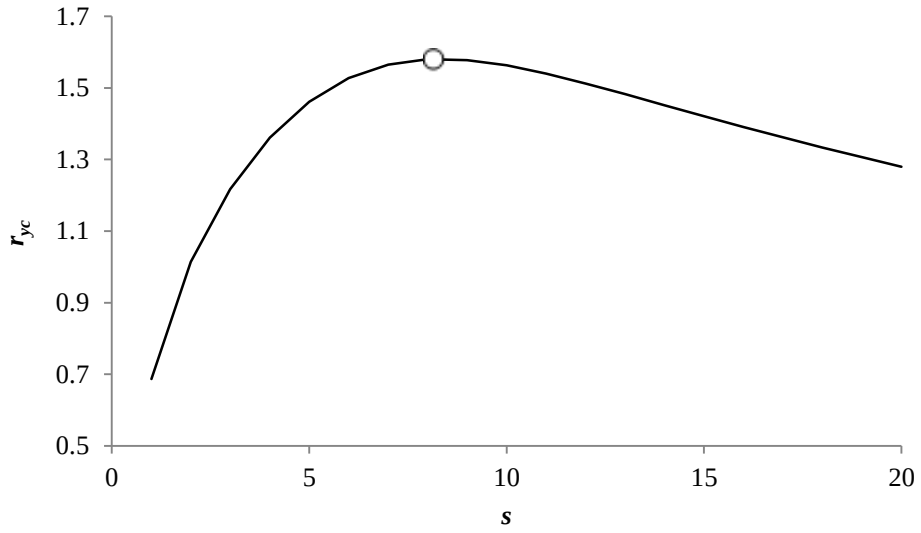

(b) Trend of the correlation coefficient for the second pulse

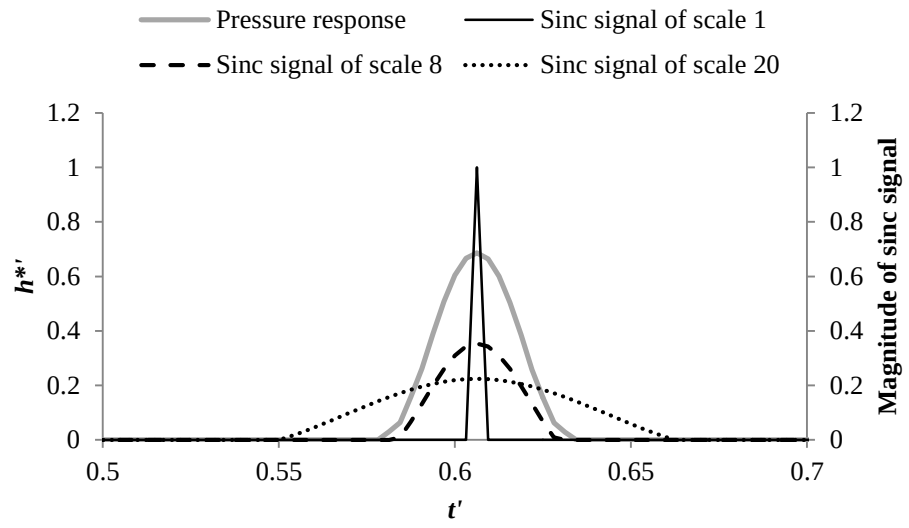

(c) Comparison between the time signal and the sinc signals of three different scales

Figure 7.6 – MCA result on the pressure trace in Figure 7.3 (a) with the normalising parameter

With the incorporation of the normalising parameter, the MCA can identify the most similar sinc signal to each pulse signal. This means that by comparing pulse signals through the sinc signal of best-match, it is possible to detect and measure the dilation of pulse signals.

7.3 Measurement of signal dilation

To illustrate the measurement of signal dilation using the MCA, unsteady friction was incorporated in the numerical simulation and the resultant pressure trace is shown in Figure 7.7. The pulses in the trace are dilated by unsteady friction and hence the scale of the best-matching sinc signal is expected to differ for these pulses. The scales of sinc signal that gave the maximum correlation coefficient for up to the 10^{th} pulse of the trace are presented in Table 7.1. The shown scales are relative to the matching scale to the first pulse of the trace. For each scale, the time width of a sinc signal increases by 1.43 ms ($\Delta t' = 0.0125$). The result without friction is also provided in the table for comparison.

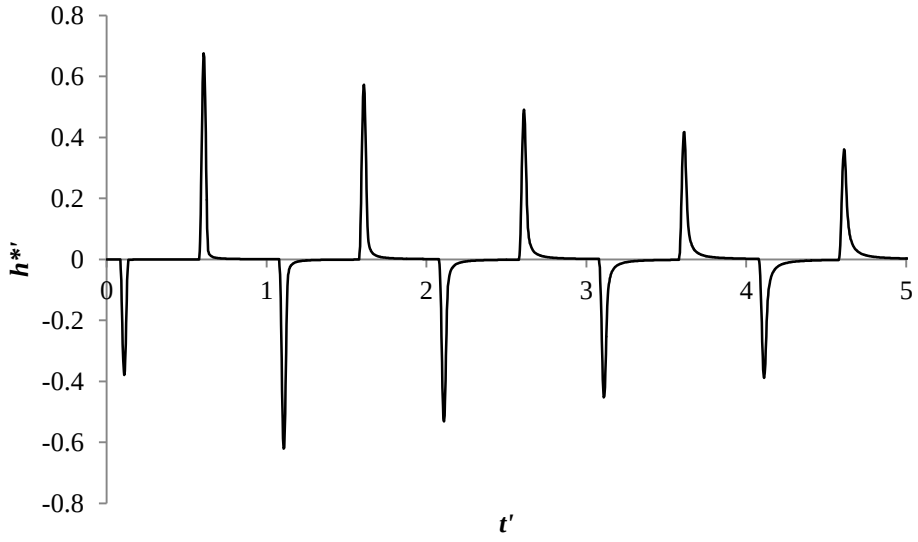

Figure 7.7 – Numerical pressure trace with unsteady friction

Pulse #	#2	#3	#4	#5	#6	#7	#8	#9	#10
No friction	0	0	0	0	0	0	0	0	0
Unsteady friction	1	1	1	1	2	2	3	3	4

Table 7.1 – Summary of MCA results (Numerical)

Without unsteady friction, the shape of the pulse remains unchanged with time and hence all the pulses gave the maximum correlation coefficient with the same sinc signal, resulting in the relative scale of zero. The unsteady friction induces the signal dilation and as a result, the pulses matched the best with the sinc signals of greater scales than that for the first pulse. By the 10^{th} pulse, the relative scale increased to 4, indicating that the width of the pulse increased by 2.86 ms ($\Delta t' = 0.025$). This example has demonstrated that the MCA captures the signal dilation and manifests it in terms of the difference in the scale of the best-matching sinc signal.

Using the MCA with Equation 7.1, the dilation effect of leaks on signals will be studied. The dilation is measured relative to the first pulse of the pressure trace. The pressure signals are acquired from intact and leaky pipeline systems whose details will be covered in the following section. Results from the fault-free intact pipeline are used as a benchmark for the analysis of leak reflections. The comparison of the results from the two systems will separate

out the dilation effect of a leak on the signal from that of the unsteady friction, thus enabling a more accurate presentation of the significance of leak effects.

7.4 Experimental setup

Pressure signals were measured in the pipeline system depicted in Figure 7.8. A transient generator and a pressure transducer were installed next to the closed downstream boundary. The injected pulse signal had the time width of 5.5 ms and the average magnitude was 10.35 m. A leak was represented by a side discharge valve located 27.06 m from the upstream boundary. The opening area of the valve was varied to create three leaks with different discharges. Each leak produced a reflected signal having the magnitude of 12% (small leak), 26% (medium leak) and 45% (large leak) of the introduced transient signal, giving a good range of leak sizes. The side discharge was fully closed to create a system with no leak. Measured pressure traces without the leak and with the smallest and the largest leaks are presented in Figure 7.9. Each pressure response is an average trace of 30 datasets. This averaging process reduces the noise in the measurements and reveals the useful information of the traces. The first leak reflection in each trace is circled in Figures 7.9 (b) and (c).

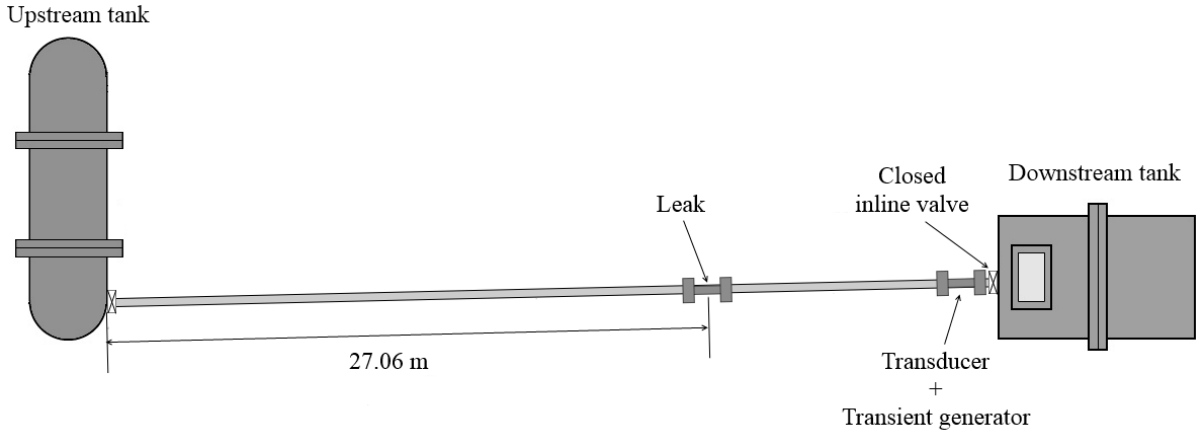

Figure 7.8 – Test setup

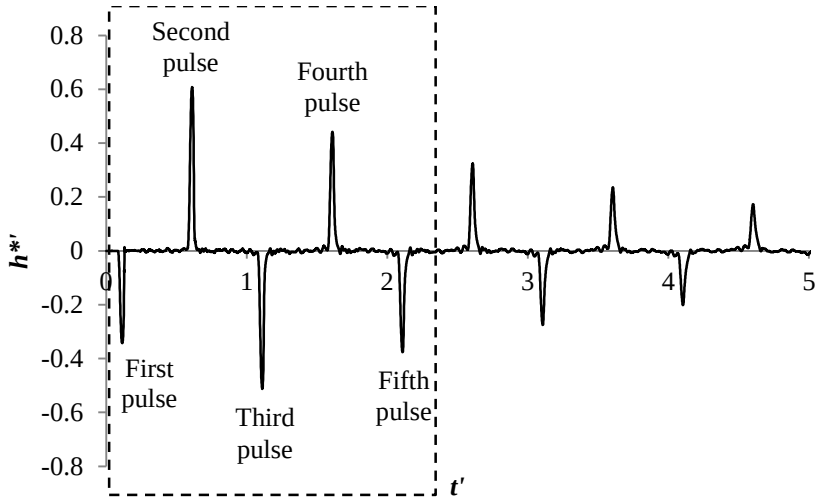

(a) Averaged pressure trace without leak

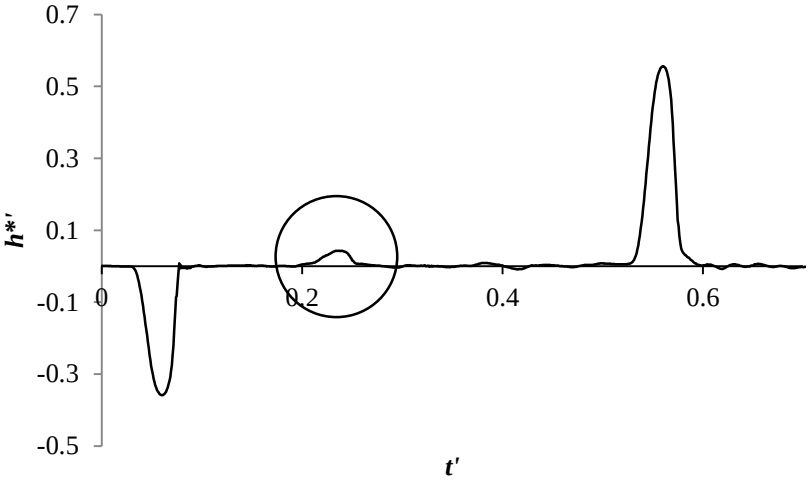

(b) Averaged pressure trace with the smallest leak

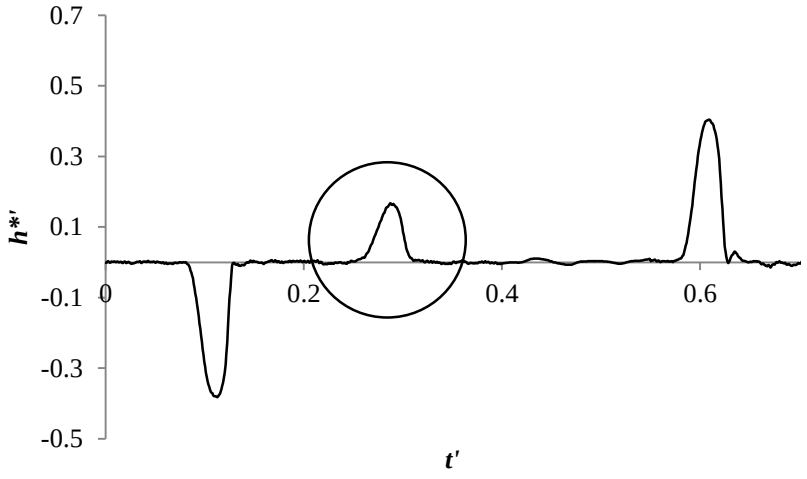

(c) Averaged pressure trace with the largest leak

Figure 7.9 – Measured pressure traces with and without leak

7.4.1 Base-line calibration

A pressure trace starts to oscillate at the fundamental frequency of the system about the base pressure as time progresses. Figure 7.10 (a) shows the later part of the pressure trace in Figure 7.9 (a) with the grey line. The black line in the figure indicates the apparent base line oscillation. The pressure pulses are superimposed onto this oscillating base line and hence the shape of the pulse is distorted from the correct form. This distortion affects the MCA results as will be discussed in the subsequent section, and thus it is important to calibrate the base line of the pressure trace prior to the analysis. The calibration process involves a subtraction of the base line oscillation (black line in Figure 7.10 a) from the measured pressure trace. The resultant pressure trace is compared to the original trace in Figure 7.10 (b). The calibration process removed the oscillation and the base of the pressure pulses is at zero as shown by the broken line in the figure.

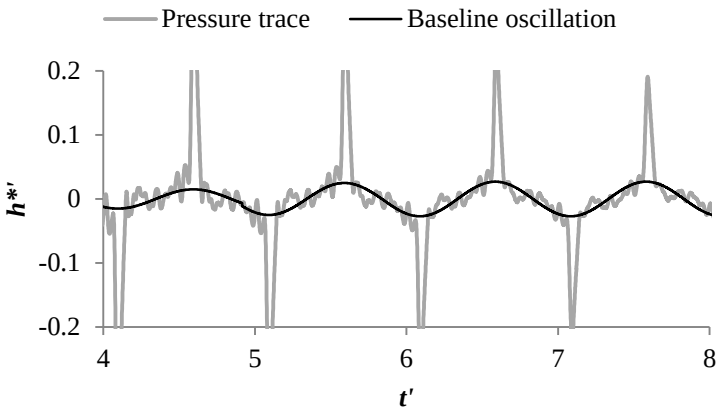

(a) Measured pressure trace and the observed base line oscillation

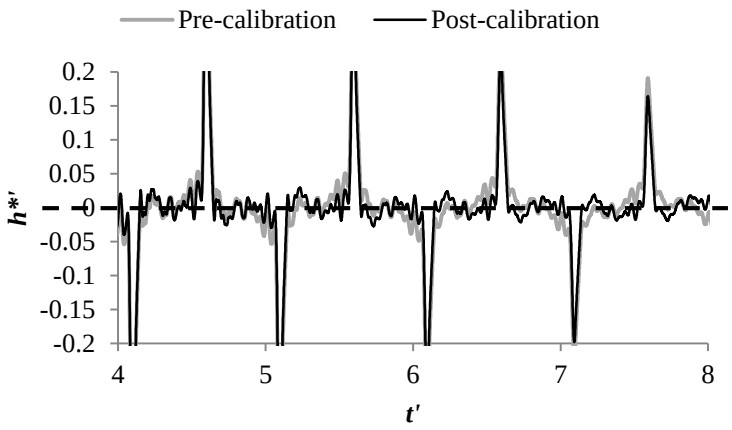

(b) Comparison of the pressure traces before and after the calibration process

Figure 7.10 – Illustration of the base-line calibration

This calibration process is implemented also on the pressure response with leak. The magnitude of the largest leak reflection considered in this study is comparable to that of the 10th pulse in Figure 7.9 (a) and the influence of the base-line oscillation can be considerable as will be illustrated in the next section. The traces from the leaky system are calibrated using the same method.

7.5 Results and discussions

The MCA result of the fault-free trace is given in Figure 7.11 which shows the development of the signal dilation over a period of time. The x-axis is the pulse number as indicated in Figure 7.9 (a). The scale on the y-axis is relative to the matching scale to the first pulse. These results show that the signal was dilated at almost a constant rate up to the 13th pulse, but the rate of dilation slowed down near the end of the measurement. This trend indicates the signal has lost most of its high frequency content by this time. As the high frequency content of a signal characterises its profile, the signal will look similar in the later periods after losing most of its high frequency components. Between the first and second pulses, the scale of the sinc signal increased by 1, indicating that the time width of the pulse increased by 0.2 ms which corresponds to 3.6% of the original signal width. This result will be used as a reference for the subsequent study with leaks.

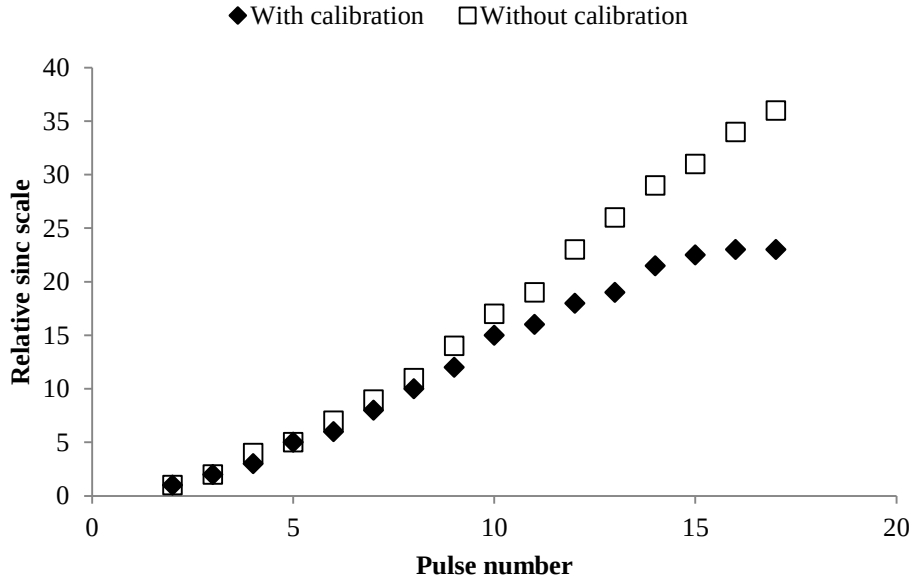

Figure 7.11 – Development of signal dilation with pulse number

Figure 7.11 also shows the MCA result of the same pressure trace, but without the base-line calibration. The significance of this process becomes apparent from the 10th pulse onward. The difference in the two MCA results increases with time as the magnitude of the signal attenuates and the relative weight of the base-line oscillation on the signal grows. By the 17th pulse, the difference in the relative scale increases to 13.

7.5.1 Dilation of leak reflections

The dilation of the first leak reflection was measured relative to the first signal and the results are shown in Figure 7.12. The correlation coefficients were normalised by the maximum coefficient value obtained with each pulse in order to cancel out the dependence of the coefficient on the magnitude of test signals. The circle in the figure indicates the scale of the sinc signal that gave the greatest correlation coefficient. The maximum correlation coefficients for the three leak reflections were observed with the same sinc signal, which also matched the best with the first signal. The previous analysis with the fault-free system showed that a signal was dilated by 3.6% of the original signal width after traveling a distance of 2L. A leak reflection travels less than half of that distance before it is measured and hence unsteady friction is expected to only cause minor dilation on the reflected signal during its travel. Therefore the observed results imply that unsteady leak effects are not significant and the degree of influence is considered less than 3.6% of the signal width.

To further confirm the results in Figure 7.12, Figure 7.13 presents the comparison between the leak reflections and the first pulse signal in the time domain. The leak reflections were shifted along the time axis so that they aligned with the first signal. The similarity in the time width of each leak reflection was found in the figure and it was also comparable to the time width of the first signal. Such observations are consistent with the MCA results in Figure 7.12. These outcomes suggest that the leak does not impose significant frequency dependent changes on pressure responses in terms of signal dilation.

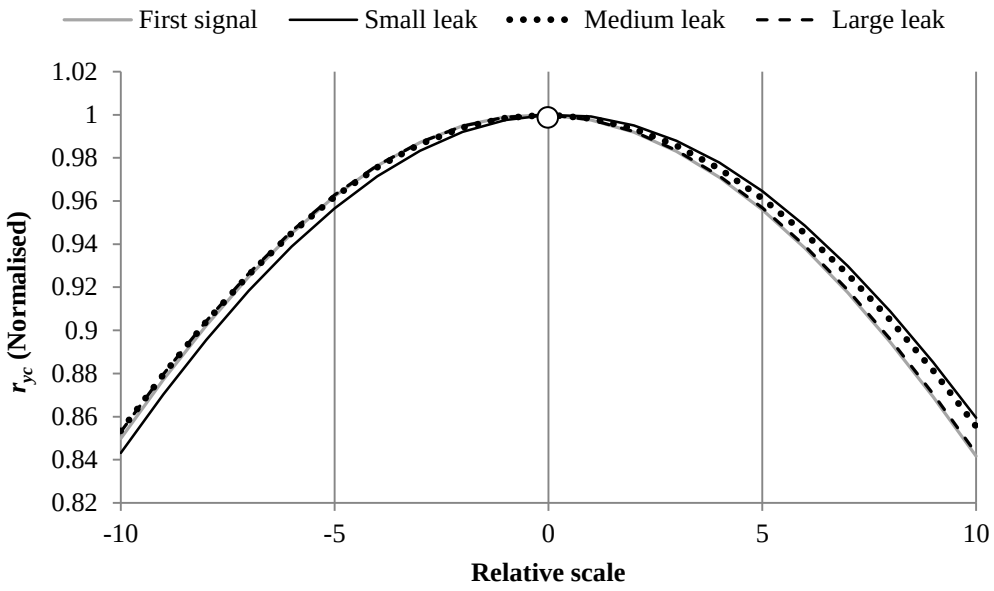

Figure 7.12 – Normalised MCA results on the average pressure traces with three leak sizes

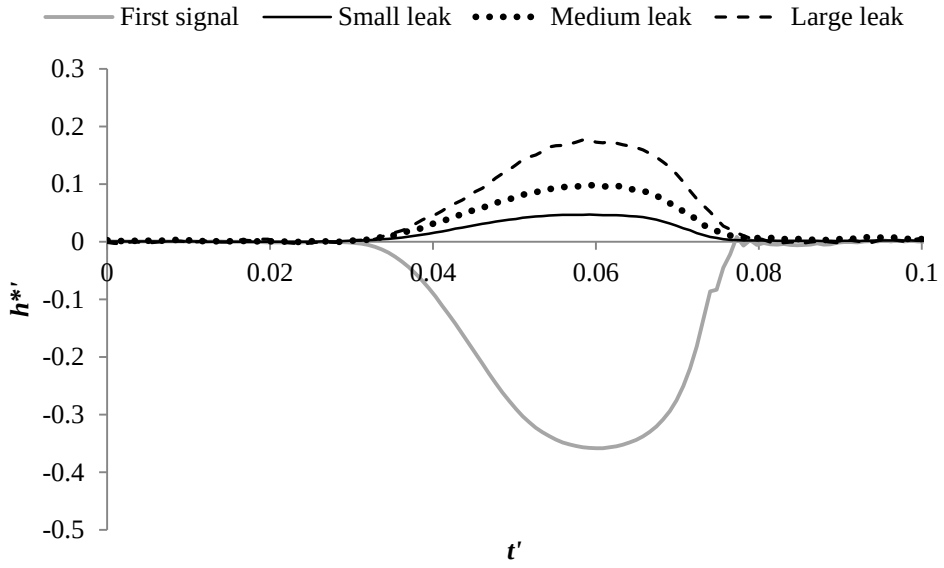

Figure 7.13 – Comparison between the leak reflections and the first signal in the time domain

While it would be possible to inspect the dilation of the signal via comparisons in the time domain as shown in Figure 7.13, the MCA provides a more convenient and systematic inspection and quantification of the signal dilation. Visual inspection of the signal dilation requires the judgment of the signal width. However, it is often difficult to identify the ends of the signal, especially after the signal has been dilated, and so the judgment regarding the signal width may not be consistent across the individual pulse signals and may lead to

inaccurate results. Such inconsistency will not arise with the MCA. An ability to capture the evolution of changes from the raw pressure trace as demonstrated in Figure 7.11 is another advantage of the MCA over the visual inspection.

This study has investigated the dynamic behaviour of leak in the time domain. The difficulty with such investigations in the time domain is defining a parameter which can quantify the profile of the signal. This study used a normalised correlation coefficient as an indicator of the frequency dependent changes on the pressure responses. The next section presents a more detailed analysis of the dynamic behaviour associated with leaks that will be carried out in the frequency domain using system response concept. The frequency-domain technique is able to investigate the influence of leaks on newly flow responses.

7.6 Frequency-domain based method for study into frequency dependent effect of leak

A system response function is a mathematical model which describes the characteristics of a system (Romagnoli and Palazoglu 2006, Brandt 2011, Feng *et al*. 2011). In Chapter 5, two forms of system response functions were introduced; an impulse response function (IRF) and a frequency response function (FRF). They are system response functions in the time and the frequency domains respectively. A system response function can be determined from measured input and output signals and the required mathematical manipulations for its extraction are simpler in the frequency domain. Assuming a system of interest produces a single output signal from a single input signal as shown in Figure 7.14, its FRF ($F(f)$) is given by the ratio of the output to the input in the frequency domain, denoted as $Y(f)$ and $U(f)$ in the figure respectively (Lynn 1982, Ljung 1999, Romagnoli and Palazoglu 2006, Brandt 2011). Mathematically it is written as:

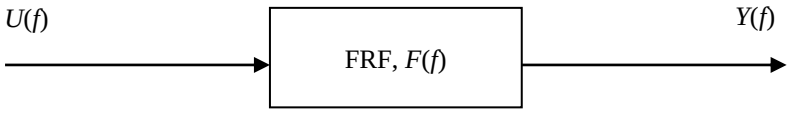

Figure 7.14 – System involving a single input and a single output

$$F(f) = \frac{Y(f)}{U(f)} \tag{7.2}$$

The FRF describes the behaviour of a system having one input and one output and such a system is known as a single-input-single-output (SISO) system. However, in general, many systems in the field of hydraulics, structures and acoustics have multiple inputs and multiple outputs (MIMO). In MIMO systems, each output is produced by a linear combination of all the inputs. For a system having two inputs (U_1 and U_2) and two outputs (Y_1 and Y_2), for example, the input-output relationships can be written as:

$$Y_1 = F_{11} \times U_1 + F_{12} \times U_2 \tag{7.3}$$

$$Y_2 = F_{21} \times U_1 + F_{22} \times U_2 \tag{7.4}$$

The notation of '(f)' has been dropped for simplicity. F_{ij} in the equations is a FRF describing the relationship between the jth input and the ith output. A graphical representation of Equations 7.3 and 7.4 is shown in Figure 7.15.

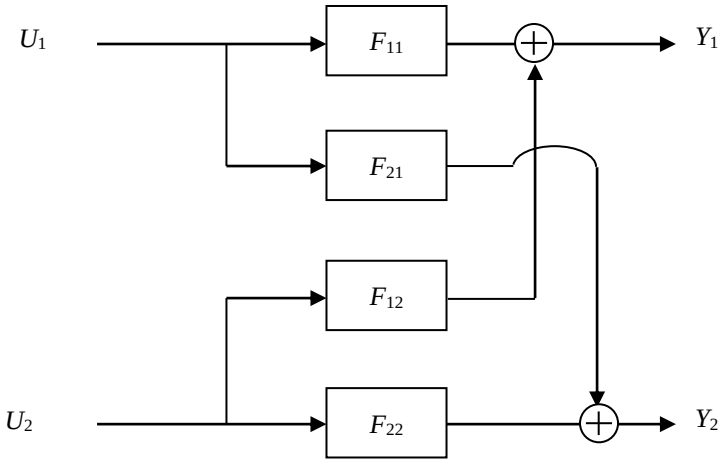

Figure 7.15 – Block diagram of a two-input-two-output system

Any of the FRFs (F_{ij}) in the figure may be zero, in which case the input, U_j, does not have an effect on the output, Y_i. Equations 7.3 and 7.4 can be rewritten using matrix notation as:

$$\begin{bmatrix} Y_1 \\ Y_2 \end{bmatrix} = \begin{bmatrix} F_{11} & F_{12} \\ F_{21} & F_{22} \end{bmatrix} \begin{bmatrix} U_1 \\ U_2 \end{bmatrix} \tag{7.5}$$

The matrix in Equation 7.5 will be referred to as a *frequency response matrix* (FRM) in this work. This is analogous to a transfer function matrix which is a FRM expressed in the Laplace domain (Pota 1996, Romagnoli and Palazoglu 2006, Fadali and Visioli 2009).

The FRM of Equation 7.5 can be extracted from measured inputs and outputs in the similar manner to Equation 7.2, which can be extended for the FRM as follows (Romagnoli and Palazoglu 2006, Bendat and Piersol 2010, Brandt 2011):

$$[F] = [G_{yu}][G_{uu}]^{-1} \tag{7.6}$$

in which $[F]$ is a frequency response matrix with dimension (2,2), $[G_{yu}]$ is a cross-spectral matrix between the input and output with dimension (2,2) and $[G_{uu}]$ is a input cross-spectral matrix with dimension (2,2) for a two-input-two-output system. In general, for a system involving m inputs and n outputs, the FRM would be a n-by-m matrix. Equation 7.6 must be solved for each frequency of interest and it is valid provided that an inverse of $[G_{uu}]$ exists. Since matrix inversion is computationally inefficient, alternative methods for determination of the FRM have been proposed in the literature and they are reviewed in the following section.

7.7 Methods for the identification of frequency response matrix

A FRM can be determined analytically, numerically or experimentally. However, analytical methods are only applicable to systems with simple geometries such as ducts and expansion chambers (Boij and Nilsson 2003, 2006, Kooijman *et al*. 2008) and only numerical or experimental techniques are appropriate for more general systems.

7.7.1 Numerical approaches

A numerical technique that can deal with systems with complex geometries and flows, based on Computational Fluid Dynamics (CFD), was proposed in Polifke *et al*. (2001) and it has been utilised in other papers (Föller and Polifke 2010, 2012, Lacombe *et al*. 2013). The method couples numerical transient simulations by CFD and a post-processing of the simulation data by system identification tools to determine the FRM. Various elements such as cylindrical backward-facing steps, sudden area expansions, T-junctions and cylindrical orifices have been analysed by the method (Föller *et al*. 2010, Lacombe *et al*. 2013). Comparisons with the experimental data generally show good agreement for these pipe elements. However, the use of CFD dictates that end users must make decisions on various

factors that affect the accuracy of simulations. These factors include, for example, the inclusion of physical phenomena, existing flow characteristics, appropriate mathematical models and discretization of the simulations (Versteeg and Malalasekera 2007). In addition, while this technique is less computationally expensive than solving the full set of the Navier-Stokes equations, since only a single flow simulation is required for the FRM extraction, it was noted in Foller and Polifke (2010) that the determination of the FRM by this method still takes a few days. Other numerical approaches also exist but all of them are based on the Navier-Stokes equations with different levels of approximations (Bailly and Juve 2000, Rao and Morris 2006, Kierkegaard *et al*. 2010, 2012). The use of simpler versions of the governing equations is less computationally demanding and has been shown to work in certain systems, but the appropriate level of simplification must be selected depending on the system of interest. Experimental approaches described next allow a fast FRM extraction without making any assumptions about the unknown system except its linearity and they have the capability to handle systems with simple or complex geometries (To and Doige 1979a, b, Munjal 1987).

7.7.2 Experimental approaches

It is known that when an unknown system is connected in series with two other systems of known properties (reference systems) as depicted in Figure 7.16, the FRM of the unknown system can be estimated from the FRMs of the reference systems and the Fourier-transformed responses measured at four locations, two on each side of the unknown system (Lung and Doige 1983, Kojima and Edge 1994).

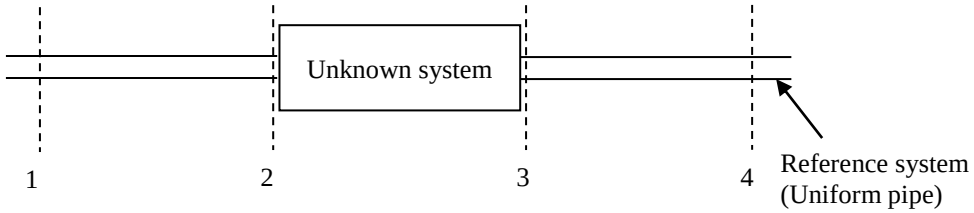

Figure 7.16 – Test section with reference system connected in series

To and Doige (1979a) derived expressions for the FRM of expansion chambers with and without insertion pipes and chambers with a partition (orifice plate within the chamber). In the derivation, the exact geometry of these systems was assumed to be known a priori. For systems of unknown geometry, an experimental technique was also presented. In all these

cases, the system of interest was assumed to be connected in series with identical reference systems (uniform pipe sections). The proposed methods enabled the FRM extraction solely from measured transient pressures. The flow variables were either set to zero by blocking the measurement station or replaced by multiple pressure measurements. Systems with and without the base flow were considered, but only the cases with a stationary medium were tested experimentally. The experimentally determined FRM of a uniform pipe section and the large expansion chamber exhibited some noise at lower frequencies (< 300 Hz), but a good match between the theoretical and experimental FRMs was observed for the frequency range greater than 300 Hz with the discrepancy of less than 1%.

While the method proposed by To and Doige (1979a, b) was verified experimentally, the assumptions made in the derivation of the given formulae and the tested system conditions did not promote the method for more general cases. Lung and Doige (1983) made some modifications to this method to consider systems with a substantial base flow. The revised test setup is given in Figure 7.17 in which, compared to Figure 7.16, an extension pipe of known FRM is added either side of the unknown system. The proposed formulation removed the assumption of the identical reference systems and it was tested experimentally with mufflers, variable area ducts and complex pipe networks. The experimental results presented were in close agreement to the theoretical FRMs, showing the feasibility of the proposed technique for a broad range of systems. The inclusion of the extension pipe enabled the measurement sensors to be kept away from possible disturbances occurring in the vicinity of the unknown system. However, a shortcoming of this approach is that the extracted FRM from the measured pressures is a combination of the FRMs of the extension pipes and the unknown systems. Determination of the FRM of the unknown system therefore involves matrix inversion which adds computational inefficiency to the overall process.

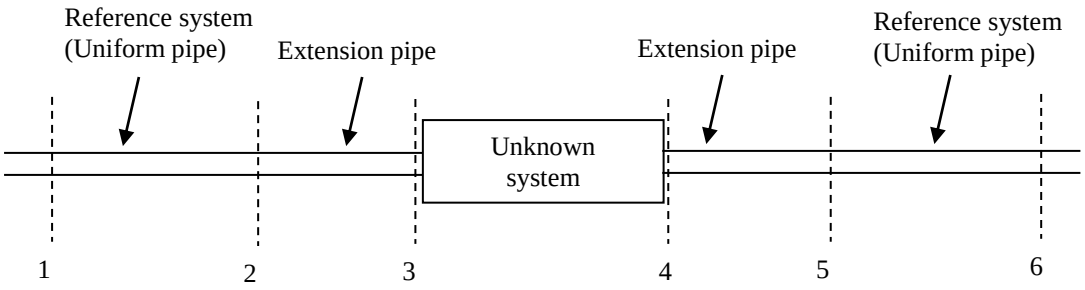

Figure 7.17 – Modified test section with extension pipes

As an alternative, expressions which directly determine a FRM were derived and they have been used extensively to analyse systems in the fields of (aero-) acoustics, hydraulics and automotive industry (Stirnemann *et al*. 1987, Johnston *et al*. 1994, Kojima and Edge 1994, Song and Bolton 2000, Bonfiglio *et al*. 2005 Earnhart *et al*. 2010, Hua and Herrin 2013, Rousselet *et al*. 2013). The new equations are formulated with the pressure and flow variables at the boundaries of the testing system and are presented below.

7.7.3 Equations for identification of frequency response matrix

Let a system to be investigated be a uniform pipe section of length l as shown in Figure 7.18. The input and output variables are measured at the stations 3 ($x = x$) and 4 ($x = x+l$) respectively.

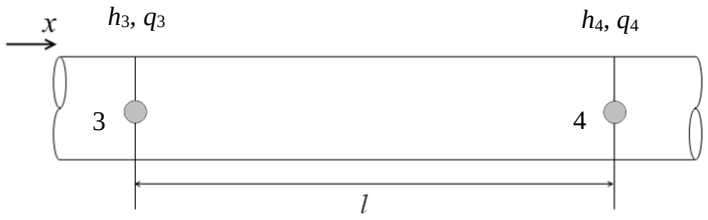

Figure 7.18 – Uniform pipe section with measurement points

As derived in the previous section, the input and output variables to and from a system are related by the FRM of the system as follows:

$$\begin{bmatrix} q_4 \\ h_4 \end{bmatrix} = \begin{bmatrix} F_{11} & F_{12} \\ F_{21} & F_{22} \end{bmatrix} \begin{bmatrix} q_3 \\ h_3 \end{bmatrix} \tag{7.7}$$

in which the subscript of 3 denotes the input variables and 4 is for the output variables (see Figure 7.18). This matrix equation forms two equations containing four unknowns, F_{11} through to F_{22}. In order to solve for these FRFs, four simultaneous equations are required and hence two independent sets of measurements must be obtained. Expressing the pressure and flow measured in the second test as *h'* and *q'*, the matrix equation for the second set of measurements is given as:

$$\begin{bmatrix} q_4' \\ h_4' \end{bmatrix} = \begin{bmatrix} H_{11} & H_{12} \\ H_{21} & H_{22} \end{bmatrix} \begin{bmatrix} q_3' \\ h_3' \end{bmatrix} \tag{7.8}$$

Since both tests are conducted in the same system, the FRM remains the same as in the first test. From Equations 7.7 and 7.8, the following equations are formed:

$$q_4 = F_{11} \times q_3 + F_{12} \times h_3 \tag{7.9}$$

$$h_4 = F_{21} \times q_3 + F_{22} \times h_3$$

$$q_4' = F_{11} \times q_3' + H_{12} \times h_3' \tag{7.10}$$

$$h_4' = F_{21} \times q_3' + F_{22} \times h_3'$$

Rearranging Equation 7.10 for F_{12}:

$$F_{12} = \frac{q_3' - F_{11} * q_3'}{h_3'} \tag{7.11}$$

Substituting Equation 7.11 into Equation 7.9 and further manipulation gives:

$$F_{11} = \frac{\frac{q_4}{h_3} - \frac{q_4'}{h_3'}}{\frac{q_3}{h_3} - \frac{q_3'}{h_3'}} \tag{7.12a}$$

Similarly:

$$F_{12} = \frac{\frac{q_4}{q_3} - \frac{q_4'}{q_3'}}{\frac{h_3}{q_3} - \frac{h_3'}{q_3'}} \tag{7.12b}$$

$$F_{21} = \frac{\frac{h_4}{h_3} - \frac{h_4'}{h_3'}}{\frac{q_3}{h_3} - \frac{q_3'}{h_3'}} \tag{7.12c}$$

$$F_{22} = \frac{\frac{h_4}{q_3} - \frac{h_4'}{q_3'}}{\frac{h_3}{q_3} - \frac{h_3'}{q_3'}} \tag{7.12d}$$

All the FRFs are now expressed as functions of the pressure and flow responses at the boundaries of the system under test. Equation 7.12 is valid for systems which can be described by a 2-by-2 FRM.

Commonly the pressure and flow responses at the system boundaries are determined indirectly from the pressures measured at stations 1, 2, 5 and 6 in Figure 7.19 and the known characteristics of the reference systems (Lung and Doige 1983, Munjal 1987, Johnston *et al*. 1994, Kojima and Edge. 1994). This is because the flow response is difficult to measure directly and, for certain systems, it is not possible or desirable to measure the pressures in the vicinity of the system boundaries. For example, the flow response at point 3 (q_3) can be obtained from the pressure responses at point 1 and 2 (h_1 and h_2) and the FRMs of the reference system and the extension pipe (ε and γ in Figure 7.19) via the KDP method described in Chapter 6. The pressure response at point 3 (h_3) can also be determined from the same set of pressures. In Figure 7.19, steps for determining the pressure and flow responses at point 3 are summarised.

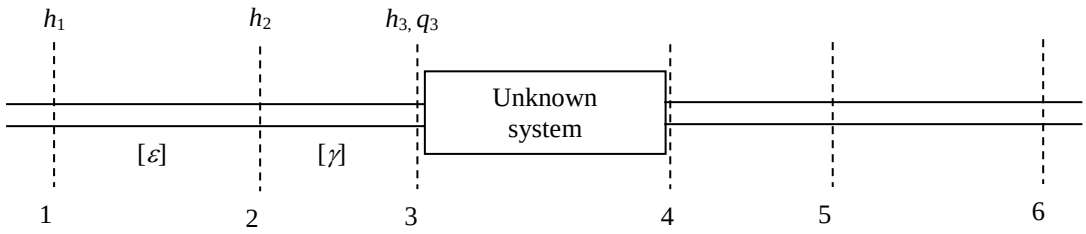

Step 1: Determine the flow response at point 2, q_2 from the measured pressure responses at points 1 and 2 (h_1 and h_2) and the known FRM, ε

Step 2: Determine the pressure and flow responses at point 3 (h_3 and q_3) from the measured pressure and flow response at point 2 (h_2 and q_2) in Step 1 and the known FRM, γ

Figure 7.19 – Process of obtaining the responses at the system boundary from the measured responses and the known FRMs

As mentioned earlier, the determination of the FRM from Equation 7.12 requires two sets of measurements which are independent of each other. The two commonly used methods to create such data sets are the two-load and two-source methods. In the two-load method, tests are conducted with two different terminal impedances (Z_a and Z_b) with the transient source located on one side of the test component as shown in Figure 7.20 (a). The two-load method has been used in several studies (To and Doige 1979a, b, Lung and Doige 1983, Kojima and Edge 1994, Hua and Herrin 2013, Rousselet *et al*. 2013). The key condition for successful identification with this method is to create a sufficient change in the termination impedances. The standard of this method (ASTM E2611-09) suggests using an absorptive load which produces minimum reflection on one end of the system and place either the open or closed end on the other system boundary which is expected to give significant reflections. However, as pointed out by some researchers (Munjal and Doige 1990, Åbom 1991, Johnston *et al*. 1994), creating such different loads may be difficult in some systems.

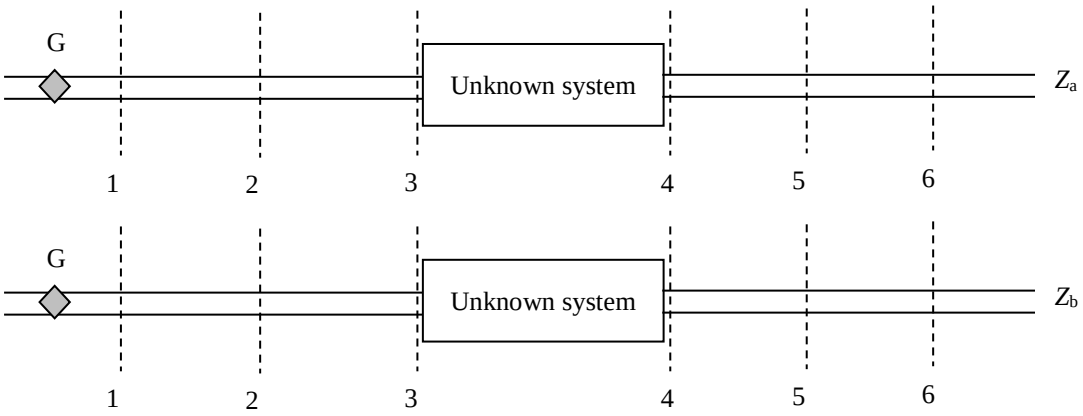

(a) Two-load method

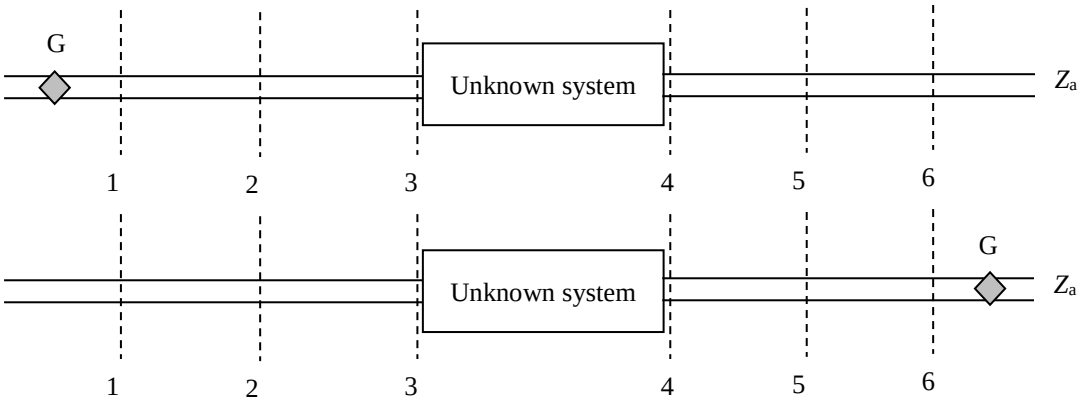

(b) Two-source method

Figure 7.20 – Two methods for creating two test conditions

The two-load method would fail if the impedance of one load approaches the other. In contrast, the two-source method works with any combination of terminal impedances and is a good alternative to the two-load method. This method places the generator on either side of the test component as shown in Figure 7.20 (b). It was shown experimentally that the two-source method was superior to the two-load method and it has been utilised in numerous studies in the past (Stirnemann *et al*. 1987, Munjal and Doige 1990, Åbom 1991, Johnston *et al*. 1994, Pedrosa *et al*. 2011, Hu *et al*. 2012). As it is difficult to have two significantly different loads in pressurised pipelines, the present study uses the two-source method to create two independent sets of measurements. Note that Equation 7.12 holds for the two-source method as well as the two-load method since the extraction of FRM is independent of the methods to create the two test conditions (Munjal and Doige 1990). The numerical verification of the two-source method and Equation 7.12 will be presented in the next section.

7.8 Numerical example of identification of frequency response matrix

The validity of Equation 7.12 is demonstrated using responses from the numerical pipeline system. Hydraulic components considered in the following examples are a pipe section, a reference point in a pipeline and a leak. In these examples, it is assumed that the pressure and flow responses at the system boundaries are directly available. While the flow responses will be determined by the KDP method in the subsequent experimental study, the accuracy of the KDP method has already been demonstrated in Chapter 6 and hence these numerical examples focus on errors in the FRM extraction method (Equation 7.12).

7.8.1 Pipe section

The theoretical FRM of a pipe of length l is given in Equation 7.13:

$$[F]_{pipesection} = \begin{bmatrix} \cosh(\mu l) & -\frac{1}{Z_C}\sinh(\mu l) \\ -Z_C \sinh(\mu l) & \cosh(\mu l) \end{bmatrix} \tag{7.13}$$

The derivation of Equation 7.13 is found in Chapter 3. The FRM of this type is known as a field matrix (Chaudhry 1987) and it describes the relationship between the head and flow at

the boundaries of the chosen pipe section as shown in Figure 7.21 (a). The pipe section is bounded by broken lines in the figure. For illustrative purposes, unsteady friction effects are neglected. The measurement points 1 and 2 were 700 m and 900 m from the upstream end and hence the length of the pipe section was 200 m. The two sets of data were obtained by the two-source method. The locations of the generator were 600 m and 1000 m from the upstream boundary. In each test, the generator produced an impulse signal having the magnitude of 1% of the steady base flow of the system. Examples of the measured head and flow responses at the 700-m point are shown in Figures 7.21 (b) and (c). The head and flow are non-dimensionalised by the steady head at the measurement point and the initial steady flow respectively. For the extraction of the FRM, only the first pulse signal of measured traces was used (as boxed in Figures 7.21 b and c). The measured responses were fast Fourier-transformed and the FRM of the pipe section was determined from Equation 7.12. The magnitude and phase of the extracted FRM are presented in Figure 7.22. The frequency on the x-axis is normalized by the fundamental frequency of the system. In the figure, the theoretical FRM is also plotted for comparison. The magnitude of FRM is in the form of a hyperbolic cosine or a hyperbolic sine which oscillates at the frequency related to the length of the pipe section and the wave speed. The results showed an excellent match between the theoretical and the extracted FRMs.

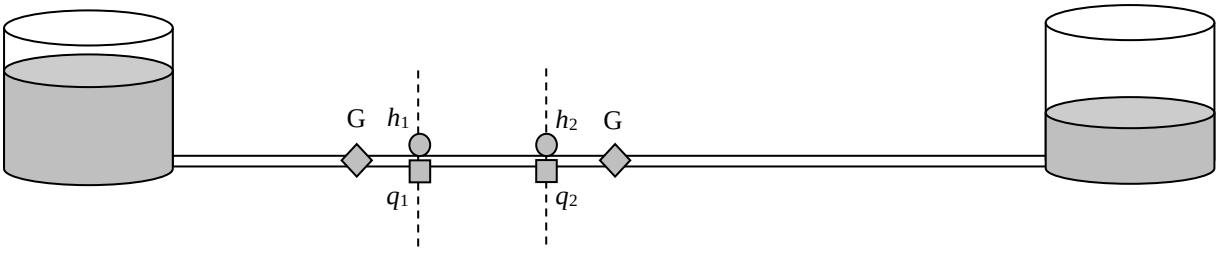

(a) Test setup

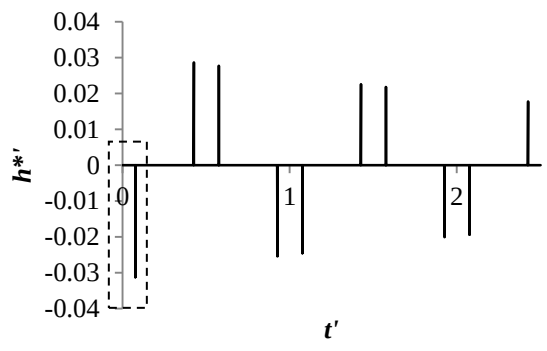

(b) Pressure response, h_1*

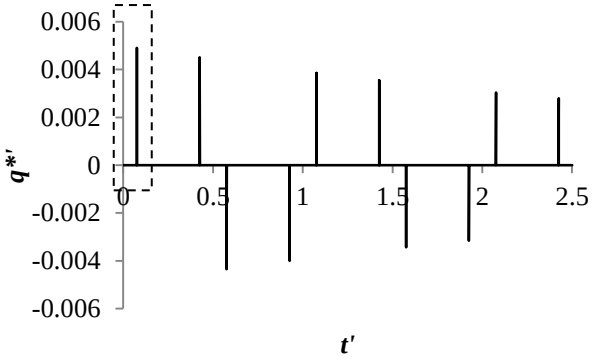

(c) Flow response, q_1*

Figure 7.21 – Test configuration and measured pressure and flow responses

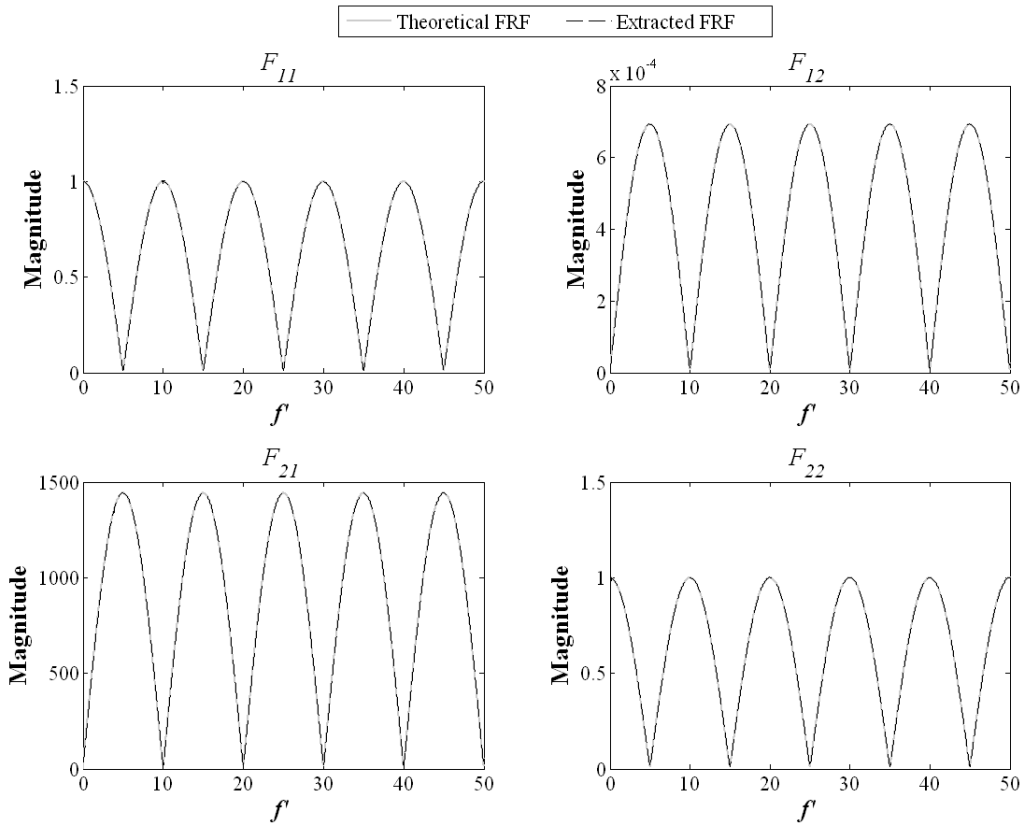

(a) Theoretical and extracted magnitudes of FRM of a pipe section

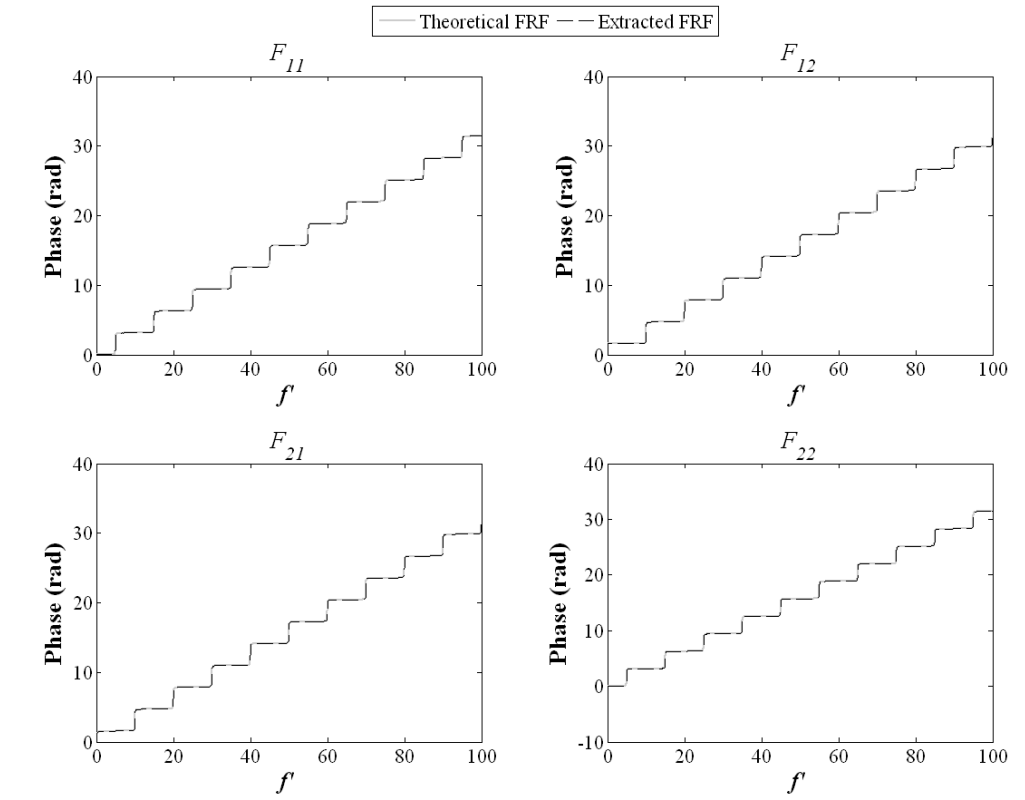

(b) Theoretical and extracted phases of FRM of a pipe section

Figure 7.22 – Comparison between the theoretical and extracted FRMs

Note that the extraction is also possible using responses containing multiple pulses. The time duration of the trace becomes shorter with the use of a single pulse signal, but it does not lead to inferior results. This is because the amount of extractable information of the system depends on the bandwidth of the introduced signal, and a single pulse signal and a longer time trace have the same bandwidth. As an illustration, the FRM of the pipe section was extracted again using the longer time trace—whose examples are shown in Figure 7.21 (b) and (c)—and it is presented in Figure 7.23 along with the FRM determined from the first pulse in each time trace. The two FRMs overlapped perfectly which indicates that the use of either type of the input and output data for the extraction of FRM is equally valid. Only the magnitude of the FRM is shown in Figure 7.23, but a very good agreement was also observed for the phase of the FRM.

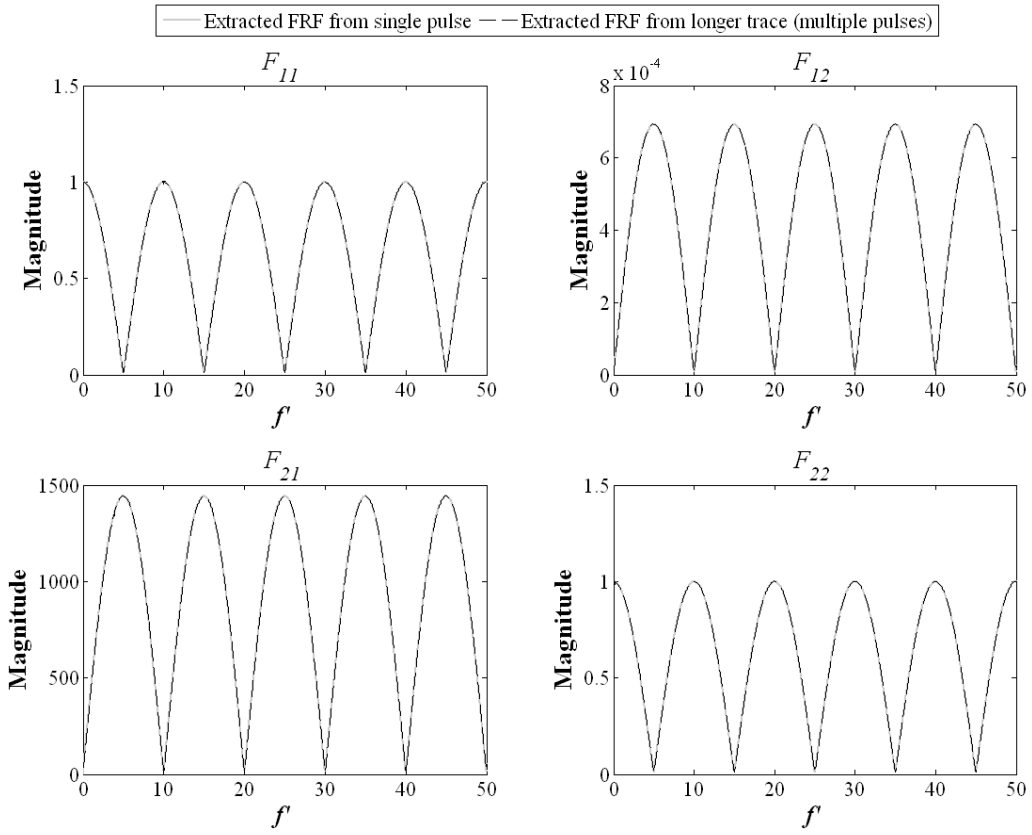

Figure 7.23 – Comparison between the extracted FRM from a single pulse signal and a longer time trace

The use of a longer time trace for extracting FRM has been shown to give the identical result to the use of a single pulse. However, care is needed when using the transient trace. It is important that the output trace captures all the pulse signals measured at the input. This is because the extraction method is based on the transfer matrix method which carries out

simulations by transferring the head and flow information from one point in the system to another. If the output trace misses a part of the trace measured at the input, the transfer of the information is incomplete and the extraction of the FRM will be unsuccessful. The required duration of the measurements depends on the locations of the transient source and the component under test. The situation becomes more complicated in real systems in which unknown sources of transient reflections may exist within the system. For this reason, the use of a full transient trace, from the initiation of the transient to its decay, is therefore recommended where multiple pulses are required, because it eliminates the need to determine the optimal duration of the measurements. In the laboratory environment, the FRM extraction from the first pulse of the trace will be sufficient.

7.8.2 Pipe point / leak

The verification of Equation 7.12 for the identification of FRM continues with two other hydraulic components: a leak and a reference point in the pipeline. These two components are assumed to have no physical length and their FRMs relate the flow and head on either side of the component. Their FRMs are known as a point matrix and others such as valves, orifices and junctions are also described by their respective point matrices (Chaudhry 1987). The FRM of the pipe reference point is given as:

$$[F]_{point} = \begin{bmatrix} 1 & 0 \\ 0 & 1 \end{bmatrix} \tag{7.14}$$

which signifies the identical flow and head signal on either side of the pipe reference point. The FRM of the leak is:

$$[F]_{leak} = \begin{bmatrix} 1 & -\dfrac{Q_{L0}}{2(H_{L0} - z_L)} \\ 0 & 1 \end{bmatrix} \tag{7.15}$$

where Q_{L0} is the steady flow out of the leak, H_{L0} and z_L are the base head and the elevation head at the leak respectively. The derivation of Equation 7.15 is given in Chapter 3. The relationship between the head and flow responses on either side of the leak is more easily

interpreted from the dimensionless form of this equation. Assuming the dimensionless flow and head responses at the leak are given by the following:

$$q_L' = \frac{q_L}{Q_{L0}} \tag{7.16}$$

$$h_L' = \frac{h_L}{H_{L0} - z_L} \tag{7.17}$$

then the resultant FRM becomes:

$$[F]_{leak,ND} = \begin{bmatrix} 1 & -0.5 \\ 0 & 1 \end{bmatrix} \tag{7.18}$$

It is observed from Equation 7.18 that the head response either side of the leak is identical as indicated by the value of 1 on the bottom right of the FRM. In contrast, the flow response on the downstream side of the leak is smaller than that on the upstream side of the leak by half of the normalised head response.

Similar to the example with the pipe section, the FRM of a pipe point and a leak were extracted from the measured responses. The test setup is shown in Figure 7.24. The locations of the generator and the characteristics of the introduced signal were the same as in the previous example. The pipe point or the leak was placed 800 m from the upstream end of the pipeline system.

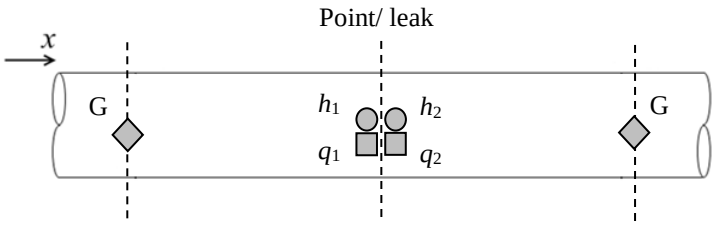

Figure 7.24 – Test setup for the identification of the FRM of a pipe point and a leak

The determined FRM of the pipe reference point and the leak are shown in Figure 7.25 (a). All the individual FRFs are in the form of a horizontal line. The three FRFs, F_{11}, F_{21} and F_{22} are identical for the two components and the extracted FRFs gave an excellent match with

their theoretical forms. The theoretical value of F_{12} is zero for the pipe reference point and the extracted F_{12} also gave the value of zero. The magnitude of F_{12} for the leak is re-plotted in Figure 7.25 (b). The extracted FRF for the leak had the magnitude of 0.5037, which was different by 0.74% from the theoretical magnitude of 0.5. This difference is attributed to the linearization of the orifice equation in the transfer matrix equation (see Chapter 3) and it is not the error related to the extraction procedure. All the determined FRFs were real with a phase of zero.

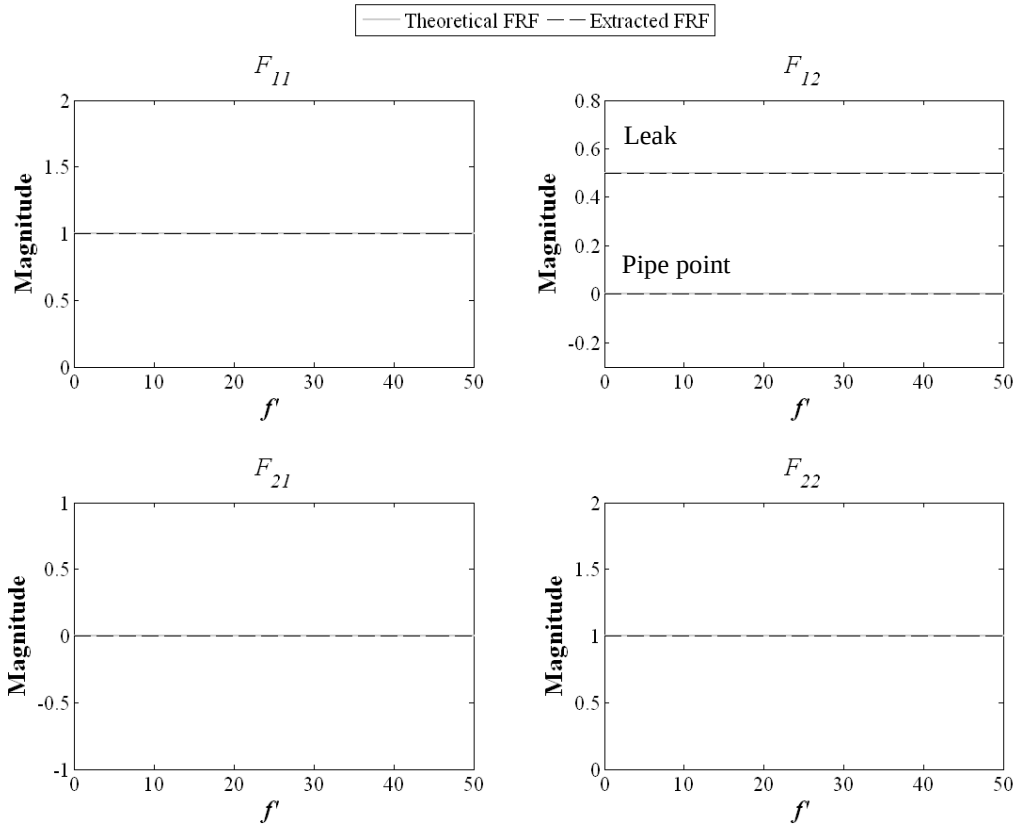

(a) Theoretical and extracted FRM of a pipe point and a leak

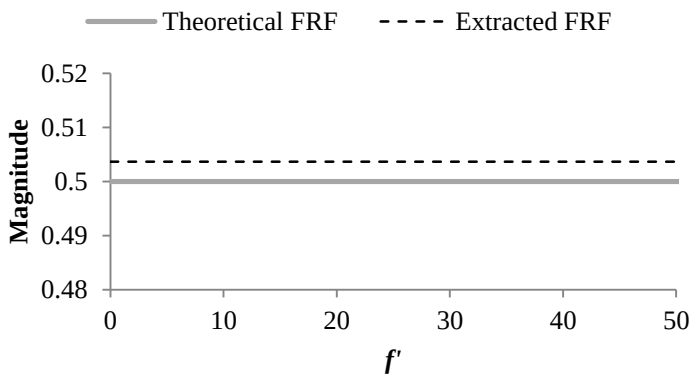

(b) Enlarged view of F_{12} of a leak

Figure 7.25 – Comparison between the theoretical and extracted FRMs

The above numerical examples have demonstrated the ability of Equation 7.12 to give accurate estimations of the FRM of two types; a field matrix and a point matrix. Since major hydraulic components can be described by FRMs of either of these types, the successful outcomes from these examples also imply the applicability of the extraction method to various other hydraulic components.

The present study examines whether a leak causes frequency dependent effects on signals by observing its FRM extracted from the measured data. For this purpose, firstly, it is necessary to understand the influence of the frequency-dependent effects on the FRM. A well-known frequency dependent phenomenon in pipelines is unsteady friction and its effects on the FRM of a numerical pipe section will be investigated next.

7.9 Consideration of frequency dependent effect on frequency response matrix

In the time domain, the frequency dependent effects are manifested as the attenuation and dilation of signals. The following example will demonstrate changes imposed on the FRM of the pipe section in Figure 7.21 (a) due to the presence of unsteady friction. The effect of steady friction was neglected to clearly illustrate the changes imposed by unsteady friction.

The magnitude of F_{11} with and without unsteady friction is shown in Figure 7.26 (a). The two FRFs appeared to match well in the figure. However, the FRF with unsteady friction has a weak dependence on frequency. As a better presentation of this phenomenon, the linear trend lines though each of the FRFs were obtained and they are plotted in Figure 7.26 (b). The trend line for the FRF with unsteady friction had a positive gradient, indicating an increase in the average magnitude of the FRF with frequency. The FRF without friction did not exhibit such behaviour and the average magnitude of the FRF remained the same as indicated by the horizontal trend line in Figure 7.26 (b). The trend lines for F_{12} and F_{21} are also presented in the figure which shows a similar behaviour with frequency. Note that the magnitudes of these FRFs were normalised so that they were in the same order of magnitude to that of F_{11}. The remaining FRF, F_{22} behaved in the same way as F_{11} and so it is omitted from the figure. The trend lines though all the FRFs without friction were identical to each other.

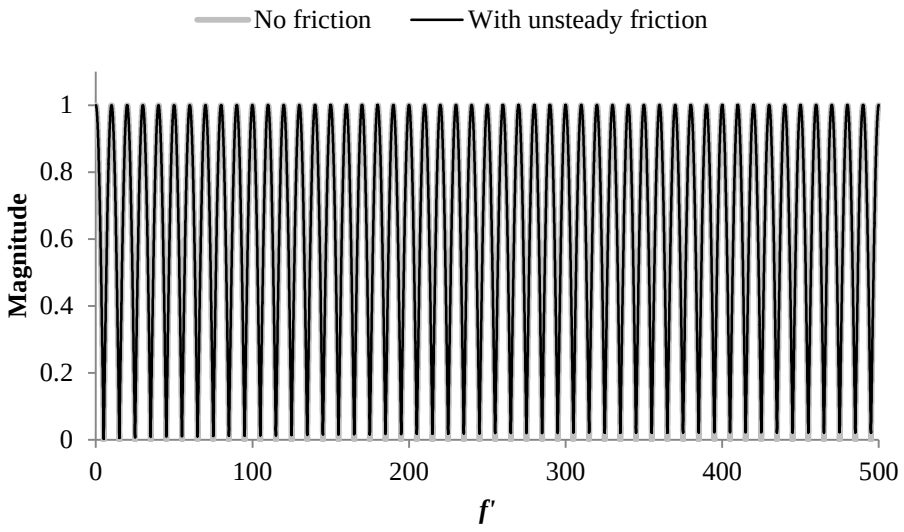

(a) Magnitude of F_{11} with and without unsteady friction

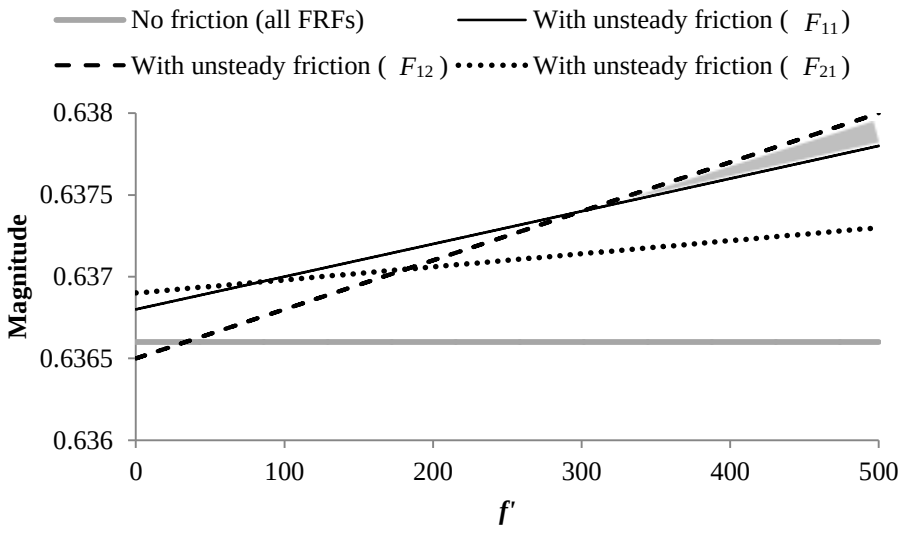

(b) Trend lines of the FRFs (F_{11}, F_{12} and F_{21}) with and without unsteady friction

Figure 7.26 – Frequency dependent effect on FRM

The physical interpretation of the observed behaviour of FRFs is given as follows. Consider a section of a pipeline shown in Figure 7.27. The transient generator is on the upstream side of the test section. When the generator produces a negative pressure pulse, the measured head and flow responses, h_1, h_2, q_1 and q_2 will have negative amplitude as illustrated in the figure.

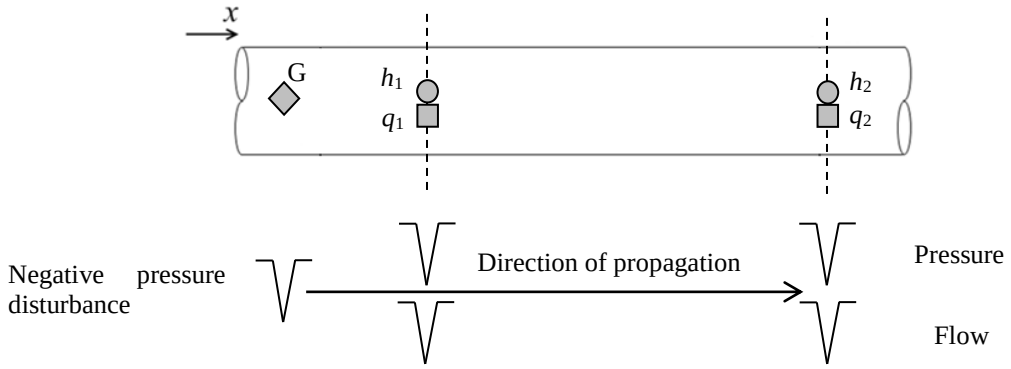

Figure 7.27 – Pressure and flow measured at the boundaries of the test pipe section

The equation for the flow at the outlet, q_2 is given by:

$$q_2 = q_{1,m} - h_{1,m} \tag{7.19}$$

in which $q_{1,m} = F_{11} \times q_1$ and $h_{1,m} = F_{12} \times h_1$. The FRFs, F_{11} and F_{12} can be considered as the amplification factors for the spectra of the head and flow at the inlet and so the increasing trend of the FRFs found in Figure 7.26 indicates an increase in the weight of higher frequency components of the signal. Hence the modified responses, $q_{1,m}$ and $h_{1,m}$ have higher frequency components of a greater magnitude than the original responses. Between these responses, the high frequency of the head response is larger as indicated by the shade in Figure 7.26 (b). The spectrum of the outlet flow signal, q_2 therefore has the smaller high frequency components than that of the input flow response, q_1 and its time-domain signal is attenuated and dilated. Since the outlet of the test section is located further from the generator, it makes sense for the signals at the outlet to be more affected by unsteady friction. Therefore the results in Figure 7.26 are reasonable from a physical perspective. A similar interpretation applies when the generator is placed on the downstream side of the test section in which case the flow signals would have positive amplitude.

In the next section, the FRM of a pipe reference point and a leak will be determined experimentally. It is anticipated that the FRM of a leak would exhibit similar behaviour found in Figure 7.26 (b) compared to that of a pipe reference point if a leak imposes frequency dependent changes on a signal.

7.10 Experimental extraction of frequency response matrix

A schematic diagram of the test setup is shown in Figure 7.28 (a). The system had a base flow with the flow Reynolds number of 10940. A solenoid-driven valve is used to generate pressure and flow pulses and it was placed 29.28 m (G_1 in the figure) and 12.12 m (G_2 in the figure) from the upstream tank in the first test condition and the second test condition respectively. The generated pulse signal is given in Figure 7.28 (b). It had a time width of 5 ms ($\Delta t'$ = 0.073) and the corresponding frequency spectrum is presented in Figure 7.28 (c). Note that the pressure data irrelevant to the generated signal was removed to minimise the influence of high frequency noise. Three flush-faced, high speed pressure measuring transducers, T_1, T_2 and T_3 were used in the tests and they were placed 14.59 m, 20.80 m and 27.01 m from the upstream boundary. As well as pressure, the system wave speed and flow were measured by these transducers. The transducers T_1 and T_2 were used to predict the flow response on the upstream side of the test point, and T_2 and T_3 were used for the downstream flow response via the KDP method.

The accuracy of the extracted FRM depends on the accuracy of the transducers. While the accuracy of an individual transducer is not critical, its relative accuracy in relation to other transducers is important as the extraction method of Equation 7.12 involves ratios of the responses measured at different locations in the system (Johnston *et al*. 1994, Kojima and Edge 1994, Earnhart *et al*. 2010). Prior to experiments, all three transducers were cross-calibrated against each other. After the calibration, the difference in signal magnitude was of the order of 0.01%. The average difference in the signal width was observed to be 1% and this was at the limitation of the instruments. The implications of these instrument errors will be discussed in Section 7.12 and the Appendix. In the next section, the FRM of a pipe reference point is experimentally determined which will be used as a baseline for comparison with the leak results.

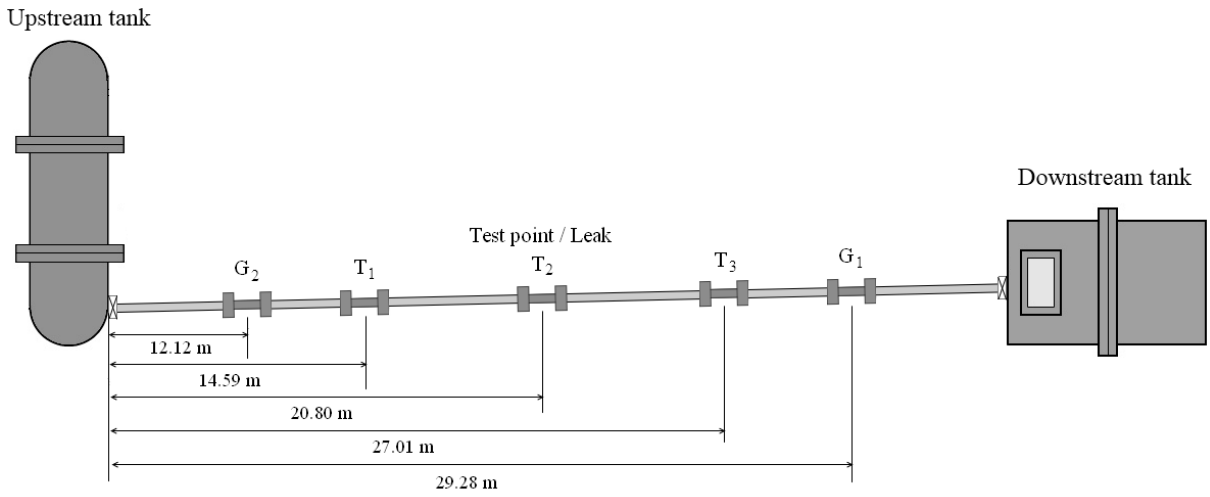

(a) Test setup

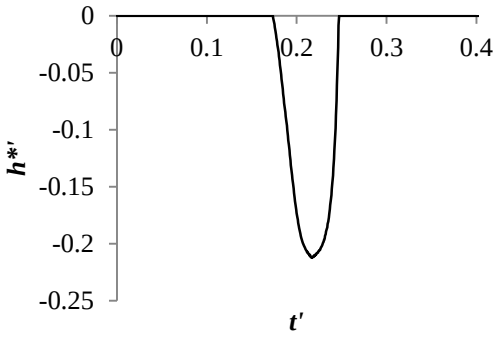

(b) Generated signal

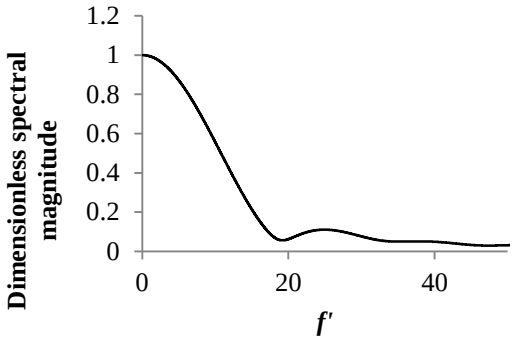

(c) Frequency spectrum of the generated signal, normalised by its maximum spectral magnitude

Figure 7.28 – Test configuration and the generated transient signal in the time and frequency domains

7.11 Determination of frequency response matrix of pipe point

The extraction method was first tested with a reference point in a rigid pipe. Its FRM was given in Equation 7.14 and it is repeated here in the form of a matrix equation with the input and output variables.

$$\begin{bmatrix} q_2 \\ h_2 \end{bmatrix} = \begin{bmatrix} 1 & 0 \\ 0 & 1 \end{bmatrix} \begin{bmatrix} q_1 \\ h_1 \end{bmatrix} \tag{7.20}$$

The midpoint of the test section with the transducer T_2 was selected as the test point (Figure 7.28 a). Assuming head conservation across this point, the pressure head either side of the

point is given by the middle transducer (T_2). All three pressure measurements were used to estimate the flow response on either side of the reference point. The magnitudes of F_{11} and F_{12} are shown in Figure 7.29. Since the pressure head either side of the point was measured by the same transducer this makes F_{21} and F_{22} trivial and only F_{11} and F_{12} are shown in Figure 7.29. Each result in the figure is the average of 30 tests. The x-axis of the plot is the logarithmic dimensionless frequency. Note that the magnitudes of F_{11} and F_{12} at the zero frequency were 1.001 and 3.935×10^{-8} respectively. Compared to the corresponding theoretical values of 1 and 0, it is seen that the extraction method successfully determined the correct magnitude of the FRFs. The figure shows the magnitudes of the FRFs are constant (within 0.05%) up to the dimensionless frequency of 5 but there is a large spike at the dimensionless frequency of 18.6 for both FRFs.

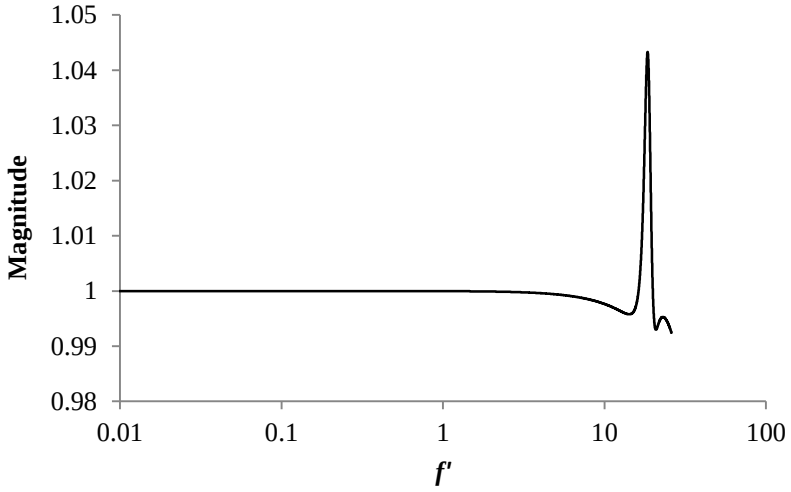

(a) Magnitude of F_{11}

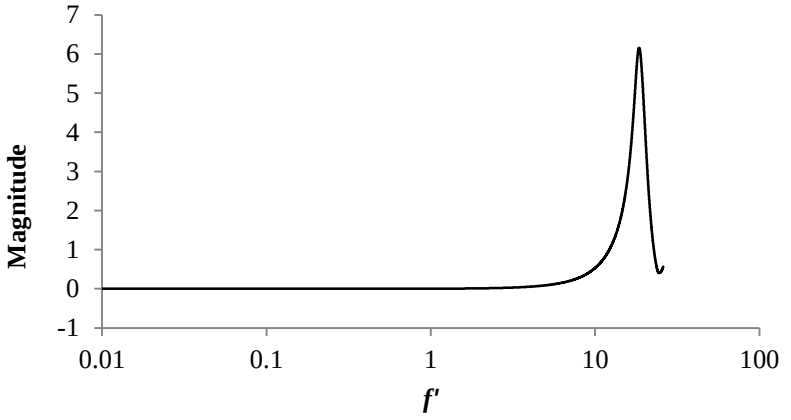

(b) Magnitude of F_{12}

Figure 7.29 – Magnitudes of the extracted FRFs, F_{11} and F_{12}

An additional test was conducted with a signal of a different width. The second test signal is shown in Figure 7.30 (a) along with the original test signal. The time width of the second signal (labelled as Signal 2 in the figure) was 7 ms ($\Delta t'$ = 0.101) whereas the original signal (labelled as Signal 1) had the time width of 5 ms ($\Delta t'$ = 0.073). The magnitudes of F_{11} extracted from these signals are given in Figure 7.30 (b) which shows the spikes at two different dimensionless frequencies; 18.6 for Signal 1 and 12.6 for Signal 2. This difference is attributed to the difference in their frequency spectra which are presented in Figure 7.30 (c). The frequency spectrum of Signal 1 hits the first local minimum at the dimensionless frequency of 19 whereas it occurs at a lower frequency for Signal 2 (f' = 12.7). These frequencies agree well with the spiking frequency observed in Figure 7.30 (b).

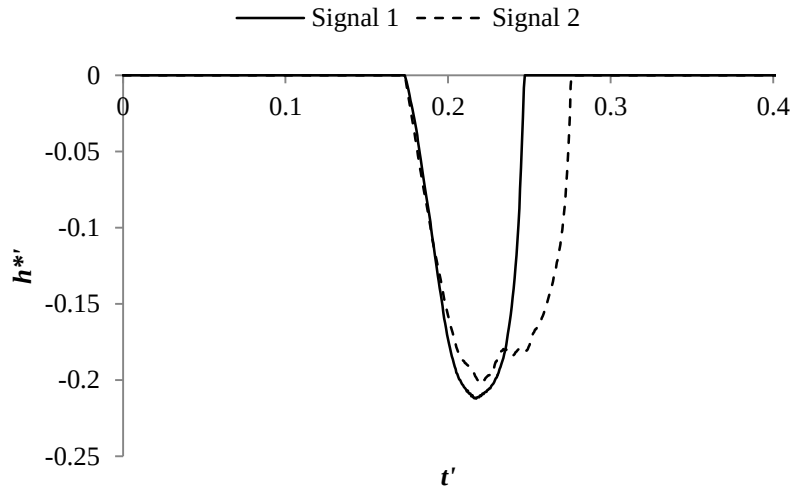

(a) Signals having different time widths

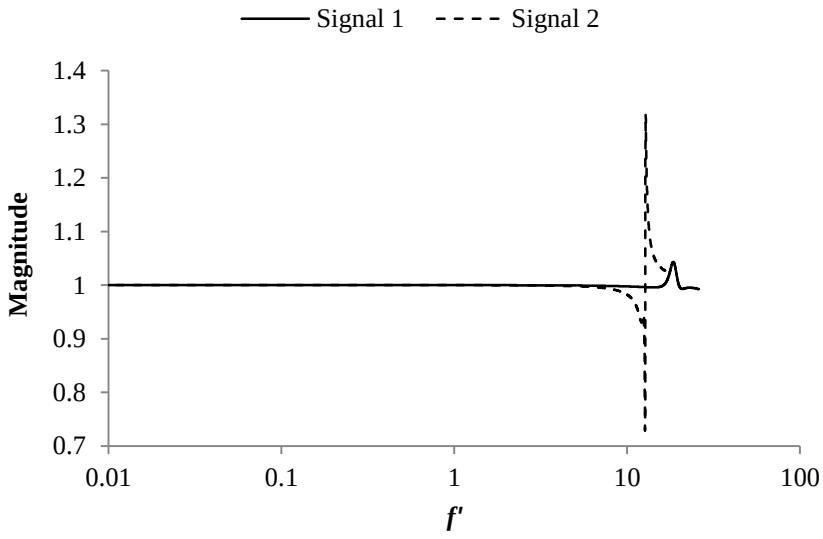

(b) Magnitude of F_{11} extracted from the signals in (a)

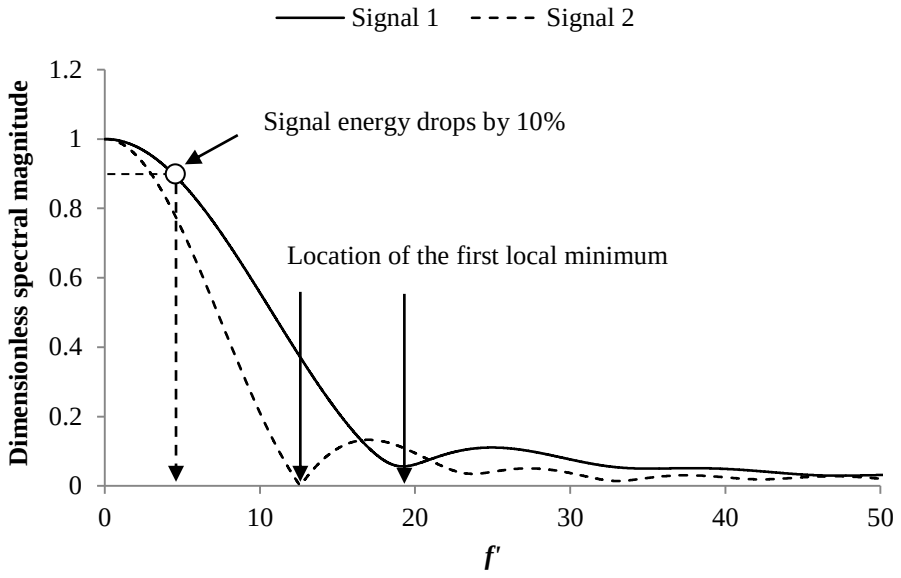

(c) Frequency spectra of the two signals. The spectral magnitude is normalised by the maximum spectral magnitude of each signal

Figure 7.30 – Relationship between the spiking behaviour of FRM and local minima of the signal spectrum

The relationship between the spiking behaviour of the extracted FRF and the minimum point of the frequency spectrum found above suggests that a pair of frequency spectra is different to each other in a way that the frequencies of local minima do not match. As observed in Equation 7.12, the mathematical manipulations for the FRM extraction involve division of frequency spectra. The quotient from a pair of slightly different spectra will exhibit erroneous behaviour when the magnitude of the spectrum on the denominator becomes small. The unmatched spectra suggest the inconsistency in the widths of the signals in the time domain.

7.12 Effects of inconsistent width on frequency response matrix

A numerical study was conducted to further examine the spiking phenomenon seen in Figure 7.30. The effect of the inconsistent signal width on the extracted FRM of a test point is investigated with pairs of signals having the width differences of 1%, -1% and 10%. Note that the pressure transducers used in the experiments were found to give the width difference of approximately 1% of the averaged signal width. The positive width difference signifies that the width of input signals is greater than that of the output signals. Unlike the numerical examples presented earlier, for these examples, a rectangular-shaped signal with a width of 100 time counts of the MOC simulations was used since it was not possible to create an error

of 1% or 10% of the signal width with an impulse signal. Note that a case with -10% difference was omitted as its effect can be deduced from the results of other test scenarios.

The magnitudes of F_{11} extracted from these pairs of responses are given in Figure 7.31 (a). In the figure, the magnitude shows its local maxima and minima in the neighbourhood of 20, 40 and 60 dimensionless frequencies. As observed experimentally, near these frequencies, the spectrum of the input signal marked the lowest magnitude as shown in the figure with the dashed grey line. It was also found that the locations of these extremes shifted for the signals with different widths (not shown), which agrees with the finding in Figure 7.31 (b).

The magnitude of F_{11} up to 10 dimensionless frequencies is re-plotted in Figure 7.31 (b) in order to observe its behaviour prior to the spike. The magnitude exhibits a frequency dependent change. The positive error in the signal width gave a lower F_{11} magnitude than the true value but the magnitude gradually increased with frequency, leading to the positive spike. An opposite phenomenon was seen for the negative width error. The discrepancy in the initial magnitude and the degree of change with frequency was amplified with the larger width difference. The magnitudes of the other FRFs showed the same behaviour with frequency (not shown) but the magnitudes of F_{12} and F_{21} remained insignificant as assumed theoretically. The change in phase was observed and the phase of F_{11} is presented in Figure 7.31 (c). It was found that the positive width difference resulted in the increasing phase with frequency and the opposite outcome was obtained from the negative width difference. The same trend was seen for F_{22}.

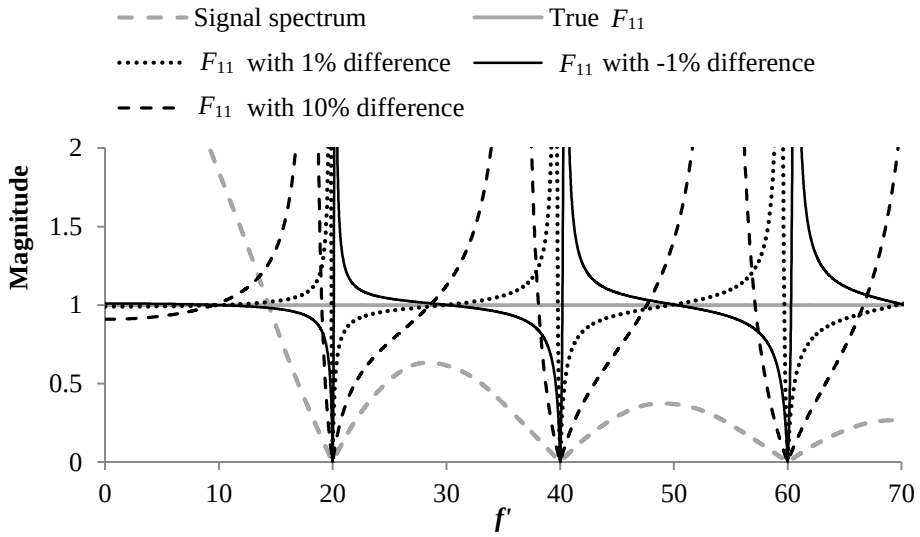

(a) Magnitude of F_{11} with the width differences of 1% (dotted line), -1% (solid line) and 10% (broken line)

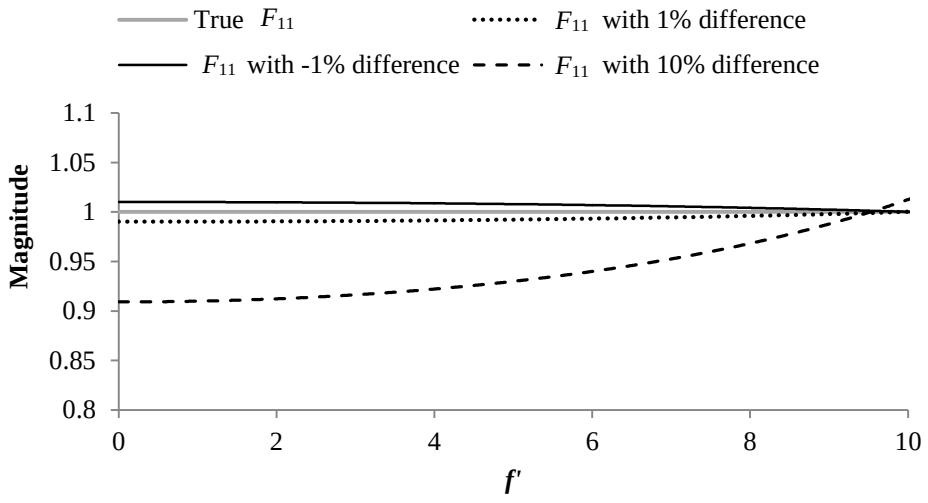

(b) Re-plot of (a) up to *f'* = 10

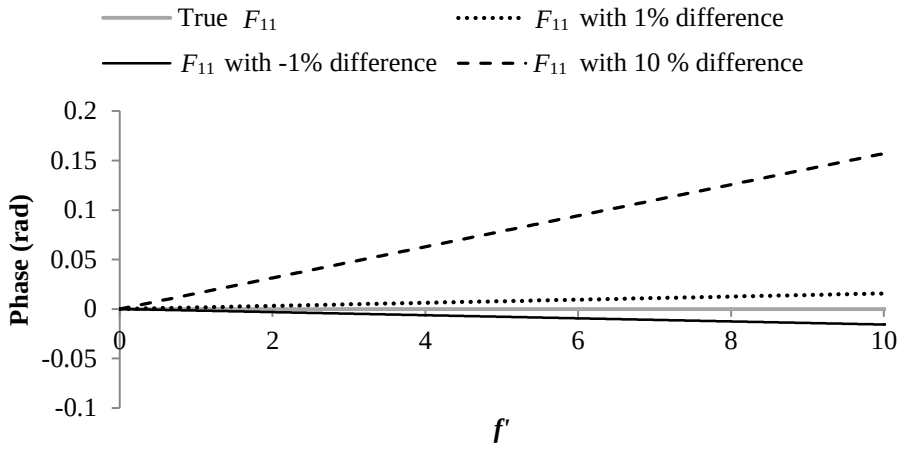

(c) Phase of F_{11} for the three cases in (a)

Figure 7.31 – Effect of inconsistent signal width on the extracted FRM

The discrepancy in the signal width was unavoidable with the transducers and the measurement instruments available in the laboratory. Therefore the uppermost frequency (bandwidth) was set to mitigate the effect from the inconsistent width. A few definitions of bandwidth exist and the half-power bandwidth and 3-dB bandwidth are often used practically in signal processing (Phillips and Parr 1995, Ambardar 1999). These have the frequency range over which the magnitude exceeds half and $1/\sqrt{2}$ times its maximum respectively. Any other definitions of bandwidth are equally valid and the best definition depends on a particular application. For this work, as will be discussed, the results exhibited variability with the increase in frequency. In order to achieve a good degree of confidence in the results and to keep a sufficient distance away from the local minima, the limiting magnitude of the

signal energy is set as 90% of the maximum amplitude. Signal 1 was used for the rest of the work and its spectrum falls by 10% of its maximum magnitude at the dimensionless frequency of 4.51 which corresponds to 66 Hz (Figure 7.30 c). This frequency was taken as the bandwidth of this signal.

Figure 7.29 is re-plotted for the range up to the bandwidth in Figures 7.32 (a) and (c). The phase of the FRFs is also given in Figures 7.32 (b) and (d). As the scope of this work is to observe the behaviour of leak with frequency, the y-axis of the figures shows the absolute difference in the magnitude of FRF from its value at the zero frequency. If the FRF does not exhibit any frequency dependent behaviour, the plot would show a horizontal line with a value of zero. The error bars indicate the 95% confidence interval of the results. For the magnitude of F_{11} shown in Figure 7.32 (a), note that the y-axis is of a reduced scale to highlight any behaviour in the data. The average result shows little deviation in the frequency range and the discrepancy from the theoretical value of unity was below 0.1%. The phase of F_{11} showed a greater spread in the results but the average result deviated from the theoretical value of zero only by 0.025 radians at the bandwidth frequency. The magnitude of F_{12} shows a similar behaviour to the magnitude of F_{11}. It started deflecting slightly after the dimensionless frequency of 1 and it was out by 4.7% of the theoretical value at the end of the shown frequency range. Both the deflection and the spread in the results were the most significant for the phase of F_{12} shown in Figure 7.32 (d). The greater error in the F_{12} is likely due to the equation for F_{12} (Equation 7.12b) which has more flow inputs than F_{11}. The flow is predicted by the KDP method and therefore, unlike the pressure head, the flow response is affected by at least two sources of error; error from the transducers and the prediction error from the KDP method. Note that such behaviour was not observed in the numerical examples as the flow was obtained directly from the MOC model. However, a separate numerical study of the FRM extraction involving the use of the KDP method indicated a similar tendency. Therefore the additional error introduced by the flow prediction can be considered as the cause of the observed erroneous behaviour of F_{12}.

The 95% confidence interval of the results increased with frequency. As observed in Figure 7.30, signals of different widths have different frequency spectra and the level of this difference determines the location of the spikes and the degree of deflection of the response (see Figure 7.31 b). Thus it is possible for the response extracted from a certain dataset to

have a slightly different spiking frequency and a rate of deflection to the one from another dataset. This slight inconsistency across datasets led to the observed variability in the results.

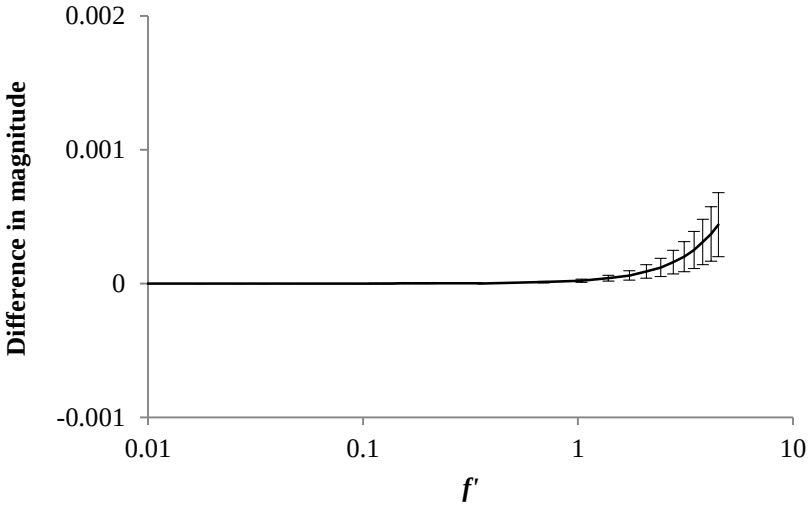

(a) Magnitude of F_{11}

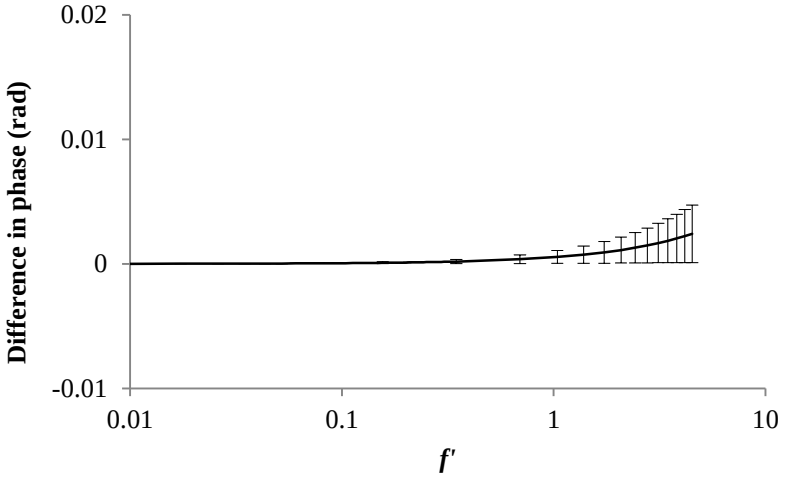

(b) Phase of F_{11}

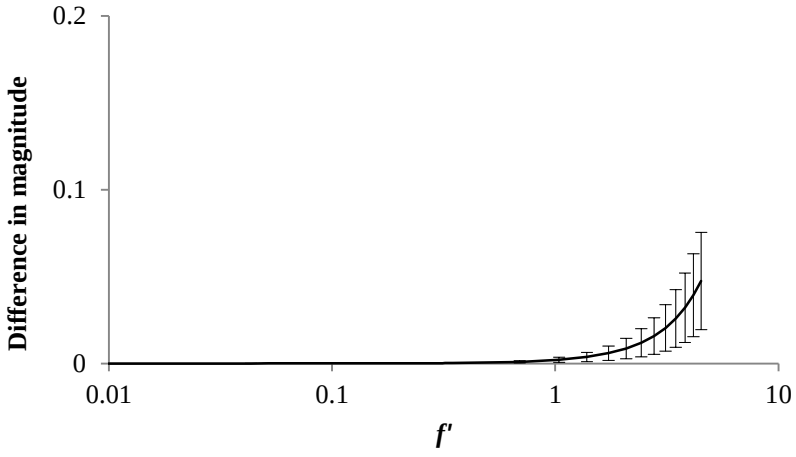

(c) Magnitude of F_{12}

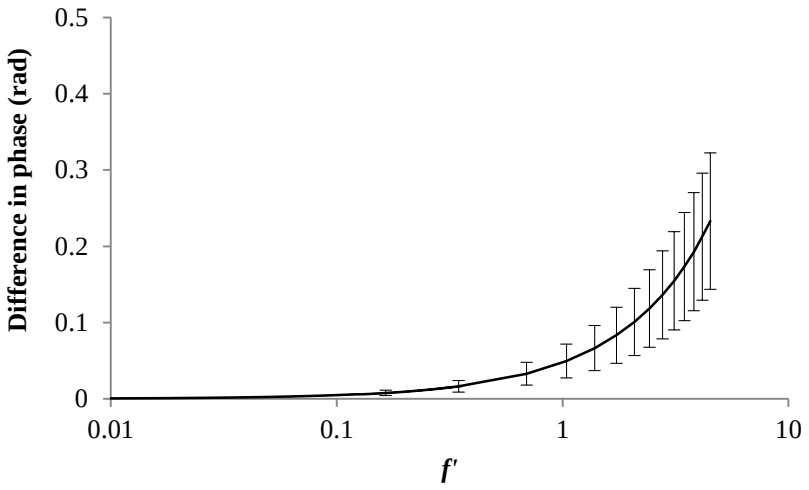

(d) Phase of F_{12}

Figure 7.32 – Extracted FRM of pipe point

The deflecting nature of the extracted responses in Figure 7.32 is purely due to the error in the data as a reference point in a pipe does not cause a frequency dependent phenomenon. This preliminary work has revealed the potential errors in the present work. While a great deal of caution was given in the selection of the pressure transducers, the observed level of error was inevitable as the behaviour being studied lies near the limit of the measurement and transient generation equipment.

There exist possible sources of errors other than the inconsistent signal width, such as the inconsistent signal magnitudes and the error associated with handling of the measured data. These effects were investigated and the results are given in the Appendix. It was found that inconsistencies in the signal magnitudes affected the magnitude of the FRM, but its behaviour with frequency was unchanged. Careful handling of data led to minimum deviations in the resultant FRM. Since the present study focuses on the behaviour of FRM with frequency, these sources of errors were considered less critical for this study.

In the next section, the frequency dependent effects of leaks will be identified as deviations from the experimentally determined FRM of the test point. Since the leak tests are conducted under the same laboratory conditions as for the pipe point, the comparison between their results should exhibit some differences if the frequency dependent effects of leaks are significant.

7.13 Determination of frequency response matrix of leaks

The pipe reference point used in the previous investigation was replaced by a leak for the subsequent study. The leak was created by a side discharge valve and the pressure at this point was measured by the transducer T_2 in Figure 7.28 (a). In some literature, the data acquisition at or in the vicinity of the object of interest is avoided in order to keep away from possible disturbances created by the object (Stirnemann *et al*. 1987, Kojima and Edge 1994). A comparison of the measured pressure signals at the three measurement stations is shown in Figure 7.33. The pressure signals in the figure are normalised by the minimum amplitude of each signal. The figure indicates that the leak discharge does not appear to produce unfavourable high-frequency noise and hence measuring pressure at the leak was considered acceptable in this study. The pressure pulses in Figure 7.33 appear almost identical to each other and thus the pressure head either side of the leak was assumed to be identical. This allows the use of the single transducer for their measurements. This assumption was further supported by the result from the MCA in Section 7.5.1.

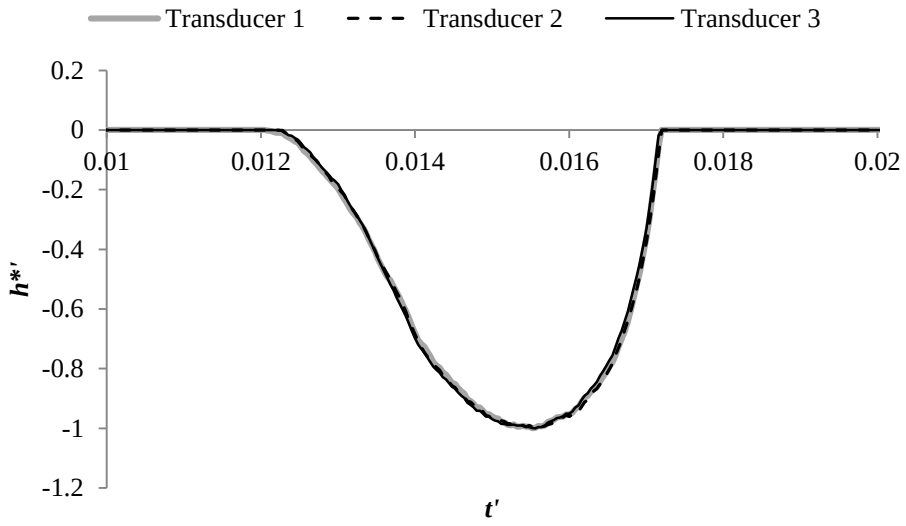

Figure 7.33 – Measured pressure traces at three measurement stations. Pressure signals are normalised by the magnitude of each signal

Tests were carried out under three different system base flow conditions. The three base flows were 3.13×10^{-4} m^3/s (Leak size 1), 3.47×10^{-4} m^3/s (Leak size 2) and 3.79×10^{-4} m^3/s (Leak size 3). In all tests, the leak discharge was 48% of the total base flow. The leak size was made deliberately large in order to clearly identify the leak reflections.

The leak transfer matrix was extracted in the same way as in the case with the pipe reference point (referred to as the no-leak case). In Figure 7.34, the average results of the leak cases are presented. The average results from the three system conditions were very similar to each other for F_{11}. Although the slight deviation started to appear at higher frequencies for F_{12}, the same trend with frequency was seen in all cases. The characteristics of the leak were the same for the three test conditions and the consistency of the experimental results, across three different cases and 42 independent runs, successfully demonstrated this fact.

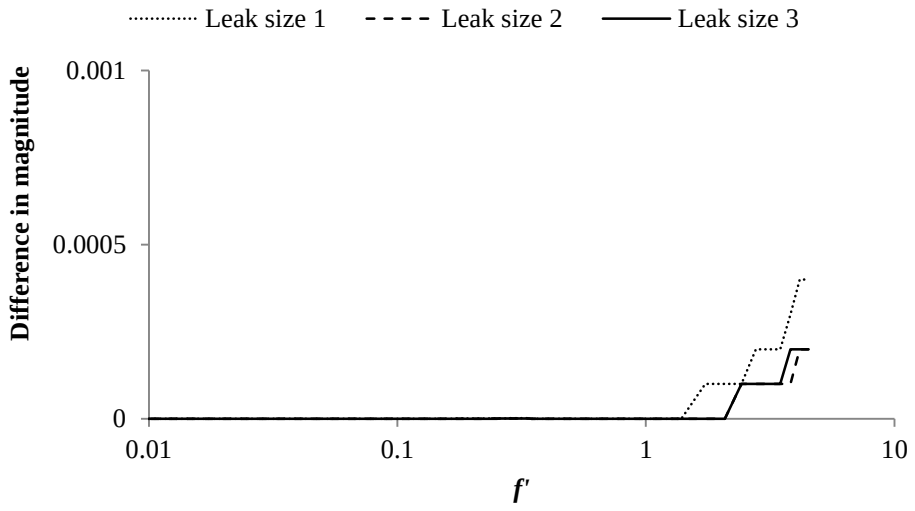

(a) Magnitude of F_{11}

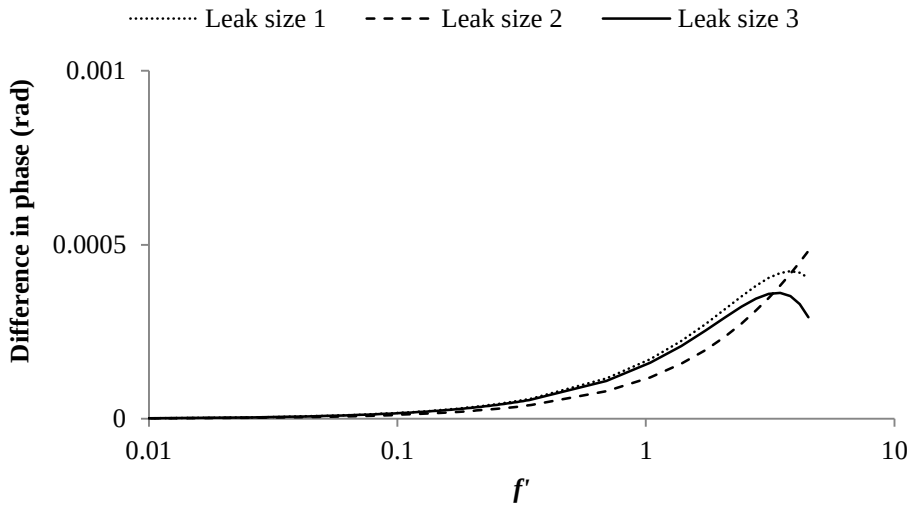

(b) Phase of F_{11}

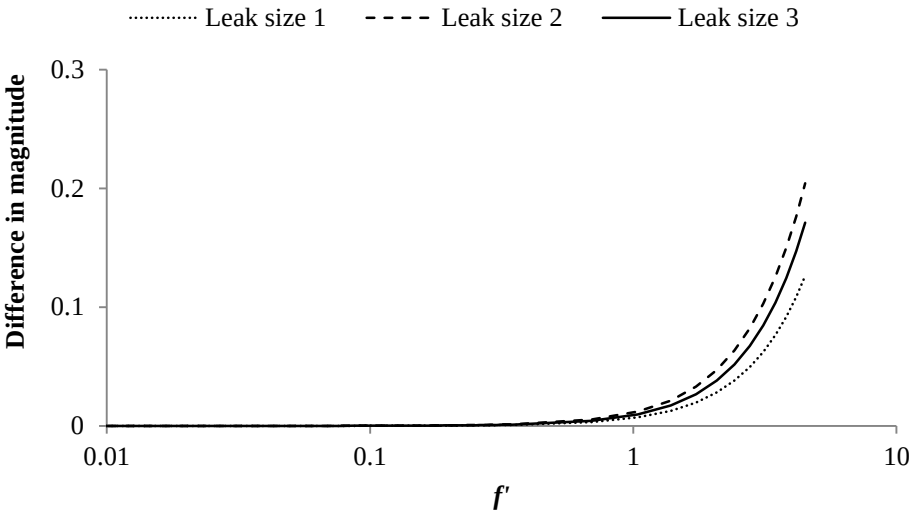

(c) Magnitude of F_{12}

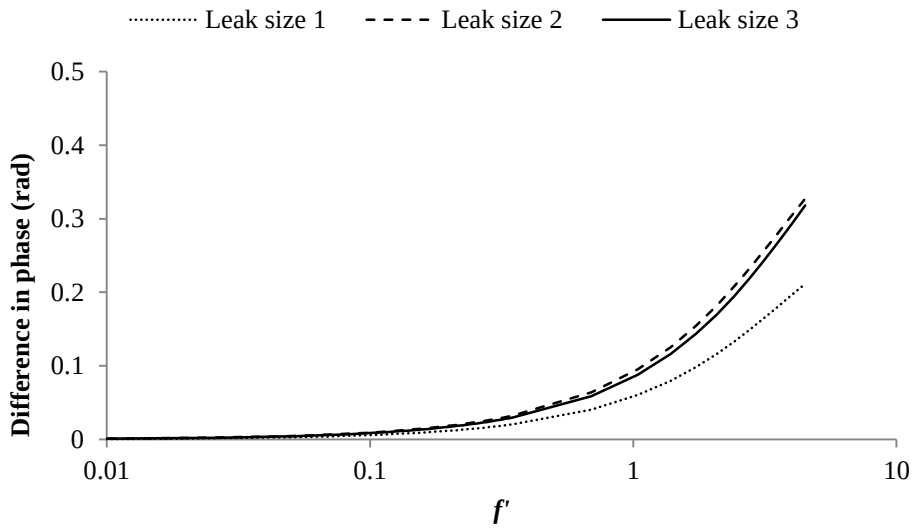

(d) Phase of F_{12}

Figure 7.34 – FRM of three leaks

The extracted FRFs, F_{11} and F_{12} for three system conditions are individually presented in Figures 7.35, 7.36, 7.37 and 7.38, accompanied by the average no-leak result and its 95% confidence interval. The average magnitude and phase of F_{11} for all leak sizes were within the confidence interval of the no-leak result. Given the variability of F_{11} is very small, it can be considered that F_{11} for the leak is very similar to that of the no-leak case which agrees with the theory (see Equations 7.17 and 7.18, the first parameter of each FRM).

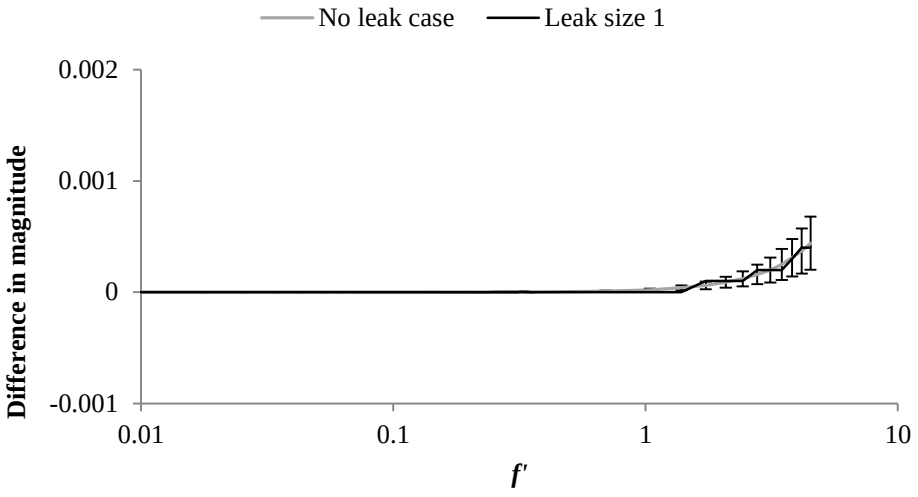

(a) Leak size 1

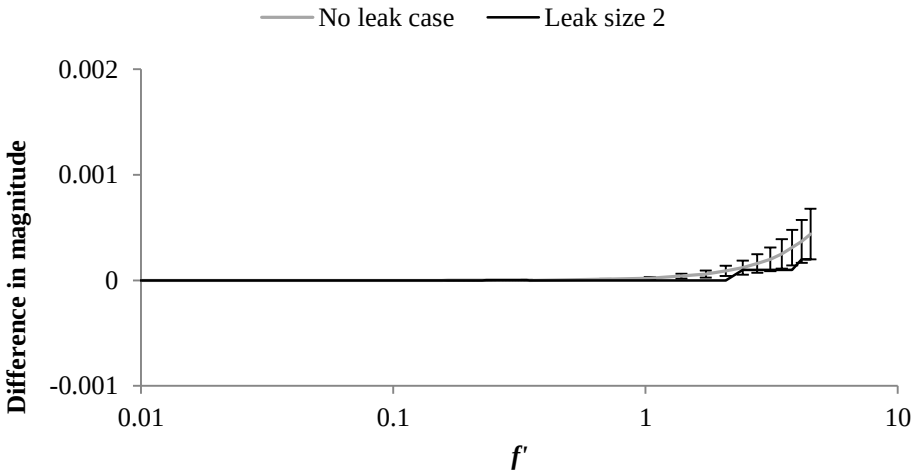

(b) Leak size 2

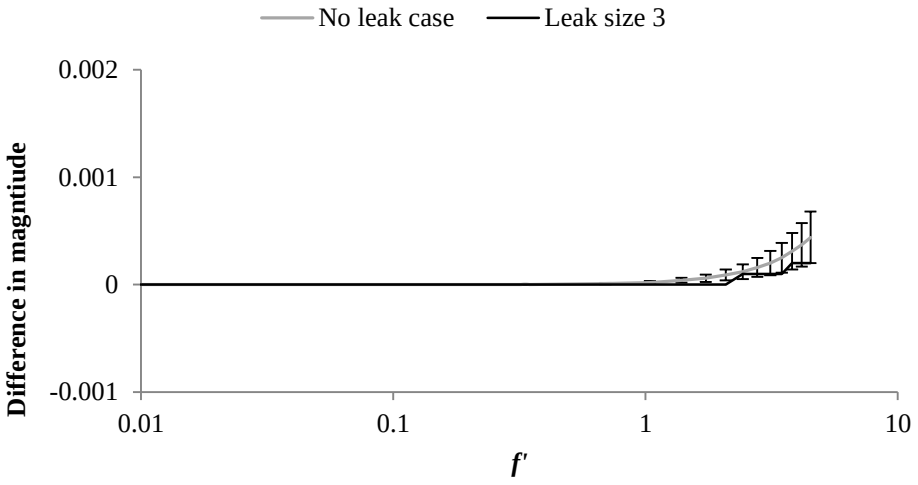

(c) Leak size 3

Figure 7.35 – Comparison between the no-leak and leak cases - Magnitude of F_{11}

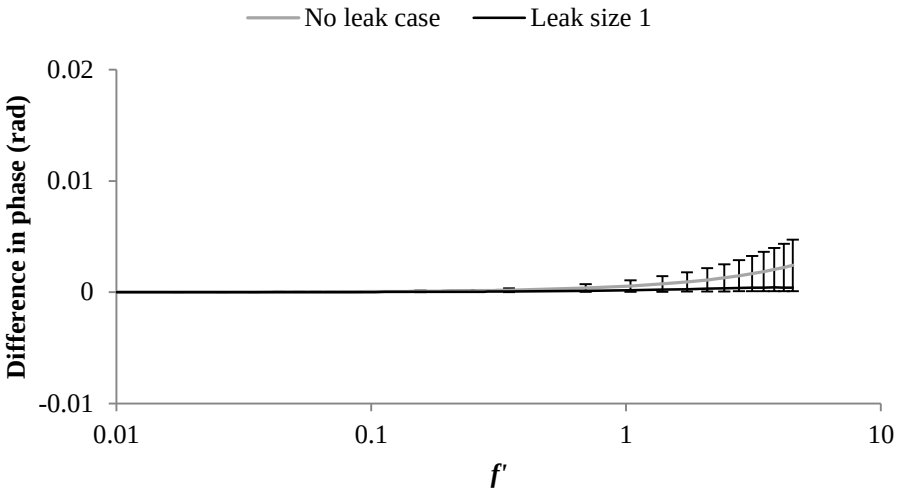

(a) Leak size 1

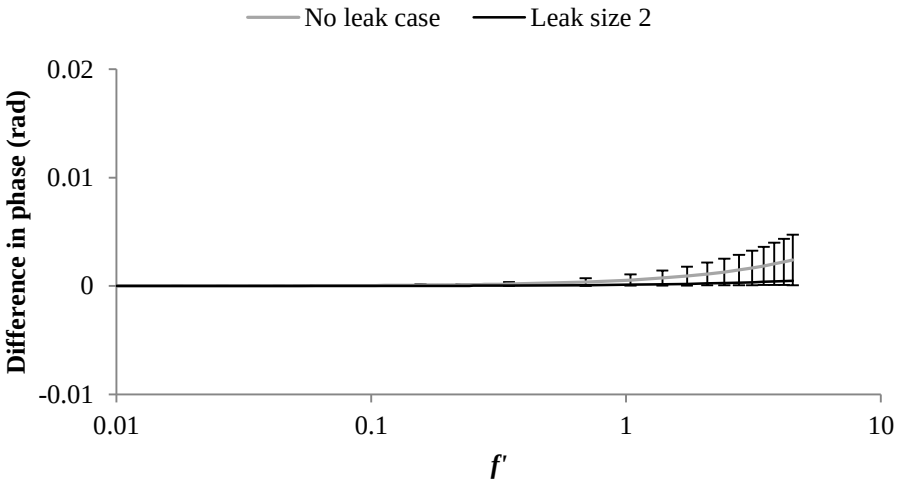

(b) Leak size 2

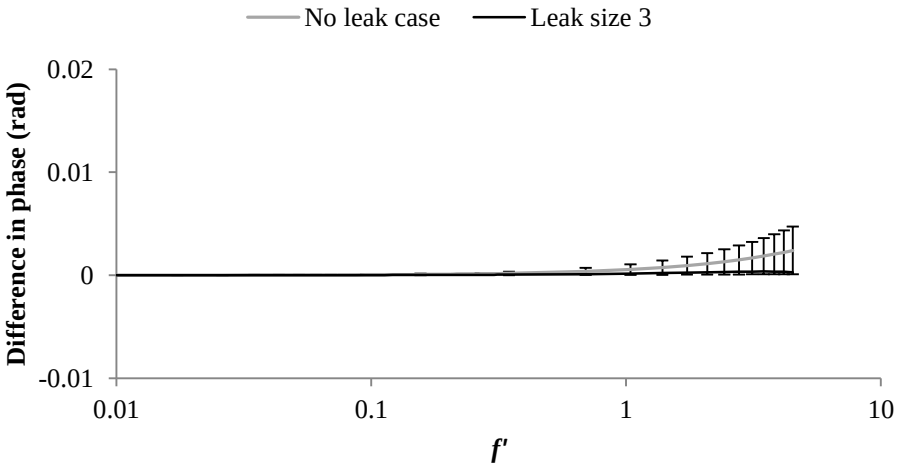

(c) Leak size 3

Figure 7.36 – Comparison between the no-leak and leak cases - Phase of F_{11}

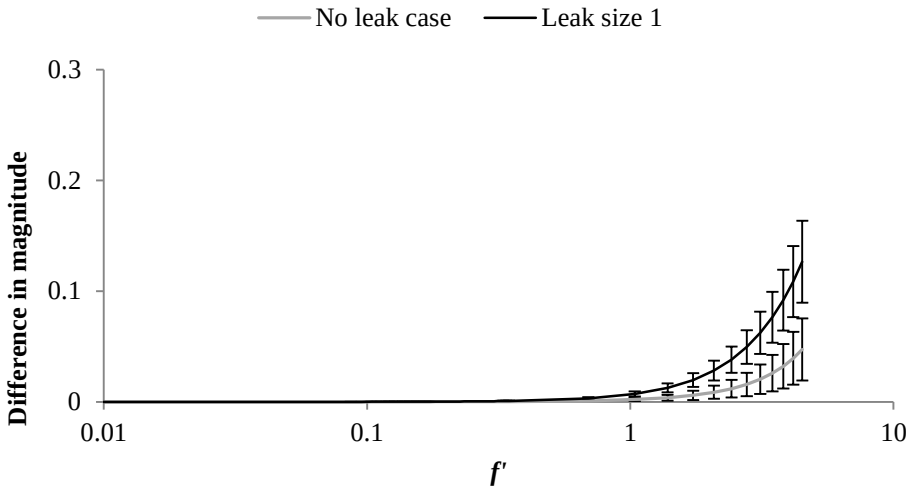

(a) Leak size 1

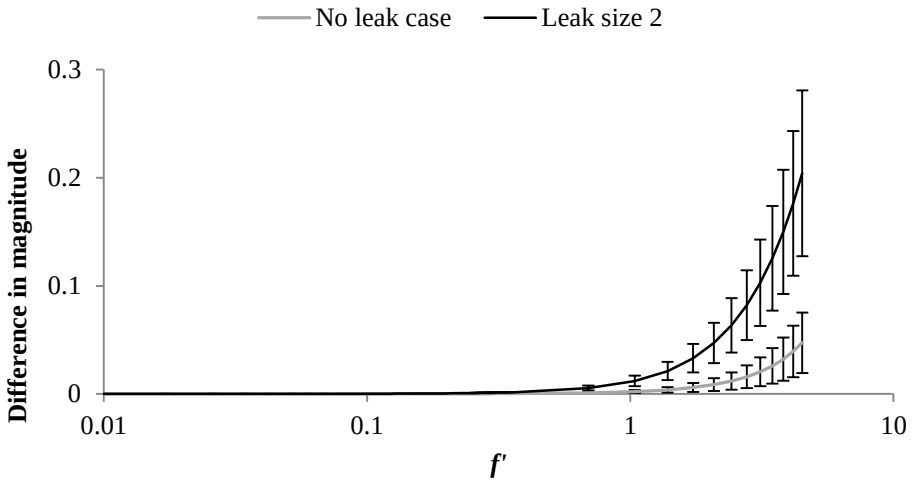

(b) Leak size 2

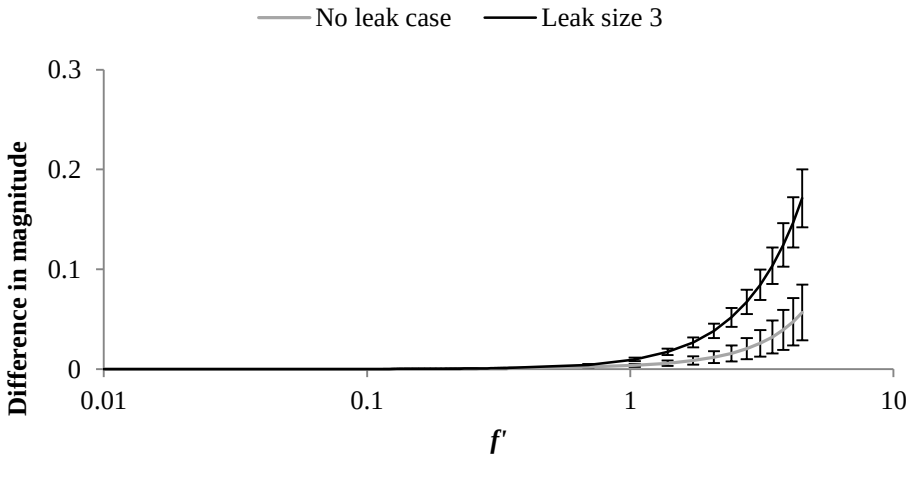

(c) Leak size 3

Figure 7.37 – Comparison between the no-leak and leak cases - Magnitude of F_{12}

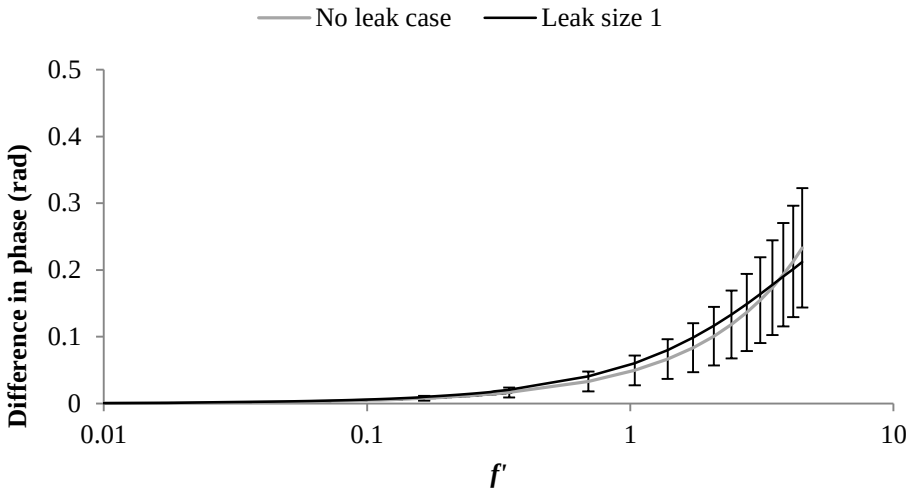

(a) Leak size 1

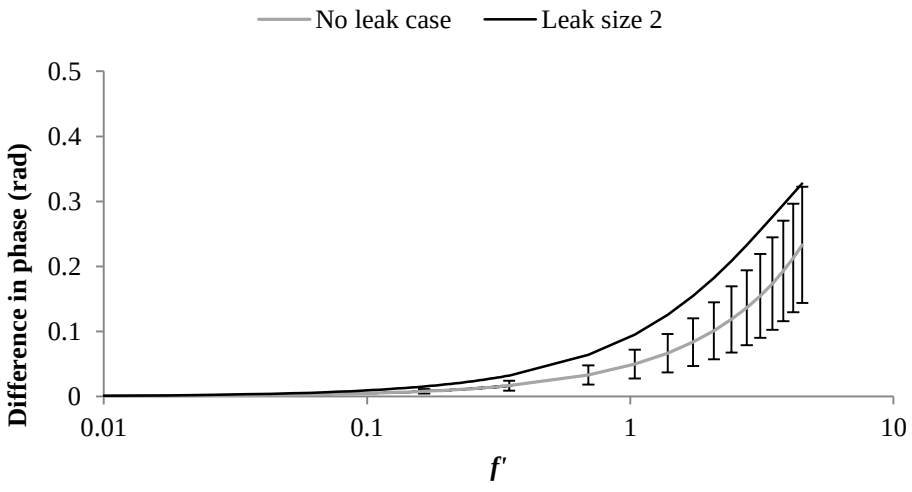

(b) Leak size 2

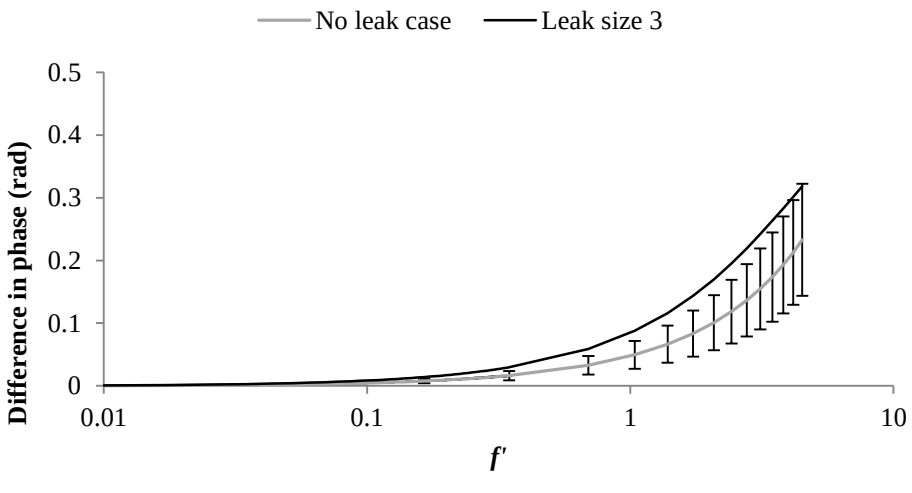

(c) Leak size 3

Figure 7.38 – Comparison between the no-leak and leak cases - Phase of F_{12}

In contrast to the results for F_{11}, the extracted F_{12} for the leak showed a greater deviation from the no-leak results. The maximum difference between the averages of the leak and no-leak case was observed at the bandwidth frequency and it was 11.8% for the magnitude and 16.3% for the phase of the leak element F_{12}. At this frequency, the size of the 95% confidence interval was 0.028 and 0.089 radians for the magnitude and phase respectively.

While the phase gave a large percentage difference, the average phase for the leak was found to be near or within the confidence interval of the no-leak result (Figure 7.38), making its deviation from the no-leak case less certain. The average magnitudes of F_{12} exhibited a greater degree of deflection and were outside the 95% confidence interval of the no-leak result. In Figure 7.37, the 95% confidence intervals of the leak results are also provided. The fact that these confidence intervals do not overlap with that of the no-leak case improves confidence in the observed differences in behaviour.

The physical interpretation of the results is given with the aid of the following numerical example. It is known that any periodic signal can be represented by a sum of sinusoids of different magnitudes and frequencies according to a Fourier series (Beerends *et al*. 2003). Figure 7.39 (a) shows an approximation to a square wave obtained from the first 20 partial sums of the Fourier series. In order to reproduce the experimental results in Figures 7.37 and 7.38, the magnitudes and phases of the 2^{nd} to the 20^{th} sinusoids were increased by certain percentages of the originals. The differences in the magnitude and phase are given relative to the original magnitude and period of each sinusoid respectively. The percentage difference applied to each sinusoid is shown in Figure 7.39 (b) in which a value on the x-axis represents the *n*-th sinusoid. A varying rate of growth in the percentage is to replicate the behaviour found in Figures 7.37 and 7.38. The largest percentage change was 45% for the 20^{th} sinusoid. For the purpose of a clear illustration of the effects of the magnitude and phase changes, the percentage change is set considerably higher than the difference found from the experimental results. In this illustration, either the magnitude or the phase was modified at a time in order to isolate the effect from one another.

In Figure 7.40 (a), the effect of the magnitude change on the boxed section (see Figure 7.39 a) of the signal is shown. The increase in the magnitude of the high frequency sinusoids resulted in enhancement of a high frequency oscillation at the top of the signal and gave a

noisier appearance to the overall signal. Such an observation is in agreement with the interpretation presented earlier in Section 7.9. The signal in Figure 7.39 (a) for the time range between t = 0.4 s to 0.6 s is re-plotted in Figure 7.40 (b). Since the high-frequency sinusoids define the profile of a wavefront, the changes to these are more noticeable around the wavefront as indicated in the figure. Compared to the original signal, the modified signal has a sharper profile which implies that the variation in the magnitude is also responsible for the change in the signal shape.

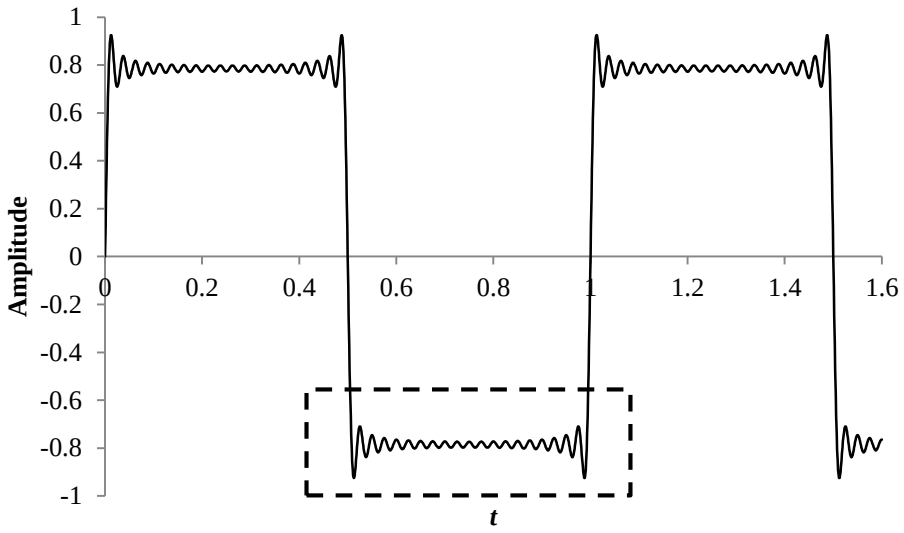

(a) Approximation to a square wave with 20 partial sums of the Fourier series

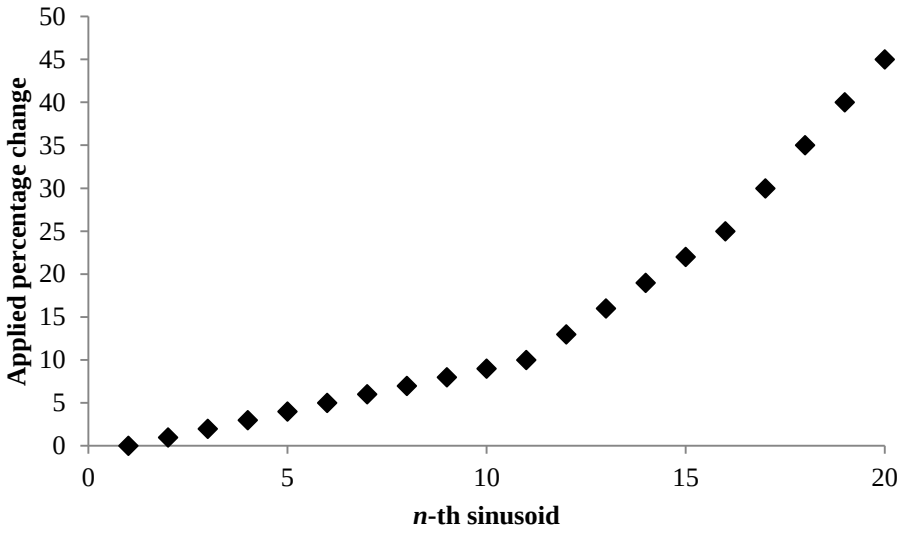

(b) Applied percentage difference to each sinusoid

Figure 7.39 – Signal and applied modification used to imitate the experimental results

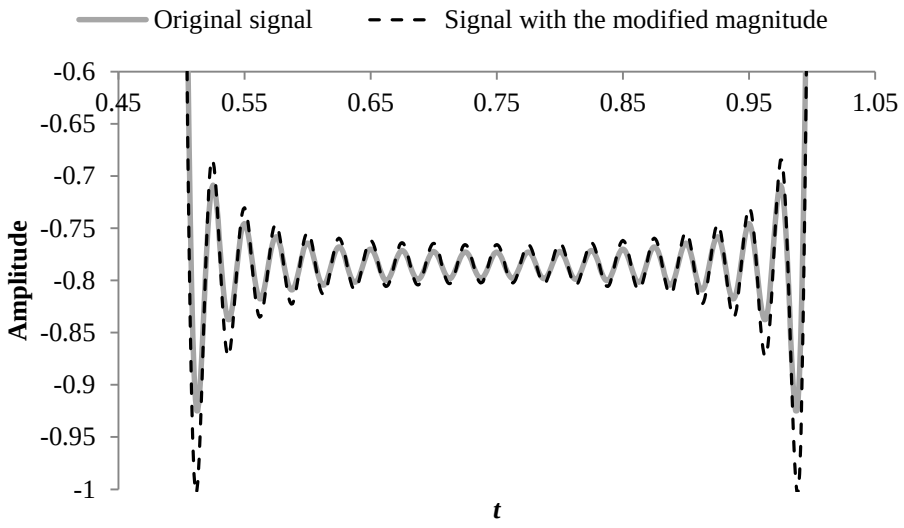

(a) Effect of the magnitude change

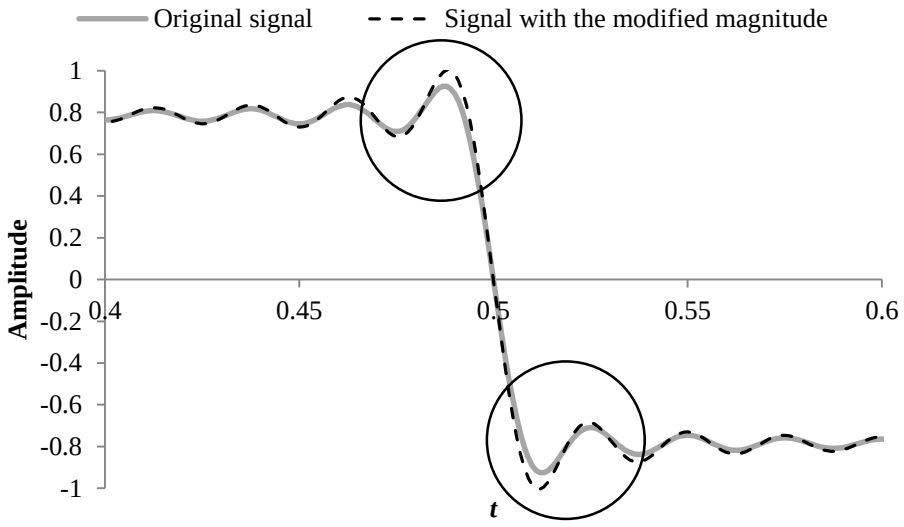

(b) Re-plot of (a) for the time range t = 0.4 to 0.6 s

Figure 7.40 – Effect of the change in magnitude of the composing sinusoids

The influence of the modified phase is shown in Figures 7.41 (a) and (b) where very little change to the overall signal was observed. Instead of amplifying the high-frequency oscillation, the phase change slightly moved the mean value of the oscillation. Another difference from the magnitude effect is the time shift of the signal as illustrated in Figure 7.41 (c). The signal with the modified magnitude crossed the x-axis at the same point in time (t = 0.5 s) as the original signal but the change in the phase shifted the point of intersection to t = 0.4996. While these differences contribute to the overall change to the signal, their degree of influence is significantly smaller than that from the magnitude change. The magnitude and

phase of the average leak results were found to differ from that of the no-leak results by the same order of magnitude (11.8% for the magnitude and 16.3% for the phase). The findings from this numerical study therefore suggest that the observed difference in the phase can be viewed as insignificant and the changes on the signal profile are dominantly due to the change in the magnitude of the composing sinusoids.

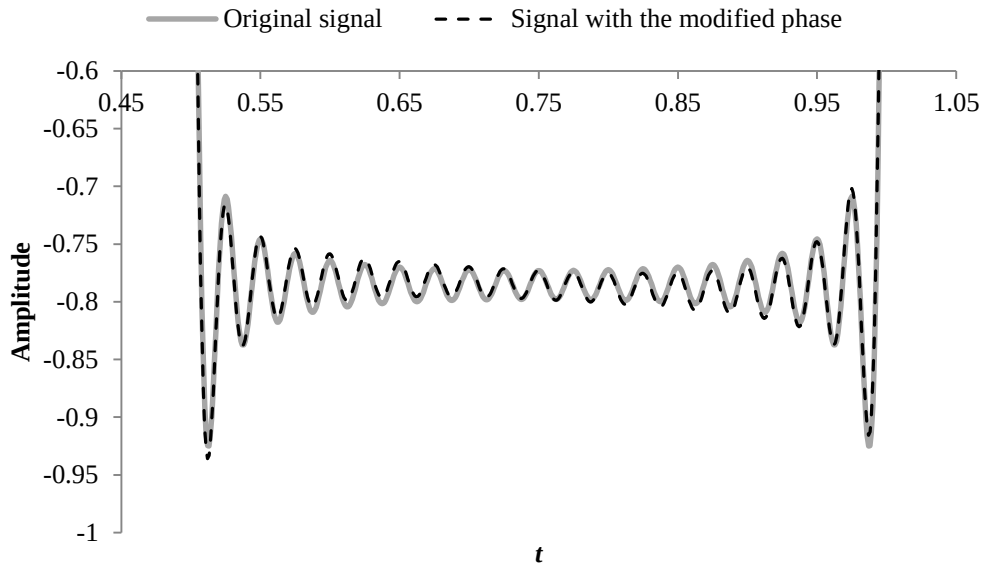

(a) Effect of the magnitude change

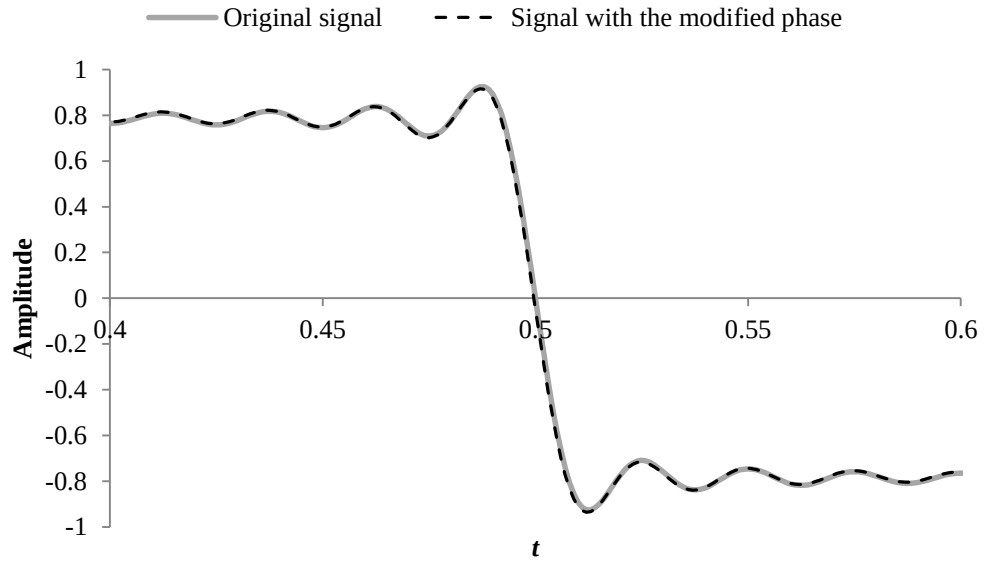

(b) Re-plot of (a) for the time range *t* = 0.4 to 0.6 s

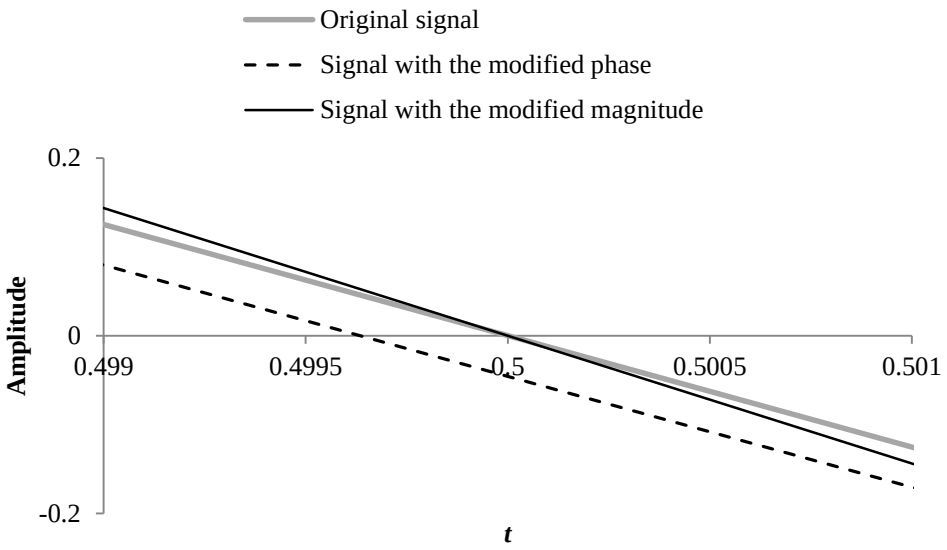

(c) Comparison between the effects from the magnitude and phase changes

Figure 7.41 – Effect of the change in phase of the composing sinusoids

The observed behaviour of F_{12} implies that the leak flow exhibits frequency dependent characteristics. This particular FRF describes the leak flow which is a function of the head at the leak. The leak head was, however, assumed identical to the heads either side of the leak and hence the frequency dependency of the leak head cannot be identified in this study.

7.14 Comparison between two methods of analysis

The time-domain MCA was used to detect the change in the signal width of the leak reflections as a sign of the frequency dependent phenomenon. As the width of the leak reflection is compared to that of the injected signal, these signals must be clearly isolated. This requirement restricts the use of the method only to discrete signals. The analysis was conducted with a single variable—pressure in this case—and the relationship to the flow cannot be examined. To ensure good results with this technique, the analysing signal that is correlated with the transient signals must share the same features as the transient signals.

The frequency-domain method utilises both transient pressure and flow data and examines the unsteady leak effects from all aspects of the signal. From this point of view, it gives a more complete picture of the leak behaviour than the time-domain analysis. This method also offers flexibility in the form of the transient signal and it works well with both discrete and

continuous signals. Since more than one pressure measurements are handled simultaneously in the analysis, the relative accuracy of the pressure sensors is critical for accurate results. A transient generator with good repeatability will also enhance the accuracy. Compared to the time-domain method, the behaviour of higher frequency components are better captured by this frequency approach. However, great care must be taken when interpreting results for the higher frequency components as they are more vulnerable to background noise. Effects of data contamination can be mitigated by employing signals with a large bandwidth to maintain a sufficient signal-to-noise ratio for the frequency range of interest.

7.15 Summary

The behaviour of the orifice-based element in unsteady flow was examined in various ways in the past: in terms of the discharge coefficient of the orifice, the velocity distributions in the neighbourhood of the orifice and the relationship between the pressure and flow at the orifice. This present study aimed to study the dynamic behaviour of a leak by observing the signal dilation, which is a result of frequency-dependent changes on the spectrum of the signal. Two methods were used to detect and quantify the frequency-dependent changes, one in the time domain and the other in the frequency domain.

The multi-correlation analysis (MCA) introduced in Chapter 5 was selected as the time-domain based method of analysis owing to its ability to demonstrate and quantify the dilation of the signals. To suit the aim of the present study, a normalising parameter was added to the original formulation that enabled identification of the best-matching analysing signal to the signal under test. In the experiments, three different-sized leaks were produced by a side discharge valve. The leaks gave reflected signals with magnitudes of 12%, 26% and 45% of the incident signal. The measured pressure traces containing the incident signal and leak refection were analysed by the MCA. The difference in the scale of the best-matching analysing signal for the incident and reflected signals was used as an indication of changes in the signal shape. The results showed that, regardless of the leak size, both the incident and reflected signals gave the best match to the same analysing signal which means that no significant signal dilation took place after encountering the leak. This observation suggests that the effects of an unsteady leak on the pressure signals are frequency independent.

The second method analysed the signals in the frequency domain, which allowed the examination of the influence of a leak on an individual frequency components of the signal. The introduced method determines the system response—referred to as the frequency response matrix (FRM)—of a leak from the measured responses and observes any frequency dependent changes in that response. This FRM is equivalent to an impulse response function (IRF) discussed in Chapter 5, but it is for systems involving more than one input and one output. As with the IRF, the FRM provides the complete characteristics of the system under test and it is independent of the type of the input signal used for its extraction provided a signal bandwidth is similar in all tests. This approach has been successfully applied in the investigations on, for examples, pumps, silencers and automotive compressors.

The FRMs of the pipe reference point (no-leak) and the leak were determined from the measured pressure responses. The comparison of these FRMs exhibited a distinct difference in the magnitude of the matrix entry F_{12} with a maximum difference of 11.8% at a bandwidth frequency of 66 Hz. Since the average results of all leak sizes were clearly outside of the 95 % confidence interval of the no-leak result, the unsteady dynamic effect of these leaks on flow response can be considered frequency dependent. The entry F_{12} describes the characteristics of the flow out of the leak. While this leak flow is related to the leak head, its frequency dependency could not be identified in the present study as the analysis was based on the assumption that the pressure heads at the leak are identical to each other.

Since the entry F_{12} is relatively flat at lower frequencies, the frequency dependent phenomenon would be of concern when the injected signal is sharp and thus contains high frequency components. If it continues depart from the no-leak result with increasing frequency, the use of the steady orifice equation will not be adequate to model the leak behaviour in unsteady transient flows. In order to incorporate the leak effect, the determined F_{12} can be multiplied to the steady-state leak entry F_{12} as an empirical modification factor.

Chapter 8 Conclusions and Recommendations

The aim of this thesis was to present effective ways to utilise fluid transients. While they can cause catastrophic damage to hydraulic structures, they can also offer useful information regarding the system if used appropriately. This thesis explored three ways to make use of transients; in fault detection, measurement of unsteady flow and in the study of the dynamic behaviour of hydraulic systems. Conclusions from each topic are presented individually in the following three sections.

8.1 Conclusions for proposed improvements on conventional impulse response function

Fluid transients are utilised as a pipe condition assessment tool due to their fast travel speed and long transmission range. A transient-based fault detection method uses an impulse response function (IRF) of the pipeline system, which is determined from measured transient signals. The use of an IRF is superior to a measured transient trace because of its input independence and its ability to represent signals with impulses.

However, an experimentally obtained IRF consists of pulses of a finite width instead of impulses. Such a difference is due to a combination of a frequency-dependent phenomenon and a low frequency content of the input signal which was demonstrated in Chapter 5. Since pulses of smooth profile have no clear reference point for identifying travel time, two methods were proposed to improve the conventional IRF—the input-dilation method and multi-scale correlation analysis.

The results from the input-dilation method showed some enhancement in the magnitude and the sharpness of the IRF. However, this method also amplified the noise in the IRF which poses difficulties in locating small signals. Also the maximum achievable magnitude and the sharpness of the IRF are restricted by the low-pass filter used for noise removal and hence the effectiveness of this method is limited.

Another method, the multi-correlation analysis is composed of two processes: denoising using wavelets and signal enhancement via multiple cross correlations. The introduced denoising technique gave a superior result compared to the use of the low-pass filter. It was able to remove both low- and high-frequency noise whilst retaining the sharpness of the IRF. The small pulses from fault reflections were enhanced through iterations of cross correlation. The resultant IRF clearly showed boundary reflections as well as small leak reflections through the presence of ridge and trough lines on the three-dimensional representation of the multiple cross correlations.

The IRF is an attractive tool for analysis and monitoring of a system that offers the above-mentioned benefit. The proposed methods have been shown to provide further confirmation of the extracted IRF and improve its detection ability when dealing with laboratory and field data.

Determination of the IRF only requires measured data of one system variable. Pressure was used in this work because it is the most readily measurable variable in pipelines. As a fault-detection tool, the information provided by the IRF may be sufficient. However, hydraulic systems are often modeled as a system of two variables—pressure and flow—and this additional variable is able to give more detailed information about the system, which will be useful in modeling and understanding the real system dynamics. Yet, the analysis with two variables is hindered by the difficulty in unsteady flow measurements at the same response time and precision as the pressure measurements. This thesis examined the Kinetic Pressure Difference (KDP) method for unsteady flow measurement both numerically and experimentally as a potential technique for high-speed unsteady flow measurements.

8.2 Conclusions for the Kinetic Pressure Difference method for unsteady flow measurements

The Kinetic Pressure Difference (KDP) method gives flow rates from the transient pressure signals and the system wave speed. It is a good candidate for an unsteady flow meter and it has been used in experiments in the past. This part of the thesis provided more detailed verification of the method with the aim of promoting its use under various system conditions.

The accuracy of the method was verified numerically by varying the significance of the neglected nonlinear term arising from the friction term in the momentum equation. The results indicated that the method gives flow predictions with acceptable accuracy (~1%) provided the resonance of the system is avoided. The subsequent experimental verification tested the method under three system conditions. It was observed that the method is better suited to predicting the volume and the maximum magnitude of the flow pulse rather than its profile which is more vulnerable to background noise. The average errors in the predicted flows were in the order of 0.1% for the static steady state and the laminar flow condition, and 1% for the turbulent flow condition.

The sensitivity of the KDP method to various system parameters was examined. The results point to the importance of an accurate wave speed measurement, because the error in this parameter contaminates the predicted flow response.

A case study was presented that considered a scenario with a step flow perturbation which, unlike discrete pulse perturbations, drives the system to go from one state to another. Such a transition of the steady state violates the assumption made in the derivation of the underlying transfer matrix equations and the impact of this violation on the prediction accuracy was investigated. The KDP method was able to capture the form of the flow perturbation very well, but the predicted flow perturbation took place about a different mean flow to that of the correct flow response. This deviation comes from the changing mean states of the measured pressure responses. The difference in the mean flows was 3.53% when the size of the transient was 25.9% of the mean flow, indicating that the KDP method is able to predict the step perturbation with reasonable accuracy even under these conditions. An important implication of this result is that it is possible to measure an instantaneous flow rate solely with pressure transducers.

As an unsteady flow meter, the observed errors are comparable to the accuracy of the existing commercial flow meters in steady flow measurements and thus this study has shown the great potential of this method. The KDP method will be convenient for the use in pipeline systems where pressure transducers are already installed and also for the testing of turbo machinery such as pumps. The field of application may be extended to automobile and aircraft industries where the optimum fuel-to-air ratio of an engine is needed.

The successful verification of the KDP method also means that a more in-depth analysis of system component is possible from the measured pressure trace. The system component of concern was a leak in this thesis and the observation of its dynamic behaviour was made in the time and frequency domains.

8.3 Conclusions for study on unsteady dynamic behaviour of leak

Experimental investigations were carried out both in the time and frequency domains in order to confirm the frequency dependent behavior of leak in rapidly-changing unsteady flow.

The investigation in the time-domain involved detection and quantification of the signal dilation, which is one of the effects of a frequency dependent phenomenon on signals as observed with unsteady friction. The method of analysis was the MCA with a normalising parameter. This new formulation of the MCA was employed to identify the best-matching sinc signal to the signal under test. The dilation of the signal was detected from the difference in the scale of the best-matching sinc signal to each pulse in the pressure trace. The MCA was implemented on the pressure traces with reflections from three different-sized leaks. The results indicated that the leak reflections do not exhibit significant dilation compared to the input signal.

The frequency-domain based method inspected the frequency dependent nature of the leak by extracting its frequency response matrix (FRM), which is equivalent to a frequency response function for systems involving multiple inputs and multiple outputs. From the measured flow and pressure responses, the FRMs of a point in a uniform pipe and the leak were determined experimentally. Amongst the four entries of the FRM, this study focused on two of them. The first one describes a relationship between the flows on either side of the test component (F_{11}) and the other is for the upstream pressure and the downstream flow response (F_{12}). The entry F_{12} was derived from the steady orifice equation and signifies the flow out of the leak. The extracted FRMs showed that the entry F_{11} for the leak and no-leak cases were in close agreement with each other. A significant deviation from the no-leak case was observed with the entry F_{12}. Comparisons of the average results from the two cases gave the maximum differences of 11.8% and 16.3% for the magnitude and phase respectively. Despite the difference in the average results, the average phase of the leak case was found to be near or

within the 95% confidence interval of the leak result, making its deviation from the no-leak case unclear. A more definite deviation was observed with the magnitude of F_{12} whose average result was outside the 95% confidence interval of the no-leak result. It was also found that the 95% confidence intervals of the no-leak and leak results did not overlap. These observations suggest that the parameter F_{12}, and hence the leak flow, exhibits frequency dependent characteristics. While the leak flow is a function of the leak head, due to the assumption made in this study, the frequency dependent nature of the leak head could not be identified.

The methods of analysis in the time and frequency domains were compared. The time-domain method detects the frequency-dependent phenomenon primarily from the change in the signal width and it is less sensitive to the change in the signal profile. In contrast, the frequency-domain based method examines the entire pulse signal for frequency dependent signatures and thus it is considered to be a more detailed method of analysis. Disadvantages of this method include the requirement for high accuracy apparatuses compared to the time-domain method and its susceptibility to background noise.

8.4 Future work

In this thesis, the application and verification of the input-dilation method, MCA and the KDP method were carried out in the laboratory. The effectiveness of these methods should be further tested in a severe field environment with greater noise.

The work on the frequency dependence of leaks demonstrated the behaviour of the lower frequency components. The bandwidth of the investigation should be broadened for a further study that will give a more complete description of leak behaviour. The results will also be enhanced by transducers with improved relative accuracy. The use of accurate transducers may enable tests without a base flow. The experiments carried out in this thesis had a base flow through the system in order to create a large pressure loss in between the transducers. Transducers come with a certain level of uncertainty and the pressure differential between the transducers must be larger than the uncertainty of the transducers for accurate pressure measurements. However, the presence of system base flow induces pressure fluctuations that

appear as noise on the measured pressure. Reduction of the system noise may further improve the accuracy of the results.

Similar studies should be conducted on other hydraulic elements and pipe defects in order to determine if they have distinctive frequency dependent characteristics. Such knowledge will be of considerable value in the development of more accurate numerical models. Since observations made in the frequency domain can be translated to their time-domain equivalent, outcomes of this study will be beneficial for time-domain based condition monitoring techniques.

The work on leaks was meant to be exploratory and this thesis aimed to show an approach that can be taken to investigate the dynamic characteristics of hydraulic components. It is expected for a future study to involve more extensive analysis with a broader parameter range and/or system conditions.

References

Åbom, M. (1991). "Measurement of the scattering-matrix of acoustical two-ports." *Mechanical Systems and Signal Processing*, 5(2), 89-104.

Adamkowski, A. and Lewandowski, M. (2012). "Investigation of hydraulic transients in a pipeline with column separation." *Journal of Hydraulic Engineering*, 138(11), 935-944.

Al-Khomairi, A.M. (2005). "Use of the steady-state orifice equation in the computation of transient flow through pipe leaks." *Arabian Journal for Science and Engineering*, 30(1B), 33-46.

Ambardar, A. (1999). *Analog and Digital Signal Processing*. 2nd Edition, Brooks/Cole Publishing Company, U.S.A.

ASTM E2611-09. (2009). "Standard test method for measurement of normal incidence sound transmission of acoustical materials based on the transfer matrix method."

Ayala-Cabrera, D., Herrera, M., Izquierdo, J., Ocaña-Levario, S. and Pérez-García, R. (2013). "GPR_based water leak models in water distribution systems. *Sensors*, 13

Bailly, C. and Juve, D. (2000). "Numerical solution of acoustic propagation problems using linearized Euler equations." *AIAA journal*, 38(1), 22-29.

Balcomb, J., Demuth, H., and Gyftopoulos, E. (1961). "A crosscorrelation method for measuring the impulse response of reactor systems." *Nuclear Science and Engineering*, 11, 159-166.

Beck, S., Williamson, N., Sims, N., and Stanway, R. (2002). "Pipeline system identification through cross-correlation analysis." *Proceedings of the Institution of Mechanical Engineers, Part E: Journal of Process Mechanical Engineering*, 216(3), 133-142.

Beck, S., Curren, M., Sims, N., and Stanway, R. (2005). "Pipe network features and leak detection by cross-correlation analysis of reflected waves." *Journal of Hydraulic Engineering*, 131(8), 715–723.

Beerends, R.J., ter Morsche, H.G., van den Berg, J.C. and van de Vrie, E.M. (2003). *Fourier and laplace transforms*. Cambridge University Press, UK.

Bendat, J. and Piersol, A. (2010). *Random data: analysis and measurement procedures*. 4th Edition, Hoboken, N.J., John Wiley & Sons.

Bergant, A. and Simpson, A.R. (1994). "Estimating unsteady friction in transient cavitating pipe flow." *2nd International Conference on Water Pipeline Systems*, Edinburgh, Scotland, 3-15.

Bergant, A., Simpson, A.R., and Vítkovský, J.P. (1999). "Review of unsteady friction Models in transient pipe flow." *9th International Meeting on the Behaviour of Hydraulic Machinery Under Steady Oscillatory Conditions*, International Association of Hydraulic Research, Brno, Czech Republic.

Bergant, A., Simpson, A.R., and Vítkovský, J.P. (2001). "Developments in unsteady pipe flow friction modelling." *Journal of Hydraulic Research*, 39(3), 249-257.

Bimpass, M., Amditis, A. and Uzunoglu, N. (2011). "Design and implementation of an integrated high resolution imaging ground penetrating radar for water pipeline rehabilitation." *Water Resource Management*, 25, 1239-1250.

Black, P. (1992). "A review of leak detection technologies." *Pipeline System – Fluid Mechanics of Its Application*, Kluwer Academic Publishers, 287 – 298.

Boij, S. and Nilsson, B. (2003). "Reflection of sound at area expansions in a flow duct." *Journal of Sound and Vibration*, 260(3), 477-498.

Boij, S. and Nilsson, B. (2006). "Scattering and absorption of sound at flow duct expansions." *Journal of Sound and Vibration*, 289(3), 577-594.

Bonfiglio, P., Pompoli, F. and Prodi, N. (2005). "On the comparison of different techniques for measuring complex acoustical properties of fibrous and porous materials." *12th International Congress on Sound and Vibration*, Lisbon, 11-14 July 2005.

Bradley, A. (2003) "Shift-invariance in the discrete wavelet transform." *Proceedings of VIIth Digital Image Computing: Techniques and Applications*, 10-12 December 2003, Sydney.

Brandt, A. (2011). *Noise and vibration analysis: signal analysis and experimental procedures*. Chichester ; Hoboken, N.J. : Wiley, 2011.

Brekke, H. (1984). *A stability study on hydro power plant governing including the influence from a quasi nonlinear damping of oscillatory flow and from the turbine characteristics.* PhD dissertation, University of Trondheim, The Norwegian Institute of Technology.

Brereton, G. J., Schock, H. J., and Bedford, J. C. (2008). "An indirect technique for determining instantaneous flow rate from centerline velocity in unsteady duct flows." *Flow Measurement and Instrumentation*, 19(1), 9-15.

Brunone, B., Golia, U.M., and Greco, M. (1991). “Some remarks on the momentum equation for fast transients.” *Proceedings of International Conferenceon Hydraulic Transients with Water Column Separation*, IAHR, Valencia, Spain, 201-209.

Brunone, B., and Berni, A. (2010). “Wall shear stress in transient turbulent pipe flow by local velocity measurement.” *Journal of Hydraulic Engineering*, 136(10), 716-726.

Brunone, B. (1999). “Transient test-based technique for leak detection in outfall pipes.” *Journal of Water Resources Planning and Management*, ASCE. 125(5), 302 – 306.

Burger, H. C., van Brummelen, A. G. W., and Dannenburg, F. J. (1956). "Theory and experiments on schematized models of stenosis." *Circulation Research, Journal of the American Heart Association*, 4, 425-429.

Carstens, M.R. and Roller, J.M. (1959). “Boundary-shear stress in unsteady turbulent pipe flow.” *Journal of the Hydraulics Division*, 67-81.

Cassa, A., van Zyl, J. and Laubscher, R. (2010). “A numerical investigation into the effect of pressure on holes and cracks in water supply pipes” *Urban Water Journal*, 7(2), 109-120.

Cataldo, A., Persico, R., Leucci, G., De Benedetto, E., Cannazza, G., Matera, L. and DeGiorgi, L. (2014). “Time domain reflectometry, ground penetrating radar and electrical resistivity tomography: A comparative analysis of alternative approaches for leak detection in underground pipes” *NDT&E International*, 62, 14-28.

Catania, A. E., and Ferrari, A. (2009). “Development and assessment of a new operating principle for the measurement of unsteady flow rates in high-pressure pipelines.” *Flow Measurement and Instrumentation*, 20(6), 230-240.

Chatzigeorgiou, D., Youcef-Toumi, K. and Ben-Mensour, R. (2015) “Design of a novel in-pipe reliable leak detector” *IEEE/ASME Transactions on Mechatronics*, 20(2), 824-833.

Chaudhry, M. H. (1987). *Applied Hydraulic Transients*, Van Nostrand Reinhold Company Inc, New York.

Chen, H., Washio, S., and Takahashi, S. (2006). ”Observation of unsteady nonlinear relationship between pressure drop across and flow rate through a restrictor in sinusoidally fluctuating oil hydraulic flows.” *Nihon Kikai Gakkai Ronbunshu, B Hen/Transactions of the Japan Society of Mechanical Engineers*, Part B, 72(8), 1920-1926.

Chen, Y., Sun, Y. and Pickwell-Macpherson, E. (2010). “Improving extraction of impulse response functions using stationary wavelet shrinkage in terahertz reflection imaging.” *Fluctuation and Noise Letters*, World Scientific Publishing Company, 9(4), 387-394.

Clark, C., and Cheesewright, R. (2006). “Experimental determination of the dynamic response of Coriolis mass flow meters.” *Flow Measurement and Instrumentation*, 17(1), 39-47.

Clark, C., Cheesewright, R., and Shiwen, W. (2008). “Prediction of the dynamic performance of fast response Coriolis meter systems.” *IEEE Transactions on Instrumentation and Measurement*, 57(1), 95-9.

Coifman, R. and Donoho, D. (1995). “Translation-invariant de-noising.” *Wavelets and Statistics*, 103, 125-150. Springer, New York.

Collins, R.P., Boxall, J.B., Karney, B.W., Brunone, B. and Meniconi, S. (2012). “How severe can transients be after a sudden depressurization?” *Journal – American Water Works Association*, 104(4), 67-68.

Colombo, A.F. and Karney, B.W. (2002). “Energy and costs of leaky pipes: toward a comprehensive picture.” *Journal of Water Resources Planning and Management*, November/December, pp. 441 – 450.

Colombo, A.F. and Karney, B.W. (2009). “Leaks and water use representation in water distribution system models: Finding a working equivalence.” *Journal of Hydraulic Engineering*, 234–239.

Colombo, A.F., Lee, P.J., and Karney, B.W. (2009). "A selective literature review of transient-based leak detection methods." *Journal of Hydro-environment Research*, 2(4), 212-227.

Contractor, D. N. (1965). "The reflection of waterhammer pressure waves from minor losses." *Journal of Basic Engineering, ASME*, 87, 445-452.

Cosham, A., Hopkins, P. and Macdonald, K. (2007). “Best practice for assessment of defects in pipelines – corrosion” *Engineering Failure Analysis*, 14, 1245-1265.

Covas, D. and Ramos, H. (1999). “Leakage detection in single pipelines using pressure wave behaviour.” *Water Industry System: Modelling and Optimisation Application.* 1, 287–299.

Covas, D., Stoianov, I., Butler, D., Maksimovic, C., Graham, N., and Ramos, H. (2001). “Leakage detection in pipeline systems by inverse transient analysis - from theory to

practice." *Sixth International Conference on Computing and Control in the Water Industry* (*CCWI*), Leicester, England, September 2001.

Covas, D., Ramos, H., and A. Betâmio de Almeida (2005). "Standing wave difference method for leak detection in pipeline systems." *Journal of Hydraulic Engineering*, 131(12), 1106-1116.

Covas, D. and Ramos, H. (2010). "Case studies of leak detection and location in water pipe systems by inverse transient analysis." *Journal of Water Resources Planning and Management*, 136(2), 248-257.

Covas, D., Mano, J., Ramos, H., Graham, N., and Maksimovic, C. (2004). "The dynamic effect of pipe-wall viscoelasticity in hydraulic transients. Part I—experimental analysis and creep characterization." *Journal of Hydraulic Research*, 42(5), 516–530.

Daily, J.W., Hankey, W.L., Olive, R.W. and Jordaan, J.M. (1956). "Resistance coefficients for accelerated and decelerated flows through smooth tubes and orifices." *Transactions of the ASME*, 78, 1071-1077.

Doebelin, E.O. (1990). *Measurement systems: application and design*, McGraw-Hill.

Donoho, D. and Johnstone, I. (1994) "Ideal spatial adaptation vie wavelet shrinkage." *Biometrika*, 81, 425-455.

Dragotti, P. and Vetterli, M. (2000). "Shift-invariant Gibbs free denoising algorithm based on wavelet transform footprints." *Proceedings of SPIE - The International Society for Optical Engineering*, 4119, 821-830.

Duan, H., Lee, P.J, Ghidaoui, M., and Tung, Y. (2010). "Essential system response information for transient-based leak detection methods." *Journal of Hydraulic Research*, 48(5), 650-657.

Duan, H., Lee, P.J, Ghidaoui, M., and Tung, Y. (2011). "Leak detection in complex series pipelines by using system frequency response method." *Journal of Hydraulic Research*, 49(2), 213.

Duan, H., Lee, P.J, Ghidaoui, M., and Tung, Y. (2012a). "System response function based leak detection in viscoelastic pipeline." *Journal of Hydraulic Engineering*, 138(2), 143–153.

Duan, H., Lee, P.J, Ghidaoui, M., and Tung, Y. (2012b). "Extended blockage detection in pipelines by using system frequency response analysis." *Journal of Water Resources Planning and Management*. 138(1), 55–62.

Duan, H., Lee, P.J, Kashima, A., Lu, J., Ghidaoui, M. and Tung, Y. (2013). "Extended blockage detection in pipes using the system frequency response: Analytical Analysis and experimental verification" *Journal of Hydraulic Engineering*, 139, 763-771.

Duan, H., Lee, P.J, Ghidaoui, M., and Tuck, J. (2014). "Transient wave-blockage interaction and extended blockage detection in elastic water pipelines." *Journal of Fluids and Structures*, 46, 2-16.

Durst, F., Ismailov, M., and Trimis, D. (1996). "Measurement of instantaneous flow rates in periodically operating injection systems." *Experiments in Fluids*, 20(3), 178-188.

D'Souza, A. F., and Oldenburger, R. (1964). "Dynamic response of fluid lines." *Journal of Basic Engineering, Transactions of the ASME, Series D*, 83(3), 589-598.

Earles, S. W. E., and Zarek, J. M. (1965). "Reflection of pressure waves at sharp-edged orifices." *Engineer*, 219(5692), 383-386.

Earnhart, N., Marek, K. and Cunefare, K. (2010) "Evaluation of hydraulic silencers" *NOISE-CON 2010*, 19-21 April, Baltimore, Maryland.

Eiswirth, M., and Burn, L.S. (2001). "New methods for defect Diagnosis of water pipelines." *4th International Conference on Water Pipeline* Systems, 28-30 March, York, UK.

El-Abbasy, M., Senouci, A,. Zayed, T., Mirahadi, F. and Parvizsedghy, L. (2014). "Condition prediction models for oil and gas pipelines using regression analysis." *Journal of Construction Engineering and Management*, 140.

Fadali, M.S. and Visioli, A. (2009). *Digital Control Engineering: analysis and design*. Elsevier.

Feng, T., Wang, J., Liu, B., Li, N. and Wu, X. (2011). "Measurement of transfer matrix of the duct silencer." *2011 International Conference on Consumer Electronics, Communications and Networks*, XianNing, China, 16-18 April 2011, 5039-5041.

Ferrante, M. and Brunone, B. (2003). "Pipe system diagnosis and leak detection by unsteady state tests. 1. harmonic analysis." *Advance Water Resources*, 26, 107–116.

Ferrante, M., Massari, C., Brunone, B., and Meniconi, S. (2011). "Experimental evidence of hysteresis in the head-discharge relationship for a leak in a polyethylene pipe." *Journal of Hydraulic Engineering*, 137(7), 775-780.

Ferrante, M. (2012). "Experimental investigation of the effects of pipe material on the leak head-discharge relationship." *Journal of Hydraulic Engineering*, 138, 736-743.

Fodor, I. and Kamath, C. (2003). "Denoising through wavelet shrinkage: an empirical study." *Journal of Electronic Imaging*, 12(1), 151-160.

Föller, S. and Polifke, W. (2010). “Determination of acoustic transfer matrices via large eddy simulation and system identification.” *16th AIAA/CEAS Aeroacoustics Conference*, Stockholm, Sweden, 7-9 June 2010.

Föller, S., Polifke, W. and Tonon, D. (2010). “Aeroacoustic characterization of t-junctions based on large eddy simulation and system identification.” *16th AIAA/CEAS Aeroacoustics Conference*, Stockholm, Sweden, 7-9 June 2010.

Föller, S. and Polifke, W. (2012). “Identification of aero-acoustic scattering matrices from large eddy simulation. Application to a sudden area expansion of a duct.” *Journal of Sound and Vibration*, 331(13), 3096-3113.

Fuchs, H. and Riehle, R. (1991). “Ten years of experience with leak detection by acoustic signals analysis.” *Applied Acoustic*. 33, 1-19.

Fugal, L. (2009). *Conceptual wavelets in digital signal processing: an in-depth, practical approach for the non-mathematician*. Space & Signals Technical Publishing.

Funk, J. E., Wood, D. J., and Chao, S. P. (1972). "The transient response of orifices and very short lines." *Journal of Basic Engineering, Transactions of the ASME, Series D*, 94(2, June), 483-491.

Gajan, P., Mottram, R., Hebrard, P., Andriamihafy, H. and Platet, B. (1992). “The influence of pulsating flows on orifice plate flowmeters” *Flow Measurement and Instrumentation*, 3(3), 118-129.

Gong, J., Lambert, M., Simpson, A. and Zecchin, A. (2012). “Distributed deterioration detection in single pipes using the impulse response function” 14th Water Distribution Systems Analysis Conference, Adelaide, SA, Australia, 24-27 Septemper.

Graf, F. (1990). “Using ground-penetrating radar to pinpoint pipeline leaks.” *Materials Performance*, 29 (4) (1990), 27–29.

Guendel, R.E., and Cesnik, C.E.S. (2001). “Aerodynamic impulse response of a panel method.” *42nd AIAA/ASME/ASCE/AHS/ASC Structures, Structural Dynamics, and Materials Conference*, Seattle, WA, United States; 16 - 19 April 2001, 1, 242-254.

Guo, X., Yang, K., and Guo, Y. (2008). “Hydraulic pressure signal denoising using threshold self-learning wavelet algorithm.” *Journal of Hydrodynamics*, 20(4), 433-439.

Gyaourova, A., Kamath, C. and Fodor, I. (2002). “Undecimated wavelet transforms for image de-noising.” *Technical report*, Lawrence Livermore National Laboratory, Livermore.

Hatemi-J, A. (2014). “Asymmetric generalized impulse response with an application in finance.” *Economic Modelling*, 36, 18-22.

Hayase, T., Cheng, P. and Hayashi, S. (1995). “Numerical analysis of transient flow through a pipe orifice.” *JSME International Journal, Series B*, 38(2), 157-163.

Hazelden, G., Ragula, G., and Roubal, M. (2003). "The use of broadband electromagnetic technology for integrity inspection of a 760 mm (30 in.) cast iron and steel line." *22nd World Gas Conference*, Tokyo, Japan, 1-6.

Henry, M. P., Clark, C., Duta, M., Cheesewright, R., and Tombs, M. (2003). ”Response of a Coriolis mass flow meter to step changes in flow rate.” *Flow Measurement and Instrumentation*, 14(3), 109-18.

Holmboe, E.L. and Rouleau,W.T. (1967). “The effect of viscous shear on transients in liquid lines.” *Journal of Basic Engineering, Transactions of the American Society of Mechanical Engineers*, 89, 174-180.

Hopkins, P. (2007). “Pipelines: Past, present and future.” *The 5th Asian Pacific IIW International Congress*, Sydney, Australia, 7-9 March 2007.

Hu, Y., Galland, M.A. and Chen, K. (2012). “Acoustic transmission performance of double-wall active sound packages in a tube: Numerical/experimental validations.” *Applied Acoustics*, 73(4), 323-337.

Hua, X. and Herrin, D.W. (2013). “Practical considerations when using the two-load method to determine the transmission loss of mufflers and silencers.” *SAE International Journal of Passenger Cars-Mechanical Systems*, 6(2), 1094-1101.

Hughes, P. (2012). “Repairing subsea pipelines without welding.” *Offshore World*, 18.

Jaeger, C. (1977). *Fluid Transients*. Blackie & Son Limited, Bishopbriggs, Glasgow.

Japan Water Research Centre. (2013). “Leakage rate in the United Kingdom”. *Hot News*, 363. (in Japanese)

Johnston, D., Longmore, D. and Drew, J. (1994). “A technique for the measurement of the transfer matrix characteristics of two-port hydraulic components.” *Fluid Power Systems and Technology*, 1, 25-33.

Jol, H.M. and Smith, D.G. (1995). “Ground penetrating radar surveys of peatlands for oilfield pipelines in Canada.” *Journal of Applied Geophysics*, 34(2), 109-123.

Jönsson, L. (2001). “Experimental studies of leak detection using hydraulic transients.” *Proceedings of International Conference of 29th IAHR Congress*, IAHR, Beijing, China.

Jönsson, L., and Larson, M. (1992). “Leak detection through hydraulic transient analysis.” *Pipeline systems*, Kluwer Academic Publishers, Netherland, 273–286.

Joy, J., Peter, A. and John, N. (2013). “Denoising using soft thresholding.” *International Journal of Advanced Research in Electrical, Electronics and Instrumentation Engineering*, 2(3), 1027-1032.

Kawamata, M., Suita, M., and Honda, F. (1977). "Unsteady characteristics of orifices in decreasing flows." *Journal of the Faculty of Engineering, Ibaraki University*(25), 41-47.

Khulief, Y.A., Khalifa, A., Mansour, R.B. and Habib, M.A. (2012). “Acoustic detection of leaks in water pipelines using measurements inside pipe.” *Journal of Pipeline Systems Engineering and Practice*, 3(2), 47-54.

Kierkegaard, A., Boij, S. and Efraimsson, G. (2010). “A frequency domain linearized Navier–Stokes equations approach to acoustic propagation in flow ducts with sharp edges.” *Journal of Acoustic Society of America*, 127(2), 710-719.

Kierkegaard, A., Boij, S. and Efraimsson, G. (2012). “Simulations of the scattering of sound waves at a sudden area expansion.” *Journal of Sound and Vibration*, 331 (5), 1068-1083.

Kim, S. H. (2005). “Extensive development of leak detection algorithm by impulse response method.” *Journal of Hydraulic Engineering*, 131(3), 201–208.

Kim, Y. (2008). *Advanced Numerical and Experimental Transient Modelling of Water and Gas Pipeline Flows Incorporating Distributed and Local Effects*. PhD thesis, University of Adelaide.

Kishawy, H.A. and Gabbar, H.A. (2010). “Review of pipeline integrity management practices.” *International Journal of Pressure Vessels and Piping*, 87(7), 373-380.

Kojima, E. and Edge, K. (1994). “Experimental determination of hydraulic silencer transfer matrices and assessment of the method for use as a standard test procedure.” 7th *bath International Fluid Power Workshop*, September, 1994, 221-241.

Kooijman, G., Testud, P., Aurégan, Y. and Hirschberg, A. (2008). “Multimodal method for scattering of sound at a sudden area expansion in a duct with subsonic flow.” *Journal of Sound and Vibration*, 310(4-5), 902-922.

Kunio, J., Yoo, T., Hou, K., Bolton, J.S. and Enok, J. (2009). “A comparison of two and four microphone standing wave tube procedures for estimating the normal incidence absorption coefficient.” *38th International Congress and Exposition on Noise Control Engineering 2009, INTER-NOISE 2009*, 2, 1057-1065.

Lacombe, R., Föller, S., Jasor, G., Polifke, W., Aurégan, Y. and Moussou, P. (2013). "Identification of aero-acoustic scattering matrices from large eddy simulation. Application to whistling orifices in duct." *Journal of Sound and Vibration*, 332(20), 5059-5067.

Lee, P.J., Vítkovský, J.P., Lambert, M.F., Simpson, A.R., and Liggett, J. (2004). "Frequency response leak detection using inline valve closures." *9th International Conference on Pressure Surges*, BHR Group, 24-26 March, Chester, UK, 239-253.

Lee, P.J. (2005). *Using system response functions of liquid pipelines for leak and blockage detection*. PhD Thesis. University of Adelaide.

Lee, P.J., Vítkovský, J.P., Lambert, M.F., Simpson, A.R., and Liggett, J. (2005a). "Frequency domain analysis for detecting pipeline leaks." *Journal of Hydraulic Engineering*, 131(7), 596–604.

Lee, P.J., Vítkovský, J.P., Lambert, M.F., Simpson, A.R., and Liggett, J. (2005b). "Leak location using the pattern of the frequency response diagram in pipelines: A numerical study." *Journal of Sound and Vibration*, 284(3), 1051–1073.

Lee, P.J., Lambert, M., Simpson, A., and Vítkovský, J.P. (2006a). "Experimental verification of the frequency response method of leak detection." *Journal of Hydraulic Research*, 44 (5), 451-468.

Lee, P.J., Vítkovský, J.P., Lambert, M.F., Simpson, A.R., and Liggett, J. (2006b). "Experimental verification of leak detection in pipelines using linear transfer functions." *Journal of Hydraulic Research*, 44(5), 693–707.

Lee P.J., Vítkovský, J.P., Lambert, M.F., Simpson, A.R., Liggett, J. (2007a). "Leak location in pipelines using the impulse response function." *Journal of Hydraulic Research*, 45(5), 643-652.

Lee, P.J., Lambert, M.F., Simpson, A.R., Vítkovský, J.P. and Misiunas, D. (2007b). "Leak Location in Single Pipelines Using Transient Reflections." *Australian Journal of Water Resources*, 11(1), 53-65.

Lee, P.J. and Vítkovský, J.P. (2008). "Discussion of standing wave difference method for leak detection in pipeline systems" by Dídia I. C. Covas, Helena M. Ramos, António Betâmio de Almeida. *Journal of Hydraulic Engineering*, 137(7), 1027–1029.

Lee, P.J., Vítkovský, J.P., Lambert, M.F., Simpson, A.R., Liggett, J.A. (2008). "Discrete blockage detection in pipelines using the frequency response diagram: numerical study." *Journal of Hydraulic Engineering*, 134(5), 658–663.

Lee, P.J., Duan, H., Ghidaoui, M., and Karney, B. (2013). “Frequency domain analysis of pipe fluid transient behaviour.” *Journal of Hydraulic Research*, 51(6), 609-622.

Lee, P.J., Duan, H., Tuck, J., and Ghidaoui, M. (2014). “Numerical and experimental study on the effect of signal bandwidth on pipe assessment using fluid transients.” *Journal of Hydraulic Engineering*, 141(2), 04014074.

Li, H., Dallabetta, M., and Demuth, H. (1994). “Measuring the impulse response of linear systems using an analog correlator.” *Proceedings of the 1994 IEEE Symposium on Circuits & Systems*, Part 5, May 30-June 2, London, England, 65-68.

Liggett, J.A. and Chen, L. (1994). “Inverse transient analysis in pipe network.” *Journal of Hydraulic Engineering*, ASCE. 120(8), 934 – 955.

Liou, C.P., and Tian, J. (1995). “Leak detection – transient flow simulation approaches.” *Journal of Energy Resource Technology*, Transactions of ASME, September, 117, 243-248.

Liou, J.C. (1998). “Pipeline leak detection by impulse response extraction.” *Journal of Fluids Engineering*, ASME. 120, 833 – 838.

Liu, J., Li, X. and Zhang, H. (2009). “Noise reduction for oil pipline pressure time series based on wavelet filtering technology”. *Proceedings of the IEEE International Conference on Automation and Logistics Shenyang*, China, August 2009.

Liu, Z., Kleiner, Y., Rajani, B., Wang, L. and Condit, W. (2012). “Condition assessment technologies for water transmission and distribution systems.” Office of Research and Development, National risk management Research Laboratory – Water Supply and Water Resources Division.

Ljung, L. (1999). *System identification: theory for the user*. P T R Prentice Hall, Englewood Cliffs, New Jersey.

Lung, T and Doige, A.G. (1983). “A time-averaging transient testing method for acoustic properties of piping systems and mufflers with flow.” *Journal of Acoustic Society of America*, 73(3), 867-876.

Lynn, P. (1982). *An introduction to the analysis and processing of signals*. The Macmillan Press Ltd, London and Basingstoke.

McCloy, D. (1966). "Effects of fluid inertia and compressibility on the performance of valves and flow meters operating under unsteady conditions." *Journal of Mechanical Engineering Science*, 8(1), 52-61.

Mangell, A. (2008). “*Go with the flow*”. Nuclear Engineering International, 53, 18-19.

Manhartsgruber, B. (2008). “Instantaneous liquid flow rate measurement utilizing the dynamics of laminar pipe flow.” *Journal of Fluids Engineering*. 130, 1214021-1214028.

Marie-Magdelein, A., Fortes-Patella. R., Lemoine. N. and Marchand, N. (2012). “Application of unsteady flow rate evaluations to identify the dynamic transfer function of a CavitatingVenturi.” *IOP Conf. Series: Earth and Environmental Science*, 15, 26th IAHR Symposium on Hydraulic Machinery and Systems.

Martin, D.J. and Burrows, C.R. (1979). “The dynamic characteristics of an electro-hydraulic servovalve.” *Journal of Dynamic Systems, Measurement, and Control*, 98(4), 395-406.

Martins, J.C. and Seleghim, P.Jr. (2010). “Assessment of the performance of acoustic and mass balance method for leak detection in pipelines for transporting liquids.” *Journal of Fluids Engineering*, 132(1), 0114011-0114018.

Meniconi, S., Brunone, B., and Ferrante, M. (2011a). “In-line pipe device checking by short period analysis of transient tests.” *Journal of Hydraulic Engineering*, 713–722.

Meniconi, S., Brunone, B., Ferrante, M., and Massari, C. (2011b). “Potential of transient tests to diagnose real supply pipe systems: What can be done with a single extemporary test.” *Journal of Water Resources Planning and Management*, 238–241.

Meniconi, S., Brunone, B., and Ferrante, M. (2012). “Water hammer pressure waves at cross-section changes in series in viscoelastic pipes.” *Journal of Fluids Structures*, 33(1), 44–58.

Meniconi, S., Duan, H., Lee, P.J., Brunone, B., Ghidaoui, M. and Ferrante, M. (2013). “Experimental investigation of coupled frequency and time-domain transient test-based techniques for partial blockage detection in pipelines.” *Journal of Hydraulic Engineering*, 139(10), 1033-1040.

Mohapatra, P. and Chaudhry, M. (2011). “Frequency responses of single and multiple partial pipeline blockages.” *Journal of Hydraulic Research*, 49(2), 263-266.

Moody, L.F. and Princeton, N.J. (1944). “Friction factors for pipe flow.” Transactions of the ASME. 66(8), 671-684.

Mpesha, W., Gassman, S.L. and Chaudhry, M.H. (2001). “Leak detection in pipes by frequency response method.” *Journal of Hydraulic Engineering*, ASCE. 127(2), 134-147.

Mpesha W., Chaudhry, M.H. and Gassman, S.L. (2002) "Leak detection in pipes by frequency response method using a step excitation." *Journal of Hydraulic Research*. 40(1), 55-62.

Munjal, M. L. (1987). *Acoustic ducts and mufflers with application to exhaust and ventilation system design*. New York, Wiley.

Munjal, M. L. and Doige, A. G. (1990). "Theory of a two source-location method for direct experimental evaluation of the four-pole parameters of an aeroacoustic element." *Journal of Sound and Vibration*, 141(2), 323-333.

Nakamura, H., Asano, I., Adachi, M., and Senda, J. (2005). "Analysis of pulsating flow measurement of engine exhaust by a Pitot tube flowmeter." *International Journal of Engine Research*, 6(1), 85-93.

Nash, G. and Karney, B. (1999). "Efficient inverse transient analysis in series pipe systems." *Journal of Hydraulic Engineering*, 125(7), 761-764.

Nayak, C. (2014). "Fault detection in fluid flowing pipes using acoustic method." *International Journal of Applied Engineering Research*, 9(1), 23-28.

Ozevin, D. and Yalcinkaya, H. (2014). "New leak localization approach in pipelines using single-point measurement." *Journal of Pipeline Systems Engineering and Practice*, 5(2), 04013020.

Pan, Q., Zhang, L., Dai, G. and Zhang, H. (1999). "Two denoising methods by wavelet transform." *IEEE Transactions on Signal Processing*, 47(12), 3401-3406.

Pedrosa, A.M., Denia, F.D. and Fuenmayor, F.J. (2011). "Experimental measurement of acoustic properties by a tow source method with simultaneous excitation." *18th International Congress of Sound & Vibration*, Rio De Janeiro, Brazil, 10-14 July, 2011.

Peng, Z., Liu, Y. and Han, X. (2012). "Application research of the signal processing method based on db5 wavelet transform in leakage location of ship pipeline." *Applied Mechanics and Materials*, 203, 103-107.

Pereira, M. (2009). "Flow meters Part 1 18 in a series of tutorials in instrumentation and measurement." *IEEE Instrumentation & Measurement Magazine*, 12(1), 18-26.

Pezzinga, G. (2000). "Evaluation of unsteady flow resistances by quasi-2D or 1D models." *Journal of Hydraulic Engineering.* 126(10), 778-785.

Pezzinga, G. (2009). "Local balance unsteady friction model." *Journal of Hydraulic Engineering*. 135(1), 45-56.

Phillips, C. and Parr, J. (1995). *Signals, systems, and transforms*. Englewood Cliffs, N.J., Prentice Hall.

Polifke, W., Poncet, A., Paschereit, C. and Döbbeling, K. (2001). "Reconstruction of acoustic transfer matrices by instationary computational fluid dynamics." *Journal of Sound and Vibration*, 245(3), 483-510.

Pota, H.R. (1996). "MIMO systems—Transfer Function to State-Space." *IEEE Transactions on Education*, 39(1).

Prenner, R.K. (2000) "The calculation of the transient response of small orifices in the lateral pipe of a T-junction". *4th International Conference on Hydroscience & Engineering*, Seoul, Korea, 26 - 29 September, Proceedings, Sep. 2000.

Prieto, G.A., Lawrence, J.F. Chung, A.I. and Kohler, M.D. (2010). "Impulse response of civil structures from ambient noise analysis." *Bulletin of the Seismological Society of America*, 100(5), 2322-2328.

Rachid, F.B.F. and Mattos, H.S.C. (1998). "Modelling of pipeline integrity taking into account the fluid-structure interaction." *International Journal of Numerical Methods in* Fluids, 28(2), 337-355.

Ramos, H., Covas, D. and Borga, A. (2004). "Surge damping analysis in pipe systems: modeling and experiments." *Journal of Hydraulic Research*, 42(4), 413-425.

Rao, P. and Morris, P. (2006). "Use of finite element methods in frequency domain aeroacoustics." *AIAA Journal*, 44(7), 1643-1652.

Raufi, F. and Bahar, O. (2012). "Simulation study of damage detection in steel shear frame buildings using impulse response and wavelet analysis." *Scientific Research and Essays*, 7(24), 2122-2142.

Romagnoli, J.A. and Palazoglu, A. (2006). *Introduction to process control.* Taylor & Francis

Rousselet, B., Gibiat, V., Guilain, S. and Lefebvre, A. (2013). "Determination of the transfer matrix of an automotive compressor under realistic flow conditions." *Proceedings of Meetings on Acoustics*, 19(1).

Sabra, K.G., Winkel, E.S., Bourgoyne, D.A., Elbing, B.R., Ceccio, S.L., Perlin, M. and Dowling, D.R. (2007). "Using cross correlations of turbulent flow-induced ambient vibrations to estimate the structural impulse response. Application to structural health monitoring." *Journal of Acoustical Society of America*, 121(4), 1987-1995.

Sattar, A.M. and Chaudhry, M.H. (2008). "Leak detection in pipelines by frequency response method." *Journal of Hydraulic Research*, 46(sup1), 138-151.

Shibata, A. (2014). *Mizu de sekai wo seisuru nippon*. PHP Kenkyuuzyo. (in Japanese)

Silva, R.A., Buiatti, C. M., Cruz, S. L., and Pereira, J. A. F. R. (1996). "Pressure wave behaviour and leak detection in pipelines." *Computers & Chemical Engineering*, 20, 491-S496.

Silva, W.A., Piatak, D.J., and Scott, R.C. (2005). "Identification of experimental unsteady aerodynamic impulse responses." *Journal of Aircraft*, 42(6), 1548-1552

Skwarek, V., Windorfer, H., Hans, V. (2001). "Measuring pulsating flow with ultrasound." *Measurement*, 29, 225-36.

Smith, L.A., Field, K.A., Chen, A.S.C., and Tafuri, A.N. (2000). "Options for leak and break detection and repair for drinking water systems." *Battelle Press*, Columbus, Ohio, USA.

Smith, S. (1999). *The Scientist and Engineer's Guide to Digital Signal Processing*. 2nd Edition, California Technical Publishing, San Diego, California.

Soares, A.K., Covas, D.I.C., and Reis, L.F.R. (2008). "Analysis of PVC pipe-wall viscoelasticity during water hammer." *Journal of Hydraulic Engineering*, 134(9), 1389-1394.

Song, B. and Bolton, J. (2000). "A transfer-matrix approach for estimating the characteristic impedance and wave numbers of limp and rigid porous materials." *Journal of Acoustical Society of America*, 107(3), 1131-1152.

Srirangarajan, S., Allen, M., Preis, A., Iqbal, M., Lim, H.B. and Whittle, A.J. (2013). "Wavelet-based burst event detectionand localization in water distribution systems." *Journal of Signal Processing Systems*, 72(1), 1-16.

Stephens, M., Lambert, M., Simpson, A., Vítkovský, J. and Nixon, J. (2005). "Using field measured transient responses in a water distribution system to assess valve status and network topology." *7th Annual Symposium on Water Distribution Systems Analysis*, American Society of Civil Engineers, 15-19 May, Anchorage, Alaska, USA.

Stirnemann, A., Eberl, J., Bolleter, U. and Pace, S. (1987). "Experimental determination of the dynamic transfer matrix for a pump." *Journal of Fluid Engineering*, 109, 218-225.

Streeter, V. L., Wylie, E. B., and Bedford, K. W. (1998). *Fluid Mechanics*, WCB/McGraw-Hill.

Suo, L. and Wylie, E.B. (1989). "Impulse response method for frequency dependent pipeline transients." *Journal of Fluids Engineering*, 111(12), 478-483.

Szymkiewicz, R. and Mitosek, M. (2014). “Alternative convolution approach to friction in unsteady pipe flow.” *Journal of Fluids Engineering*, 136(1).

Tafuri, A. (2000). “Locating leaks with acoustic technology.” *Journal of AWWA*. 92(7), 57-66.

Takadou, S. (2011). *Tokoton yasashii suidou no hon*. Nikkan Kougyou Shinbunsya. (in Japanese)

Tamura, E. and Iwamoto, J. (2005). “A study on pulsating flow through a pipe with an orifice (An observation of flow field by Laser Doppler Velocimeter) (Japanese).” *Nihon Kikai Gakkai Ronbunsyu, Series B*, 71(704), 47-54.

Tang, X., Liu, Y. and Zheng, L. and Wang, C. (2009) “Leak detection of water pipeline using wavelet transform method.” *2009 International Conference on Environmental Science and Information Application Technology*. 217-220.

Teixeira, A. P., Guedes Soares, C., Netto, T. A., and Estefen, S. F. (2008). "Reliability of pipelines with corrosion defects." *International Journal of Pressure Vessels and Piping*, 85(4), 228-237.

Thornton, J., Sturm, R. and Kunkel, G. (2008). *Water loss control*. 2nd Edition, McGraw Hill.

To, C. and Doige, A. (1979a). “A transient testing technique for the determination of matrix parameters of acoustic systems, I: Theory and principles.” *Journal of Sound and Vibration*, 62(2), 207-222.

To, C. and Doige, A. (1979b). “A transient testing technique for the determination of matrix parameters of acoustic systems, II: Experimental procedures and results.” *Journal of Sound and Vibration*, 62(2), 223-233.

Todorovska, M.I. and Trifunac, M.D. (2008). “Earthquake damage detection in the Imperial County Services Building III: Analysis of wave travel times via impulse response function.” *Soil Dynamics and Earthquake Engineering*, 28(5), 387-404.

Torrence, C. and Compo, G. (1998). “A practical guide to wavelet analysis.” *Bulletin of the American Meteorological Society*, 79(1), 61-78.

Trengrouse, G.H., Imrie, B.W. and Male, D.H. (1966). “Comparison of unsteady flow discharge coefficients for sharp-edged orifices with steady flow values.” *Journal of Mechanical Engineering Science*, 8(3), 322-329.

Unsal, B., Trimis, D., and Durst, F. (2006). ”Instantaneous mass flowrate measurements through fuel injection nozzles.” *International Journal of Engine Research*, 7(5), 371-380.

Utsuno, H., Tanaka, T., Fujikawa, T. and Seybert, A.F. (1989). “Transfer function method for measuring characteristics impedance and propagation constant of porous material.” *Journal of Acoustical Society of America*, 86(2), 637-643.

Vardy, A.E., Hwang, K-L, and Brown, J.M. (1993). “A weighting function model of transient turbulent pipe friction.” *Journal of Hydraulic Research*, 31(4), 533-548.

Vardy, A.E. and Brown, J.M.B. (1995). “Transient, turbulent, smooth pipe friction.” *Journal of Hydraulic Research*, 33(4), pp. 435 – 456.

Vardy, A.E. and Brown, J.M.B. (2003). “Transient turbulent friction in smooth pipe flows.” *Journal of Sound and Vibration*, 259(5), 1011-1036.

Vardy, A.E. and Brown, J.M.B. (2004). “Transient turbulent friction in fully rough pipe flows.” *Journal of Sound and Vibration*, 270(1-2), 233-257.

Versteeg, H. and Malalasekera, W. (2007). *An introduction to computational fluid dynamics: The finite volume method*. 2nd Edition, Harlow, England.

Vítkovský, J.P., Lambert, M.F., Simpson, A.R., and Bergant, A. (2000). “Advances in Unsteady Friction Modelling in Transient Pipe Flow.” *The 8th International Conference on Pressure Surges*, BHR, Hague, Netherlands, 471-482.

Vítkovský, J.P. (2001). *Inverse analysis and modelling of unsteady pipe flow: theory, applications and Experimental verification*. PhD Thesis, University of Adelaide.

Vítkovský, J.P., Simpson, A.R., Lambert, M.F. (2002). “Minimization Algorithms and Experimental Inverse Transient Leak Detection.” EWRI, Roanoke VA.

Vítkovský, J. P., Lee, P. J., Stephens, M. L., Lambert, M. F., Simpson, A. R., and Liggett, J. A. (2003a). "Leak and blockage detection in pipelines via an impulse response method." *Pumps, Electromechanical Devices and Systems Applied to Urban Water Management*, Valencia, Spain, 423–430.

Vítkovský, J.P., Liggett, J.A., Simpson, A.R., Lambert, M.F. (2003b). “Optimal measurement site locations for inverse transient analysis in pipe networks.” *Journal of Water Resources Planning and Management*, 129 (6), 480-491.

Vítkovský, J.P., Bergant, A., Lambert, M.F., Simpson, A.R. (2003c). “Unsteady Friction Weighting Function Determination from Transient Responses.” *Pumps, Electromechanical Devices and Systems Applied to Urban Water Management*, Valencia, Spain, 781-789.

Vítkovský, J.P., Bergant, A., Simpson, A.R. and Lambert, M.F. (2006). “Systematic evaluation of one-dimensional unsteady friction models in simple pipelines.” *Journal of Hydraulic Engineering*, 132(7), 696-708.

Vítkovský, J. P., Lambert, M. F., Simpson, A. R., and Liggett, J. A. (2007). "Experimental observation and analysis of inverse transients for pipeline leak detection." *Journal of Water Resources Planning and Management*, 133(6), 519-530.

Wang, R., Wang, Z., Wang, X., Yang, H. and Sun, J. (2014). “Pipe burst risk state assessment an classification based on water hammer analysis for water supply networks.” *Journal of Water Resources Planning and Management*, 140(6).

Wang, X.J., Lambert, M.F., Simpson, A.R., Liggett, J.A. and Vítkovský, J.P. (2002). “Leak Detection in Pipeline Systems Using the Damping of Fluid Transients.” *Journal of Hydraulic Engineering*, 128(7), 697 – 711.

Wang, X.-J., Lambert, M.F., and Simpson, A.R. (2005). “Detection and location of a partial blockage in a pipeline using damping of fluid transients.” *Journal of Water Resources Planning and Management*, 131(3), 244-249.

Washio, S., Takahashi, S., Yu, Y., and Yamaguchi, S. (1996). “Study of unsteady orifice flow characteristics in hydraulic oil lines.” *Journal of Fluids Engineering*, 118(4), 743-748

Wiklund, D. and Peluso, M. (2002) “Quantifying and specifying the dynamic response of flowmeters.” 810-822.

Wylie, E. B., and Streeter, V. L. (1993). *Fluid Transients in Systems*, Prentice Hall, Englewood Cliffs, New Jersey, USA.

Yamaguchi, A. (1976). “Non-steady characteristics of orifices.” *Bulletin of the JSME*, 19(131), 505-512.

Yang, J., Wen, Y., Li, P. and Wang, X. (2013). “Study on an improved acoustic leak detection method for water distribution systems.” *Urban Water Journal*, 10(2), 71-84.

Yokota, S., Kim, D., and Nakano, K. (1992). “An Unsteady Flow Rate Measurement Method Utilizing Dynamic Characteristics between Pressure and Flow rate along a Pipeline.” *JSME International Journal*, 35(4), 591-597.

YongLiang, Z. and Vairavamoorthy, K. (2005). “Analysis of transient flow in pipelines with fluid-structure interaction using method of lines.” *International Journal of Numerical Methods in Engineering*, 63(10), 1446-1460.

Young, R.K. (1993). *Wavelet Theory and Its Applications*. Kluwer Academic Publishers.

Zhao, T., Kitagawa, A., Kagawa, T., and Takenaka, T. (1987). "A real time method of measuring unsteady flow rate and velocity employing differential pressure in a pipe." *JSME International Journal*, 30(260), 263-270.

Zielke, W. (1968). "Frequency-dependent Friction in Transient Pipe Flow." *Journal of Basic Engineering*, 90, 109-115.

APPENDIX Sensitivity analysis of the FRM extraction method

The implementation of the FRM extraction method in real systems may be affected by several kinds of error. The error types can be largely split into two categories and the first one is the error in measurements. The second type of error arises when handling time-domain signals. The sensitivity of the method to these errors was investigated. This analysis aims to identify errors that give a frequency-dependent trend to the extracted FRM. The induced transient signal was an impulse. Throughout this section of work, the transducer measuring the upstream response (h_1 and q_1) was assumed to contain errors. Refer to Figure A1 for the configuration of the test setup.

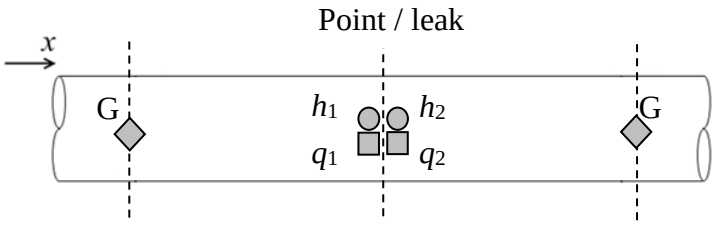

Figure A1 – Test setup

A.1 Effect of inconsistent gains of transducers

An inconsistent gain of transducer leads to a discrepancy in signal amplitude. It was assumed that the transducer upstream of the pipe point had an error of ± 1% and + 10% in its gain respectively. The magnitudes of the resultant F_{11} are show in Figure A2 which shows that the positive 1% error led to a reduction in magnitude by 1% of the true response and vice versa. The difference in the magnitude grew with the degree of error between the transducers. The magnitude of F_{22} exhibited the same behaviour as F_{11} and the other FRFs remained insignificant. While the magnitudes of the FRFs were affected by the inconsistent transducer gains, their behaviour with frequency was unchanged.

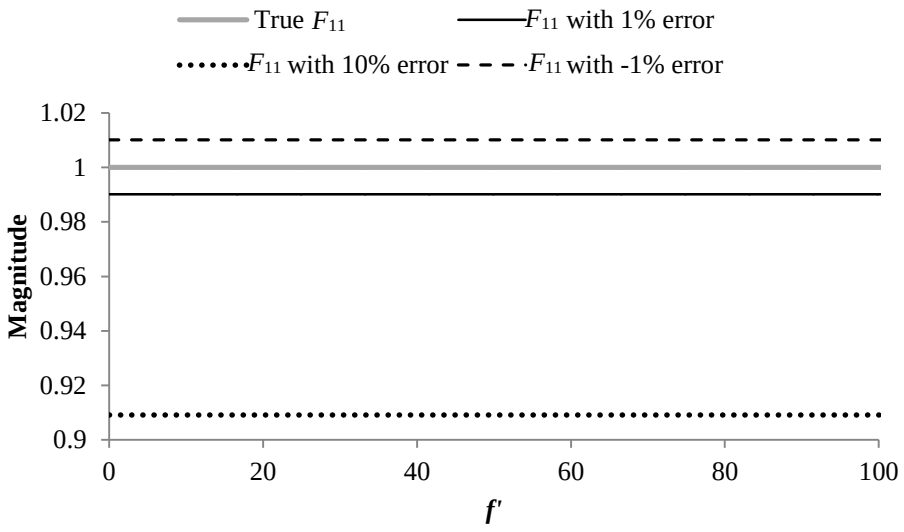

Figure A2 – Magnitude of F_{11} with relative error in the transducer gains

A.2 Effect of judgement of signal boundaries

During experiments, the base pressure fluctuates because of the base flow. This fluctuation makes it difficult to identify the start and the end point of signals. The effect of fluctuation is more severe for leak reflections due to their small magnitude. In the following example, the sensitivity of the choice of the base level was examined. The original pressure trace is presented in Figure A3 (a), in which the small positive pulse signal (circled in the figure) was the leak reflection. Figure A3 (b) gives the seven leak reflections (labelled as Reflection 1 through to Reflection 7) used for this sensitivity test. These were produced by shifting the base level in Figure A3 (a) by - 0.08 m, - 0.05 m, - 0.02 m, 0, 0.02 m, 0.05 m and 0.08 m of pressure head. Note that only the sensible choices of the reflection were tested. The ends of the signal were identified as the points where the signal crossed the x-axis. The resultant magnitude of F_{11} is shown in Figure A3 (c). The results of seven F_{11} deviated only slightly at higher frequencies but they generally lined up very closely to each other (note the scale of the y-axis). The maximum difference in the magnitude was 4.8×10^{-5}. Although not shown here, other FRFs were equally insensitive to the leak reflections in Figure A3 (b). Therefore, the extracted FRM is considered practically unaffected by the choice of the signal boundaries.

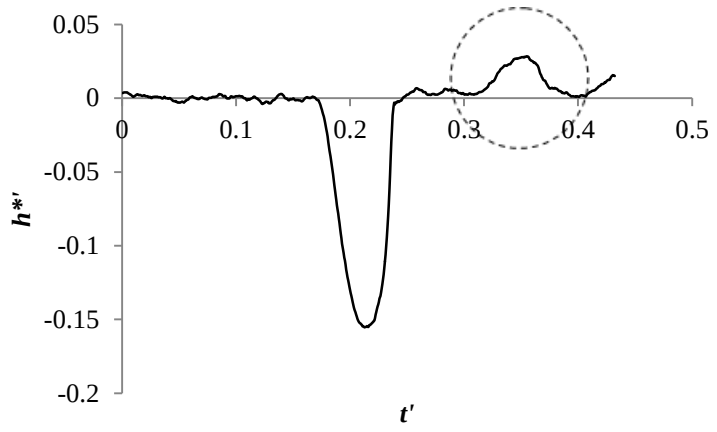

(a) Measured pressure trace with leak

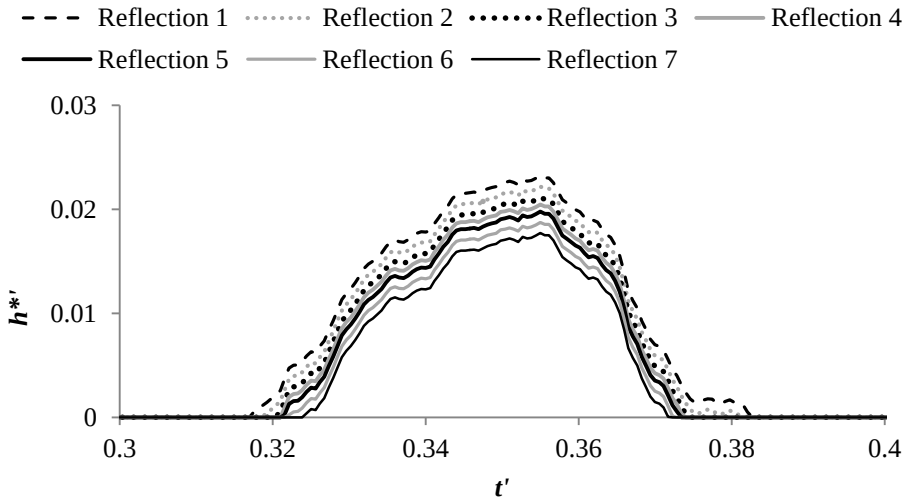

(b) Leak reflection with different base lines

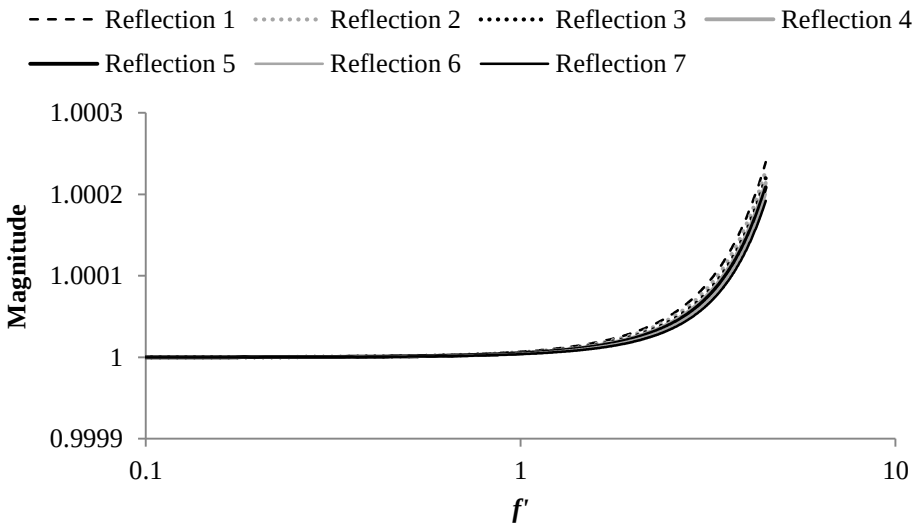

(c) Magnitude of F_{11}

Figure A3 – Errors associated with the judgement of signal boundaries